Title
Vision restoration in animal models of human blindness using natural and engineered light-gated receptors

Author
Gaub, Benjamin Merlin

Publication Date
2015

Peer reviewed|Thesis/dissertation

Vision restoration in animal models of human blindness using natural and engineered light-gated receptors

By

Benjamin Merlin Gaub

A dissertation submitted in partial satisfaction of the

requirements for the degree of

Doctor of Philosophy

in

Neuroscience

in the

Graduate Division

of the

University of California, Berkeley

Committee in charge:

Professor Ehud Y. Isacoff, Chair

Professor John G. Flannery

Professor Christopher Chang

Professor Marla Feller

Spring 2015

Abstract

Vision restoration in animal models of human blindness using natural and engineered light-gated receptors

by

Benjamin Merlin Gaub

Doctor of Philosophy in Neuroscience

University of California, Berkeley

Professor Ehud Y. Isacoff, Chair

In the first part of my work, I describe the design and characterization of new optical tools using azobenzene-based chemicals to install light-sensitivity to ligand-gated receptors. Light as a stimulus allows for precise temporal and spatial control, it is technically easy to deliver to the sample and can be patterned by means of spatial light modulation or holographics. These properties make it desirable to remote control the activity of receptors and receptor subtypes by light. To achieve optical control of ligand-gated receptors, a link between ligand activation and light-sensitivity is needed. The Isacoff lab was at the forefront of developing a technique called chemical "optogenetics", in which light-sensing and ligand-gating functions are combined in a single molecule, the 'photo-switch' that can be covalently tethered to the receptor, rendering it light-sensitive. The attachment site of the photo-switch on the receptor determines the directionality of the response, with some positions causing light induced activation or agonism while others lead to antagonism or light-induced receptor block. Using this technique, I developed and characterized various light-gated nicotinic acetylcholine receptors (LinAChRs), which are the focus of chapter 2. These optically controlled LinAChRs can be used as tools to investigate contribution of specific receptor subtypes to physiological function as well as study their role in diseases – experiments that were not possible before with pharmacological agents.

I further expanded the technique of chemical optogenetics from ion channels to G-protein coupled receptors (GPCRs). GPCRs are membrane bound receptors that modulate important physiological processes, like cellular excitability, plasticity, signaling and behavior, to name a few. They are also indicated in many diseases, making them the largest drug targets in the body. To demonstrate the ability to optically control GPCRs, I focused on a specific family of GPCRs, the metabotropic glutamate receptors (mGluRs). With the use of a glutamate-based photo-switch, I designed multiple subtypes of light-gated metabotropic glutamate receptors, or 'LimGluRs', and showed light induced agonism and antagonism in cultured HEK cells and neurons as well as in zebrafish, *in vivo*. This study is described in chapter 3. Following initial characterization of LimGluRs, these new tools served as the basis for further studies investigating metabotropic

glutamate receptor stoichiometry, cooperativity and conformational dynamics, shedding light on mGluR function at the molecular level.

In the second part of my thesis, I describe the application of light-gated receptors towards restoration of visual function in animal models of human blindness. Inherited retinal degeneration is one of the leading causes of blindness and affects more than 1 in 3000 people worldwide. Most of these retinal dystrophies are caused by genetic mutations in photoreceptor genes that lead to progressive loss of rods followed by the loss of cones, leaving the retina insensitive to light. Optogenetic treatments aim to restore light-sensitivity by installing optical actuators in the remaining cells of the retina, using viruses as gene delivery vehicles. Recent studies have demonstrated that optogenetic treatment can restore light sensitivity to retinal explants, drive light responses in the visual cortex and enable innate and learned visually guided behavior in animal models of retinal degeneration. It remains unclear, however, which target cells are best suited to act as artificial photoreceptors, what optical actuators are optimal to photo-sensitize the respective target cells and how well the treatments can be translated between different model organisms. To answer some of these questions, I used the light gated ionotropic glutamate receptor LiGluR as optical actuator. LiGluR had been previously developed in the Isacoff lab and applied to the retina in the Flannery lab. The advent of the red-shifted photo-switch $MAG0_{460}$ allowed me to stimulate with light in the visible part of the spectrum, a major improvement over previous studies. I installed LiGluR upstream in the degenerating retina, in ON-bipolar cells (ON-BCs) as well as downstream in retinal ganglion cells (RGCs) and compared the output from these two target cells. While both approaches restored light responses in retinal explants and enabled innate and learned visually guided behavior in blind mice *in vivo*, there was a clear difference in response properties: the downstream targets showed a highly synchronized retinal output whereas upstream target cells had a more diverse output, potentially encoding a higher level of information content by engaging synaptic connections in the inner plexiform layer. We concluded that downstream targets would be suited for late stage treatments whereas upstream targets would be better suited for early stage intervention, in which retinal circuitry would likely be more preserved. In this study, we also demonstrated that our treatment could be translated from mice to dogs by showing restoration of light responses in retinal explants from blind dogs following *in vivo* treatment. These results are summarized in chapter 4.

A major drawback from state-of-the-art optogenetic treatments is the relative insensitivity of current optical actuators to light. Most actuators require very bright light for activation, which is potentially toxic to the remaining cells of the retina. In order to enhance light-sensitivity, I turned to light-gated GPCRs for their ability to amplify signals via G-protein cascades. Specifically, I expressed the retina-native GPCR rhodopsin ectopically in ON-BCs of blind mice and found a 1000-fold improvement in sensitivity when compared to the ion channel cousin channelrhodopsin2 (ChR2) under the same conditions. Furthermore, rhodopsin expression restored light responses in the visual cortex and, albeit displaying slower kinetics, enabled treated mice to distinguish dynamic spatial patterns moving at 0.6 cycles per second from equi-luminescent static patterns. Although the molecular mechanism by which rhodopsin depolarizes ON-BCs remains unknown at this time, the notion that ectopically expressed light gated GPCRs can restore visual function in extremely low light conditions is remarkable. This study is described in chapter 5.

Finally, in the last chapter of my dissertation, I describe the design and prototyping of a sensory substitution device, developed as navigational aid for the blind. Inspired by bats and by a

rare group of blind human echolocators that produce emit sampling sounds via tongue clicks and use the reflected echoes as navigational cues, I helped develop a device for ultrasonic echolocation that enables “sight-through-sound”. Our prototype, the ‘Sonic Eye’ allowed naïve users to make laterality and depth judgments indicating that humans have an innate capacity for echolocation. Experienced users were able to accurately locate objects in space when blindfolded solely by interpreting the reflected echoes

This thesis is dedicated to my family for planting the seed of curiosity that keeps me thriving in science and their never-ending support throughout my scientific journey

Table of contents

Abstract....1
Table of contents ii
List of figures v
Acknowledgment....vii

Chapter 1 Introduction 1
The healthy and the degenerated retina…….... 1
Retinal therapies for congenital blindness……..... 4
Considerations for optogenetic gene therapies……..... 7
Alternative non-invasive avenues…….....……11

Chapter 2 Optochemical control of genetically engineered neuronal nicotinic acetylcholine receptors…… 12
Introduction…….....…. 12
Results…… 13
Photoswitchable tethered ligand design……...…….. 13
Attachment site screening……..... 13
Photoactivation of engineered nicotinic acetylcholine receptors…….. 15
Photoinhibition of engineered nicotinic acetylcholine receptors…….. 18
Thermal relaxation of the photoswitchable ligands……..…… 18
Discussion…….. 22
Materials and Methods……....…….. 24
Supplementary Information…….…… 26
Supplementary Methods…….……..…….....…….....…… 31

Chapter 3 Optical control of metabotropic glutamate receptors…….…….. 35
Introduction……..……. 35
Results…….…….. 38
Tether model pharmacology and Monte Carlo simulations..…… 38
Photo-antagonism by D-MAG-1: LimGluR2-block …….……...…… 39

Photo-agonism by D-MAG-0: LimGluR2…… 40
Generalization of photocontrol to mGluR3 and mGluR6…… 42
Optical control of excitability in hippocampal neurons…… 43
Optical control of synaptic transmission…… 44
Optical control of tonic inhibition by LimGluR2-block…… 46
Optical control of excitability in hippocampal slices…… 46
Optical control of zebrafish behavior…… 48
Discussion…… 50
Materials and Methods…… 52
Supplementary Figures…… 57

Chapter 4 Restoration of visual function by expression of a light-gated mammalian ion channel in retinal ganglion cells or ON-bipolar cells…… 64
Introduction…… 64
Results…… 66
Restoration of light response to the retina of *rd1* mouse by LiGluR in RGCs or ON- BCs…… 66
Kinetics and frequency detection supported by light-sensitive RGCs and ON-BCs …… 71
Differences between light-induced RGC firing with LiGluR in RGCs versus ON-BCs …… 71
LiGluR restores innate and learned associative light-guided behavior …… 72
LiGluR in RGCs restores the retinal light responses in a canine model of retinal blindness …… 76
Discussion…… 78
Methods…… 82
Supplementary Note…… 89
Supplementary Figures…… 92

Chapter 5 Optogenetic vision restoration using rhodopsin for enhanced sensitivity..... 100
Introduction..... 100
Results..... 104
Rhodopsin can be expressed ectopically in ON-bipolar cells of the *rd1* mouse retina..... 104
Rhodopsin expression in ON-BCs restores light responses to retinal explants *in vitro*..... 104
Rhodopsin activation in ON-BCs drives cortical responses *in vivo*..... 105
Rhodopsin expression restores innate light avoidance and enables learned visually-guided behavior in *rd1* mice..... 106
Discussion..... 110

Materials and Methods..... 113
Supplementary Material..... 117

Chapter 6 A device for human ultrasonic echolocation..... 120
Introduction..... 120
Specifications and signal processing.....124
Methods..... 127
Results..... 130
Discussion..... 132
Summary and Conclusion..... 135

Chapter 7 Conclusion and future directions..... 137

References..... 140

List of figures

Figure 1.1 Schematic organization of neurons in the mammalian retina..... 3

Figure 1.2 Photochemical tools for controlling neural function..... 6

Figure 2.1 Photoswitchable ligand design for the optical control of neuronal nicotinic acetylcholine receptors.....14

Figure 2.2 Choice of cysteine attachment sites for photoswitchable ligand conjugation..... 16

Figure 2.3 Photoactivation of nicotinic acetylcholine receptors with a tethered agonist.....17

Figure 2.4 Molecular model of a nicotinic acetylcholine receptor with a virtually tethered photoswitchable agonist.....19

Figure 2.5 Photoinhibition of nicotinic acetylcholine receptors with a tethered antagonist 20

Figure 2.6 Thermal relaxation of the photoswitchable agonist and antagonist..... 21

Figure 3.1 Design of photoswitches for light-control of mGluR2.....37

Figure 3.2 Monte Carlo simulations and cysteine-scanning of mGluR2 LBD..... 39

Figure 3.3 Photo-antagonism and photo-agonism of mGluR2.....41

Figure 3.4 Extension of photoswitching from mGluR2 to mGluR3 and mGluR6…….42

Figure 3.5 LimGluR2 hyperpolarizes and reduces excitability in cultured hippocampal neurons 44

Figure 3.6 Optical activation of LimGluR2 reversibly decreases excitatory and inhibitory postsynaptic currents and increases paired pulse facilitation at hippocampal autapses……..... 45

Figure 3.7 LimGluR2-mediated control of neuronal excitability in hippocampal slice….. 47

Figure 3.8 Agonism of endogenous group II mGluRs and photo-agonism of LimGluR2 increases escape response probability in zebrafish larvae……49

Figure 4.1 LiGluR-MAG0460 expressed in HEK cells is activated by visible light, relaxes in the dark and detects changes in light intensity..... 66

Figure 4.2 LiGluR expression downstream in RGCs and upstream in ON-bipolar cells restores light responses in the rd1 mouse retina in vitro..... 69

Figure 4.3 LiGluR-MAG0460 in RGCs and ON-BCs of rd1 mouse retina drives light responses with similar characteristics…….....70

Figure 4.4 LiGluR expression downstream in RGCs synchronizes responses …….74

Figure 4.5 LiGluR expression restores innate and learned light guided behavior in *rd1* mice *in vivo*..... 75

Figure 4.6 LiGluR expression in RGCs restores light responses in the *rcd1* canine retina *in vitro* ……..... 77

Figure 5.1 Rhodopsin can be expressed ectopically in ON-bipolar cells of the *rd1* mouse retina..... 102

Figure 5.2 Rhodopsin expression in ON-BC restores light responses to retinal explants *in vitro*.....103

Figure 5.3 Rhodopsin activation in ON-BCs of rd1 mice drives cortical responses

in vivo …….....108
Figure 5.4 Rhodopsin expression restores innate light avoidance and enables learned visually guided behavior in *rd1* mice …… 109

Figure 6.1 Device layout..... 123
Figure 6.2 Schematic of waveforms.....123
Figure 6.3 Measurement of transfer functions for ultrasonic microphones and ultrasonic speaker as a function of angle …….....125
Figure 6.4 Two alternative forced choice spatial localization testing..... 126
Figure 6.5 Ten-position localization in three trained participants …….. 136

Acknowledgment

This work is a collaborative effort of many talented scholars without whom it would have not been possible to produce this thesis. I wish to express my deepest gratitude towards those who helped me along this journey, keeping me sane and upbeat when the science was letting me down, providing guidance when I felt lost, providing mentorship and stewardship in this sometimes very chaotic road to graduation. Thank you!

Foremost I wish to thank professor Ehud Isacoff. It was he who enabled me to come to Berkeley by providing several letters of support and recommendations based on a short conversation we had in his office when I met him as a prospective student. My guerilla tactic worked and with Ehud's blessing I received the Fulbright scholarship, got hands on electrophysiology experience in Axel Borst's lab at the Max Planck Institute in Munich, Germany and got admitted to Berkeley. Ehud continued his endless support throughout my PhD, providing the vision, the big picture, and being a true scientific role model. He also facilitated a number of collaborations and most generously hired two technitians to help me with my projects, which really propelled my research.

I owe so much gratitude to John Flannery, who adopted me in his lab and provided me with endless guidance and mentorship along with great Jazz music and Werner Herzog movies. He volunteered a lot of his valuable time to discuss my projects at any time of the day and allowed me to use all of his reagents and facilities. He is a very generous and altruistic man, one of a kind.

I would like to direct special thanks to my thesis committee members Marla Feller and Chris Chang for providing helpful advice during my thesis meetings. During my second year, I had the pleasure to teach for David Presti who took me under his wing and showed me how to be a good teacher and lecturer. I truly admire his personable style of teaching and it was very special to work for and with him.

The members of the Isacoff lab were instrumental to my success. Mike Berry, a friend and college who I have spent close to 4 years of my PhD should receive special mention. We designed, conducted and analyzed many of the experiments that are mentioned in this thesis together. It's been a true pleasure collaborating with Mike. Amy Holt joined our small subgroup to assist with animal physiology and thanks to her patience and skills she succeeded in experiments that led to two publications. Andreas Reiner, a postdoc in the lab, should receive special praise for his immense and never ending support in designing and analyzing experiments, teaching me new skills and being instrumental in preparing my manuscripts. Josh Levitz was a very important collaborator for the experiments described in chapter 3 and has continued to be one of my favorite lab mates to bounce ideas around with and get advice from. I would like to thank Sandra Wiese for her endless support in adding new experiments to our animal protocols as well as keeping all the paperwork and regulations in check. Cherise Stanley and Zhu Fu helped tremendously with molecular biology. Holly Aaron helped me with

microscopy. Elizabeth Carrol and Adam Hoagland helped me with design and alignment of light sources. Harald Janoviak taught me electrophysiological techniques. Shai Berlin, Susy Kohout, Drew Friedman and Carlos Pantoja were inspiring me with their ideas that they communicated during my lab meetings.

The members of the Flannery lab were equally instrumental to my success. I would like to say special thanks to Meike Visel who happily packaged countless vectors during my PhD and who ensured that I wouldn't forget how to speak German. Trevor Lee and Leah Byrne helped me with intraocular injections and were always a good resource for discussing ideas. Cameron Baker and Tim Day were a pleasure to work with and kept the lab spirit at an all time high.

Jascha Sohl-Dickstein, Santani Teng, Alex Maki-Jokela and Nicol Harper should receive special praise for inviting me in to the Sonic Eye project described in chapter 6. It was a very special experience to conduct science among friends and colleges without professorial guidance. I am very grateful for Jeff Hawkins providing us a generous goodwill donation that helped propel the project as well as providing good network opportunities.

I would like to thank Dirk Trauner at the LMU in Munich for making all the wonderful photo-switches that allowed me to do most of the experiments described in my thesis. I would like to thank my collaborator at Stanford, Jerome Lecoq for all the time and energy that he devoted to our *in vivo* calcium imaging project. I would also like to thank my collaborator at UC Davis, Chris Fortenbach for the many hours of recordings that he invested in a perfectly dark room in an attempt to record light signals from single bipolar cells in retinal slices. I would like to also thank my collaborator Ken Greenberg who was a great mentor in the beginning stages of the project described in chapter 5. Furthermore I want to thank Frank Werblin and Hillel Adesnik for generously allowing me to perform electrophysiological recordings in their labs using their equipment.

I would like to thank the Fulbright foundation for supporting me financially and Kate Leiva and Tom Koerber at IIE for being great student coordinators.

Finally, without the endless support from my entire family and my dear friends at the Asilomar house I couldn't have accomplished this body of work.

Chapter 1 Introduction

The eye is a beautifully complex organ. Charles Darwin noted "that the eye...could have been formed by natural selection seems, I freely confess, absurd in the highest possible degree"[1]. Its intricate design is what creationist often time use as a prime example of irreducible complexity – an organ so complicated that it couldn't function in the absence of any of its pieces and therefore cannot have evolved from a more primitive form. But in fact, by conservative estimates, it only takes about 400 thousand generations[2] to form complex lens-eyes from simple photoreceptive spots, and well over 50 different types of eyes have evolved independently from one another in the animal kingdom[3]. Much more surprising to me is the strict conservation of the light sensitive proteins, the opsins and their ligand, retinal[4]– every visual animal relies on this system in order to see. In this thesis, I have expanded nature's set of photoreceptors by design of novel light sensors that I applied towards restoration visual function. That is a humbling thought.

The healthy and the degenerated retina

The retina is a 200μm thick neural tissue that lines the back of the eye, and it serves the purpose to convert photons into an electrical signal that can be used to construct an image by the brain. The retina is a fairly well studied system. It contains approximately 55 cell types[5] that are functionally and morphologically distinct. The neurons are highly organized in three layers, with cell bodies stacked tightly against each other, forming the nuclear layers, and their processes forming synaptic connections in the plexiform layers (see Fig 1.1). The outer nuclear layer (ONL) contains ciliated light-sensing cells, the rod and cone photoreceptors. The inner nuclear layer (INL) contains horizontal, bipolar cells (BC) and amacrine cells and the ganglion cell layer (GCL) contains retinal ganglion cells (RGCs). Müller Glia cells span all three layers of the retina, may act as fiberoptic guides[6] and support the retina with nutrients and scaffolding. Astrocytes are associated with RGC axons that form the optic nerve and maintain neuronal homeostasis and metabolic processes[7]. Retinal pigment epithelium cells are located in the back of the eye, proximal to rods and cones. They recycle and supply the chromophore 11-cis retinal, absorb scattered light and phagocytose photoreceptor outer segments[8].

When light enters the eye, photons are captured by rod and cone photoreceptors and converted to an electrical signal via the transduction cascade. Photoreceptor outer segments have membrane disks that are filled with opsin and retinal. Light absorption leads to isomerization from 11-cis to all-trans retinal, which leads to activation of a G-protein cascade via conformational changes in the opsin. The information is passed to BC, which in turn signal to RGCs. The signal leaves the retina through the axons of RGCs that form the optic nerve and is relayed via the lateral geniculate nucleus (LGN) to

the visual cortex for higher order visual processing. Along this vertical axis of information flow the number of cells in the retina converge from 100 mio photoreceptors to 10 mio BCs to 1 mio RGCs[9] while the transmitted information becomes richer, already forming visual percepts at the level of the RGCs. Increments and decrements of light are encoded at the first visual synapse between photoreceptors and BCs, motion (via direction selectivity) and contrast (via lateral inhibition) arise at the synapse between BCs and RGCs[10]. In addition, information flows horizontally through a long reaching network of interneurons, the horizontal cells in the OPL and amacrine cells in the IPL.

Vision is arguably our most important sensory modality and vision loss due to genetic or environmental causes is devastating. Many forms of blindness are caused by inheritable genetic mutations, with no effective cure to date (but see: [11,12]). There are currently 212 genes that are known to be involved in degenerative diseases[13]. Most diseases are caused by mutations that don't cluster around a single gene[14], making it difficult to find a 'one size fits all' treatment. Most inherited degenerative diseases cause photoreceptor cell death, ultimately leading to blindness but the underlying mechanisms are diverse. Age related macular degeneration, the leading cause of blindness with 9 mio Americans affected, and Stargardt's macular dystrophy are characterized by the dysfunction and degeneration of the retinal pigment epithelium. Choroiderimia (1:50.000) is characterized by progressive atrophy of choroid, retinal pigment epithelium and photoreceptors. Glaucoma (1:40 adults> 40 years of age) leads to optic nerve damage and loss of RGCs, whereas retinitis pigmentosa (1:4000) and Leber's congenital amaurosis (1:50.000) lead to loss of rod photoreceptors that is followed by loss of cones. Owing to the diversity of the different phenotypes of retinal degeneration, a total of 33 clinical trials have been approved, are currently in progress or have been completed to date [15]. The approaches that are currently explored in these clinical trials are outlined in the next paragraph.

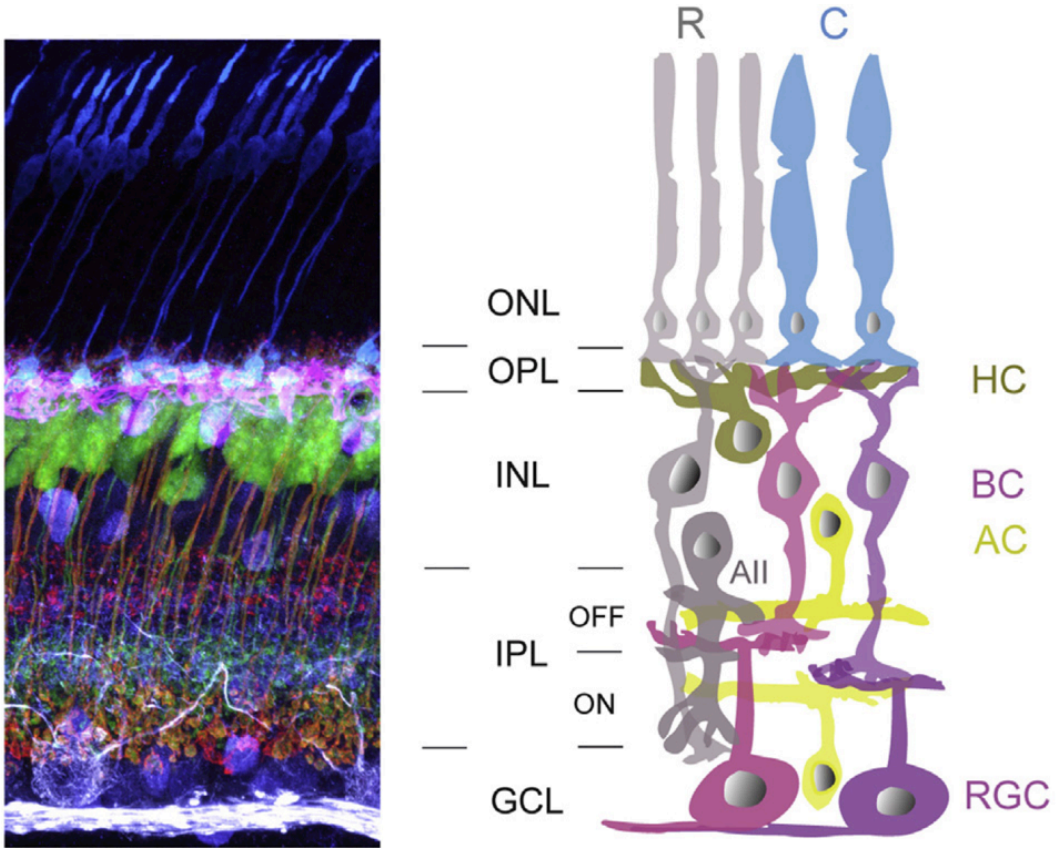

Fig. 1.1 Reproduced from[16] with permission. Schematic organization of neurons in the mammalian retina. (Left) Vertical section of mouse retina showing labeling of the major neuronal cell types. Immunostaining for cone photoreceptors (anti-cone arrestin, blue), horizontal cells (anti-calbindin, pink), bipolar cell terminals (anti-synatotagmin2 and anti-PKC, red), amacrine cells (anti-calretinin, purple), and ganglion cells (SMI-32, white). Immunolabeling was performed on a retina from a transgenic line in which a subtype of bipolar cell (ON- type) express yellow fluorescent protein (green). ONL: outer nuclear layer, OPL: outer plexiform layer, INL: inner nuclear layer, IPL: inner plexiform layer and GCL: ganglion cell layer. (Right) Schematic of the retina. R: rod photoreceptor, C: cone photoreceptor, HC: horizontal cell, BC: bipolar cell, AC: amacrine cell, RGC: retinal ganglion cell. The rod pathway (cells shaded in gray) conveys scotopic information to the photopic cone pathway, via the AII amacrine cell. Colored cells represent cone pathways. Neurons that are depolarized by light increments restrict their synaptic connectivity to the ON sublamina of the IPL, whereas connections of cells that are hyperpolarized instead form the OFF sublamima.

Retinal therapies for congenital blindness

Following the onset of degeneration, despite the death of major cell classes, the surviving cells of the retina remain morphologically intact and electrically active, allowing a window of opportunity for treatment[17]. The types of treatment that have been explored differ in stage of development, invasiveness, cost, sensitivity to light, response kinetics and the resolution that can be obtained, among many others. The effected cell type and stage of disease will determine which therapy is most suitable for which condition.

Retinal implants record information about the visual world through imaging sensors and convert photons into electric signals that are used to directly stimulate the degenerating retina via implanted microchips. This technology is among the most developed technologies for the blind and one such device, the Argus II has recently been approved by the FDA[18]. The implants differ in the placement of the imaging sensor and the electrodes relative to the retina. In epi-retinal arrays, the electrodes are placed in the vitreous in proximity to the RGCs and the electrodes receive input from imaging sensors that are external to the eye. For sub-retinal arrays, the imaging sensors are coupled to the electrodes (for example via photovoltaics) and the electrodes are positioned between the retina and the retinal pigment epithelium contacting amacrine and BCs. Supra-choroidal devices are placed between the choroid and the sclera and the receive input from external sensors.

The retinal implants have been successful in restoring some aspects of visual function in patients with retinitis pigmentosa. Treated subjects were able to perceive light and perform statistically better on object localization and motion discrimination. The best visual acuity in a treated subject was 20/1260[12]. Despite these advances, the surgical procedure required to insert the implants is very invasive and costly (with an estimated 100.000$ per treatment) and the spatial resolution that the implants offer is rather poor (the equivalent of a 60 pixel camera). Since the electrodes are randomly placed onto the retina, the stimulating signal from the electrodes is not always congruent with the native circuitry of the retina. Furthermore, the distance from electrodes to the cells is not homogenous leading to varying amounts of stimulating current that each cell is receiving. This makes it a hard task for the brain to decipher the incoming information. The number and spacing of electrodes as well as the contact of electrodes with the tissue have to be improved to give the user a better image.

Stem cells have the ability to self-renew and to differentiate into any class of cells, giving rise to the desired tissue. It is easy to see the potential of stem cells for treating retinal diseases. The adult human retina does not have any endogenous stem cells, but embryonic stem cells (ESC) and induced pluripotent stem cells (iPSC) can be introduced as tissue transplants or in the form of dissociated cells. Sub-retinal transplantation bears potential to replace degenerated retinal pigment epithelium cells for age related macular

degeneration or Stargardt's macular dystrophy. A recent study demonstrated that transplantation of human iPSC derived retinal pigment epithelial cells into retinal degeneration rats promoted photoreceptor survival via phagocytosis of the xenografted cells[19]. Similarly, sub-retinal transplantation of stem cells bears potential to replace photoreceptors in diseases like retinitis pigmentosa. Studies in mouse models of retinal degeneration show successful migration, differentiation and integration of ESC derived transplanted photoreceptor precursor cells[20] and even functional restoration of visually-guided behavior[20,21]. Furthermore, sophisticated 3D culturing systems have been developed to differentiate stem cells into self organizing layered structures, called 'optical cups' resembling retinas *in vitro*[22,23]. These optical cups express markers of most retinal cell types and the cells at the outermost layer, presumably photoreceptors, showed outer segment disk formation and responded to light[22]. Optic cups could be used to model development of retinal degeneration, serve as a test bed for screening drugs or as a source for transplantable photoreceptor progenitor cells. For all these applications, it is important that potentially harmful proliferating cells are excluded from the pool transplantable cells due to toxicity and tumorgenicity. Methods have to be optimized to increase the number of optimally differentiated cells, improve on integration, function and long-term survival of engrafted cells before moving to clinical trials.

Neuroprotection aims to prevent or slow cell death that occurs during retinal degeneration. Neuroprotective therapy has mostly focused on targeting the apoptotic pathway but more recently necrosis, autophagy and inflammation pathways are being investigated. Monoclonal antibodies, small inhibitory RNA and neuroprotective peptides have been developed to interfere with apopototic pathways[24]. The ciliary neurotrophic factor CNTF is the most prominent candidate for neuroprotective therapy. CNTF has been shown to have a neuroprotective effect on rod photoreceptors[25], cone photoreceptors[26] as well as RGCs[27] in animal models of retina degeneration. Two trials have been completed to date that found evidence for cone photoreceptor protection and outer segment regeneration in patients with retinitis pigmentosa and age related macular degeneration[28]. Novel neuroprotective agents may be discovered from high throughput screening of plant extracts on human cell lines as well as from stem cell derived 'optic cups'.

Gene therapy describes a technique using safe, pseudotyped viruses, to deliver therapeutic DNA to a cell type of interest. If the identity of the mutant gene is known, and the mutant gene itself is non-toxic, delivering a healthy copy of that same gene may suffice as treatment. The gene replacement approach has been demonstrated in two extremely successful clinical trials, one treating young patients with Leber's congenital amaurosis[29] and the other treating patients with choroiderimia[30]. There are a total of 5 gene therapy clinical trials ongoing in the United States to treat retinal diseases. The eye is an ideal tissue to develop gene therapy. The anatomy of the retina is very stereotyped with morphologically distinct cell classes and cell specific promoter elements that allow for cell specific gene expression. Furthermore, the eye is a relatively immune privileged organ, the blood brain barrier ensures that most of the virus is retained in the eye, and the

injected virus is confined to a small volume allowing for a single treatment to be effective. Eyes come in pairs so one eye can be sham treated as internal control for the experimental eye.

With the advent of new genome editing techniques, it is now possible to modify genomic DNA by either disrupting/silencing toxic genes or by correcting mutations. Zink finger nucleases (ZFNs), transcription activator-like effector nucleases (TALENs) or the CRISPR/Cas9 system can be used to induce DNA double strand breaks at specific sites in the genome. DNA double strand breaks can be used to prevent expression of mutant proteins that are toxic to the cell (e.g. P23H rhodopsin[31]) or correct the mutant sequence by site-specific incorporation of a template sequence via non-homologous end joining. However exciting, a high number of cells would need to be transduced for this approach to be successful in restoring visual function. Additionally, gene correction relies on cellular DNA repair mechanisms. DNA repair occurs mostly during the replication phase, but is down regulated in post-mitotic cells. Minimizing off target DNA breaks will be another important issue.

Gene therapy can also be utilized to introduce foreign DNA to retinal cells, giving them a gain of function. Recently, optogenetics has revolutionized the field of neuroscience by allowing orthogonal control of electric signaling in specific neurons *in vivo* using light. Virally introduced DNA that encodes for optical actuators can be used to install light sensitivity to the remaining neurons of the degenerating retina, thus creating 'artificial photoreceptor cells'. This approach has been shown to restore aspects of visual function in animal models of human blindness[32-37]. Three different classes of optical actuators have been described[38]: i) optogenetic actuators like microbial opsins use an exogenous opsin and endogenous photoswitch ii) optopharmacologic actuators are exogenous photoswitchable ligands that act on endogenous channels, and iii) optogenetic pharmacological actuators require introduction of both an exogenous channel and an exogenous photoswitchable ligand (see Fig 1.2). Human clinical trials have not been initiated to date. Light sensitivity, toxicity of light levels and photo-switches, safety of viral vectors as well as potential immune responses to xenoplants remain to be tested first in non-human primates. Specifically, patients with retinitis pigmentosa that have lost their photoreceptors, could benefit from gene augmentation therapy.

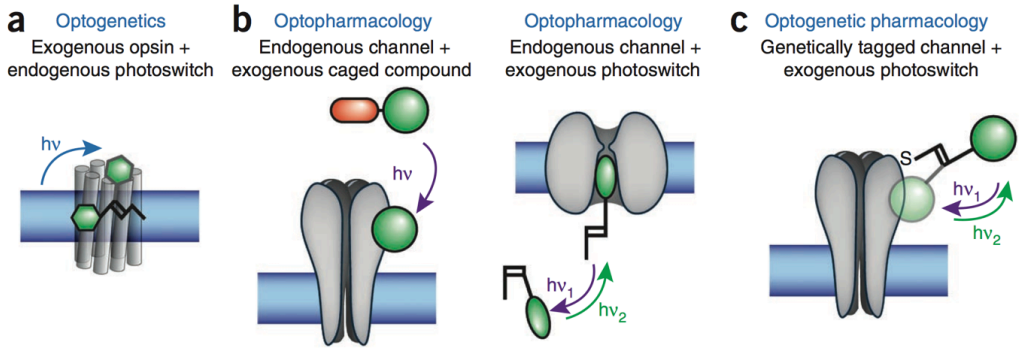

Figure 1.2 (reproduced with permission from the authors) Photochemical tools for controlling neural function. (**a**) Optogenetics. (**b**) Optopharmacology. **(c**) Optogenetic pharmacology.

Considerations for optogenetic gene therapies

Gene transfer to the retina

Inserting foreign DNA into specific cells of an adult organism is not a trivial task to solve. Cells have developed clever ways to identify foreign DNA, distinguish it from the cells' own DNA and selectively degrade only the non-native DNA for protection and integrity of the genetic information. Viruses have evolved mechanisms to trick or escape the cells' protective mechanism allowing them to insert foreign DNA into the nucleus. In recent years, scientists have harnessed this mechanism and turned virulent virions into therapeutic gene delivery vehicles that can deliver DNA cargo to specific cells.

Herpes virus, lenti virus, adeno virus and adeno-associated virus have shown to be effective in animal models of retinal diseases[39-41]. Of these, the most widely used virus variant for gene therapy is the non-pathogenic parvovirus adeno-associated virus (AAV), due to its high efficiency, stable gene transfer and low toxicity compared to the other vectors[42,43]. AAV requires a helper virus such as the adenovirus to replicate[44]. The virion shell is 25nm in diameter and encapsulates a 4.7kb single stranded DNA. AAV has two open reading frames, one that encodes for proteins of the replication machinery and another that encodes structural proteins that form the capsid[44]. There are 11 naturally occurring AAV capsid variants, called serotypes (AAV1-AAV11) and over 100 AAV variants with varying efficiency for infecting retinal cells, a property called tropism[44]. However, the infectious properties of naturally evolved AAVs don't match with the therapeutic need for gene delivery vectors. To solve this problem, novel variants have been designed to tailor AAVs for cell specific gene delivery.

The capsid genes specify which cells the virus can integrate into via cell surface receptor interactions (e.g heparansulfate for AAV2). Mutations in the capsid genes can lead to novel AAV variants with altered tropism. Mutants have been generated by rational design[45], in which structural knowledge of AAV can be used to improve viral properties, or by directed evolution whereby selection processes allow beneficial mutations to accumulate from a large library of capsid mutants[44,46-48]. For all therapeutic vectors, the viral replication genes have been replaced by therapeutic cargo DNA, consisting of promoter element followed by the gene of interest. The viral payload must not exceed 4.7kb.

The therapeutic vector can be delivered to the retina by intravitreal or sub-retinal intraocular injection. Intravitreal injections, whereby the virus is deposited in the vitreous humour, lead to pan-retinal expression, are less invasive and relatively easy to perform making them therapeutically relevant. However, expression in the inner retina is limited due to the inner limiting membrane that acts as a vector trap[49] or barrier, especially in larger animal models. Sub-retinal injections, whereby the virus is deposited between the retina and the RPE, causing a local retinal detachment or bleb, lead to strong

and dense expression in the inner retina. However, expression is limited to the area underneath the bleb, the success rate is lower and the procedure is more invasive.

Cell specific targeting can be achieved with cell specific promoter elements that facilitate gene transcription only in one particular cell type. Such promoters have been identified for some cells, for example rod photoreceptors (rho) cone photoreceptors (mCAR[33]) and ON-BCs (grm6[36]) but remain elusive for amacrine cells and RGC subtypes. Another approach utilizes directed evolution to screen for capsid variants that can only integrate in one cell type. For example, the Müller cell specific capsid SsH10 was identified[48] using this technique. Cell specific capsids can be used in combination with ubiquitous promoters (e.g. CMV) leading to higher levels of transgene expression compared to most cell specific promoters. Moreover, insufficient amounts of protein for example in a heterozygous mouse[50] with 50% of normal rhodopsin expression levels as well as excessive amounts of protein for example in a mouse with 123% of normal rhodopsin expression[51] can lead to retinal degeneration. A precise amount of transgene expression may be required for specific therapies to be effective. Cell specific promoters are in limited supply and don't allow for fine-tuning, whereas cell specific capsids allow precise titration of protein levels using a wide range of different promoter elements.

Cellular targets

One possibility is the non-targeted approach using a ubiquitous promoter that drives strong transgene expression without targeting individual cell types. This approach is based on the radical belief that the brain is plastic enough to decode the new signals that are originating from various cell types. Although recent results from patients with implanted microelectronic prosthesis supports the notion that the brain can adapt to a new retina signal, the quality of the restored visual function would likely be rather poor.

Cell specific targeting is currently limited by the availability of cell specific promoters. Transgene expression can be restricted to the RGC layer via a combination of the AAV2 capsid and the hSynapsin promoter[34,52]. This approach does not distinguish between ON and OFF RGCs, practically turning all RGCs into ON or OFF RGCs depending on the transgene. The main advantages of targeting the cells furthest downstream in the retinal circuitry are the large size allowing for high amounts of expression, easy access from the vitreous and robustness to degeneration in the case of retinitis pigmentosa. However, direct stimulation of RGCs shortcuts the retinal circuitry above, eliminating the option of motion sensing via direction selective RGCs and contrast enhancement via lateral inhibition. Resolution would be compromised owing to the large dendritic arbor of RGCs (200-400um). Moreover, RGCs axons project to the brain, which creates a safety concern in case of adverse reactions, e.g. inflammation.

ON-BCs and remnant cone photoreceptor cell bodies are promising upstream targets. Proximity of the target cell to the photoreceptor layer should improve the quality of the restored visual function provided that the retinal circuitry is still intact[53]. The

vertical On and Off pathways stay segregated providing a signal that is more congruent with the wild type circuitry, and the number of potential target cells is much larger compared to RGCs due to convergence[9]. However, the number of retinitis pigmentosa patients with intact retinal circuitry or remnant cones may be limited. Generally speaking, this approach would be most applicable for an early stage intervention. It is still unclear weather optogenetic treatment can halt or reverse retinal degeneration. Recent evidence from canine studies and human clinical trials on Leber congenial amaurosis suggest that restoring function in RPE cells does not reverse or halt the apoptotic pathways[54] and thus, installing photo-sensitivity to upstream cell targets may only provide a temporary cure.

In the future as more cell specific promoters and AAV capsids become available, AII amacrine cells will be interesting target cells. They are the most abundant amacrine cells of the retina, they are quite resistant to reorganization and can drive both ON and OFF pathways in the rod system.

Choice of optical actuator

Optical actuators have very different properties in regard to light-sensitivity, on and off kinetics, spectral sensitivity, immunogenicity and availability or delivery of the ligand and receptor. It is important to keep in mind the trade-off between different properties (e.g. inverse relationship between speed and sensitivity) and the molecular components of the target cell that might favor the choice of ion channel or G-protein coupled receptors (GPCRs) as actuator.

One important class of optical actuators are naturally occurring opsins. They come in two flavors: i) microbial opsins, which are light-sensitive ion channels and pumps found in algae and bacteria, and ii) vertebrate opsins, which are light sensitive GPCRs found in mammalian photoreceptor cells. Both vertebrate and microbial opsins bind the bioavailable chromophore vitamin A or retinal. Once the receptor is virally delivered and expressed in the target cell, the system can function autonomously without reapplication of chromophore.

Microbial opsins have been extensively characterized and applied as optogenetic visual prosthetics[32,33,35-37,46]. These opsins are appealing due to fast kinetics, enabling RGC firing rates of up to 200Hz[46], lack of bleaching due to covalent binding of retinal and availability of a wide range of mutants with improved properties like red shifted adsorption spectra[55,56], super fast kinetics or higher sensitivity[56]. However, microbial opsins require high light intensities for activation, they are potentially toxic to cells over time[57] and could induce immune responses due to their microbial origin. Furthermore, these optical actuators shortcut the target cell's molecular machinery, eliminating the option for adaptation or signal amplification.

The vertebrate opsins rod opsin and blue, red and green cone opsins have been studied less extensively. Once heterologously expressed, these light-gated GPCRs bear

potential to tap into the target cell's native machinery in principle allowing for amplification via second messenger cascades and adaptation[58] via phosphorylation, the success of which is determined by the molecular machinery present in the target cell. These GPCR systems are very sensitive to light but display slow kinetics due to lack of terminating factors in the target cells[59].

An alternative approach uses azobenzene-based chemicals as small molecule photo-switches that can be tethered to ligand gated receptors, turning them into optical actuators. The strength of this approach lies in the ease of tuning these systems via chemical engineering. Photo-switches have been red shifted in their spectral sensitivity[60], the attachment sites have been changed shifting the function from agonism to antagonism[61-63] and this strategy has been universally applied to ion channels[61-64] as well as GPCRs[65]. Due to receptor turnover, the azobenze photo-switch has to be re-applied for continuous function. Currently this is only possible via intraocular injection.

Alternative non-invasive avenues

Sensory substitution presents an interesting approach to partially restore visual experience and provide a sense for the surroundings, especially spatial cues. The sensory loss is compensated either by input from other sensory modalities or assisted by artificial receptors that are coupled to the brain via human-machine interfaces. The strength of this approach lies in its non-invasive nature, and thus presents an opportunity to test and prototype devices without the costly and time consuming hurdle of clinical trials and FDA approval.

The most basic forms of sensory substitution devices for the blind are tactile vision substitution devices, most notably the cane and braille. Auditory for vision substitution devices are more advanced and offer better resolution, among them are ultrasonic or laser rangefinders and video to audio mapping software like the VOICe[66,67] that can be used in combination with a smartphone.

There is mounting evidence from a group of legally blind human echolocators[68] that auditory signals are well suited to substitute for visual input. These blind human echolocators produce sampling sounds via mouth clicks that allow them to create a spatial map of their environment using the reflected echoes. They can use these echoes to orient themselves, thus enhancing navigation and mobility, to an astonishing degree – some of them, most famously Daniel Kish[68], can ride a bike, despite being blind. Functional magnetic resonance imaging (FMRI) studies have shown that echolocation produces visual sensation in experienced echolocators[69,70]. Surprisingly it was mostly visual and not auditory brain areas that were recruited for active echolocation. Echolocation can be potentially augmented by shifting the sampling sounds from audible wavelengths to the ultrasonic space. Technologically assisted echolocation has the potential to improve the resolution, allow for more complex sampling sounds (e.g frequency ramps), produce fewer reveberations and is less prone to interference with natual sounds providing an exciting avenue for future experimentation.

Chapter 2 Optochemical control of genetically engineered neuronal nicotinic acetylcholine receptors

This chapter was published in Nature Chemistry volume 4, in January 2012 with me a co-author.

Introduction

Acetylcholine (ACh) and its receptors have always been at the forefront of new developments in physiology. With its isolation as "Vagusstoff" in 1921, Otto Loewi established that a small diffusible molecule could mediate nervous activity and shaped the concept of a neurotransmitter[71]. Nicotinic ACh receptors (nAChRs) were among the first ion channels investigated long before the advent of molecular cloning and heterologous expression[72]. Numerous techniques in biophysics and chemical biology, including patch clamp electrophysiology[73], cryo-electron microscopy[74], and the expansion of the genetic code[75], were developed using nAChRs, and the powerful methods of molecular cloning were applied to nAChRs early on[76,77]. These studies established that nAChRs are pentameric ligand-gated cation channels that are expressed throughout the mammalian nervous system and at the neuromuscular junction[71]. The neuronal nAChR subtypes are composed of α2-α10 and β2-β4 subunits and can assemble both as heteromeric [e.g. $(\alpha4)_2(\beta2)_3$] and homomeric [e.g. $(\alpha7)_5$] pentamers[71]. Whereas the function of muscle nAChRs is well established, the physiological roles of neuronal nAChRs are still being unraveled. For instance, they have been strongly implicated in the pathophysiology of several psychiatric disorders as well as nicotine addiction and Alzheimer's disease[71,78]. However, progress in this regard has been held back by the lack of subtype-selective nAChR pharmacology and the difficulties associated with selectively targeting nAChRs in different parts of the brain.

These issues can be addressed using an approach called "Optochemical Genetics"[79,80]. In essence, this is an effort to photosensitize innately "blind" receptors using synthetic photoswitches. These can be covalently attached as photoswitchable tethered ligands (PTLs), which require a reactive functional group for bioconjugation - typically the sulfhydryl group of a cysteine[9,10]. By introducing the cysteine through genetic manipulation, these receptors can be targeted in a subtype-selective manner based on the subunit that contains the mutation[81]. Furthermore, the mutant receptors can be expressed in specific cell types in the brain and controlled with the millisecond precision and subcellular spatial resolution only light can provide[9,10]. This has already been achieved with voltage-gated ion channels and glutamate receptors. We now demonstrate that our approach towards photosensitizing Nature's molecular machines can be applied to pentameric ligand-gated ion channels as well, introducing the genetically targeted, Light-controlled nAChR (LinAChR).

Results

Photoswitchable tethered ligand design.

The development of LinAChR first required the design and synthesis of proper PTLs. Our PTLs typically consist of a maleimide as a cysteine reactive group, an azobenzene photoswitch, and a ligand head group that resembles known receptor agonists or antagonists. Three compounds known to interact with nAChRs guided the choice of the ligand: the photoaffinity label **AC-5** (**1**), the agonist homocholine phenyl ether (**HoChPE**) (**2**), and the antagonist **MG-624** (**3**). The presence of an aromatic ring separated by 7 atoms from the ACh moiety in **AC-5** (Fig. 2.1a), which acts as a full agonist at muscle nAChRs[82], suggests that the steric bulk of an azobenzene photoswitch may be tolerated in PTLs that act as tethered agonists. Although the much shorter molecule **HoChPE** is an agonist of nAChRs[83,84], the stilbene derivative **MG-624** is a potent antagonist of neuronal receptors[85]. Based on the steric similarity of stilbenes and azobenzenes, we therefore anticipated that corresponding PTLs could function as antagonists. Based on these model compounds, we synthesized Maleimide-Azobenzene-AcylCholine (**MAACh**) (**4a,b**) (Fig. 2.1a), a putative photoswitchable agonist for nAChR. We also synthesized Maleimide-Azobenzene-HomoCholine (**MAHoCh**) (**5a,b**) (Fig. 2.1b), wherein the choline moiety was replaced with homocholine and the spacer was removed to resemble **MG-624**. **MAACh** and **MAHoCh** were prepared by multistep total synthesis, as detailed in Supplementary Fig. S2.1. By taking absorbance measurements of the ligands in solution, we determined that both molecules can be maximally converted to their *cis* isomer by illumination with 380nm light and can then be reset to the *trans* isomer by 500nm illumination or thermal relaxation in the dark (Supplementary Fig. S2.2).

Preferably, a photosensitive receptor would be inactive in the dark, where azobenzene photoswitches generally reside in a *trans* configuration (Fig. 2.1c). Illumination with 380nm light would produce the *cis* configuration of the azobenzene and activate the receptor. Deactivation could then be achieved through conversion of the photoswitch back to its inactive *trans* configuration by illumination with 500nm or by thermal relaxation in the dark. Likewise, a tethered antagonist should block the receptor in its *cis* configuration (i.e. at 380nm), but should leave the receptor unimpaired in its *trans* configuration (at 500nm or in the dark), allowing it to be activated by free acetylcholine (Fig. 2.1d).

Attachment site screening.

These functional requirements can be met by the proper choice of cysteine attachment sites, which we decided to place on the β2 or β4 subunits of heteropentameric neuronal nAChRs. Using the X-ray structure of an acetylcholine binding protein (AChBP) in complex with carbamylcholine (PDB ID:1uv6)[86] and the model of AC-5 docked into the *Torpedo* nAChR[82] we identified an antiparallel beta sheet in the β subunit facing the ligand-binding site as a potential region for PTL attachment. Based on the calculated structures of our PTLs and distance measurements in the protein structures, we decided to install cysteines in positions S32, R34, E61, T63, R113, N115, and S117 of the β4

nAChR subunit. Homologous residues with identical numbering were chosen for β2. These residues are shown mapped onto a homology model of the
α 4 β 2 receptor[21] (PDB ID:1ole) (Figs. 2.2a,b), based on the structure of AChBP[22]. A sequence alignment that relates these positions on various complementary subunits to AChBP is also provided (Supplementary Fig. S2.3).

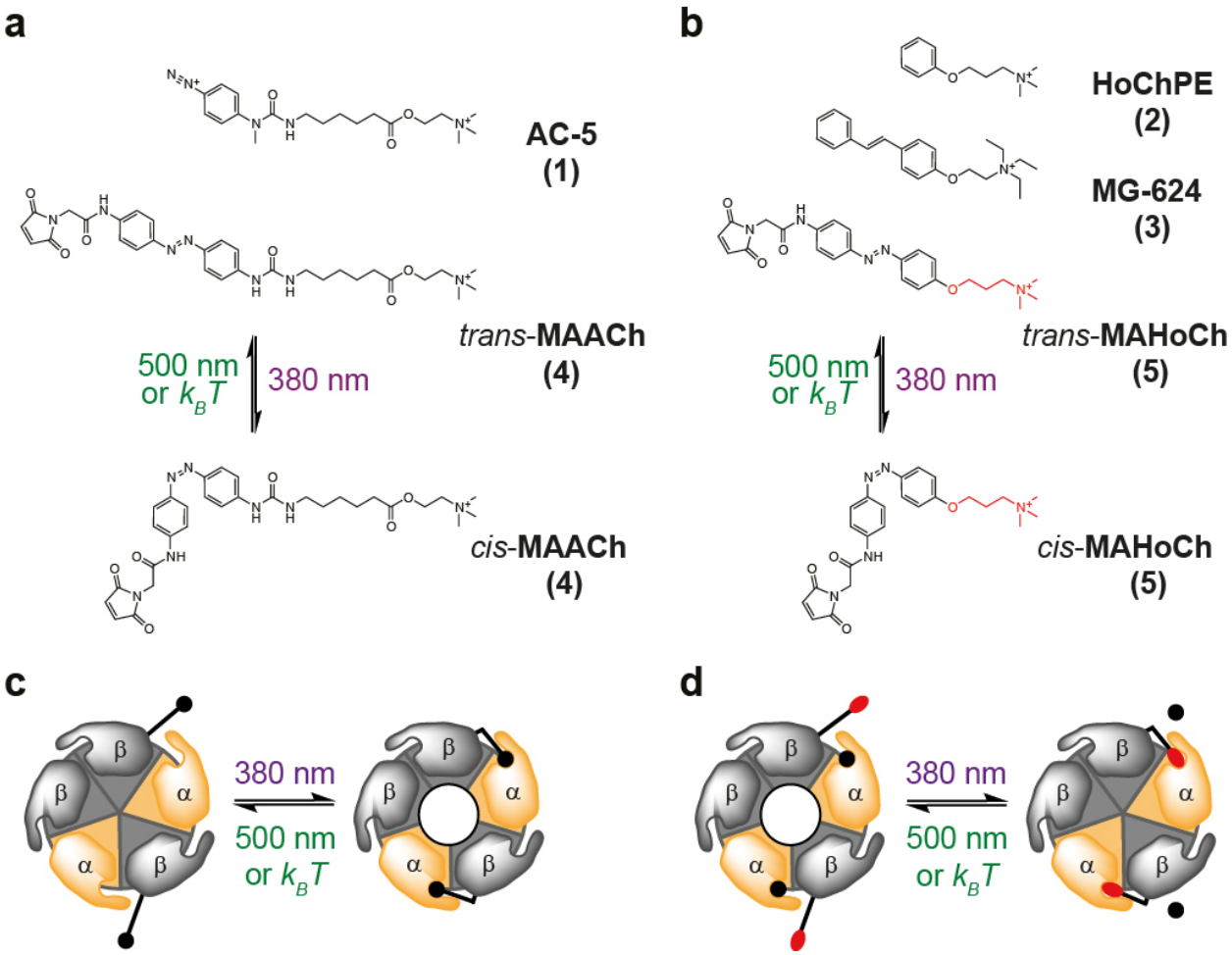

Figure 2.1: Photoswitchable ligand design for the optical control of neuronal nicotinic acetylcholine receptors. (**a, b**) Structures of **AC-5** and **MAACh** (**a**) as well as **HoChPE, MG-624** and **MAHoCh** (**b**). The PTL molecules photoisomerize from *trans* to *cis* upon illumination with 380nm light and revert to *trans* under 500nm light or in the dark. (**c**) A tethered agonist is converted from its *trans* to its *cis* configuration under 380nm light, thus activating heteropentameric nicotinic ACh receptors. Illumination with 500nm light or thermal relaxation deactivates the receptor. (**d**) A tethered antagonist is converted from its *trans* to its *cis* configuration under 380nm light, blocking heteromeric nicotinic ACh receptors from binding to ACh (black). Illumination with 500nm light or thermal relaxation unblocks the receptor, allowing it to be activated by the neurotransmitter α4β2 receptor[87] (PDB ID:1ole) (Figs. 2.2a,b), based on the structure of AChBP[88]. A sequence alignment that relates these positions on various complementary subunits to AChBP is also provided (Supplementary Fig. S2.3).

Our choice of cysteines was further validated by molecular docking studies, which were carried out using the same homology model (Fig. 2.2c). Unconstrained *cis*-**MAACh** and *trans*-**MAACh** were docked into the α4β2 model, while allowing rotatable bonds in the ligand to move freely. We found that the maleimide moiety of **MAACh** comes very close to several of the engineered cysteine mutants shown in Fig. 2.2b in the *cis* form of the azobenzene photoswitch, in particular to cysteines in positions 61, 63 and 117 (Fig. 2.2c), but extends past most of them in its *trans* form (Fig. 2.2d). Molecular modeling studies with **MAHoCh** were not undertaken due to the lack of ligand similarity in the antagonist-bound AChBP structures[89] and the absence of a homology model of an antagonist-bound heteromeric neuronal nAChR.

To test our predictions experimentally, we first introduced the seven independent cysteine mutations into the β4 subunit. We then screened α4β4 mutant nAChRs heterologously expressed in *Xenopus* oocytes, since this particular heteropentamer desensitizes very slowly compared to nAChRs composed of other neuronal subunits[90]. The oocyte system was chosen for its robust expression of heteromeric nAChRs and the lack of endogenous receptors. By contrast, non-neuronal mammalian cell lines often express nAChRs poorly and many neuronal mammalian cell lines possess endogenous nAChRs, which would complicate the screening process.

Using two-electrode voltage clamp recordings, we screened these α4β4 mutants for *cis*-agonism by treating oocytes with **MAACh** in the dark and then looking for current induction upon illumination with 380nm light. We identified three cysteine mutations on the β4 subunit where **MAACh** could evoke a photoactivatable current in the *cis* but not the *trans* configuration: E61C, R113C, and S117C. In the structure of carbamylcholine-bound AChBP[86], the distances from the alpha carbons of each of the three positions and the carbonyl carbon of carbamylcholine were very similar (10.43 Å, 11.28 Å and 12.11 Å for the E61C, R113C, and S117C mutants, respectively). The remaining residues were farther away (19.03 Å, 14.28 Å, 16.39 Å, and 16.54 Å for S32C, R34C, T63C, and N115C, respectively).

Photoactivation of engineered nicotinic acetylcholine receptors.

For comprehensive electrophysiological analysis, these mutant β4 subunits were expressed as α3β4 heteropentamers, which have a more established presence in the nervous system[91]. After labeling the α3β4 E61C receptor with **MAACh**, illumination with 380nm light produced an inward current that could be reversed with 500nm light (Fig. 2.3a). The amplitude of the photoactivatable current was 6.8±1.3 % (mean±SEM, n=10) of the saturating cholinergic current and the receptor still responded normally to perfusion of ACh in the dark. Neither the E61C mutation nor **MAACh** conjugation greatly changed the EC50 of the receptor for ACh (Fig. 2.3b, Supplementary Table S2.1)). **MAACh** labeling at the other two residues, β4R113C and β4S117C also produced photoactivatable currents of similar magnitude (Supplementary Fig. S2.4).

Next, we transposed the E61C mutant from the β4 to the β2 subunit, and tested whether **MAACh** conjugation at the β2E61C position could photoactivate the neuronal α4β2 receptor. Indeed, the **MAACh**-labeled α4β2E61C receptor also produced an inward

current under 380nm light, which could be terminated with 500nm light (Fig. 2.3c). The amplitude of the photoactivatable current was 16.1±2.1% (mean±SEM, n=15) of the saturating cholinergic current. The E61C mutation increased the EC50 of the α4β2 receptor for ACh. Labeling with **MAACh** did not change this EC50 further (Fig. 2.3d, Supplementary Table S2.1).

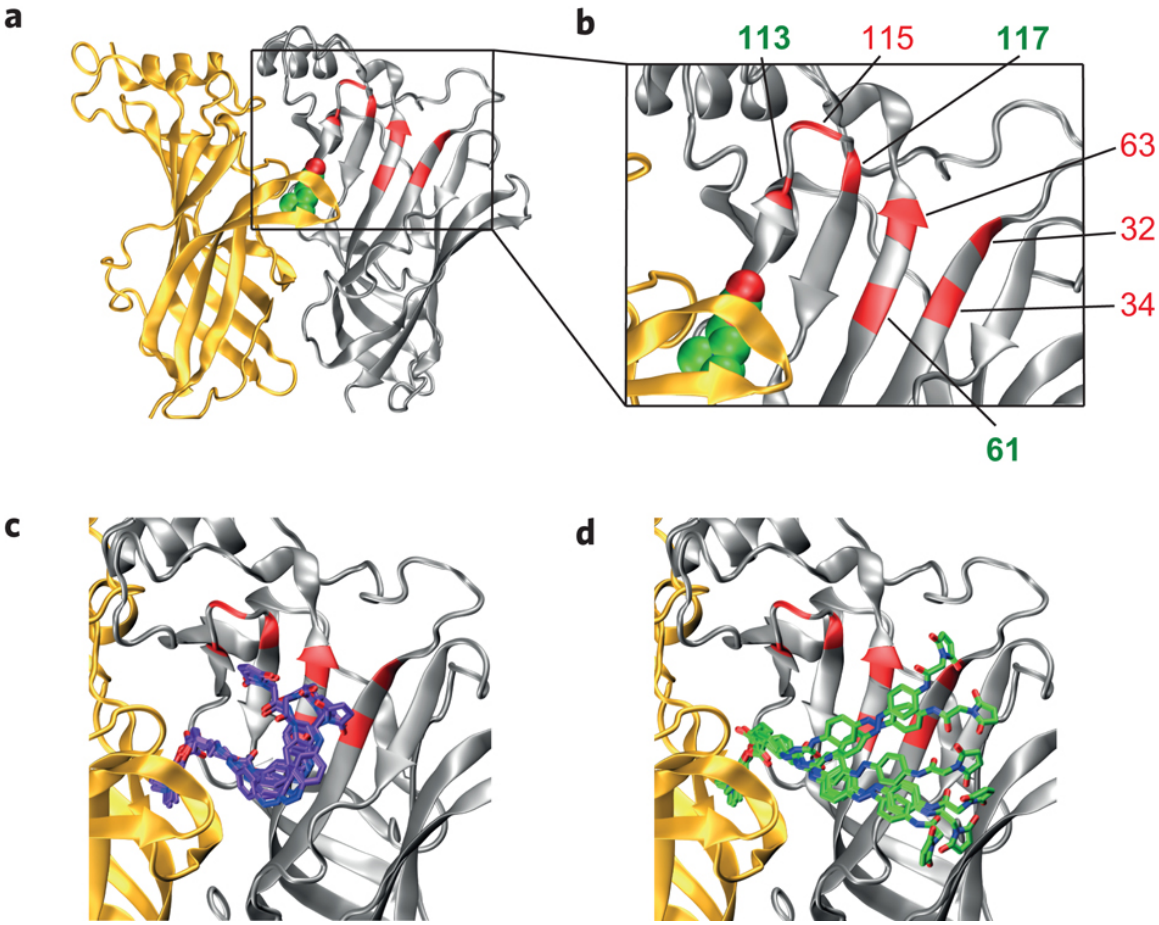

Figure 2.2. Choice of cysteine attachment sites for photoswitchable ligand conjugation. (**a**, **b**) Homology model of the α4β2 nAChR with ACh (green and red spheres) docked in the binding site and the engineered cysteine mutants shown in red and numbered in the zoomed in view of the receptor (**b**). Only one α/β (α-yellow, β-grey) interface is shown for clarity. (**c**, **d**) Docking results with unconstrained *cis*-**MAACh** (violet) (**c**) and *trans*-**MAACh** (green) (**d**) in the α4β2 homology model. Six of the most energetically favorable conformations are shown

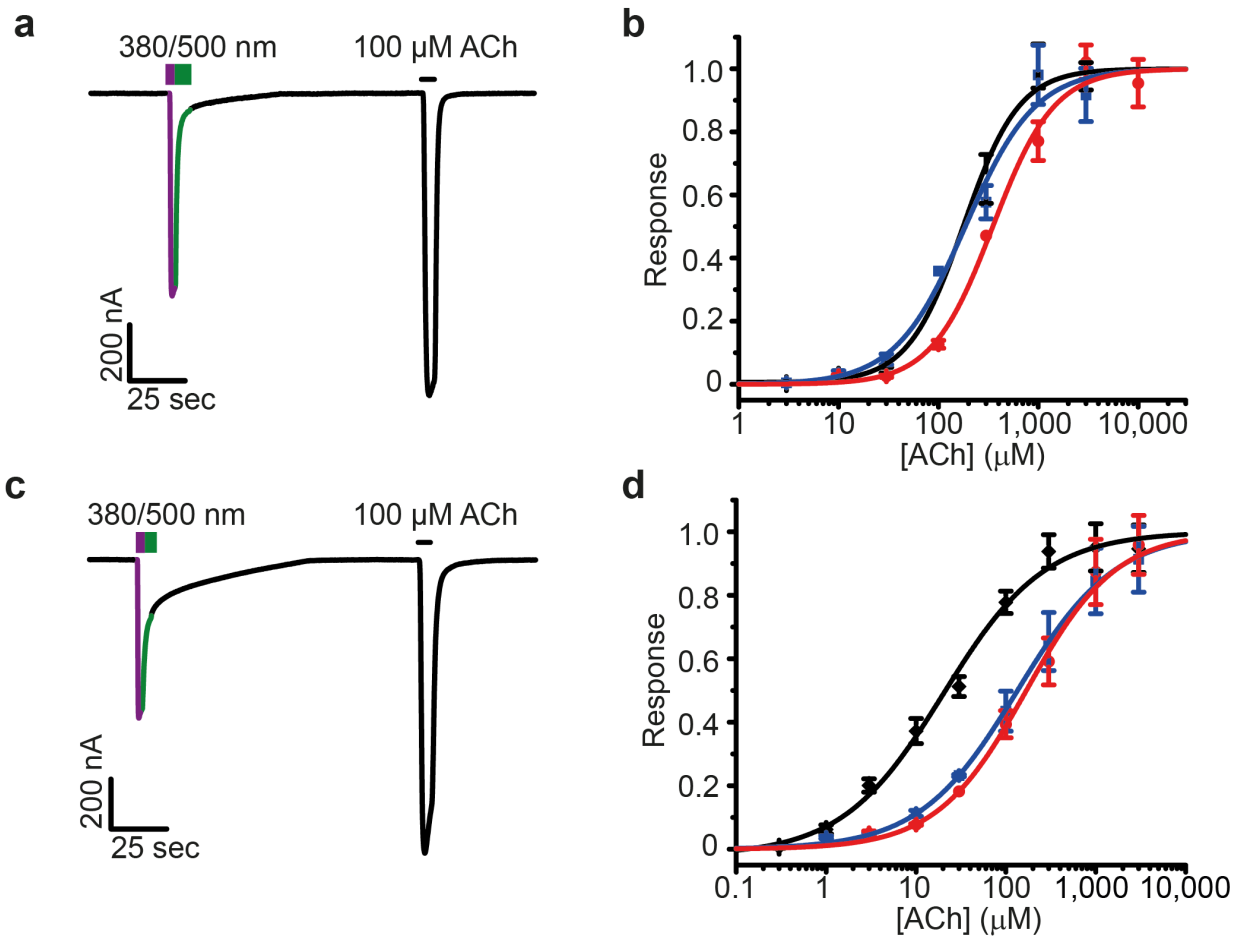

Figure 2.3. Photoactivation of nicotinic acetylcholine receptors with a tethered agonist. (**a**, **c**) Photoactivation of the α3β4E61 (**a**) and the α4β2E61C (**c**) mutant receptors by tethered **MAACh** in *Xenopus* oocytes. 380nm light (violet) triggers photoactivatable current and 500nm light (green) shuts it off. (**b**, **d**) ACh dose response curves for the α3β4 (**b**) and the α4β2 (**d**) wild type (black), E61C mutant (blue) and the E61C mutant with tethered **MAACh** in the dark (red). Data are mean±SEM, n=5.

The prominence of the E61C mutant motivated us to carry out another molecular docking study, wherein the maleimide moiety of **MAACh** was "virtually tethered" to be in the proximity of the sulfhydryl group of the E61C residue (Figs. 2.4a,b). Allowing the remainder of the PTL to move about freely resulted in docking of the ligand head group into the ligand-binding site in all conformations. By contrast, none of the tethered *trans*-**MAACh** conformations reached the ligand-binding site (Figs. 2.4a,b; Supplementary Fig. S2.5). These molecular docking studies corroborate our finding that the agonist is only able to reach the ligand-binding site and activate the receptor in its *cis* but not its *trans* configuration.

Photoinhibition of engineered nicotinic acetylcholine receptors.

We then proceeded to test the effect of **MAHoCh** attached to the three *cis*-agonist active cysteine mutants in α3β4 heteromeric nAChRs. After treating oocytes with the PTL in the dark, we determined that illumination with 380nm and 500nm light did not produce photoactivatable current with any of the three mutants (Supplementary Fig. S2.6). Instead, illumination with 380nm light dramatically reduced the response of the α3β4E61C receptor to ACh, while 500nm light restored the initial response to ACh (Fig. 2.5a). This indicates that tethered **MAHoCh** acts as a *cis*-antagonist of the α3β4E61C receptor. ACh-evoked currents were not substantially modulated by illumination at the α3β4R113C and α3β4S117C receptors (data not shown). To characterize the light-dependent block of the α3β4E61C receptor at different concentrations of ACh, we compared the amount of current observed under 380nm and 500nm illumination for the same cells. The percentage of current blocked under 380nm light ranged from 80±5% at 30μM ACh to 68±4% at a saturating 10mM ACh (mean±SEM, n=5) (Fig. 2.5b). Tethering **MAHoCh** at the α4β2E61C receptor produced a similar photoinhibition of the cholinergic current (Fig. 2.5c). The percentage of current blocked under 380nm light at the α4β2 receptor ranged from 75±10% at 100μM ACh to 81±7% at a saturating 3mM ACh (mean±SEM, n=5) (Fig. 2.5d).

In control experiments, we did not observe any photoactivation after treating oocytes expressing either α3β4E61C or α4β2E61C nAChRs with **AcAACh** (**6a,b**), a non-reactive analogue of **MAACh** (Supplementary Fig. S2.7). Furthermore, treatment of wild type receptors with either **MAACh** or **MAHoCh** did not impart any photosensitivity (Supplementary Fig. S2.6). These results confirm that covalent modification at the genetically introduced cysteine residue is required for the optical control of LinAChR function and suggest that off-target actions of these ligands at endogenous neuronal receptors should be minimal.

Thermal relaxation of the photoswitchable ligands.

Azobenzene PTLs can be converted from their *cis* configuration to their *trans* configuration by 500nm illumination, but they also spontaneously convert to the more stable *trans* isomer *via* thermal relaxation in the dark[92]. Thus, the **MAACh**-labeled α4β2E61C receptor can be activated by 380nm light and the photoactivatable current decays over time in the dark (Fig. 2.6a). To investigate whether tethering the PTL to a receptor affects the rate of *cis*-isomer thermal relaxation, we compared the half-life of **MAACh** in solution, measured by changes in absorption at 380nm, to the calculated half-life of the decay of the photoactivatable current (Fig. 2.6b). The half-life of **MAACh** in solution was 28 seconds, close to the previously reported value of 26 seconds for a urea-azobenzene derivative[93]. In contrast, the thermal decay of the photoactivatable current could only be fit with a biexponential decay curve, with a fast half-life of 4.7 seconds and a slow half-life of 94 seconds, indicating that ligand binding increases the stability of *cis*-**MAACh**. The **MAHoCh**-labeled α4β2 E61C receptor can be blocked by 380nm light and the amount of block also decays slowly in the dark (Fig. 2.6c). We measured the half-life of *cis*-**MAHoCh** in solution to be 74.4 minutes (Fig. 2.6d). The long half-life of

cis-**MAHoCh** is likely due to the alkoxy substituent on the azobenzene, which does not destabilize the *cis* configuration to the same extent as the urea substituent in **MAACh**[92]. The thermal relaxation rate of tethered *cis*-**MAHoCh** appears to be of the same order of magnitude as *cis*-**MAHoCh** in solution.

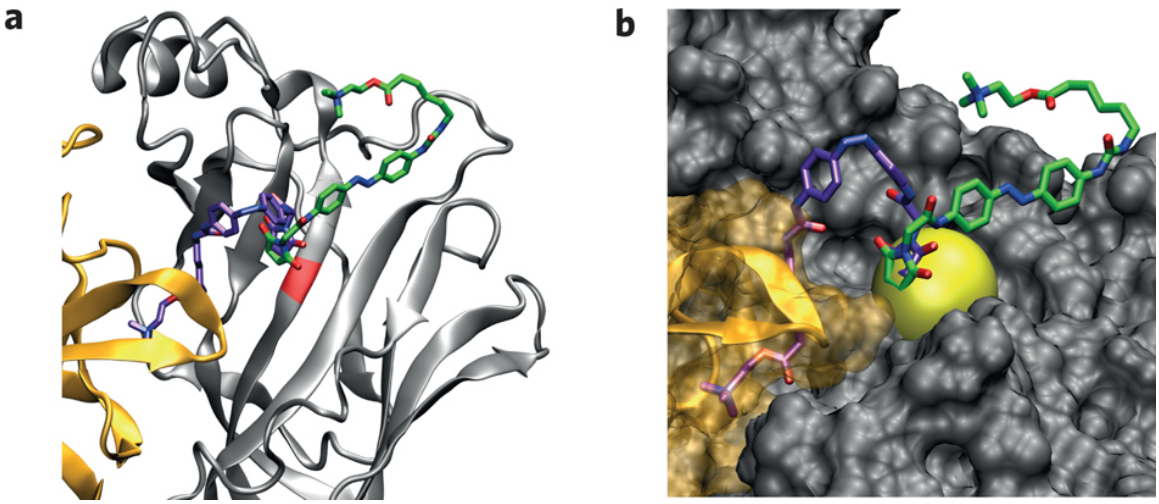

Figure 2.4: Molecular model of a nicotinic acetylcholine receptor with a virtually tethered photoswitchable agonist. (**a**, **b**) Docking results with constrained *cis*-**MAACh** (violet) and *trans*-**MAACh** (green) in the α4β2 homology model. The maleimide is constrained to be near the sulfhydryl group of C61. Ribbon (**a**) and surface (**b**) views of the minimum energy conformations are shown. The positional constraint (sphere) is shown in bright yellow.

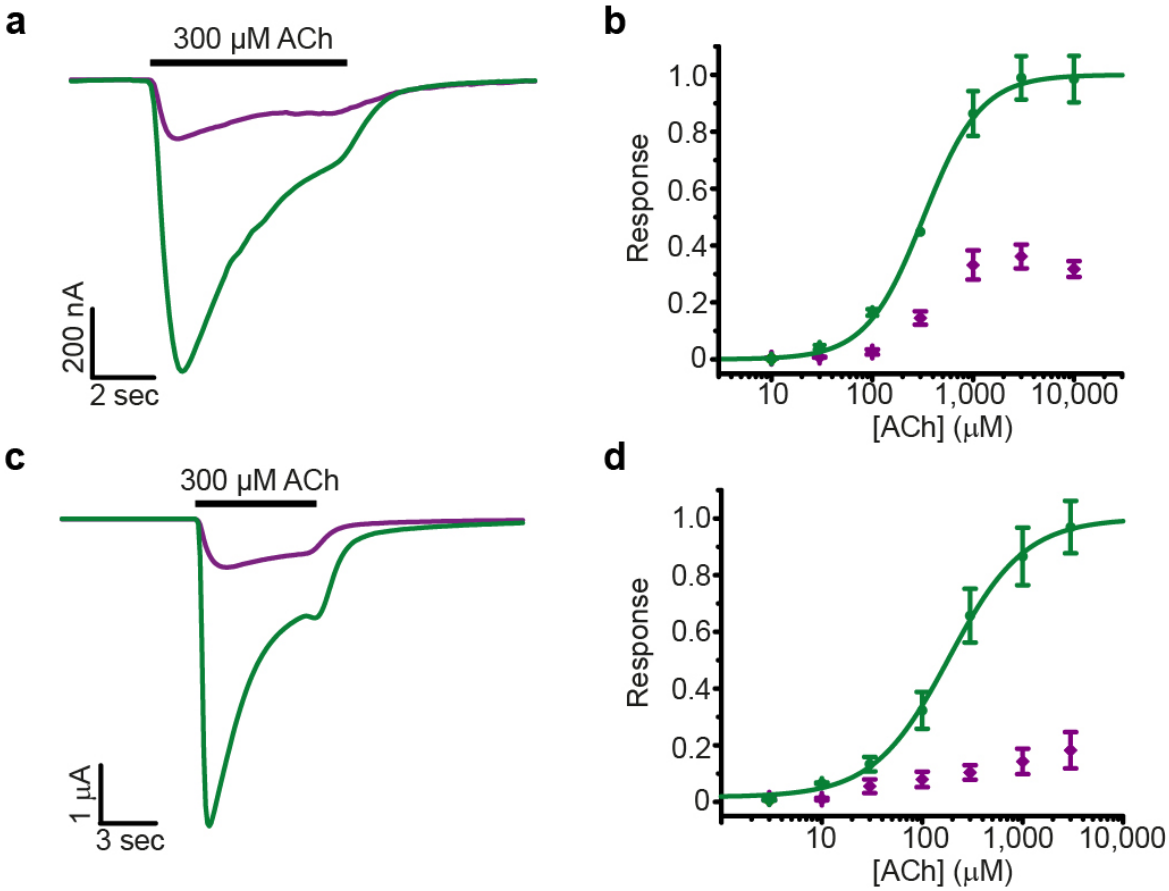

Figure 2.5: Photoinhibition of nicotinic acetylcholine receptors with a tethered antagonist. (**a**, **c**) Photo-block of the cholinergic current of the α3β4E61C (**a**) and α4β2E61C (**c**) mutant receptors by tethered **MAHoCh**. Current is shown in response to 300µM ACh under 380nm light (violet) and 500nm light (green). (**b**, **d**) ACh dose response curves for the α3β4E61C (**b**) mutant and the α4β2E61C (**d**) mutant with tethered **MAHoCh** under 500nm light (green) and 380nm light (violet). Data are mean±SEM, n=5.

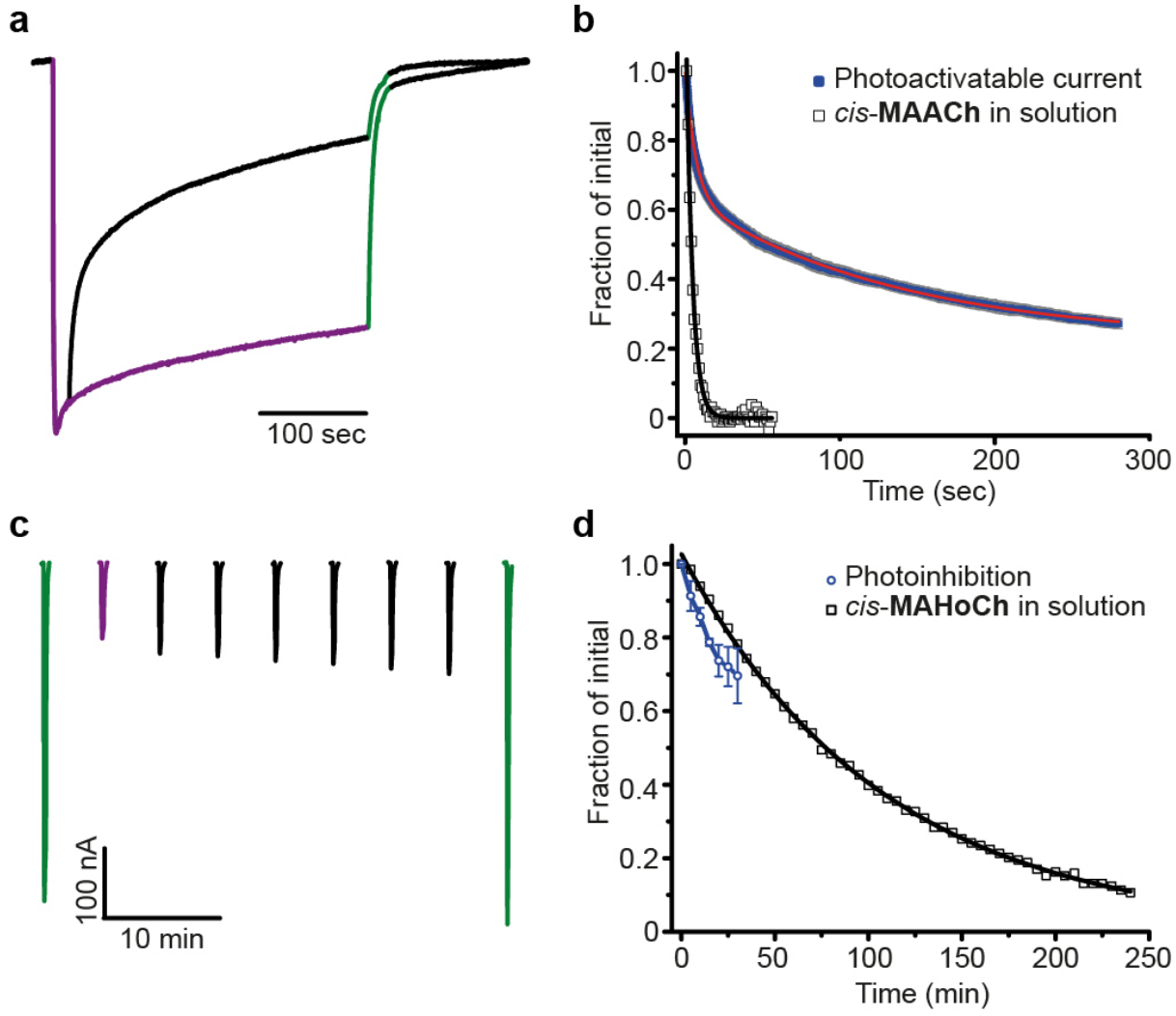

Figure 2.6: Thermal relaxation of the photoswitchable agonist and antagonist. (**a**) Normalized photoactivatable current decay of the α4β2E61C receptor in the dark with tethered **MAACh**. Decay of the photoactivatable current over time under 380nm illumination (violet) and in the dark (black). (**b**) Thermal relaxation of *cis*-**MAACh** in phosphate-buffered saline (open squares) fitted with a monoexponential decay function (black) ($t_{1/2}$ = 28sec). Decay of the photoactivatable current (mean (blue) ± SEM (gray), n=4) fitted using a biexponential decay function (red, $t_{1/2}(1)$ = 4.7sec, A(1) = 0.36, $t_{1/2}(2)$ = 94sec, A(2) = 0.41). Both measurements are normalized. (**c**) Decay of the photo-block of cholinergic current of the α4β2E61C receptor in the dark with tethered **MAHoCh** measured in *Xenopus* oocytes. 100μM ACh is perfused under 500nm (green) light, 380nm (violet) light and in the dark (black). (**d**) Thermal relaxation of *cis*-**MAHoCh** in phosphate-buffered saline (open squares) fitted with a monoexponential decay function (black) ($t_{1/2}$ = 74.4min). Decay of the photo-block of cholinergic current of the α4β2E61C receptor with **MAHoCh** (blue) (mean±SEM, n=4).

Discussion

In a classic set of studies carried out in the late 1970s and early 80s, Erlanger and colleagues demonstrated that azobenzene photoswitches could provide photosensitivity to endogenous muscle nAChRs[94,95]. These pentameric ligand-gated ion channels naturally possess a disulfide bond at the tip of the so-called C-loops in their α-subunits[71], which is in close proximity to the ligand-binding site. This disulfide could be reduced, providing a reactive thiol for covalent attachment of a PTL, although such treatment also reduced the affinity of the receptor for agonists by up to 100-fold[96]. The PTL**,** called **QBr**, consisted of a benzylic bromide (the electrophile), an azobenzene photoswitch and a benzylic trimethylammonium moiety. Once attached, **QBr** activated the channel in its *trans* form, i.e. at 500nm or in the dark, but could be switched to an inactive *cis* form by irradiation with 330nm light. The resulting light-activated nAChR could be used to reversibly stimulate *Electrophorus* electroplaques, frog muscles and rat myoballs with light[94,95,97,98]. At the time these studies were carried out, however, receptors could not be genetically manipulated and heterologously expressed and the impact of synthetic photoswitches on neuroscience research remained limited.

Due to the enormous progress of molecular biology since the 1980s, it is now possible to heterologously express mutant receptors in *Xenopus* oocytes, mammalian cells, neurons and even transgenic animals[63,99,100]. Once expressed in a cell, our engineered LinAChR (E61C) can be conjugated with either an agonist or an antagonist, providing for powerful, bidirectional control of receptor activity. Both variants of LinAChR behave like normal nAChRs in the dark but can be turned on in the absence of ACh or off in the presence of the neurotransmitter, respectively, upon irradiation with 380nm. The red-shifted PTL action spectra (compared to **QBr**) should also minimize potential phototoxic effects. In principle, their spectral sensitivity could be further moved toward lower energies through appropriate substitution of the azobenzene photoswitch[101,102].

Another field that has undergone remarkable progress in recent years is the structural biology of pentameric ligand gated ion channels (Cys-loop receptors)[103]. Several X-ray structures of homopentameric ligand-gated ion channels are now available[104,105], as are high-resolution structures of acetylcholine binding proteins (AChBPs) bound to a variety of agonists and antagonists[86,88]. Without these, it would have been difficult to design functional PTLs and choose appropriate sites for their attachment. The X-ray structure of carbamylcholine bound to AchBP[86] and the homology models of the neuronal receptors[87] proved to be most relevant for our design and computational evaluation of PTLs and were particularly helpful for identifying residues suited for the attachment of the photoswitchable agonist **MAACh**. Our molecular docking studies correctly identified positions 61 and 117 as suitable sites of attachment. The predicted site 63 turned out to be unsuitable, however, highlighting the importance of functional screening as a complement to *in silico* models.

The antagonist action of tethered **MAHoCh** is more difficult to explain based on the available X-ray structures but is consistent with the known pharmacology of nAChRs

(see Fig. 2.1). It is also consistent with the "foot in the door" mechanism of nAChR antagonism, wherein an antagonist binds but prevents the complete conformational contraction of the ligand binding site required for receptor activation[106]. Apparently, the elongation of **HoChPE** with a diazene unit bearing an aryl group is sufficient to prevent the C-loop of the receptor α-subunit from closing in sufficiently to activate the receptor. This also makes sense given the structural similarity of the azobenzene **MAHoCh** with the stilbene **MG-624**, and timethylammonium derivatives thereof, which also function as antagonists[85]. Our data demonstrate that once an attachment site is chosen, it is possible to convert a tethered photoswitched agonist into a tethered photoswitched antagonist by altering the structure of the tether and the ligand head group. This matches previous observations by Cohen *et al*. who established that elongation of a covalently attached agonist by a single methylene group could turn it into an antagonist[107]. Conversely, it might be possible to use the same tethered ligand and two different sites of attachment to achieve either photoagonism or photoantagonism[107].

The diversity of neuronal nAChRs and their structural similarities complicates the pharmacological selective targeting of specific nAChR subtypes. This study reports the reversible photoactivation and inhibition of common neuronal α4β2 and α3β4 nAChRs using light following the genetically targeted conjugation of photoswitchable tethered ligands. This initial study should enable the rational design of other light-regulated pentameric ligand-gated ion channels, homopentameric α7 nAChRs, and neuromuscular nAChRs. The lessons learned in this study should also facilitate the design of photosensitive $GABA_A$ receptors, GlyRs, $5HT_3$ or GluCl receptors. Based on the recent X-ray structure of GluCl[108] and our expertise with photoswitchable tethered glutamate derivatives[63], for instance, it should be possible to develop a hyperpolarizing light-gated chloride channel. It is also conceivable that photoswitchable tethered agonists and antagonists could be extended to muscarinic ACh receptors, which have not yet been characterized in atomic detail but for which extensive pharmacology exists[109].

In future physiological investigations, LinAChRs will be expressed in dissociated neurons, intact neuronal tissues and live animals. We expect them to function well in these systems, perhaps even better than in *Xenopus* oocytes, whose opacity makes it impossible to photoregulate receptors on the entire surface of the cell. In any case, the amount of photoactivation should be sufficient to replicate the major type of cholinergic transmission in the mammalian brain. Neuronal nAChRs are mostly located extrasynaptically and respond to low micromolar concentrations of acetylcholine diluted after synaptic release (i.e. volume transmission)[110]. Expression of the cysteine-containing subunit alone should produce functional LinAChRs in neurons that possess endogenous nicotinic receptors, which would then allow for optical manipulation of receptor function *in vitro* and *in vivo*[111]. Alternatively, native nAChR subunits can be replaced by cysteine mutants using a knock-in strategy[112], which would preserve the endogenous pattern and level of receptor expression. We intend to pursue these strategies to study the physiological and pathological roles of heteromeric nAChRs in the brain and periphery and will report the results of that investigation in due course.

Materials and methods

Synthesis of MAACh and MAHoCh: See Figure S2.1 and Supplementary Methods.

Molecular cloning. Rat nicotinic ACh receptor subunit cDNAs in the pNKS2 vector (generously provided by Dr. Annette Nicke, Max Planck Institute for Brain Research, Frankfurt am Main, Germany) were used for all experiments. To minimize non-specific labeling, the C-terminal α4C594 and the β4C75 residues were both mutated to serine. These mutations do not affect the function of the receptor[113]. These mutants were then used as a background for PTL attachment site screening. For nomenclature simplicity, the WT receptors are named in this article α3β4WT and α4β2WT, whereas the α4C594Sβ2 and the α3β4C75S background receptors are named α4β2 and α3β4, respectively. DNA was linearized with XbaI and RNA was transcribed using the mMessage mMachine SP6 transcription kit (Ambion). Surgically extracted *Xenopus laevis* oocytes were injected with 2–20 ng of channel RNA (50 nL). The cells were incubated in oocyte Ringer's solution [96 mM NaCl, 2 mM KCl, 1.8 mM $CaCl_2$, 1 mM $MgCl_2$ and 5 mM HEPES (pH 7.4)] at 18 °C for 24–48 h before experiments.

Molecular Modeling. Molecular models of α4β2 neuronal nAChR (PDB ID: 1ole)[87] and of the *Torpedo californica* nAChR[82] were used to identify endogenous cysteine residues accessible from the extracellular medium. The X-ray structure of AChBP in complex with carbamylcholine[86] was used to estimate the distance between the ammonium group of the ligand and the beta carbon of the engineered cysteine residues. The numbering of the residues in the homology model is not consistent with the protein sequence. See Supplementary Fig. S2.3 for sequence alignment and residue numbering. *Cis* and *trans* ligands were docked to the homology model of the α4β2 receptor after the addition of hydrogen atoms and the removal of non-protein moieties using Glide 5.7 as implemented in Maestro 9.2[114]. The docking consisted of a spatial fit of the ligand to the receptor grid, followed by minimization and scoring of hits based on a discretized ChemScore function[115,116]. Ligands were flexibly docked to a rigid receptor using standard precision and the top hits were examined. Docking of the constrained ligands contained an additional positional constraint that restricted the alkenyl carbons of the maleimide moiety to a shell with an inner radius of 1Å and an outer radius of 3.5Å centered at the sulfhydryl group of the C61 cysteine residue.

Photoswitch conjugation. All photoswitch compounds were dissolved in DMSO to make a 10 mM stock solution and diluted in oocyte Ringer's solution to 25μM for conjugation. For all recordings, the DMSO concentration was <0.25% (vol/vol). Oocytes were incubated in the photoswitch compound solution for 20 minutes in the dark at room temperature before electrophysiological recordings. Photoswitch conjugation was followed by a 5 minute wash in oocyte Ringer's solution.

Electrophysiology. All electrophysiology experiments were conducted at room temperature. Two-electrode voltage-clamp (TEVC) experiments were performed using an OC-725C amplifier (Warner Instruments), DigiData 1200 interface, and pClamp 8.0 software. The oocytes were placed in a perfusion chamber for recordings. All recordings were performed in oocyte Ringer's solution [96 mM NaCl, 2 mM KCl, 1.8 mM $CaCl_2$, 1 mM $MgCl_2$, 10 mM HEPES (pH 7.4)]. For each experiment, the oocyte membrane potential was held at −80 mV. An 8-line perfusion system with a VC-8 valve controller (Warner Instruments) was used for perfusion of ACh into the chamber. Data were sampled at 1 kHz, and filtered at 10 Hz. Cells were illuminated using a Lambda-LS illuminator containing a 125W xenon arc lamp (Sutter Instruments) equipped with narrow-band-pass (±10 nm) filters. The incident light intensity was 20 mW/cm^2 for both 380nm and 500nm light, measured at the aperture using a handheld optical power meter (1918-C, Newport, Inc).

Data Analysis. Dose response curves were created using the following equation:
$y = A_1 + (A_2-A_1)/(1 + 10^{((LOGx0-x)*p)})$, where p = Hill coefficient and 10^{LOGx0} = EC50.

Absorption spectra. UV-Vis spectra of the photoswitch compounds were obtained using the SmartSpec Plus Spectrophotometer (BioRad Laboratories) in PBS at pH 7.4. The change in absorbance of the compounds at 380nm over time following photoconversion to the *cis* configuration was used to determine the kinetics of thermal relaxation. The light source used for photoconversion of the ligands was the same as the one used in electrophysiological recordings.

Supplemental Information

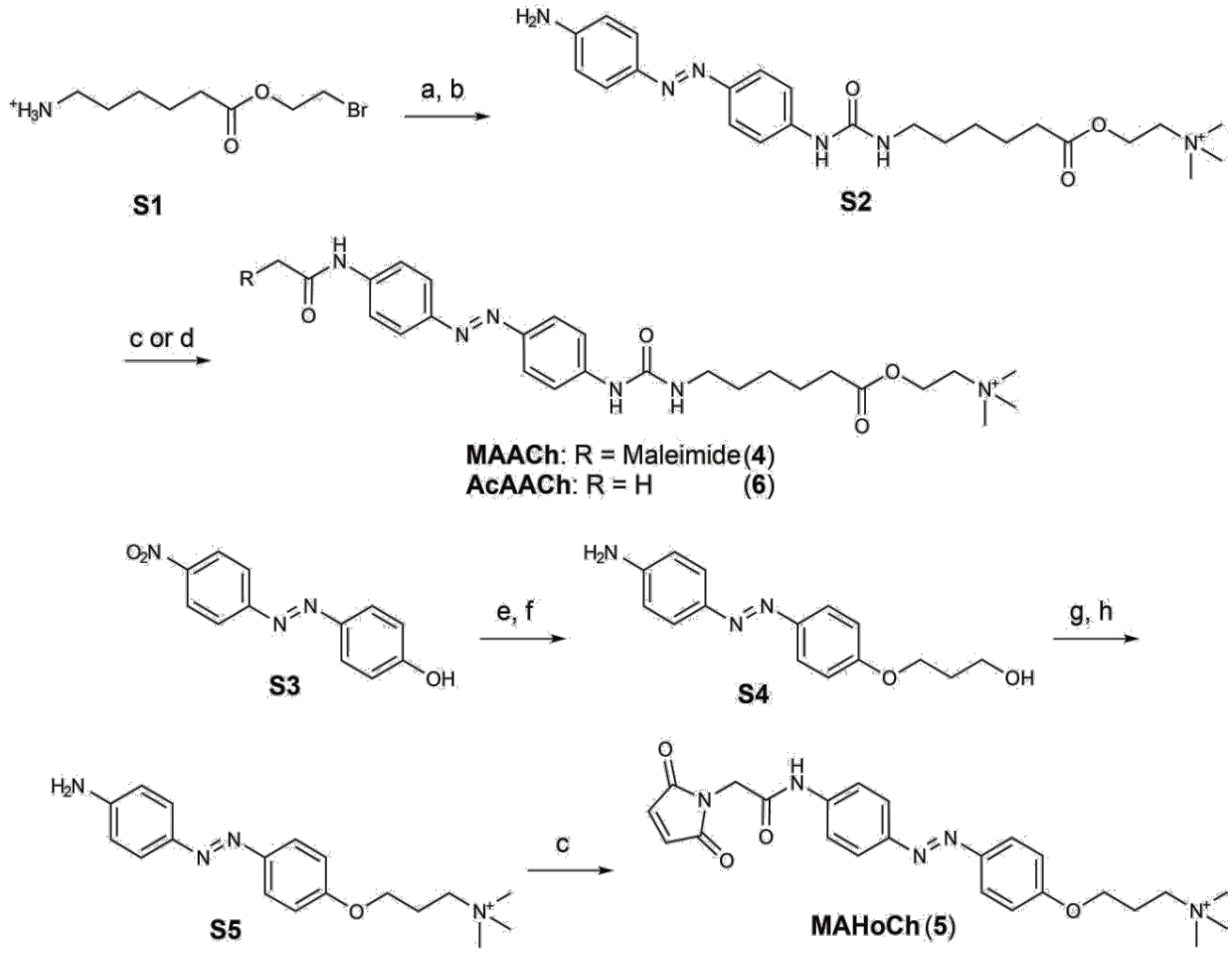

Figure S2.1. Synthesis of the photoswitchable tethered ligands. Synthesis of **MAACh**, **AcAACh** and **MAHoCh**. Reagents and conditions: a - triphosgene, $NaHCO_3$, H_2O/DCM, then 4,4'-azodianiline (33%); b - Me_3N, DMF (84%); c - maleoylglycyl chloride, DIPEA, DMF (50%); d - acetyl chloride, DIPEA, DMF (54%); e - 3-bromopropanol, cat. KI, K_2CO_3, acetone (99%); f - $(NH_4)_2S$, Na_2CO_3, H_2O/THF (87%); g - CBr_4, PPh_3, imid. THF (40%); h - Me_3N, THF (quant.).

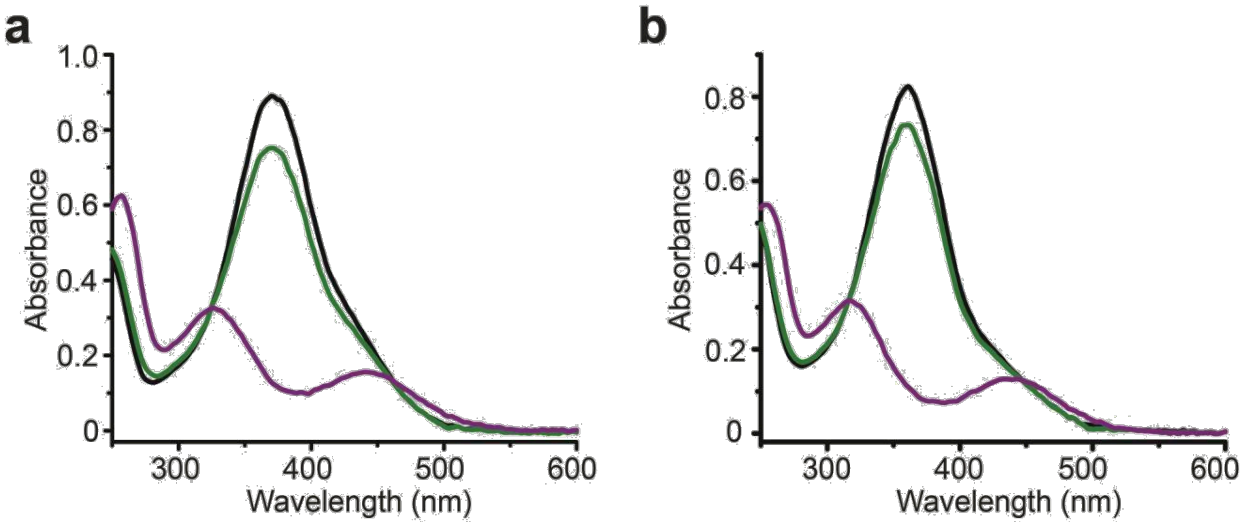

Figure S2.2. UV-Vis absorption spectra of the photoswitchable tethered ligands. (**a**, **b**) UV-Vis absorption spectra of **MAACh** (**a**) and **MAHoCh** (**b**) in phosphate buffered saline (PBS) in the dark (black), under 500nm light (green) and 380nm light (violet).

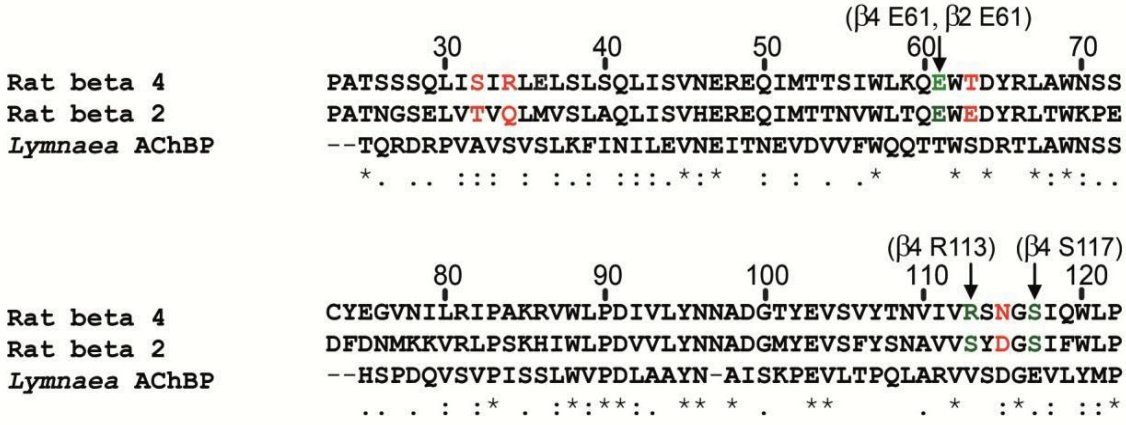

Figure S2.3. Sequence alignment showing the introduced nicotinic receptor cysteine mutants.
Sequence alignment for *Rattus norvegicus* nAChR β4, β2 subunits and the *Lymnaea stagnalis* acetylcholine binding protein (AChBP), with the cysteine mutations that produced *cis*-activation with **MAACh** colored green and the ones that didn't produce *cis*-activation in red. Alignment was performed using ClustalW 2.0[117,118]

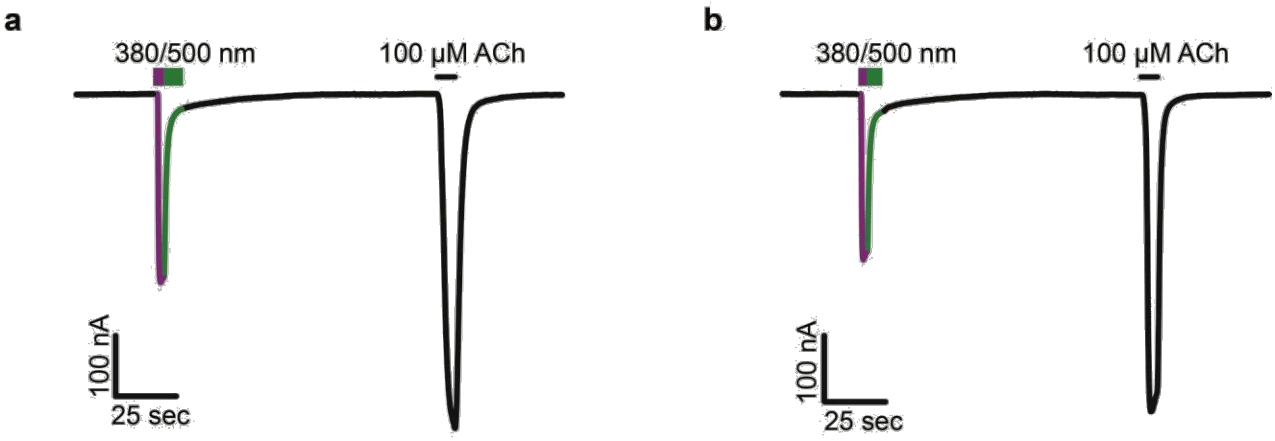

Figure S2.4. Photoactivation of additional mutant α3β4 nicotinic acetylcholine receptors with a tethered agonist. (**a**, **b**) Photoactivation of the α3β4R113C (**a**) and the α3β4S117C (**b**) mutant receptors by tethered **MAACh**. 380nm light (violet) triggers photoactivatable current and 500nm light (green) shuts it off. Representative traces, similar behavior in three other cells.

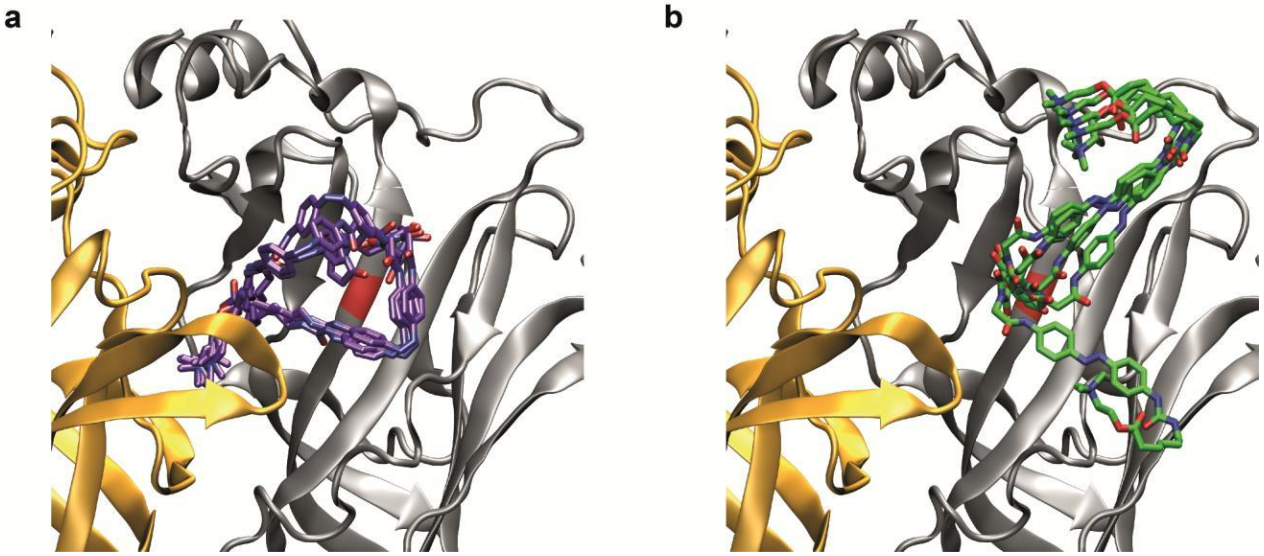

Figure S2.5. Molecular model of a nicotinic receptor with a virtually tethered photoswitchable agonist. (**a**, **b**) Docking results with constrained *cis*-**MAACh** (violet) (**a**) and *trans*-**MAACh** (green) (**b**) in the α4β2E61C homology model. The maleimide is constrained to be near the sulfhydryl group of C61. Six of the lowest energy conformations are shown.

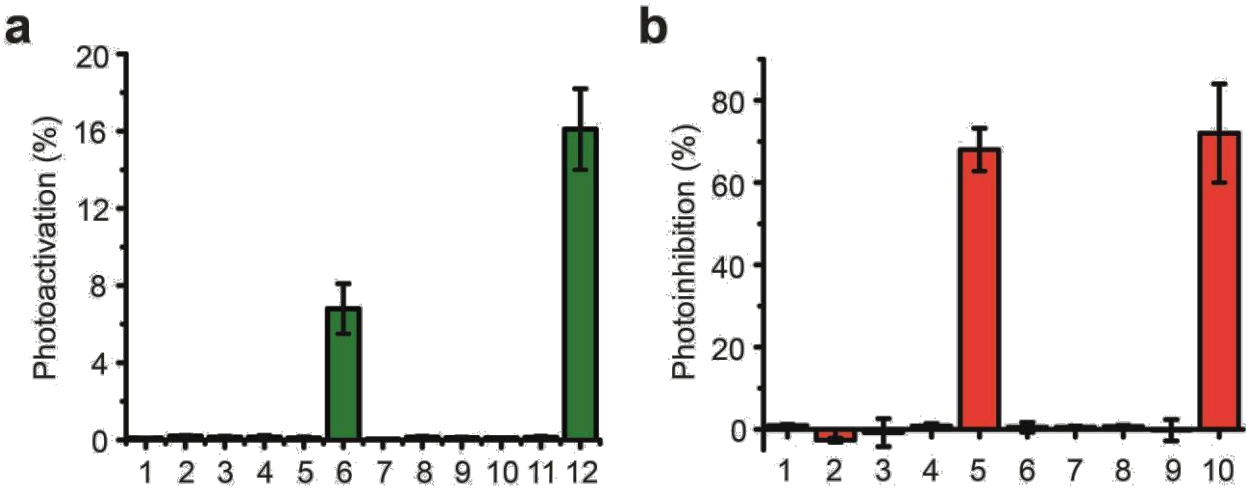

Figure S2.6. Photoregulation of nicotinic acetylcholine receptors with photoswitchable tethered ligands. (**a**) Photoactivation of heteromeric nAChRs in *Xenopus* oocytes by various PTLs. 1: α3β4WT+ **MAACh**, 2: α3β4 + **MAACh**, 3: α3β4 + **MAHoCh**, 4: α3β4E61C + **AcAACh**, 5: α3β4E61C + **MAHoCh**, 6: α3β4E61C + **MAACh**, 7: α4β2WT + **MAACh**, 8: α4β2 + **MAACh** 9: α4β2 + **MAHoCh**, 10: α4β2E61C + **AcAACh**, 11: α4β2E61C + **MAHoCh**, 12: α4β2E61C + **MAACh**. Photoactivation is shown as percent of maximum ACh current. Data are mean±SEM, n=3-15. (**b**) Photoinhibition of heteromeric nAChRs in *Xenopus* oocytes by various PTLs. 1: α3β4WT + **MAHoCh**, 2: α3β4 + **MAACh**, 3: α3β4 + **MAHoCh**, 4: α3β4E61C + **AcAACh**, 5: α3β4E61C + **MAHoCh**, 6: α4β2WT + **MAHoCh** 7: α4β2 + **MAACh**, 8: α4β2 + **MAHoCh**, 9: α4β2E61C + **AcAACh**, 10: α4β2E61C + **MAHoCh**. Photoinhibition is shown as percent of ACh current blocked under 380nm light upon perfusion of 300μM ACh for the α3β4 nAChRs and 100μM ACh for the α4β2 nAChRs. Data are mean±SEM, n=3-5.

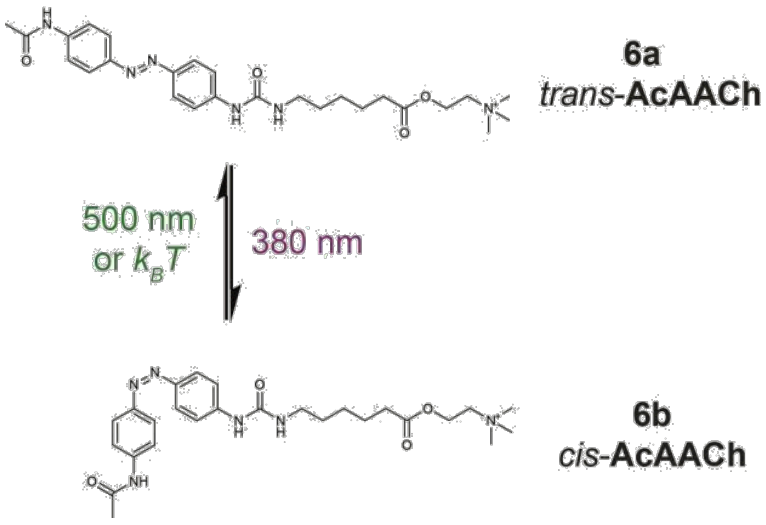

Figure S2.7. Structure of a non-cysteine reactive analog of the photoswitchable tethered agonist . Structure of Acetamide-Azobenzene-AcylCholine (**AcAACh**) (**6a**, **b**), a non-cysteine reactive analog of the PTL **MAACh**. **AcAACh** is photoisomerizable, but does not photosensitize cysteine-mutant nAChRs after treatment and wash.

Receptor	Acetylcholine EC50 (μM)	Hill coefficient
α3β4WT	178±22	1.56±0.24
α3β4E61C	186±52	1.24±0.3
α3β4E61C + **MAACh**	350±54	1.41±0.23
α3β4E61C + **MAHoCh**	323±13	1.52±0.09
α4β2WT	20±4	0.77±0.08
α4β2E61C	134±11	0.80±0.03
α4β2E61C + **MAACh**	169±39	0.87±0.11
α4β2E61C + **MAHoCh**	185±12	1.16±0.07

Table S2.1. Characterization of cysteine-mutant and photoswitchable ligand-conjugated nicotinic acetylcholine receptors.Acetylcholine EC50 values and Hill coefficients of the dose-response curves for the wild-type, cysteine-mutant and PTL-conjugated cysteine mutant α3β4 and α4β2 nAChRs. All data are mean±SEM, n=5.

Supplemental Methods

Chemical Synthesis

General methods. Reactions were carried out under N_2 atmosphere in flame dried glassware. Tetrahydrofuran (THF) was distilled from Na/benzophenone immediately prior to use. Acetonitrile (MeCN), and diisopropylethylamine (DIPEA) were distilled from CaH_2 immediately prior to use. All other reagents and solvents were used without further purification from commercial sources. Flash column chromatography was carried out with EcoChrom ICN SiliTech 32–63 D 60 Å silica gel. Reverse-phase chromatography was carried out with Waters Preparative C18 Silica Gel WAT010001 125 Å and Waters Sep-Pak Vac 20 cc C18 Cartridge s WAT036925. Reactions and chromatography fractions were monitored with either Merck silica gel 60F254 plates or Analtech C18 silica gel RPS-F 52011 plates, and visualized with 0.1N HCl. NMR spectra were measured specified solvents and calibrated from residual solvent signal on a Bruker DRX spectrometer at 500 MHz for ^{1}H spectra and 125 MHz for ^{13}C spectra and either a Bruker AVB or Bruker AVQ spectrometer at 400 MHz for ^{1}H spectra and 100 MHz for ^{13}C spectra. IR spectra were measured with a Genesis FT-IR spectrometer by thin film.

6-(2-bromoethoxy)-6-oxohexan-1-aminium (S1). Compound **S1** was prepared from 6-aminohexanoic acid according to the procedure of Chatrenet et al[119].

(*E*)-2-((6-(3-(4-((4-aminophenyl)diazenyl)phenyl)ureido)hexanoyl)oxy)-*N*,*N*,*N* trimethylethanaminium (S2). To a biphasic mixture of DCM (15 ml) and saturated aqueous $NaHCO_3$ (15 ml) was added triphosgene (108 mg, 0.36 mmol). Compound **S1** was dissolved in H_2O (5 ml) and then added dropwise over 10 min to mixture, which was allowed to stir at room temperature for 1 hr and then transferred to a separatory funnel with DCM. After extracting 3 times with DCM (15 ml) the organics were combined, washed with brine (20 ml), dried over Na_2SO_4, filtered, and removed of solvent *in vacuo*. The brown oil was dissolved in THF (3 ml), and cannulated into a solution of 4,4'-azodianiline (460 mg, 2.18 mmol) dissolved in THF (6 ml) under N_2. The flask containing isocyanate **S1** was rinsed with additional THF (3 ml), which was also cannulated into the mixture. The reaction was refluxed overnight, cooled, diluted with additional THF (25 ml) and dry-loaded onto silica gel (2 g). Silica gel chromatography through a wide column (25% EtOAc in DCM gradient to 50%) provided the primary bromide as a yellow-brown solid (170 mg, 0.36 mmol, 33% yield): ^{1}H (d_6-DMSO, 300MHz): 1.33 (s, 2H); 1.44 (s, 2H); 1.57 (s, 2H); 2.35 (s, 2H); 3.09 (s, 2H); 3.36 (s, 1H); 3.66 (s, 2H); 4.34 (s, 2H); 5.95 (s, 2H); 6.23 (s, 1H); 6.65 (s, 2H); 7.54–7.64 (m, 6H), 8.78 (s, 1H). HRMS (FAB+): calc'd for $C_{21}H_{26}BrN_5O_3$ – 475.1219, found – 475.1229 (M+).

The primary bromide (154 mg, 0.31 mol) was dissolved in DMF (3 ml) and cooled on an ice bath under N_2. The N_2 line was removed and a gentle stream of Me_3N gas was bubbled through the solution while stirring and venting into a solution of 10%

HCl for about 1 min or until a small volume increase was observed. After removal of the Me_3N stream, the reaction vessel was sealed and allowed to stir at room temperature overnight. A stream of N_2 gas was then bubbled through the reaction while stirring and vented into a solution of 10% HCl to remove the excess Me_3N, followed by addition of formic acid (1 ml) to protonate the remaining Me_3N. After removal of solvent *in vacuo*, reverse phase silica gel chromatography (15% MeCN: 0.1% formic acid in H_2O gradient to 33% MeCN) provided **S2** as a yellow solid (128 mg, 0.26 mmol, 84% yield): ^1H (MeOD, 400MHz): 1.29 (s, 2H); 1.43 (s, 2H); 1.53 (s, 2H); 2.30 (t, 2H, J=7.6); 3.06-3.11 (m, 1H); 3.55 (s, 2H); 4.39 (s, 2H); 6.60 (d, 2H, J=8.8); 7.36 (d, 2H, J=8.8); 7.54 (d, 2H, J=8.8); 7.60 (d, 2H, J=8.4); 8.42 (bs, 1H). HRMS (FAB+): calculated for $C_{24}H_{35}N_6O_3^+$ – 455.2771, found – 455.2761 (M+).

Maleoylglycyl chloride. Maleoylglycyl chloride was prepared from N-maleoyl glycine[120] by treatment with oxalyl chloride (1.05 eq.) and DMF (cat.) immediately prior to use. A suspension of the acid and oxalyl chloride in DCM was cooled in an ice bath followed by addition of a drop of DMF. The reaction was vented under gentle positive pressure from N_2 gas and allowed to warm to room temperature. After stirring for at least 15 min, the solvent was removed *in vacuo*. The white residue was dissolved in DMF for use without further purification.

(*E*)-2-((6-(3-(4-((4-(2-(2,5-dioxo-2,5-dihydro-1*H*-pyrrol-1 yl)acetamido)phenyl)diazenyl)phenyl)ureido)hexanoyl)oxy)-*N*,*N*,*N*-trimethylethanaminium
(**4a**) (**MAACh**)**.** To a solution of compound **S2** (10 mg, 20 µmol) and DIPEA (16 µl, 92 µmol) in DMF (1 ml) was added maleoylglycyl chloride (14 mg, 80 µmol of N-maleoyl glycine) in DMF (0.5 ml). The reaction was stirred for several hours, followed by removal of solvent *in vacuo*. Reverse phase silica gel chromatography (1% MeCN: 0.1% formic acid in H_2O gradient to 20% MeCN) provided **4a** (**MAACh**) as a yellow solid (6.4 mg, 10 µmol, 50% yield): ^1H (MeOD, 400MHz): 1.29 (s, 2H); 1.44 (s, 2H); 1.56 (s, 2H); 2.30 (t, 2H, J=7.6); 3.07-3.09 (m, 1H); 3.56 (s, 2H); 4.25 (s, 2H); 4.40 (s, 2H); 6.82 (s, 2H); 7.41 (d, 2H, J=8.8); 7.59 (d, 2H, J=8.8); 7.69-7.71 (m, 4H); 8.29 (bs, 1H). HRMS (ES+): calculated for $C_{30}H_{38}N_7O_6^+$ – 592.2884, found – 592.2878 (M+)**.**

(*E*)-2-((6-(3-(4-((4-acetamidophenyl)diazenyl)phenyl)ureido)hexanoyl)oxy)-*N*,*N*,*N*-trimethylethanaminium (**6a**) (**AcAACh**)**.** To a solution of compound **S2** (23 mg, 46 µmol) and DIPEA (16 µl, 92 µmol) in DMF (1 ml) was added acetyl chloride (6.5 µl, 92 µmol) in DMF (0.5 ml). The reaction was stirred for several hours, followed by removal of solvent *in vacuo*. Reverse phase silica gel chromatography (1% MeCN: 0.1% formic acid in H_2O gradient to 33% MeCN) provided **6a** (**AcAACh**) as a yellow solid (14 mg, 25 µmol, 54% yield): ^1H (MeOD, 400MHz): 1.31 (s, 2H); 1.43 (s, 2H); 1.55 (s, 2H); 2.03 (s, 3H); 2.30 (t, 2H, J=7.6); 3.07-3.11 (m, 1H); 3.57 (s, 2H); 4.41 (s, 2H); 7.42 (d, 2H, J=8.8); 7.60 (d, 2H, J=8.8); 7.69-7.72 (m, 4H); 8.31 (bs, 1H). HRMS (ESI+): calculated for $C_{26}H_{37}N_6O_4^+$ – 497.2871, found – 497.2853 (M+).

(E)-4-((4-nitrophenyl)diazenyl)phenol (**S3**)**.** Compound **S3** was prepared from 4-nitroaniline and phenol according to the method in Haghbeen *et al*.[121]

(*E*)-3-(4-((4-aminophenyl)diazenyl)phenoxy)propan-1-ol (**S4**)**.** A mixture of **S3** (200 mg, 0.82 mmol), K_2CO_3 (567 mg, 4.10 mmol), KI (~ 1 mg), and 3-bromopropanol (0.37 ml, 4.1 mmol) in acetone (25 ml) was refluxed for 4.5 hrs with stirring under N_2. After cooling, the reaction was transferred to a separatory funnel with EtOAc (50 ml), extracted twice with H_2O (20 ml), once with brine (20 ml) followed by drying of the organic layer over Na_2SO_4 and removal of solvent *in vacuo*. Silica gel chromatography (33% EtOAc in Hex gradient to 50%) provided the nitro-bromide as an orange solid (246 mg, 0.82 mmol, 99% yield): ^{1}H ($CDCl_3$, 500MHz): 1.69 (s, 1H); 2.08 (dt, 2H, J=5.5, 6.0); 3.88 (t, 2H, J=5.5); 4.21 (t, 2H, J=6.0); 7.02 (d, 2H, J=9.0); 7.92-7.96 (m, 4H); 8.32 (d, 2H, J=9.0). ^{13}C ($CDCl_3$, 125MHz): 31.9, 59.8, 65.7, 114.9, 123.1, 124.7, 125.6, 146.9, 148.2, 155.9, 162.5. HRMS (FAB+): calculated for $C_{15}H_{16}N_3O_4^+$ – 302.1141, found – 302.1146 (MH+).

To a mixture of the nitro alcohol (205 mg, 0.68 mmol), and Na_2CO_3 (324 mg, 3.06 mmol) in 1:1 THF:H_2O (30 ml) was added a solution of 20% $(NH_4)_2S$ in H_2O (0.68 ml, 2.04 mmol). The reaction was refluxed for 1 hr followed by careful acidification to pH 7 with dilute HCl deep in the hood as to prevent exposure to highly toxic H_2S gas. After cooling, the reaction was transferred to a separatory funnel with EtOAc (50 ml) and extracted three times with EtOAc (25 ml). The combined organics were washed once with H_2O (20 ml), once with sat. aq. $NaHCO_3$ (20 ml) and once with brine (20 ml) followed by drying over Na_2SO_4 and removal of solvent *in vacuo*. Silica gel chromatography (15% EtOAc in DCM gradient to 50%) provided **S4** as an orange solid (150 mg, 0.55 mmol, 81% yield): ^{1}H (CD_3CN, 500MHz): 1.96 (t, 2H); 2.69 (bs, 1H); 3.69 (s, 2H); 4.15 (t, 2H); 4.72 (bs, 2H); 6.73 (d, 2H, J=9.0); 7.04 (d, 2H, J=9.0); 7.68 (d, 2H, J=9.0); 7.78 (d, 2H, J=9.0). ^{13}C (CD_3CN, 125MHz): 32.0, 58.1, 65.1, 113.9, 114.7, 123.6, 124.4, 144.3, 146.9, 151.1, 160.6. HRMS (FAB+): calculated for $C_{15}H_{18}N_3O_2^+$ – 272.1399, found – 272.1407 (MH+).

(*E*)-3-(4-((4-aminophenyl)diazenyl)phenoxy)-*N*,*N*,*N*-trimethylpropan-1-aminium (**S5**)**.** To a solution of **S4** (143 mg, 0.53 mmol) in THF (10 ml), cooled on an ice bath was added, in the following order, PPh_3 (566 mg, 2.16 mmol), imidazole (180 mg, 2.65 mmol) and CBr_4 (211 mg, 0.64 mmol) with stirring under N_2 and subsequently warmed to room temperature. After about 10 min, a white precipitate began to form, which completely dissolved after 1 hr. After 3 hrs, an additional 0.5 eq. CBr_4 and 2 eq. PPh_3 were added and the reaction was allowed to stir overnight.

The reaction was then transferred to a separatory funnel with EtOAc (60 ml), washed twice with H_2O (30 ml) and once with brine (30 ml) followed by drying over Na_2SO_4 and removal of solvent *in vacuo*. Silica gel chromatography (25% EtOAc in Hex gradient to 50%) provided the amino-bromide as an orange solid (70 mg, 0.21 mmol, 40% yield): ^{1}H (CD_3CN, 400MHz): 2.29 (dt, 2H, J=5.5, 6.0); 3.64 (t, 2H, J=6.0); 4.14 (t, 2H, J=5.5);

4.73 (bs, 2H); 6.73 (d, 2H, J=9.0); 7.04 (d, 2H, J=9.0); 7.68 (d, 2H, J=9.0); 7.78 (d, 2H, J=9.0). ^{13}C (CD_3CN, 100MHz): 30.3, 32.0, 65.7, 113.9, 114.8, 123.6, 124.5, 144.3, 147.1, 151.2, 160.2. HRMS (FAB+): calculated for $C_{15}H_{16}BrN_3O$ – 333.0477, found – 333.0482 (M+).

The amino-bromide (49 mg, 0.15 mmol) was dissolved in THF (3 ml) and cooled on an ice bath under N_2. The N_2 line was removed and a gentle stream of Me_3N gas was bubbled through the solution while stirring and venting into a solution of 10% HCl for about 1 min or until a small volume increase was observed. Orange precipitate began to form immediately. After removal of the Me_3N stream, the reaction vessel was sealed and allowed to stir at room temperature overnight. A stream of N_2 gas was then bubbled through the reaction while stirring and vented into a solution of 10% HCl to remove the excess Me_3N. After removal of solvent *in vacuo*, reverse phase silica gel chromatography (5% MeOH:H_2O gradient to 50% MeOH) provided **S5** as an orange solid (61 mg, 0.15 mmol, quantitative yield): ^1H (MeOD, 500MHz): 2.32 (s, 2H); 3.20 (s, 9H); 3.60 (s, 2H); 4.17 (s, 2H); 6.74 (d, 2H); 7.05 (d, 2H); 7.67 (d, 2H); 7.77 (d, 2H). ^{13}C (MeOD, 125MHz): 22.9, 52.3, 63.9, 64.5, 113.8, 114.4, 123.3, 124.3, 144.1, 146.8, 151.3, 159.4. HRMS (ES+): calculated for $C_{18}H_{25}N_4O^+$ – 313.2023, found – 313.2019 (M+).

(*E*)-3-(4-((4-(2-(2,5-dioxo-2,5-dihydro-1*H*-pyrrol-1-yl)acetamido)phenyl)diazenyl)phenoxy)-*N*,*N*,*N*-trimethylpropan-1-aminium (5a) (MAHoCh). To a solution of compound **S5** (27 mg, 69 µmol) and DIPEA (24 µl, 133 µmol) in DMF (1 ml) was added maleoylglycyl chloride (14 mg, 80 µmol of N-maleoyl glycine) in DMF (0.5 ml). The reaction was stirred for several hours, followed by removal of solvent *in vacuo*. Reverse phase silica gel chromatography chromatography (1% MeOH: 0.1% formic acid in H_2O gradient to 25% MeOH) provided **5a** (**MAHoCh)** as a yellow solid (17 mg, 35 µmol, 51% yield): ^1H (MeOD, 500MHz): 2.35 (s, 2H); 3.31 (s, 9H); 3.59-3.63 (m, 2H); 4.21 (t, 2H); 4.38 (s, 2H); 6.95 (s, 2H); 7.10 (d, 2H, J=9.0); 7.73 (d, 2H, J=9.0); 7.85-7.90 (m, 4H); 8.27 (bs, 1H). HRMS (ESI+): calculated for $C_{24}H_{28}N_5O_4^+$ – 450.2136, found – 450.2132 (M+).

Chapter 3 Optical control of metabotropic glutamate receptors

This chapter was published as a technical report in Nature Neuroscience volume 16, issue 4, pages 507-516 in March 2013 with me as co-author.

Introduction

Optogenetics has revolutionized neuroscience by making it possible to use heterologously expressed light-gated ion channels and pumps to stimulate or inhibit activity in genetically selected neurons and brain regions and thereby determine their roles in circuit function and behavior[1,2]. As the flow of information through neural circuits depends on the strength of synaptic transmission, and changes in synaptic strength are critical to neural processing as well as learning and memory, an important further development would be to bring optogenetics to the native pre- and postsynaptic receptors that control synaptic transmission and plasticity.

Of special interest are GPCRs, the largest class of membrane signaling proteins, which, because of their importance to disease, are the most explored drug targets in all of biology. GPCRs respond to a wide array of stimuli and contain a seven transmembrane domain that couples to heterotrimeric G proteins, including the Gq, Gs, Gt and Gi/o families, through which they regulate a variety of other signaling proteins[3]. Recent X-ray structures have increased our understanding of how GPCRs interact with external ligands and couple intracellularly with G proteins[4]. Despite these efforts, there remains a paucity of selective pharmacological tools for GPCRs, and the specific biochemical, physiological and behavioral roles of many GPCRs are not well understood. In neural systems, GPCRs are found mostly on sensory cilia and at synapses. The same GPCR may be found on both presynaptic excitatory and inhibitory nerve terminals, as well as on dendritic spines and associated glial processes[5], making it difficult to determine its specific function in each compartment and leaving the mechanism of induction of synaptic plasticity undefined. Even though multiple GPCRs in a cell may couple to the same G proteins, they often activate distinct targets as a result of molecular interactions that colocalize them in specific protein complexes, which can lead to unique patterns of regulation[3,6,7].

Thus, to determine the function of a GPCR, one needs specific tools for subtype-selective, cell type–specific, spatially precise, and, ideally, rapid and reversible manipulation. The ability to engineer individual full-length GPCRs that can be activated or blocked by remote control could provide a general solution for these problems. GPCRs have already been engineered to respond to non-native ligands, the so-called RASSLs and DREADDs, and used to orthogonally activate G protein pathways *in vitro*[8] and *in vivo*[9]. Because these receptors lack the spatiotemporal precision of optical manipulation, interest has remained in the development of light-activated GPCRs. Until now, effort has

centered on naturally light-sensitive rhodopsin[10–12] and melanopsin[13–15] and chimeras that combine the transmembrane portions of rhodopsin with the cytoplasmic loops of adrenergic or serotonergic receptors that couple to other G proteins[16–20]. Although these foreign or chimeric receptors can be used to activate specific G proteins, they lack signaling specificity because they lack the complete sequence (and normal protein interactions) of the native GPCR. Moreover, as they require 11-*cis* retinal as a photoswitch, which is lost following photoisomerization, they cannot trigger either sustained or reproducible signals because of incomplete recovery following photo-stimulation[21].

To solve these problems, we developed an optochemical method for controlling native mammalian GPCRs with light. We employed synthetic photoswitchable tethered ligands (PTLs) that could be targeted to genetically modified versions of native receptors[1,22], as has been done to light-block K+ channels[23] and to light-activate the ionotropic kainate receptor[24]. We targeted the eight-member mGluR family. mGluRs are class C GPCRs that are allosterically regulated by glutamate binding to a large extracellular clamshell ligand-binding domain (LBD)[5]. mGluRs respond to spatially confined, temporal patterns of synaptic and extrasynaptic glutamate to regulate neuronal excitability, transmitter release and synaptic plasticity[5,25,26]. They include presynaptic receptors, which provide feedback control over glutamate release from excitatory nerve terminals and control of GABA release from inhibitory nerve terminals, postsynaptic receptors that modulate synaptic signaling in dendritic spines, and receptors in astrocytic processes that are intimately associated with synapses and respond to neuronal activity in several ways, including gliotransmitter release[27,28]. The mGluRs are divided into three groups[5]. We focused on the group II mGluRs, mGluR2 and mGluR3, which couple to the Gi/o pathway to inhibit adenylyl cyclase[29], activate GIRK channels to reduce excitability and inhibit presynaptic voltage-gated calcium channels to inhibit neurotransmitter release[30,31]. These mGluRs operate in synaptic plasticity in multiple brain regions[25,26], participate in fundamental behavioral processes, including memory[32], and represent major drug targets for neuropsychiatric disorders[33]. We extended our engineering to the group III mGluR mGluR6, which also couples to Gi/o, but has distinct expression patterns, subcellular targeting and regulation, and, as a consequence, distinct roles in neural circuits[5].

We used a combination of structural analysis and synthesis of previously unknown compounds to develop new PTLs with maleimide at one end for cysteine attachment, a photoisomerizable azobenzene linker and glutamate as the ligand at the other end. Monte Carlo simulations enabled us to determine PTL attachment points such that photoisomerization of the azobenzene would toggle the PTL from a conformation that permits glutamate binding to one that does not. The approach was successful for both photo-agonism and photo-antagonism of mGluR2. Light rapidly, reversibly and reproducibly turned mGluR2 on and off. The photo-control was bistable and could be used to toggle excitability and presynaptic inhibition in cultured neurons and brain slices. *In vivo*, mGluR2 photo-agonism was able to reversibly and repeatedly modulate escape behavior in larval zebrafish, a fast control of a previously unknown native form of regulation of the acoustic startle response (ASR). The photo-control approach was generalizable, as we transferred it to mGluR3 and mGluR6. The introduction of photosensitivity into native

GPCRs provides the means for probing their biological functions at a level of precision not previously available.

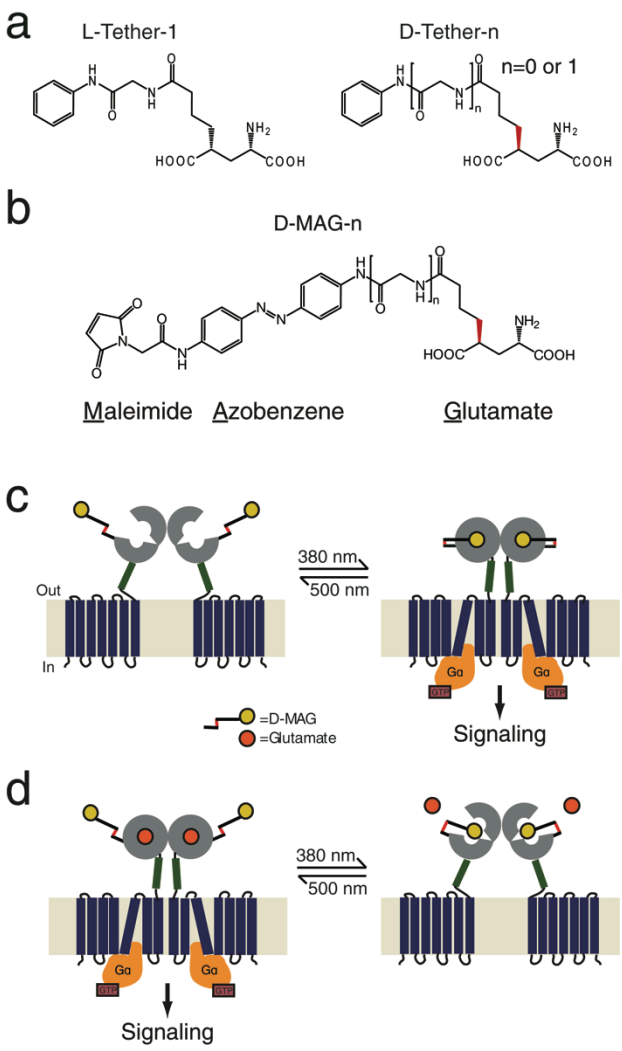

Figure 3.1, Design of photoswitches for light-control of mGluR2. a) Chemical structure of tether models including previously described L-Tether-1 and new 4′D versions with two different linker lengths (D-Tether-0 and D-Tether-1). b) Structure of D-MAG molecules. D-MAG is maximally isomerized to the *cis* state by 380-nm light and isomerized to the *trans* state by 500-nm light. Spontaneous thermal relaxation from *cis* to *trans* occurs over tens of minutes at 25 °C. c) Schematic view of light-induced agonism. mGluRs contain a ligand-binding clamshell domain (gray) that is coupled to a seven-transmembrane domain (dark blue) by a cysteine-rich domain (green). Agonist binding to the LBD initiates clamshell closure, which rearranges a dimer interface with a partner binding domain of a second subunit and transmits a conformational change via the transmembrane domain to the cytoplasmic domain, thereby activating G proteins. Under 380-nm illumination D-MAG enters the *cis* state and reorients the glutamate moiety into the ligand-binding site to drive clamshell closure and activate G protein and downstream signaling. d) Schematic of 380 nm–induced antagonism. Glutamate (dark orange circles) is shown in the bound, activated state of mGluR2. Following photoisomerization, the glutamate end of MAG enters the binding site and prevents clamshell closure, thereby deactivating the receptor.

Results

Tether model pharmacology and Monte Carlo simulations

To design photocontrol of mGluR2, we built a homology model of the mGluR2 LBD based on the mGluR3 crystal structure[34] (Supplementary Fig. 3.1a–c) and tested a series of test compounds, which we refer to as tether models (Fig. 3.1a). We found that, unlike the 4'L (γ carbon of glutamate) requirement at ionotropic glutamate receptors, 4'D stereochemistry was required for mGluR2 and that a short tether (D-Tether-0) acted as an agonist, whereas a longer tether (D-Tether-1) acted as an antagonist (Supplementary Fig. 3.1). These findings led us to synthesize D-MAG-0 and D-MAG-1 (D-maleimide azobenzene glutamate; Fig. 3.1b) with the goal of identifying attachment points for optical agonism (Fig. 3.1c) or antagonism (Fig. 3.1d). earlier experimentally determined coordinates that were validated computationally[35]. After manually positioning the glutamate group of D-MAG-0 in the binding pocket, the Monte-Carlo multiple minimum (MCMM) algorithm[36] was used to search the space accessible to D-MAG-0 with single-bond rotations as degrees of freedom. The MCMM algorithm generated 20,000 orientations and structures and, for each, automatically measured the distance from the cysteine-reactive maleimide group of MAG to every residue on the surface of the LBD. Simulations were performed for both *cis* and *trans* conformations of D-MAG-0 (Fig. 3.2a). The conformational search identified eight clusters of 3–8 residues that were frequently populated by the maleimide group of D-MAG-0 (Fig. 3.2b).

To rationally design light-gated versions of mGluR2, we used Monte Carlo simulations to identify geometrically appropriate cysteine-attachment points for the conjugation of D-MAG-0. First, we built a homology model of mGluR2 in the open, glutamate-bound state using the mGluR1 open, glutamate-bound crystal structure (PDB ID: 1EWK) as a template. We then generated molecular models of D-MAG-0 with geometries of *cis*- and *trans*-azobenzene based on earlier experimentally determined coordinates that were validated computationally[35]. After manually positioning the glutamate group of D-MAG-0 in the binding pocket, the Monte-Carlo multiple minimum (MCMM) algorithm[36] was used to search the space accessible to D-MAG-0 with single-bond rotations as degrees of freedom. The MCMM algorithm generated 20,000 orientations and structures and, for each, automatically measured the distance from the cysteine-reactive maleimide group of MAG to every residue on the surface of the LBD. Simulations were performed for both *cis* and *trans* conformations of D-MAG-0 (Fig. 3.2a). The conformational search identified eight clusters of 3–8 residues that were frequently populated by the maleimide group of D-MAG-0 (Fig. 3.2b).

Based on the Monte Carlo simulations, we selected a subset of seven residues with orientations favorable for the maleimide end of MAG to conjugate and for its glutamate end to enter the ligand-binding site without steric clashes. Seven candidate sites were identified: Q42, D146, E373 and S376 in the upper lobe of the LBD, L300 and S302 on the lower lobe, and D215 at the hinge (Fig. 3.2c). Each site was individually substituted with cysteine and coexpressed with GIRK1 in HEK293 cells.

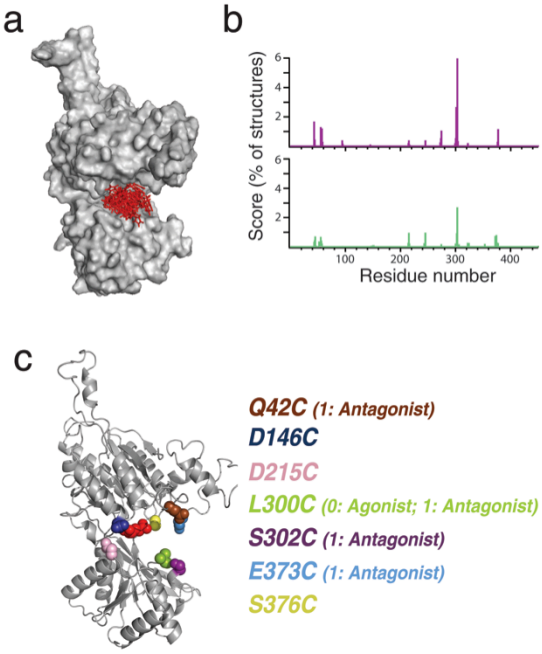

Figure 3.2. Monte Carlo simulations and cysteine-scanning of mGluR2 LBD. a) *cis*-D-MAG-0 (red stick depiction) with glutamate end bound in LBD (gray surface depiction) is shown in 20 superposed conformations calculated by Monte Carlo simulation using a homology model of the mGluR2 LBD in the open, glutamate-bound conformation. b) Results of D-MAG-0 simulations for *cis* and*trans* conformations. Lines indicate the frequency with which the maleimide end of MAG approached within 6Å of the Cα of a particular residue in the *cis* state (violet) and *trans* state (green). c) Open homology model of mGluR2 LBD showing native side chains of seven residues individually substituted to cysteine. Results of photoswitching of D-MAG-0 and D-MAG-1 attached at each of the positions where any photoresponse was observed are shown in parentheses. 0 indicates D-MAG-0 and 1 indicates D-MAG-1. Data are from ≥2 different coverslips for all conditions tested.

Photo-antagonism by D-MAG-1: LimGluR2-block

We initially focused on two of the MAG attachment sites, L300C and S302C, because of their high scores in the Monte Carlo simulations and their large photo-effects (Fig. 3.2b and Supplementary Table 2.1). Cells expressing either variant along with GIRK1 were labeled with either D-MAG-0 or D-MAG-1 (50–100 μM) for 30–60 min, patch-clamped in the whole-cell configuration and alternately challenged with 380-nm light to isomerize the photoswitch to *cis* and 500-nm light to isomerize to *trans*. This was done in the absence of glutamate to determine whether there was photo-agonism or in the presence of glutamate to determine whether there was photo-antagonism. Notably, no photoeffects were observed in cells expressing wild-type mGluR2 and labeled with D-MAG-0 or D-MAG-1 (Supplementary Table 3.1).

Following labeling at S302C and L300C with D-MAG-1, we found that illumination at 380 and 500 nm had no effect on the current (Fig. 3.3a and Supplementary Fig. 3.2a). However, in the presence of glutamate, 380-nm light induced a marked decrease in the current that was reversed by illumination at 500 nm (Fig. 2.3a and Supplementary Fig. 3.2a). Repeated switching between 380- and 500-nm light toggled the glutamate-induced current between high and low levels. The percentage photo-antagonism was 21 ± 2% (n = 7) for D-MAG-1 at L300C and 53 ± 4% (n = 5) at S302C in 1 mM glutamate. At concentrations greater than 1 mM, photoantagonism was decreased (Supplementary Fig. 3.2b,c), indicating a competitive mechanism. D-MAG-1 antagonism is consistent with the antagonism of the D-Tether-1 compound, as described above. Because of the large potency of the 302C substitution in combination with D-

MAG-1, we named this tool LimGluR2-block.

An advantageous property of the azobenzene photoswitches that we used is their thermal bistability, which makes it possible to produce persistent occupancy in the dark of the *cis* state following a photo-isomerizing light pulse[37,38]. Indeed, we found that brief light pulses at 380 nm induced antagonism that was stable in the dark until it was reversed by 500-nm illumination (Fig. 3.3b).

Photo-agonism by D-MAG-0: LimGluR2

We next turned to the version of MAG that was based on the agonist D-Tether-0, D-MAG-0. We focused on the combination of L300C and D-MAG-0 because of the utility of photo-activation, and referred to it as LimGluR2. The photo-activation of LimGluR2 by 380-nm light yielded currents about half as large as those evoked by saturating glutamate (48 ± 4% compared with 1 mM glutamate, $n = 10$; Fig. 3.3c). Illumination at 500 nm rapidly terminated the activation of the GIRK1 channels (Fig. 3.3c–f). Voltage ramps confirmed that the light activation of LimGluR2 at 380 nm was a result of the opening of the same inward-rectifying potassium conductance as was activated by glutamate (Supplementary Fig. 3.3a).

Notably, no antagonism of the glutamate response was induced by illumination at 380 nm (Fig. 3.3c and Supplementary Fig. 3.3c). This suggests that the lack of full activation by D-MAG-0 attached to L300C is not a result of partial agonism by *cis*-D-MAG-0. Application of glutamate following illumination at 380 nm increased the inward current above the level induced by light alone (Supplementary Fig. 3.3b). This result further indicates that MAG does not lock the LBD in a partially active conformation, but instead functions as a full agonist in a fraction of subunits. LimGluR2 maintained close to normal affinity for glutamate (Supplementary Fig. 3.3d) and retained the ability to be activated or antagonized by standard group II mGluR pharmacological agents (Supplementary Fig. 3.3e,f).

As with the bistability of LimGluR2-block, we found that brief activating light pulses at 380 nm evoked a period of GIRK activation that persisted for tens of seconds in the dark, and which could be rapidly turned off by illumination with 500-nm light (Fig. 3.3d). During this bout of protracted activation in the dark, the current declined by ~10–20%, which was similar to what was seen under continuous illumination of LimGluR2 at 380 nm, as well as in response to extended application of glutamate (Fig. 3.3a and Supplementary Fig. 3.4a). At moderate light intensities (10–20 mW mm–2), bistable activation and deactivation were elicited by brief light pulses (250-ms pulse at 380 nm to activate and 1-s pulse at 500 nm to deactivate) of LimGluR2-induced GIRK currents with identical amplitude and kinetics to currents induced by extended illumination (Supplementary Fig. 3.4a–c). At higher light intensities (~40 W mm^{-2}), signaling could be activated by sub-millisecond pulses of light (Fig. 3.3e), indicating that these brief pulses are sufficient to ligand the receptor and that the kinetics of effector activation and deactivation are rate-limited by subsequent signaling steps.

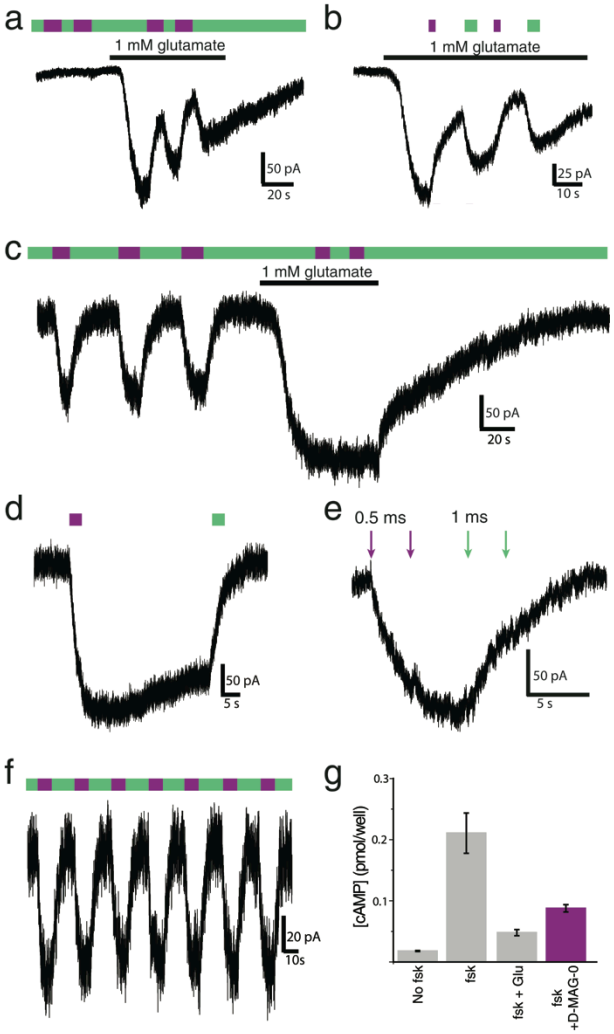

Figure 3.3. Photo-antagonism and photo-agonism of mGluR2. a–f) Effects of photoswitching D-MAG-0 and D-MAG-1 on the activation of GIRK1 current in HEK293 cells. a) When D-MAG-1 was attached to S302C (LimGluR2-block), light had no effect in the absence of glutamate, but 380-nm light evoked photo-antagonism in the presence of glutamate. Black bars indicate application of 1 mM L-glutamate. Green bars indicate illumination with 500-nm light and violet bars indicate 380-nm light. b) LimGluR2-block photo-antagonism is bistable. A brief flash of 380-nm light induced a decrease in glutamate-evoked current that was sustained in the dark until it was reversed by 500 nm. c) When D-MAG-0 was attached to L300C, 380-nm light evoked GIRK1 current on its own. The current remained activated until deactivation was initiated by 500-nm light. No photo-antagonism was seen in the presence of glutamate, indicating that D-MAG-0 was not a partial agonist of mGluR2-L300C. d) LimGluR2-mediated GIRK1 current showed sustained response in the dark following a brief illumination at 380 nm. e) At higher light intensities (~40 W mm^{-2}), 0.5-ms, 380-nm pulses could activate and 1-ms, 500-nm pulses could fully deactivate LimGluR2. The second 380-nm pulse showed minor further activation, indicating that the first pulse almost completely activated the receptors. f) GIRK1 current evoked by repetitive rounds of photo-activation and photo-deactivation of mGluR2-L300C–D-MAG-0 (LimGluR2) by pulses of 380-nm and 500-nm light, respectively. g) LimGluR2 activation reduced cAMP elevation induced by a 10-min application of 10 μM forskolin (fsk) with similar efficacy as the 1 mM glutamate application. Error bars represent s.e.m. for $n = 3$ coverslips per condition.

Repeated bouts of photoswitching of LimGluR2 yielded multiple rounds of photo-activation of GIRK1 channels without decline of the response (Fig. 3.3f), consistent with the lack of GRK-dependent desensitization of mGluR2[39,40]. Having observed the reproducibility of LimGluR2, we asked how it compares with previously described light-gated GPCRs that are made either of rhodopsin or of rhodopsin chimeras. To address this, we tested rhodopsin, the critical light-gated component of all of the previously described GPCRs. Rat rhodopsin, RO4, which also couples to GIRK1 channels[11], was expressed in HEK293 cells and the cells were incubated for 40 min in 1 μM 11-cis retinal in the dark. Illumination of cells coexpressing RO4 and GIRK1 with 490-nm light activated large inward GIRK currents (Supplementary Fig. 3.5a) that were similar in amplitude and rise time to those evoked by LimGluR2 (Supplementary Fig. 3.5b). However, the GIRK1 deactivation speed of RO4 following light turn-off was much slower than that following

light-driven deactivation of LimGluR2 (Supplementary Fig. 3.5a–c). As a result of the slow deactivation kinetics of RO4, repeated optical stimulation was limited to intervals of 90 s (Supplementary Fig. 3.5d). Even at this long interval, the RO4-mediated responses declined from pulse to pulse (Supplementary Fig. 3.5d,f). In contrast, LimGluR2 photo-responses were stable in amplitude (Fig. 3.3d and Supplementary Fig. 3.5e,f).

Having seen that LimGluR2 can photo-activate Gβγ-mediated signaling, as assayed with GIRK currents, we asked whether it could also photo-activate Gα-mediated signaling by measuring its ability to reduce cellular cAMP levels. When labeled with D-MAG-0 and stimulated with 380-nm light, LimGluR2 reduced the elevation of cAMP that was triggered by forskolin with an efficacy approaching that of 1 mM glutamate (Fig. 3.3g). This indicates that *cis*-D-MAG-0 activates mGluR2 in the same way as glutamate to induce native downstream signaling.

Generalization of photocontrol to mGluR3 and mGluR6

To determine whether the PTL approach could be generalized to other mGluRs, we tested cysteine substitutions in mGluR3, the other group II mGluR member, and mGluR6, a group III mGluR member, at residues that are homologous to L300 of mGluR2 (Fig. 3.4a). Optical control of mGluR3 is attractive because of the lack of agonists and antagonists that differentiate between mGluR2 and 3, with the exception of a recently described compound that agonizes mGluR2 and antagonizes mGluR3[41]. mGluR6 is an important target for photocontrol because of its central role in synaptic transmission from photoreceptors to ON bipolar cells in the retina.

Conjugation of mGluR3 Q306C with D-MAG-0 produced strong photo-agonism (LimGluR3) under 380-nm light (Fig. 2.4b). The photocurrents were 74 ± 12% (n = 6 cells) of the amplitude of 1 mM glutamate-evoked currents, indicating that LimGluR3 is even more efficient than LimGluR2. Conjugation of mGluR6-K306C with D-MAG-0 produced a strong photo-antagonism under 380-nm light (Fig. 3.4c). Photo-antagonism was 40 ± 3% (n = 5 cells, 1 mM glutamate) for D-MAG-0 at mGluR6-K306C. We termed this tool LimGluR6-block. Notably, photoswitching of D-MAG-0 anchored at sites of mGluR3 and mGluR6 that are homologous to mGluR2's L300 yielded similar photo-agonism in mGluR3, but photo-antagonism in mGluR6, providing a readout of the degree of geometric similarity near the LBD binding pocket.

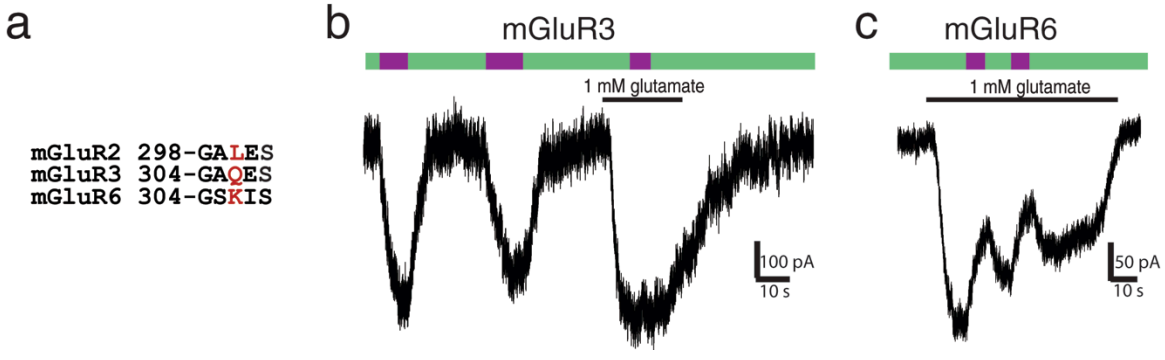

Figure 3.4, Extension of photoswitching from mGluR2 to mGluR3 and mGluR6. a) Local alignment of region containing D-MAG-0 anchoring sites in mGluR2 for LimGluR2 (red). b) When D-MAG-0 was attached to mGluR3-Q306C (LimGluR3), robust 380-nm light–induced agonism was observed. Similar to LimGluR2, no photo-antagonism was seen in the presence of glutamate. c) When D-MAG-0 was attached to mGluR6-K306C (LimGluR6-block) robust 380-nm light–induced photoantagonism was observed, indicating that the PTL approach can be extended to group III mGluRs.

Optical control of excitability in hippocampal neurons

In addition to the functional advantages over existing photoswitchable GPCRs, LimGluR2 is a native receptor that could make it possible to optically stimulate native mGluR2 targets with light. To test this, we examined the ability of LimGluR2 to optically modulate native downstream targets of mGluR2 in cultured hippocampal neurons. These targets include somatodendritic GIRK channels42 and voltage-gated calcium channels in the presynaptic nerve terminal[43,44], both of which should be within reach of mGluR2-L300C, which we found to distribute to the soma and many fine processes (Fig. 3.5a).

We first tested the expectation that activation by LimGluR2 of cell body GIRK channels would decrease excitability (Fig. 3.5b). In high extracellular potassium (60 mM) and under voltage clamp, illumination with 380-nm light evoked large inward currents that were deactivated by 500-nm light (Supplementary Fig. 3.6a). With illumination at a fixed intensity (0.4 mW mm–2 at 380 nm), photo-activation was ~5-fold faster in neurons than in HEK293 cells (single exponential fits: neurons, $\tau = 1.03 \pm 0.06$ s, $n = 5$; HEK293 cells, 5.69 ± 0.69, $n = 8$; unpaired, one-tailed t test, $P = 0.004$). This is consistent with previous observations of faster activation of GIRK channels by native GPCRs in cultured neurons compared with heterologously expressed receptors in GIRK-transfected HEK293 cells45 and suggests that LimGluR2 integrates into the native G-protein signaling machinery of neurons.

To test the ability of LimGluR2 to modulate neuronal excitability via GIRK channel activation, we performed current-clamp experiments. Neurons expressing LimGluR2 were labeled with D-MAG-0 and given depolarizing current injections, in 10-pA increments, under current clamp. This was done during alternating illumination with 380-nm and 500-nm light. Photo-activation of LimGluR2 at 380 nm decreased the number of action potentials evoked by each level of depolarization (Fig. 3.5c,d). This optical inhibition was highly reversible and repeatable (Fig. 3.5c,e,f and Supplementary Fig. 3.5b). The photo-currents were large enough to evoke a reversible 3–10-mV hyperpolarization at the resting potential (Fig. 3.5e) and, consistent with the bistability of the system, the hyperpolarization and silencing persisted for tens of seconds in the dark after activation of LimGluR2 by a brief 380-nm light pulse (Fig. 3.5e).

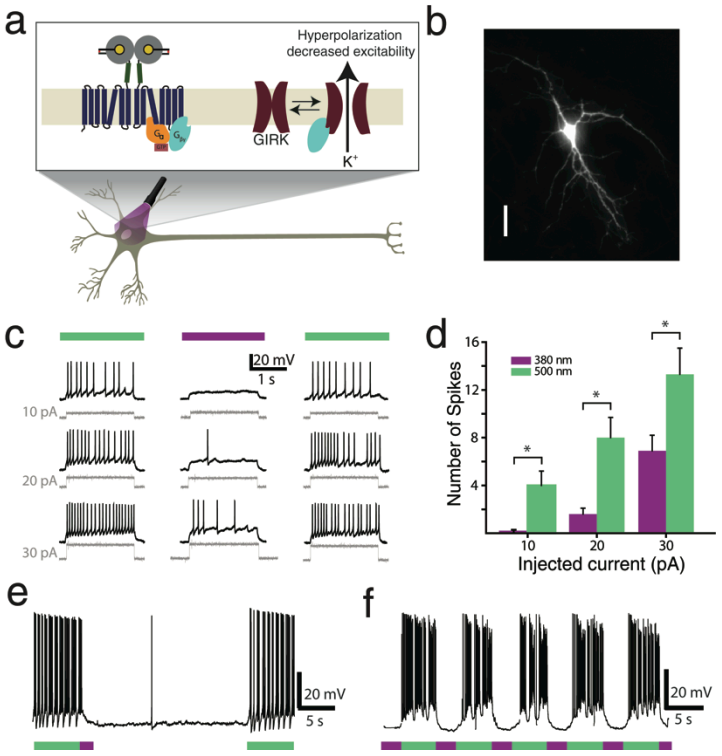

Figure 3.5, **LimGluR2 hyperpolarizes and reduces excitability in cultured hippocampal neurons.** a) LimGluR2-eGFP was widely distributed in cultured hippocampal neuron. Scale bar represents 50 μm. b) Schematic showing LimGluR2-mediated control of excitability via GIRK channels. Note that light was applied to entire field of view. c) Trains of spikes elicited by depolarizing current steps (gray traces) when LimGluR2 was off (500-nm illumination, green bar) were reversibly suppressed by activation of LimGluR2 (380-nm illumination, violet bar). Traces are from a representative cell. d) Summary of the current-step experiments shown in c for eight cells. Bars indicate the number of spikes in response to 2-s current injections under 380-nm (violet bar) or 500-nm (green bar) light and error bars indicate s.e.m. Asterisk indicates statistical significance (paired, one-tailed *t*-test, $P = 0.009$, 0.004 and 0.009 for currents of 10, 20 and 30 pA, respectively; $n = 7$ cells). e) LimGluR2-mediated hyperpolarization in a representative cell in response to brief (1 s) activation by 380-nm light (violet bar) persisted for tens of seconds in the dark before LimGluR2 deactivation by 500-nm light (green bar). The persistent activation in the dark effectively suppressed spikes. f) Representative trace showing repeatable spike silencing by photo-control of LimGluR2.

Optical control of synaptic transmission

Group II metabotropic glutamate receptors are known to traffic to presynaptic terminals and have inhibitory roles in synaptic transmission and plasticity[5,25]. We asked whether LimGluR2 would allow optical control of neurotransmitter release (Fig. 3.6a). We expressed mGluR2-L300C in low-density hippocampal cultures in which each neuron formed synapses onto itself (autapses). Cells were patch clamped and we recorded postsynaptic currents elicited by brief depolarization steps that elicited single action potentials. Excitatory postsynaptic currents (EPSCs) were detected in some cells (Fig. 3.6b) and inhibitory postsynaptic currents (IPSCs) were detected in others (Fig. 3.6c). Activation of LimGluR2 by 380-nm light rapidly and reversibly inhibited both the EPSCs (41 ± 5%, $n = 8$) and IPSCs (36 ± 3%, $n = 4$) (Fig. 3.6b,c).

In contrast with the potent inhibition by LimGluR2, there was no optical inhibition in either cells transfected with GFP instead of LimGluR2 or cells transfected with LimGluR2, but not labeled with D-MAG-0 (Fig. 3.6d). Moreover, there was no change in baseline PSC amplitude in labeled and transfected (LimGluR2) cells compared with GFP-transfected or unlabeled cells (LimGluR2, 223 ± 64 pA, $n = 12$; GFP, 262 ± 68 pA, $n = 5$; unlabeled, 232 ± 91 pA, $n = 5$). In addition, the optical inhibition of

transmission by LimGluR2 produced no change in postsynaptic current (PSC) decay time (Supplementary Fig. 3.7a), time to peak (Supplementary Fig. 3.7b) or jitter (s.e.m. of time to peak), leaving the PSCs unchanged in shape (Supplementary Fig. 3.7c).

To test whether the LimGluR2-mediated optical inhibition of transmission proceeds through a presynaptic mechanism, we performed paired pulse experiments. The optical inhibition of transmission by illumination with 380-nm light was associated with a significant increase in the relative size of the EPSC evoked by the second pulse (paired, one-tailed *t* test, $P = 0.01$; Fig. 3.6e–g). Similarly, during high-frequency (25 Hz) stimulation of autapses, 380-nm light increased short-term facilitation relative to during 500-nm light (Supplementary Fig. 3.7d–f). This indicates that activation of LimGluR2 inhibits postsynaptic currents by decreasing release probability, thereby increasing facilitation. This is exactly the mechanism by which native mGluR2 acts presynaptically via inhibition of N- and P/Q-type voltage-gated calcium channels, as has been observed for native group II mGluRs at the calyx of Held[43]. The paired pulse ratio in LimGluR2-positive cells was the same as that in GFP-transfected cells (LimGluR2, 1.5 ± 0.1, $n = 5$; GFP, 1.4 ± 0.3, $n = 4$), indicating that expression and labeling of LimGluR2 does not alter basal release.

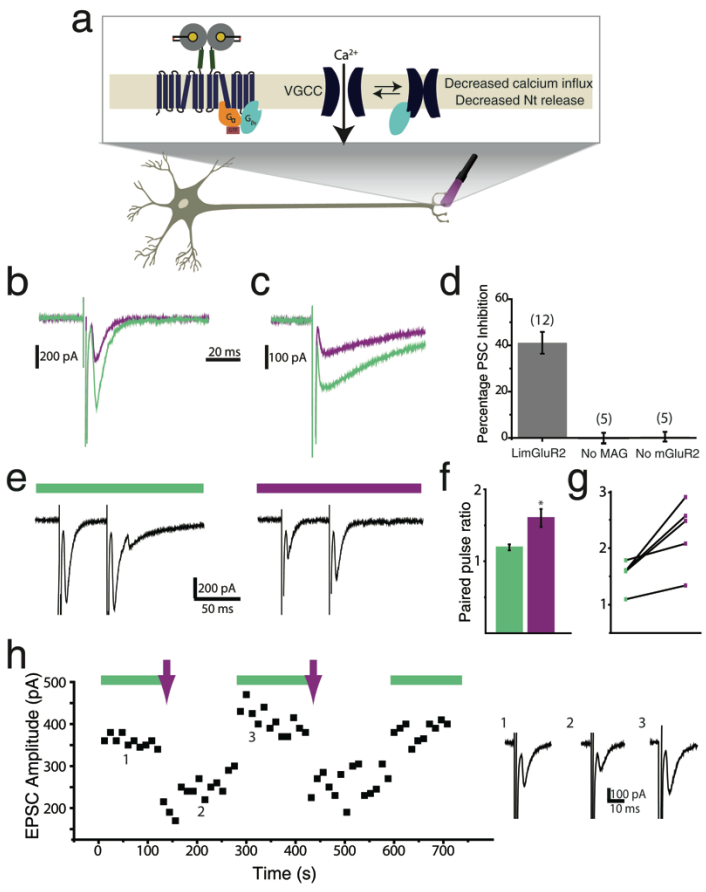

Figure 3.6, Optical activation of LimGluR2 reversibly decreases excitatory and inhibitory postsynaptic currents and increases paired pulse facilitation at hippocampal autapses. a) Schematic shows optical control of neurotransmitter (Nt) release via LimGluR2 triggered G protein suppression of opening of a presynaptic voltage-gated calcium channel (VGCC). b,c) Representative autaptic EPSC (b) and IPSCs (c) elicited by short (2 ms) depolarizing steps are decreased in amplitude by LimGluR2 activation by 380-nm light (violet traces) compared with deactivation by 500-nm light (green traces). d) Pooled inhibition of EPSCs and IPSCs by optical activation of LimGluR2 compared with controls in which mGluR2 (L300C) was expressed, but not labeled with D-MAG-0, and in which mGluR2 was not expressed. Values in parentheses denote the number of cells tested. Error bars represent s.e.m. e) Representative single sweeps of paired pulse recordings (50-ms inter-stimulus interval) of EPSCs under 500-nm light (green bar) followed by 380-nm light (violet bar). f) Summary of paired pulse ratio (PPR) values for representative cell. 380-nm light (violet bar) significantly increased the PPR compared with 500-nm light (green bar) ($n = 10$ sweeps per condition;

paired, one-tailed *t* test, **P* = 0.008). Error bars represent s.e.m. g) Plot of average PPRs measured for five autaptic cells under 500-nm light (green symbols) and 380-nm light (violet symbols). h) Representative EPSC amplitudes from a cell showing repeatable, bistable optical inhibition of an excitatory autapse. Illumination at 500 nm to deactivate LimGluR2 was followed by brief (1 s) illumination at 380 nm (violet arrows), followed by a period of darkness, until illumination at 500 nm to deactivate LimGluR2 was resumed. Inserts (1–3) show EPSCs from the indicated times.

Finally, we tested the ability of LimGluR2 to produce multiple rounds of inhibition of transmission and recovery and for the inhibition to outlast the activating light pulse as a result of the bistable nature of the photoswitch. Brief photo-activation produced sustained inhibition of synaptic transmission that persisted in the dark for minutes and could be rapidly reversed by 500-nm illumination (Fig. 3.6h and Supplementary Fig. 3.7g). We found that LimGluR2 provided a means for the reversible, repeatable optical control of presynaptic inhibition of neurotransmitter release.

Optical control of tonic inhibition by LimGluR2-block

We next assessed the ability of photoantagonism by LimGluR2-block to modulate receptor function in neurons in response to native glutamate. We tested whether photo-antagonism by LimGluR2-block could alter spike-firing patterns in cultured hippocampal neurons. In regions with high transfection efficiency (>1 transfected neuron per field of view), optical antagonism of mGluR2 with 380-nm light resulted in an increased firing frequency that was reversed by 500-nm light (Supplementary Fig. 3.8a,b). This suggests that LimGluR2-block is robust enough to alter neuronal signaling properties despite incomplete antagonism. Furthermore, this indicates that, under basal conditions, there is sufficient inhibitory tone produced by glutamate binding to mGluR2 to suppress spike firing.

We also tested LimGluR2-block in autaptic neurons. Under basal stimulation frequencies (0.1 Hz), photo-antagonism of mGluR2 induced an increase in EPSC amplitude (average increase in amplitude = 26 ± 8%, n = 6 cells; Supplementary Fig. 3.8c,d). This result is consistent with the observation that photo-antagonism of mGluR2 leads to an increase in spike-firing frequency and indicates that glutamate feedback at excitatory nerve terminals can provide inhibitory tone via mGluR2, even in a sparsely connected network. In contrast, at inhibitory autapses, LimGluR2-block did not induce a change in IPSC amplitude (average increase in amplitude = 1.0 ± 0.02%, n = 3 cells; Supplementary Fig. 3.8e,f), suggesting that inhibition of transmitter release via mGluR2 under sparse activity operates by local signaling at individual excitatory synapses, and that cross talk to inhibitory synapses may require high-frequency coordinate activity and global glutamate spillover.

Optical control of excitability in hippocampal slices

We tested LimGluR2 in organotypic hippocampal slices prepared from postnatal day 6–8 (P6–8) rats co-transfected with td-Tomato as a transfection marker. Slices were incubated with D-MAG-0 and whole-cell patch-clamp recordings were performed on cells up to two or three layers below the surface of the slice. At resting potential (–45 mV to –65

mV), LimGluR2 activation by illumination at 390 nm induced a reversible 3–8-mV hyperpolarization (Fig. 3.7a). In response to depolarizing current injections, illumination at 390 nm reproducibly decreased action potential firing (Fig. 3.7b,c), as was seen in the dissociated cultured neurons (Fig. 3.5c,d). Illumination with 500-nm light restored firing frequency to levels seen before LimGluR2 activation. In addition, LimGluR2 activation was able to decrease spontaneous spike firing (Fig. 3.7d) in a bistable, reversible and reproducible manner.

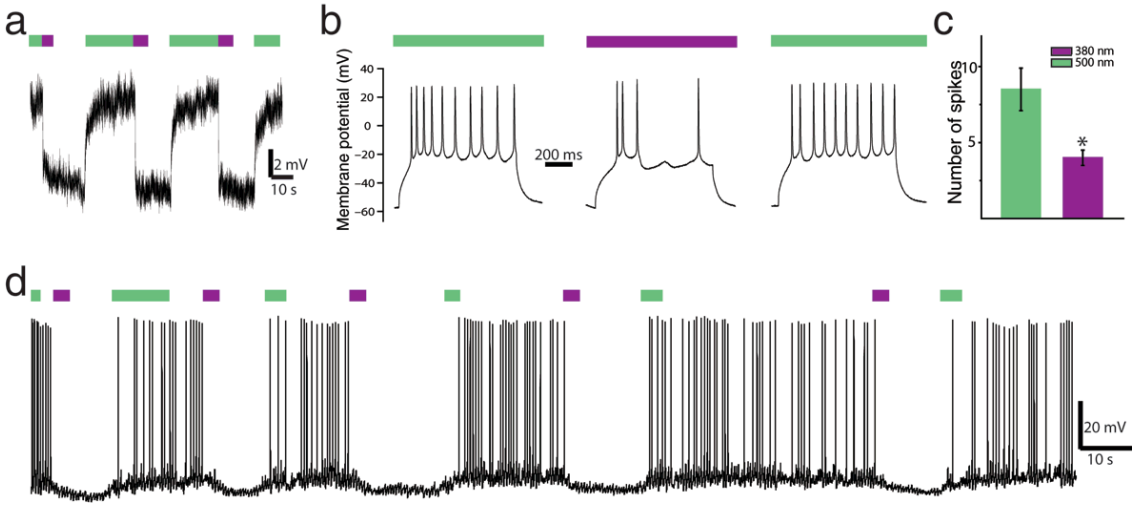

Figure 3.7, LimGluR2-mediated control of neuronal excitability in hippocampal slice. a) Hyperpolarization was triggered by illumination at 390 nm (violet bar) and reversed by illumination at 500 nm (green bar) in a representative cell. b) Representative cell recorded in whole-cell patch in cultured hippocampal slice showing spike firing in response to 1-s, 200-pA depolarizing current injections during 500-nm (green bars) or 380-nm (violet bar) illumination. LimGluR2 activation reversibly decreased the number of spikes. c) Summary of optical control of spike firing in response to current steps in LimGluR2-positive neurons (n = 6 cells). Asterisk indicates statistical significance (paired, one-tailed t test, P = 0.024) and error bars represent s.e.m. d) Representative trace showing reversible, bistable silencing of spontaneous activity by LimGluR2.

Notably, LimGluR2 expression and D-MAG-0 labeling did not adversely affect neurons, leaving the average resting membrane potential unaltered (Supplementary Fig. 3.9a). In addition, we found no photo-effects with D-MAG-0 in the absence of mGluR2-300C (Supplementary Fig. 3.9b,d) or in the presence of mGluR2-300C and absence of D-MAG-0 (Supplementary Fig. 3.9c), indicating that orthogonality is maintained in slices. These results indicate that expression, labeling and optical activation of LimGluR2 are attainable in intact tissue, providing a powerful means to probe the role of G protein signaling in general, and mGluRs in particular, in the native preparation. We next turned to *in vivo* experiments to determine whether LimGluR2 activation in neurons could alter behavior.

Optical control of zebrafish behavior

To determine whether LimGluR2 could be used *in vivo* to probe mGluR signaling in a behavioral context, we turned to the ASR of zebrafish (*Danio rerio*), a well-characterized behavior of teleosts that is similar to the mammalian startle response[46]. At 5–6 days post-fertilization (dpf), fish were individually mounted in a glass-well petri dish with the head embedded in agar and subjected to sound and vibration stimuli (900 Hz, 120 ms) ranging from low energy to high energy (0.1–10 mVpp, 0.5-mVpp increments). At lower energy levels (<2 mVpp), the sound and vibration stimulus induced forward swims, whereas higher energy levels elicited escape responses with the typical C bend[47]. We found that wild-type fish treated with the nonspecific group II mGluR agonist L-CCG-1 displayed a significantly decreased threshold of the ASR when compared with vehicle-treated fish (Mann-Whitney, $n_{ct} = n_{L\text{-}CCG\text{-}1} = 78$, $P < 0.02$, two tailed; Fig. 3.8a). This result indicates that activation of native group II mGluRs leads to a decrease in the threshold of the ASR in wild-type zebrafish.

Next, we examined whether optical activation of LimGluR2 could recapitulate the native group II mGluR signaling effect of decreasing the threshold of the zebrafish ASR. We generated transgenic zebrafish in which LimGluR2(L300C) expression was driven by repeats of the *Gal4* upstream activating sequence (UAS). We crossed these *UAS-LimGluR2* zebrafish to *elavl3-Gal4; UAS-Kaede* fish to generate *elavl3-Gal4; UAS-Kaede; UAS-LimGluR2* zebrafish. The *elavl3* promoter (also known as *HuC*) drives pan-neuronal expression of Gal4, and, consequently, of LimGluR2, as well as the Kaede fluorescent protein, which served as a marker for the *elavl3-Gal4* transgene (Fig. 3.8b). *elavl3-Gal4; UAS-Kaede; UAS-LimGluR2* zebrafish were indistinguishable in swimming behavior at 5 dpf (Supplementary Fig. 3.10c–e) and ASR (Supplementary Fig. 3.10f) from *elavl3-Gal4; UAS-Kaede* fish, which contained the neuronal driver alone. Fish health and responses to touch were unaffected by the 45-min exposure to D-MAG-0 and 1-h recovery. The ASR was also not affected in a control transgenic line that did not express LimGluR2 and was treated with D-MAG-0 (Supplementary Fig. 3.10g). These results indicate that neither pan-neuronal expression of LimGluR2 nor D-MAG-0 treatment modify health or behavior.

LimGluR2 was photo-controlled by patterned illumination applied caudal to the eyes in a region covering the cranial nerves, hindbrain and the rostral portion of the spinal circuits that control the escape response. To activate LimGluR2, we illuminated the fish with 380-nm light for 400 ms; to deactivate it, we applied 510-nm light for 1s. Activation of LimGluR2 increased the probability of an escape response (Fig. 3.8c,d). This effect was reversed by 510-nm light and could be toggled back and forth by repeatedly activating and deactivating LimGluR2 (Fig. 3.8c). The behavior of fish expressing LimGluR2, but not labeled with D-MAG-0, was not altered by light (Fig. 3.8d). In addition, labeling of fish with D-MAG-0 did not alter the basal threshold for the ASR (Supplementary Fig. 3.10h). These results suggest a role for mGluR2 in the ASR and establish that LimGluR2 can be used to study mGluR2 signaling *in vivo*.

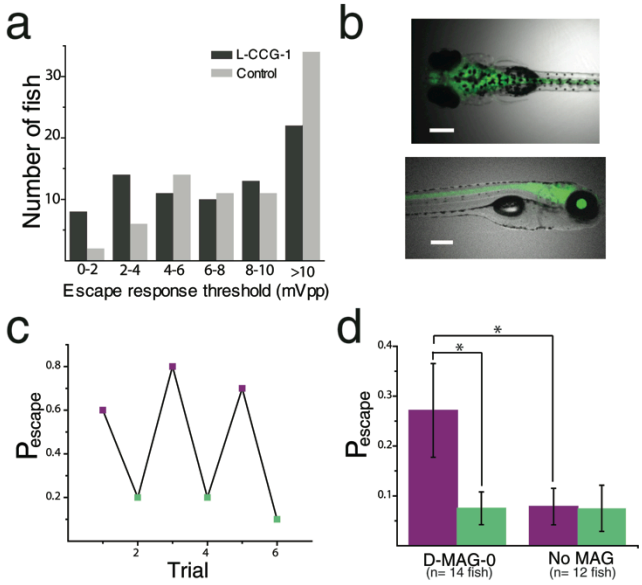

Figure 3.8, Agonism of endogenous group II mGluRs and photo-agonism of LimGluR2 increases escape response probability in zebrafish larvae. a) Treatment with the group II mGluR agonist L-CCG-1(10 μM) decreased the threshold of the wild-type zebrafish larvae ASR. The frequency distribution of minimum energy thresholds is shown. Class >10 mVpp represent fish that had an intact ASR, but that did not respond with a C bend at the highest sound energy attained by our experimental apparatus (10 mVpp). Comparison of the two groups was performed using the Mann-Whitney test ($z = 2.38$, $P < 0.02$, two-tailed distribution; $n_{control} = n_{L\text{-}CCG\text{-}1} = 78$ fish). b) UAS-GFP imaging revealed pan-neuronal expression in the *elavl3-Gal4* driver line. Scale bars represent 250 μm. c) Representative larva showing reversible modulation of escape response probability. Each data point represents the escape probability during a period of ten trials. Violet and green points represent trials after illumination at 510 and 380 nm, respectively. d) Summary of LimGluR2 modulation of escape response. Green bars indicate illumination with 510-nm light and violet bars indicate 380-nm light. Asterisks indicate statistical significance ($P = 0.007$ for comparison of 510-nm versus 380-nm illumination for MAG-labeled larvae with one-tailed paired *t* test; $P = 0.03$ for comparison of MAG-labeled and unlabeled larvae with one-tailed unpaired *t* test). Error bars represent s.e.m.

Discussion

GPCRs represent the largest family of membrane signaling proteins and respond to a wide-array of stimuli. These seven transmembrane receptors couple to distinct classes of heterotrimeric G proteins, leading to the activation or inhibition of a large number of protein targets3. The diversity of signaling is vastly greater than can be accounted for by the four classes of G proteins to which GPCRs couple. The additional diversity comes from several factors, including localization into specific subcellular compartments, corralling into signaling nanodomains with particular effectors, assembly of preformed GPCR–G protein–effector complexes, heteromultimerization into complexes with specialized properties, and unique profiles of interaction with regulatory proteins[6,7].

To elucidate GPCR function, one needs a method that combines specific pharmacology with specificity for region, cell-type and subcellular compartment. At the same time, the approach needs to allow for the GPCR to be activated at physiological rates (that is, the millisecond timescale) and to be reversible and reproducible to mimic physiological signaling and permit quantitative analysis. All of this needs to be achieved on the full-length GPCR to maintain normal targeting and interaction with signaling partners and regulators. We overcame these obstacles by developing, via the rational design and synthesis of new PTLs called D-MAGs and a simple and fast Monte Carlo simulation approach to select anchoring sites for these PTLs, photo-agonizing and photo-antagonizing versions of three of the eight mGluRs, representing two of the three mGluR groups. These approaches can readily be adapted to other target proteins and PTLs.

We most thoroughly characterized the photo-agonism with D-MAG-0 at position L300C of mGluR2 (LimGluR2). Unlike rhodopsin, which is the basis of most of the previously described light-gated GPCRs, LimGluR2 can be actively toggled both on and off in less than 1 ms, enabling signaling to be controlled on a synaptically relevant timescale and providing for fast effector kinetics. Moreover, LimGluR2 permits repetitive stimulation at high rates without decline. Rhodopsin requires constant illumination to be activated, which increases the chance of tissue damage and can act as a confounding variable for behavioral studies, while LimGluR2 is bistable, eliminating the need for constant illumination. Notably, optical control of native GPCRs provides a unique opportunity to examine the specific synaptic and circuit functions of each receptor, which emerge from their restricted effector and regulatory profiles and cannot be deduced from widespread activation of the entire signaling pathway of the G protein to which they couple.

We found that, despite their limited homology (66% identity between mGluR2 and mGluR3 and 44% identity between mGluR2 and mGluR6), photo-control could be generalized in the mGluR family from mGluR2 to the other group II member mGluR3 and the group III member mGluR6, with the same D stereoisomer linkage to the glutamate of MAG being required. Differences in photo-switching with a particular MAG at homologous sites of these three mGluRs reveals differences between their LBDs. This information may be useful for designing additional photoswitches or other pharmacological ligands as well as for probing the mechanism of clamshell closure.

The LimGluRs provide rapid, reversible, bistable and highly reproducible control

of excitability and synaptic transmission in dissociated cultured neurons and in brain slices, two of the prime *in vitro* systems in which synaptic transmission and plasticity in general, and mGluR function in particular, are studied most extensively. Although the photo-agonism and photo-antagonism of LimGluR2 are not complete, the photo-agonism induced characteristic mGluR2-dependent modulation and the photo-antagonism prevented the induction of such changes by native glutamate release. The precise temporal control, which allows the agonist or antagonist to be toggled on and off in a time-coupled manner, repeatedly and reproducibly made it possible to observe small effects that would be difficult to distinguish with classical drugs. In the case of LimGluR2-block, the photoeffect in neurons was consistent with the behavior of most neurotransmitter-gated GPCRs, which tend to be localized outside of the synaptic cleft and experience subsaturating concentrations of the neurotransmitter. The success of the D-MAG labeling and photo-control of mGluRs in brain slice suggests that the approach should also work in the mammalian brain *in vivo*, as has been shown for a similar photoswitch directed to the ionotropic kainate receptor in the mouse retina *in vivo*[48]. Indeed, we found that LimGluR2 worked effectively *in vivo* in zebrafish when D-MAG was simply added to the zebrafish larvae E3 salt water medium. We used LimGluR2 to photo-manipulate mGluR2 signaling in the context of the zebrafish ASR, a widely studied behavior that is similar in architecture and pharmacological regulation to the mammalian ASR[47]. In rodents, mGluRs have been implicated in various forms of the startle response, including regulation of paired-pulse inhibition by group II mGluRs, using pharmacological manipulation[49]. It was recently shown that group II mGluRs are expressed across all main subdivisions of the zebrafish brain[50]. Indeed, we found that conventional agonism of group II mGluRs by L-CCG-1 lowers the zebrafish ASR threshold.

The ability to target light to a subregion of the nervous system allowed us to localize the mGluR2-mediated effect on the ASR to the spinal cord and hindbrain and to find that optical activation of LimGluR2 also reduces ASR threshold; however, unlike L-CCG-1, this effect can result from acute activation of mGluR2 and can be reversed and repeated, suggesting that mGluR2 signaling could dynamically modulate escape threshold. Such information regarding the temporal dynamics of the ASR would not be possible to obtain using pharmacological approaches that require complete wash-out of ligands or addition of compounds whose activities are constrained by the pharmacokinetics of intact animals.

As with other GPCRs, mGluRs that couple to the same G protein often activate distinct effectors5 and are regulated distinctly[3,7]. Photo-agonism and photo-antagonism of group II and III mGluRs should make it possible to determine the precise spatial (pre- versus postsynaptic, synaptic versus perisynaptic versus astrocytic) and temporal properties of signaling by individual receptors to mediate lasting changes in synaptic strength. Furthermore, given that LimGluR2 maintains close to native ligand sensitivity, knock-in mice with a single point mutation to introduce a single cysteine anchor should allow for high resolution, specific photo-agonism or photo-antagonism while maintaining the receptor's native function. This would provide a new way to specifically probe the receptor's function in synaptic plasticity and learning, as well as in anxiety, depression and schizophrenia, for which they are major drug targets[3]

Methods

Chemical synthesis.

The chemical synthesis of D-MAG-0, D-MAG-1 and D-tether models was carried out as described in the **Supplementary Chemical Synthesis**.

Homology modeling and Monte Carlo simulations. Homology modeling was performed using ProMod II in the Swiss Model environment[51]. The target sequence was the rat mGluR2 LBD (residues 23–538, Uniprot ID: P31421) and the template was the open, glutamate-bound chain B of the rat mGluR1 structure (PDB ID: 1EWK) or the closed, glutamate-bound chain A of the rat mGluR3 structured (PDB ID: 2E4U). Energy minimization was performed using the Gromos96 force field in DeepView (Swiss PDB Viewer).

Models of MAG were built in Maestro 6.5 (Schrödinger) starting with the experimental structures of *cis*- and *trans*-azobenzene[35]. The MCMM search[36] (Macromodel 9.1, Schrödinger) considered all dihedral angles as degrees of freedom with the exception of those in glutamate and azobenzene. Solvent was treated implicitly using a generalized Born/surface area water model in the context of the OPLS-2005 force field[52]. Bond lengths, bond angles and dihedral angles of azobenzene were constrained to the experimental structures. Protein side chains were allowed to fluctuate while backbone atoms were frozen. After the simulation, all structures were exported from Maestro, checked for steric clashes using the command line version of MolProbity[53] and imported into Igor Pro (Wavemetrics). The distance of the maleimide group to all residues was measured for every structure and, for each residue, the number of structures with distances less than 6.5 Å was counted. Figures were made using PyMOL.

Molecular biology and gene expression in cultured cells. Cysteine mutations were introduced into mGluR2, mGluR3 and mGluR6 cDNA in the pcDNA3.1 expression vector (CMV promoter) using the QuickChange mutagenesis kit (Agilent). GIRK1 (with F137S homotetramerization mutation[54]), eYFP and RO4 were also inserted into pcDNA3.1. HEK293 and HEK293T cells were transiently co-transfected using Lipofectamine 2000 (Invitrogen) with mGluR mutants, GIRK1-F137S (homotetramerization mutant) and eYFP at a ratio of 7.5:7.5:1 with 1.6 μg of DNA total per 18-mm cover slip. RO4-transfected cells were maintained in dark room conditions. Cultured hippocampal neurons were transfected using the calcium phosphate method. Each coverslip received 1.1 μg of mGluR2-L300C DNA (or S302C) and 0.2 μg of eGFP DNA or 1.3 μg of mGluR2-L300C-GFP. mGluR2-L300C and mGluR2-S302C were inserted into a plasmid under the control of a synapsin promoter (pcDNA3.1 with the human synapsin promoter) to target expression to neurons.

Cultured cell electrophysiology. HEK293 cells were maintained in DMEM with 5% fetal bovine serum (vol/vol) on poly-L-lysine–coated glass coverslips. Dissociated hippocampal neurons were obtained from postnatal rats (P0–1) and plated at 75,000 cells per coverslip on poly-L-lysine–coated glass coverslips (12 mM). For autapse experiments, low density cultures of 25,000 cells per coverslip were used. Neurons were

maintained in media containing MEM supplemented with 5% FBS, B27 (Invitrogen) and GlutaMAX (Invitrogen).

HEK293 and 293T whole-cell patch-clamp electrophysiology was performed 24–48 h after transfection in high potassium solution containing 60 mM KCl, 89 mM NaCl, 1 mM $MgCl_2$, 2 mM $CaCl_2$ and 10 mM HEPES, pH 7.4. Glass pipettes of resistance between 3 and 6 MΩ were filled with intracellular solution containing 140 mM KCl, 10 mM HEPES, 3 mM Na_2ATP, 0.2 mM Na_2GTP, 5 mM EGTA and 3 mM $MgCl_2$, pH 7.4. Cells were voltage clamped to –60 to –80 mV using an Axopatch 200A (Molecular Devices) amplifier.

Hippocampal neuron whole-cell patch-clamp electrophysiology was performed 3–6 d after transfection (12–15 d *in vitro*). For voltage-clamp recordings, a high potassium extracellular solution containing 79.5 mM NaCl, 60 mM KCl, 1.2 mM $MgCl_2$, 2.5 mM $CaCl_2$, 10 mM glucose and 5 mM HEPES, pH 7.4 was used. For all other experiments, extracellular solution contained 138 mM NaCl, 1.5 mM KCl, 1.2 mM $MgCl_2$, 2.5 mM $CaCl_2$, 10 mM glucose and 5 mM HEPES, pH 7.4. Intracellular solution contained 140 mM potassium gluconate, 10 mM NaCl, 5 mM EGTA, 2 mM $MgCl_2$, 1 mM CaCl2, 10 mM HEPES, 2 mM MgATP and 0.3 mM Na_2GTP, pH 7.2. For current-step experiments, cells were adjusted to –50 mV with current injection before current steps were initiated to normalize spike count comparisons between cells. Only cells with a resting potential ≤–45 mV were analyzed. For autapse experiments, cells were voltage clamped to –70 and stepped to 0 mV for 2 ms. Postsynaptic currents were delayed by 3 ms, which confirmed autaptic origins of transmission. Inter-stimulus intervals were ≥12 s. EPSCs and IPSCs were identified on the basis of the kinetics of decay with EPSCs approximately ten times faster than IPSCs (~5 ms versus 50 ms), as has been described previously[55]. All pharmacological compounds were obtained from Tocris and dissolved in extracellular buffers before application using a gravity-driven perfusion system.

For most experiments, illumination was applied to the entire field of view using a Polychrome V monochromator (TILL Photonics) through a 20• objective or a Lambda DG4 high-speed wavelength switcher (Sutter Instruments) with 380-nm and 500-nm filters through a 40• objective. For bistable switching the DG-4 was coupled to the microscope through a 40• objective. Ultrafast, submillisecond photo-switching was achieved using a laser spot illumination system, for which the output of a 375/488-nm dual laser diode module (Omicron LDM) was coupled into a multi-mode fiber (10 μm, NA 0.1). The light exiting from this fiber was collimated and directed to the back aperture of the objective (Olympus 40•, NA 0.6). Intensities in the sample plane were >40 W mm^{-2}.

pClamp software was used for both data acquisition and control of illumination. To conjugate MAG, cells were incubated in 50–100 μM MAG for 30–60 min in the dark at 23–27 °C in standard extracellular cell buffers. For RO4 experiments cells were labeled with 1 μM 11-cis retinal for 40 min and experiments were performed under dark room conditions.

cAMP measurements. Intracellular cAMP levels were assayed with an ELISA system from Applied Biosystems. HEK 293T cells grown to confluence on a 24-well plate were either exposed to D-MAG-0 (50 μM for 45 min in standard extracellular buffer) or to a similar volume of standard extracellular buffer. After washing (5•, 1 ml), cells were treated with forskolin and/or glutamate or 365-nm light and disrupted in lysis buffer 10

min later. For D-MAG-0–labeled cells, 365-nm illumination was controlled with a handheld lamp and applied for 10 s immediately after forskolin addition. Serial dilutions of cAMP served as standards. Samples of cell lysate and standards were incubated with antibody to cAMP and cAMP–alkaline phosphatase in a 96-well plate. The plate was then washed, incubated with substrate and finally chemiluminescence generated at the end of enzymatic reaction was measured in a luminometer, LmaxII 384 (Molecular Devices).

Hippocampal slice gene expression and electrophysiology. Hippocampi were obtained from postnatal Sprague-Dawley rats (P7) and 400 μM slices were prepared and cultured as previously described[38]. After 3 d, slices were transfected by Biolistic gene transfer using a BioRad Helios Gene Gun and gold microcarriers coated with both mGluR2-L300C and tdTomato DNA.

Patch-clamp recordings were obtained after 6–9 d *in vitro*. Before recording, slices were incubated at 32 °C for 40 min with D-MAG-0 (50 μM) diluted in NMDG-labeling solution containing 150 mM NMDG-HCl, 3 mM KCl, 0.5 mM $CaCl_2$, 5 mM $MgCl_2$, 10 mM HEPES and 5 mM glucose, pH 7.4. Whole-cell patch-clamp recordings were performed on an upright Zeiss AxioExaminer using an Axopatch 200B amplifier (Molecular Devices). Pipettes of resistances 3–7 M were filled with solution containing 120 mM potassium-gluconate, 8 mM NaCl, 10 mM HEPES, 2 mM $MgCl_2$, 2 mM MgATP, 0.3 mM NaGTP and 10 mM EGTA, pH 7.4. Artificial cerebrospinal fluid containing 119 mM NaCl, 2.5 mM KCl, 1.3 mM $MgSO_4$, 1 mM NaH_2PO_4-H_2O, 26.2 mM $NaHCO_3$, 11 mM glucose and 2.5 mM $CaCl_2$ was continuously perfused and bubbled with 95% O_2/5% CO_2. A DG-4 (Sutter Instruments) was coupled to the microscope for photoswitching through a 40• objective. Light intensity was approximately 20 mW mm^{-2} at 390 nm and 40 mW mm^{-2} at 500 nm.

Zebrafish transgenesis. Expression of mGluR2-L300C was targeted to neurons using the UAS/GAL4 system. The transgenesis *UAS-LimGluR2(L300C)/cry:CER* construct contains the LimGluR2(L300C) open reading frame amplified from the expression vector pcDNA3.1. LimGluR2 expression is driven by an upstream sequence composed of 10• *UAS* repeats followed by the adenovirus E1b TATA box and a 5′ UTR from carp β-actin. The *UAS* sequence was amplified from the p5E-UAS vector, tol2 Kit[56]. The opposite strand contains a crystalline promoter sequence[57] driving expression of the cerulean fluorescent protein in the crystalline of the eye for easy screening of transgenic fish. The expression sequences are flanked by sites for the fish transgenesis system meganuclease Isce-1[58].

Wild-type embryos (AB line) were injected at the one-cell stage with 30 ng ml^{-1} *UAS-LimGluR2(L300C)/cry-CER* DNA, 10 units I-Sce1 (New England Biolabs R0694L), NEBuffer Isce-1 0.5•, and 0.1% Phenol Red (wt/vol). F1 embryos were raised and screened at 3 dpf by fluorescence microscopy for presence of cerulean fluorescent protein expression in the eye. F0 founder fish that generated *UAS-LimGluR2(L300C)/cry-CER*–positive F1 fish were crossed to wild-type fish to create stable lines. *UAS-LimGluR2(L300C)/cry-CER* fish were crossed to *HuC-Gal4; UAS-Kaede* (gift from the Baier laboratory, University of California, San Francisco) fish to generate *HuC-Gal4; UAS-Kaede; UAS-LimGluR2/cry-CER* fish in which Gal4 drives pan-neuronal expression of the Kaede fluorescent protein and LimGluR2(L300C).

Zebrafish behavioral assay. D-MAG-0 was diluted to 50 μM in 1 ml of a 5% DMSO Ringer buffered solution 116 mM NaCl, 2.9 mM KCl, 1.8 mM $CaCl_2$ and 5 mM HEPES, pH 7.2), and pre-illuminated with ultraviolet light (365 nm) for 45 s. The labeling solution was added to 5 dpf larvae (20–30 fish). The larvae were kept at 28.5 °C in the dark for 45 min. Next, the larvae were washed in fish medium E3 and kept in the presence of E3 in the dark for a recovery period of 1 h at 28.5 °C. Control fish were subjected to the same protocol, but in the absence of D-MAG-0. For pharmacological experiments, L-CCG-1 (Tocris) was diluted in E3 solution to a final concentration of 20 μM. Experimental and control fish were kept overnight at 28.5 °C before mounting and testing for ASR.

Larvae were mounted in a glass well petri dish dorsal side up in 2% agar E3 solution at 36 °C. Agar was removed from a region caudal to the fish otic vesicle. All experimental larvae used in experiments had an intact ASR, as determined by a light tap in the dish containing the larvae. Tail-free mounted fish were attached with adhesive tape to the surface of an 8-Ohm mini-speaker (Radioshack, 273-092). Fish were illuminated from the side with attenuated white light. Images were captured at 30 Hz by a behavioral camera (IDS, USB 2 uEye). A square wave (900 Hz, 120 ms, controllable amplitude) stimulus was generated by a function waveform generator (Agilent, 33220A) connected to the mini-speaker. Sound- and vibration-induced escapes were determined by observation in behavioral movies of characteristic C bends induced by sound and vibration stimulus. Threshold was defined as the minimum energy capable of inducing >50% C bends in a ten trial test. All experiments were performed in a climate-controlled environment at 22 °C.

The illumination source was a Lambda DG4 high-speed wavelength switcher (Sutter). A digital micro-mirror device was used to pattern illumination through a 2.5• Zeiss objective. Illumination reached the larvae from the dorsal side and covered a region caudal to the eyes and reaching almost the whole length of the spinal cord. Activation and deactivation wavelengths were 380 and 15 nm, 0.09 mW mm^{-2} for 400 ms, and 510 and 20 nm, 0.49 mW mm^{-2} for 1 s, respectively. Larvae were sound and vibration stimulated 5 s after illumination. Ten stimuli with a 10-s inter-stimulus interval were performed for each condition. Illumination and behavioral set up were mounted on a 3i Marianas system with a spinning disk confocal (Yokagawa) mounted on a Zeiss microscope.

For the L-CCG-1 experiment, 5–6 dpf wild-type zebrafish larvae were treated overnight in 20 μM L-CCG-1- or vehicle-containing E3 solution. Trials were performed with a 10-s inter-trial interval and speaker voltage was increased in steps of 500 mVpp until the threshold was reached. All fish had an intact ASR as determined by a light tap to the dish.

For swimming and escape response control experiments, zebrafish larvae were kept in E3 in 48-well microplates mounted on a plexiglass box. For fish activity measurements, an infrared CCD camera (fire-i 780b, Unibrain) from above was used with trans-infrared illumination from below (Supplementary Fig. 2.10a,b). Sound stimuli were administered by two speakers (Visaton SC 5.9) screwed to the same plexiglass plate as the micro-well plate. Stimuli (powered by a 15-W amplifier) were sent to speakers using a Native Instruments PCI-6229 DAQ controlled by Matlab. Duration and frequency were 20 ms and 900 Hz, respectively. Escapes were detected using an in-house movement threshold algorithm. The acoustic stimulus was applied 110 ms after start of the movie. A

successful escape response was counted if the difference of the integrated pixel values of the two frames immediately after the stimulus was statistically higher ($P < 0.01$) than the distribution of pixel-change values in the preceding 109 frames of recorded spontaneous activity. The accuracy of this algorithm was verified by visual inspection of movies.
Animal experiments were approved by the University of California Animal Care and Use Committee.

Statistics and data analysis. Data was analyzed using Clampfit (Axon Instruments) and Origin (OriginLab) software. Statistical analysis was performed using Microsoft Excel. All values reported are mean ± s.e.m.

Supplementary Figures

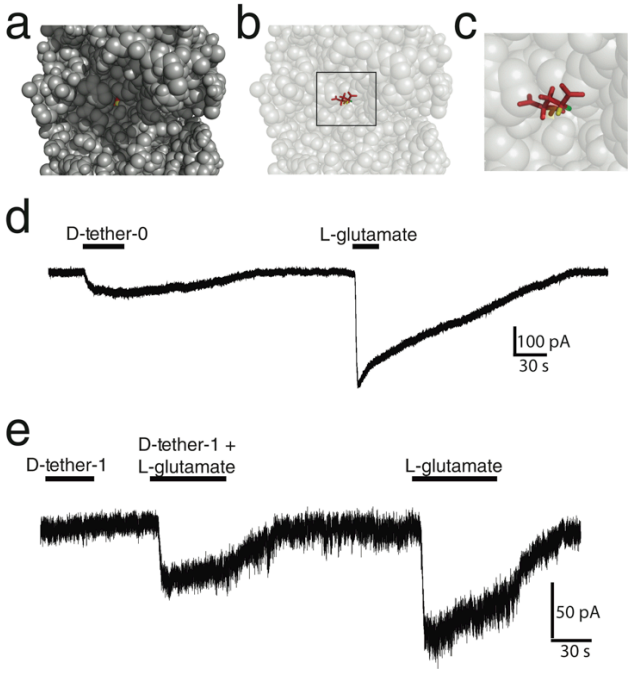

Figure S3.1, Design of photoswitches for control of mGluR2: Apparent access channel and tether model screening. a) Homology model of mGluR2 ligand binding domain in the closed, glutamate-bound, conformation (based on structure of mGluR3, PBD: 2E4U) reveals an access channel through which glutamate (red) is seen from the surface of the protein. The 4' D hydrogen of glutamate (yellow) is visible through the access channel, but the L hydrogen (green) is not. b,c) Stick representation of glutamate shows the directions in which 4'D and L substituents may project. The protein is transparent to illustrate that the orientation is the same as in A. While the 4'D position points away from the protein surface, the 4'L position points into the protein suggesting accessibility only of the former. d, e) D-Tether models of differing lengths have distinct effects on mGluR2 activation of GIRK1 channels in HEK293 cells. d) 1 mM D-Tether-0 activates mGluR2 (i.e. functions as an agonist), evoking GIRK1 current that is smaller (26 ± 5%, n=6) than that evoked by 1 mM glutamate. e) 1 mM D-Tether-1 does not activate mGluR2, but co-application with 1 mM glutamate reduces the response (45 ± 1%, n=4) compared to glutamate alone, indicating antagonistic activity.

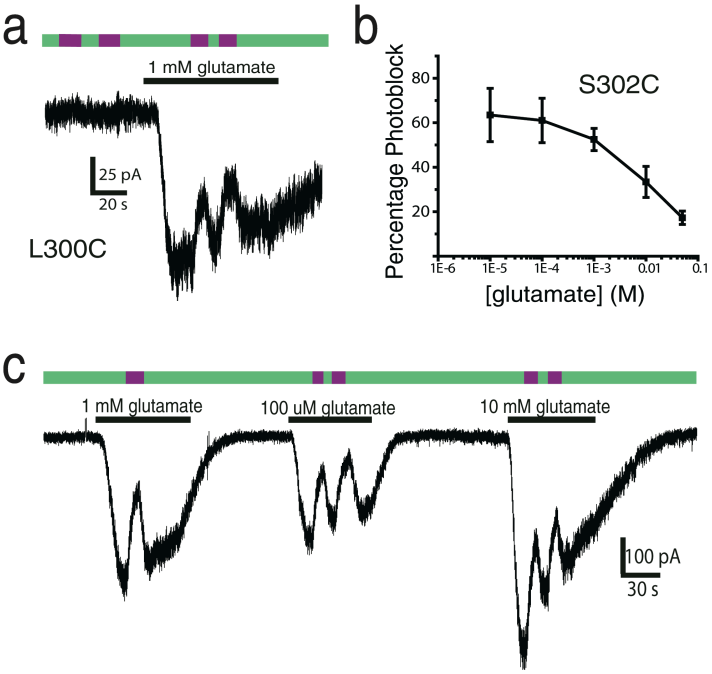

Figure S3.2, Photo-antagonism of mGluR2. a) Representative trace of currents in mGluR2-L300C after labeling with D-MAG-1. Similarly to LimGluR2-block (S302C) 380 nm light (violet bar) does not induce current in the absence of glutamate, but after application of 1 mM glutamate (black bar) induces a decrease in current amplitude. b) Glutamate-concentration dependence of photoantagonism by LimGluR-block (n=6 cells). c) Representative trace showing extent of photoblock by LimGluR2-block over a range of glutamate concentrations. After application of 10 mM Glutamate, photo-antagonism is reduced, indicating a competitive mechanism of antagonism.

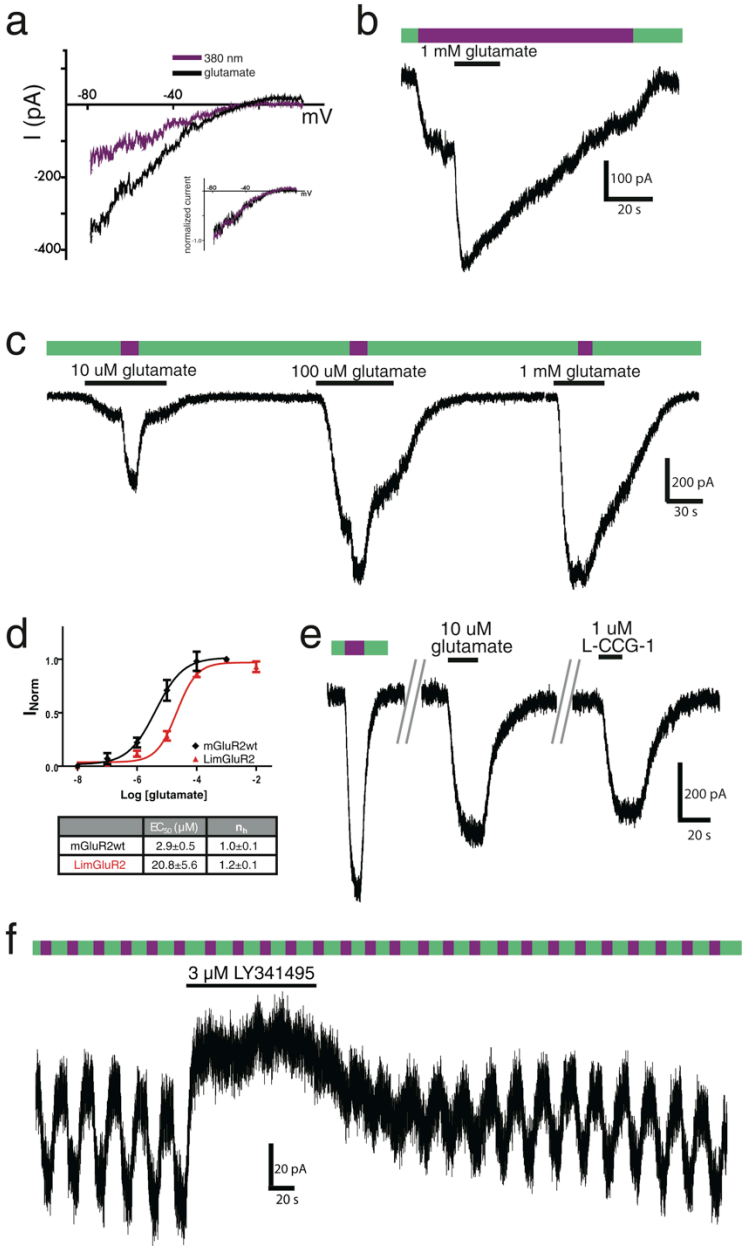

Figure S3.3, Photo-agonism of mGluR2. a) Representative trace of currents induced by either 380 nm illumination or application of 1 mM glutamate in LimGluR2 during voltage ramps from -80 to +20 mV. Ramp currents were subtracted from baseline ramps taken in absence of illumination or glutamate. Currents show inward rectification typical of GIRK current. Inset shows close overlay of normalized traces. b) When glutamate is applied after 380 nm illumination (violet bar), a further increase in inward current is seen, indicating that D-MAG-0 functions as a full agonist and does not occlude glutamate activation. Green bars indicate 500 nm illumination. c) Application of glutamate at a range of concentrations followed by photoswitching indicates that D-MAG-0 never functions as an antagonist. At sub-saturating concentrations, MAG increases inward current further indicating that it functions as a full agonist. d) Glutamate titration curves for mGluR2 and LimGluR2 indicate a minor decrease in glutamate affinity for LimGluR2. Titration curves for individual cells were fit and EC_{50} and n_h values were averaged. (n=6 cells each). e) LimGluR2 maintains sensitivity to L-CCG-1, a commonly used group II mGluR agonist. f) LimGluR2 maintains sensitivity to LY341495, a commonly used group II mGluR competitive antagonist.

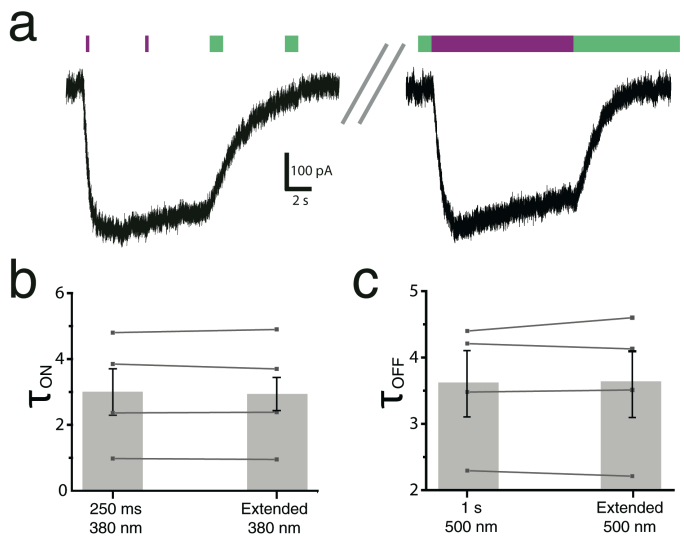

Figure S3.4, Characterization of LimGluR2 bistability and the kinetics of its activation and deactivation of GIRK. a) Representative trace showing that activation of LimGluR2 using a 250 ms pulse of illumination at 380 nm (15 mw/mm^2) and deactivation by a 1 s pulse at 500 nm (20 mw/mm^2) produce GIRK currents of similar amplitude and kinetics (of activation desensitization and deactivation) as does switching illumination between the wavelengths for extended times. b) Summary comparison of GIRK activation kinetics evoked by short pulses of illumination (250 ms at 380 nm) *versus* long exposures ($\geq$ 5 s at 380 nm). c) Summary comparison of GIRK deactivation kinetics evoked by short pulses of illumination (1 s at 500 nm) *versus* long exposures ($\geq$ 10 s at 500 nm). b, c) Lines show values for individual cells and bars show averages.

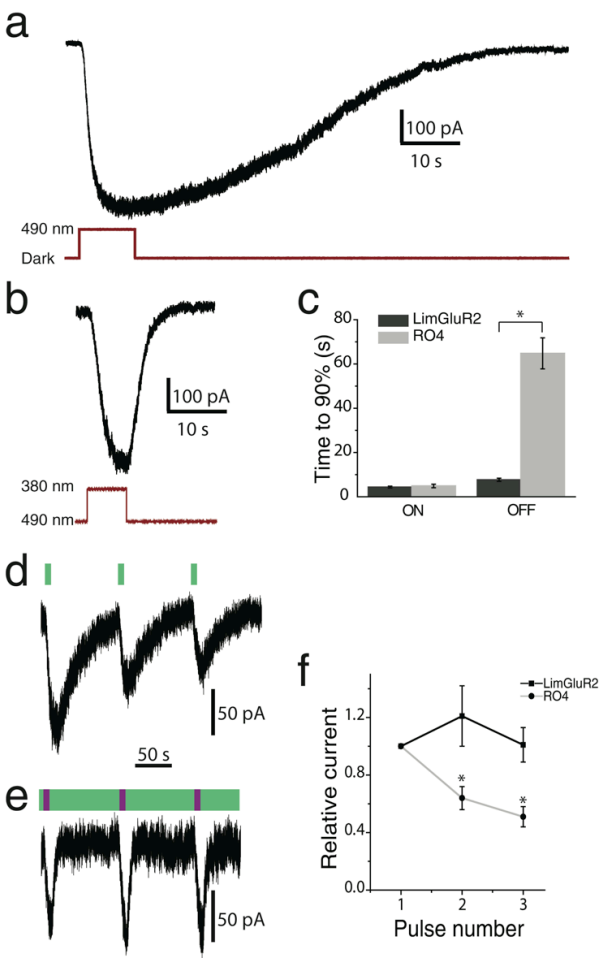

Figure S3.5, Comparison between the activation of GIRK1 channels by optical activation of rat rhodopsin (RO4) and LimGluR2 in HEK293 cells. a, b) Representative currents in response to light pulses for RO4 (a) and LimGluR2 (b) in cells co-expressing GIRK1. c) Summary of on and off kinetics for GIRK1 currents evoked by optical activation of RO4 and LimGluR2. The time to 90% off was significantly longer in RO4 (unpaired, 1-tailed t test, p=4x10^{-5}). d, e) Representative currents in response to repetitive optical activation (bouts of 10 s activation, followed by 90 s deactivation) of RO4 (d) and LimGluR2 (e). f) Summary of peak current amplitudes elicited by repeated optical activation of RO4 and LimGluR2. A significant run-down of photo-current amplitude was seen for RO4 but not LimGluR2 (* indicates p=0.016 for paired, 1-tailed t test).

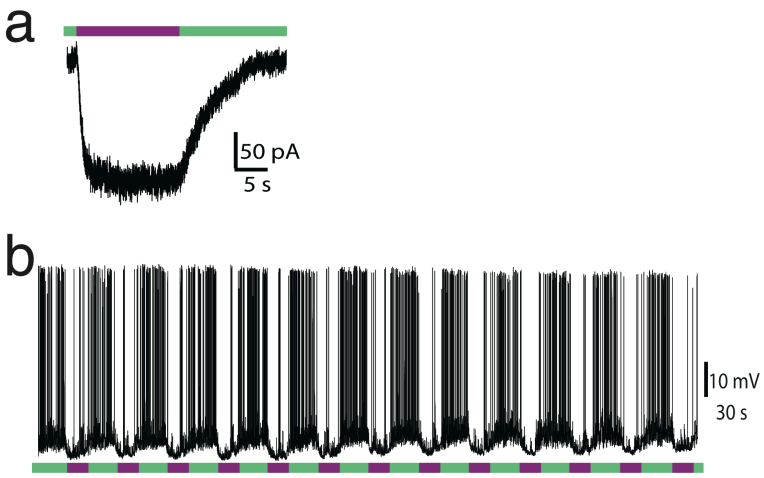

Figure S3.6, LimGluR2 mediated control of neuronal excitability. a) Representative trace of photo-current induced by illumination at 380 nm (violet bar) and extinguished by illumination at 500 nm (green bar) in a whole cell voltage-clamped neuron in 60 mM $[K^+]_o$ extracellular solution. b) Representative trace showing many rounds of repetitive suppression of spiking activity by photo-activation of LimGluR2.

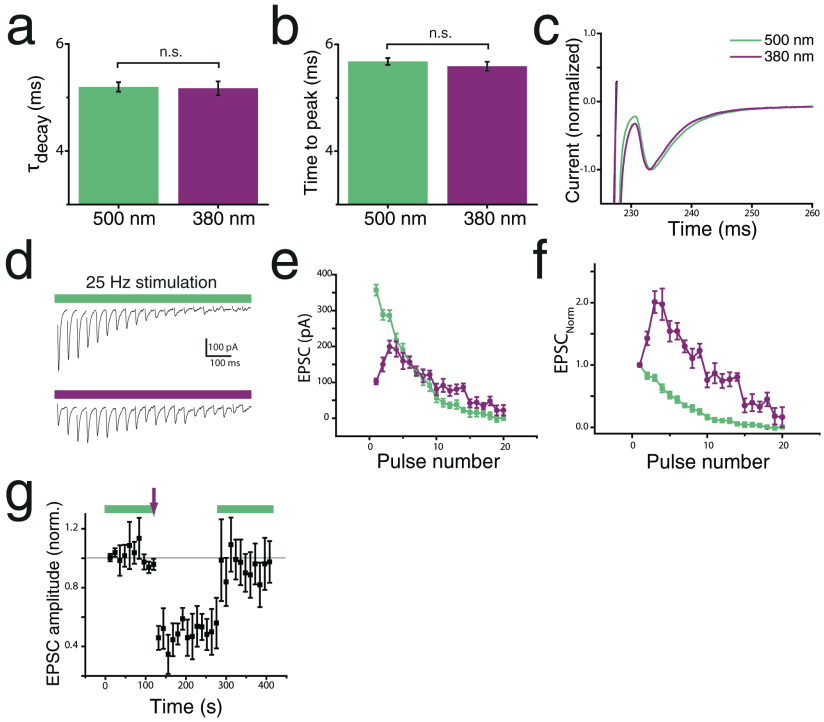

Figure S3.7, LimGluR2 inhibition of autaptic synaptic transmission. a-c) EPSC kinetics (a: decay time; b: time to peak, c: normalized overlay) are constant despite decrease in amplitude induced by optical activation of LimGluR2. a) EPSC decay time constant unchanged in 500 nm vs. 380 nm illumination (paired, 2-tailed t-test, p=0.91; n=15 sweeps/condition). b) Time to peak (time from peak of pre-synaptic spike to peak of EPSC) and jitter (S.E.M. of time to peak) are unchanged in 500 nm vs. 380 nm illumination (paired, 2-tailed t-test, p=0.74; n=15 sweeps/condition). c) Overlay of normalized average of 15 sweeps for both 380 nm and 500 nm illumination indicates no significant change in timing or shape of EPSC. Note, EPSC amplitude was reduced by 40% in this cell under 380 nm illumination. d) Representative behavior of autapse during 25 Hz stimulation under illumination with either 500 nm light (green bar) or 380 nm light (violet bar). Each trace is an average of 8 trains. e, f) Average EPSC amplitude (e) or normalized amplitude (f) during a 25 Hz train under 380 or 500 nm illumination. g) Summary of bistable inhibition in n=4 cells under the same protocol as (d): 2 minutes at 500 nm followed by 1 second of illumination at 380 nm (violet arrow) and 3 minutes in the dark before returning to 500 nm illumination for 2 more minutes.

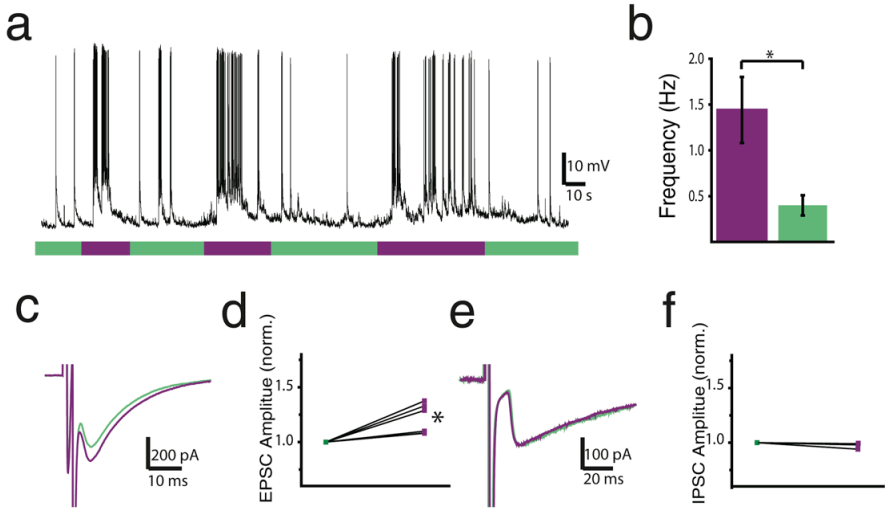

Figure S3.8, LimGluR2-block mediated modulation of excitability and transmission. a) Representative trace showing photoswitching of LimGluR2-block in a current-clamped neuron. Blockade of mGluR2 under 380 nm light increased firing frequency and was reversed by 500 nm illumination. b) Summary of firing frequency modulation in a representative cell. Firing frequency was determined for each round of photoswitching (5-20 s per photoswitch) over a 10 minute recording. (paired, 2-tailed t-test, p=0.028). c) Representative EPSCs in response to 380 nm (violet trace) or 500 nm illumination (green trace) in autaptic neurons expressing LimGluR2-block. Each trace is an average of 12 sweeps for each illumination condition. d) Summary of LimGluR2-block enhancement of EPSC amplitude. Each line reperesents a single cell and the violet point indicates the amplitude in 380 nm light and the green point indicates the amplitude in 500 nm light. All values were normalized to the amplitude in 500 nm. e) Representative IPSCs in response to 380 nm (violet trace) or 500 nm illumination (green trace) in autaptic neurons expressing LimGluR2-block. Each trace is an average of 12 sweeps for each illumination condition. f) Summary of LimGluR2-block enhancement of IPSC amplitude. IPSCs were unaffected by LimGluR2-block.

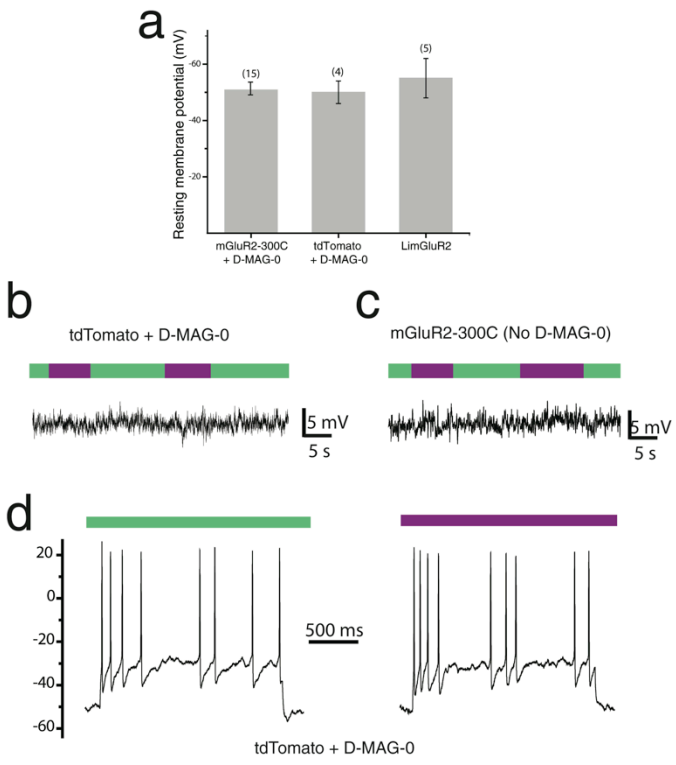

Figure S3.9, Hippocampal slice controls indicate that LimGluR2 does not harm cell health and is orthogonal. a) Average resting potential is not altered in cells expressing LimGluR2 and labeled with D-MAG-0 relative to cells with D-MAG-0 but without mGluR2-300C or unlabeled mGluR2-300C expressing cells. b) No photoswitching was seen in tdTomato-transfected cells labeled with D-MAG-0 or c) cells expressing LimGluR2 (mGluR2-300C) but not labeled with D-MAG-0. d) tdTomato-expressing cells labeled with D-MAG-0 show no change in spike firing in response to current injection when illuminated with 380 nm or 500 nm.

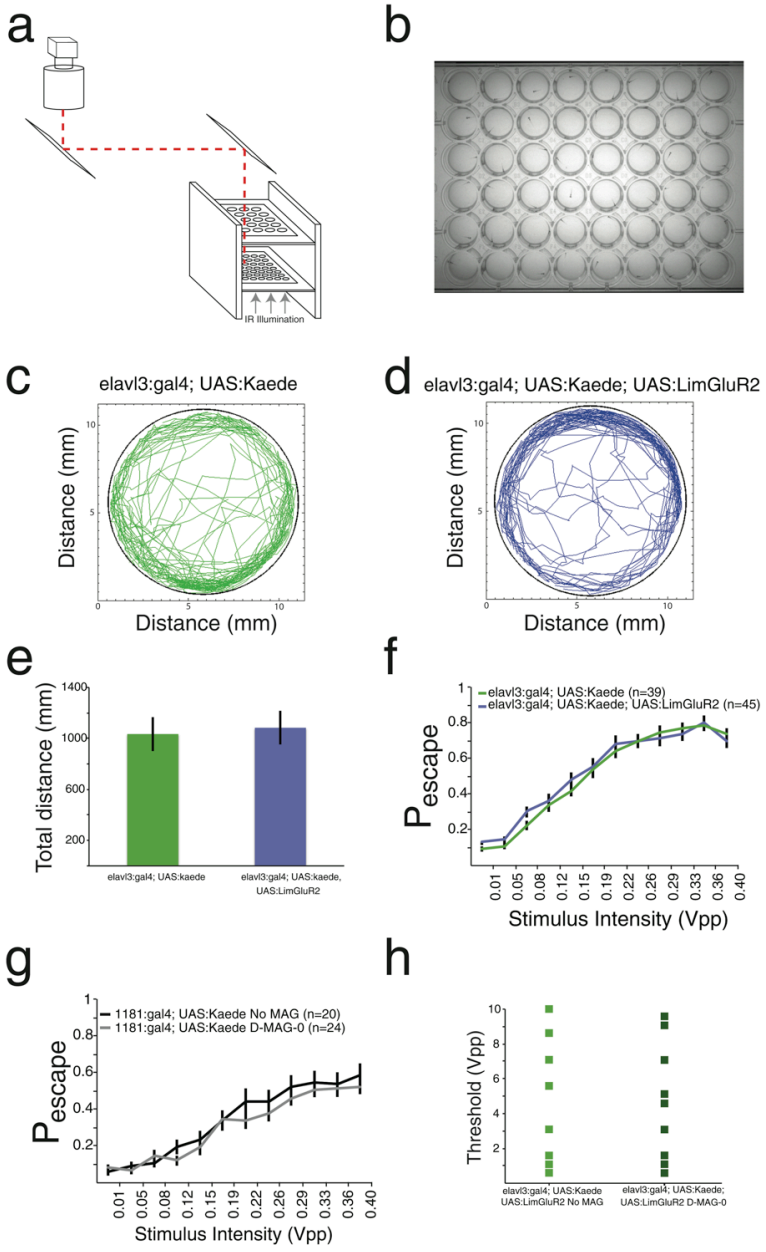

Figure S3.10. Pan-neuronal expression of LimGluR2 and labeling with D-MAG-0 do not modify basal activity levels and escape response threshold. a) Schematic of system used for measurement of swimming behavior and escape response in 48 well plates for different genetic lines with or without D-MAG-0 labeling (see Online Methods for details). b) Representative image of individual zebrafish in wells of a 48-well plate during tracking of swimming. c,d) Representative tracks of single zebrafish larvae with either GAL4 pan-neuronal driver driving Kaede fluorescent protein alone (*elavl3*:gal4; UAS:kaede control) (a) or also containing LimGluR2 (*elavl3*:gal4; UAS:kaede; UAS:LimGluR2) (b). (Tracking performed with an in-house written Matlab script.) e) Total distance travelled at 5-6 dpf by *elavl3*:gal4; UAS:kaede control (n = 24) or *elavl3*:gal4; UAS:kaede; UAS:LimGluR2 (n = 24). Larvae were imaged for 25 minutes under infrared illumination at 30fps in 48-well microplates. Total distance swum was measured by the tracking of the centroid of each fish for the duration of the recording. f) Sound stimulus intensity-probability of escape curve is not affected by LimGluR2 expression. The escape threshold of 5-6 dpf zebrafish larvae was determined by administering a randomized sequence of 120 sound stimuli at 10 different voltage levels, with a 30 second inter-stimulus interval (ISI) for *elavl3*:gal4; UAS:kaede control and *elavl3*:gal4; UAS:kaede; UAS:LimGluR2. Stimuli duration and frequency were 20ms and 900Hz, respectively. Experiment performed in a 48-well microplate, under infrared illumination and recorded at 30fps. Prior to testing larvae were acclimated for 30 minutes. Escapes were automatically determined by subtraction and thresholding of the first two frames after the stimulus. Accuracy of the detection method was verified by visual inspection of movies. g) Sound stimulus intensity-probability of escape curve is not affected by D-MAG-0 treatment. 1181:gal4; UAS:kaede 5-6dpf zebrafish larvae were treated with D-MAG-0 or control medium. Curve was determined as described above for (f). h) Labeling of *elav3*:gal4; UAS:kaede; UAS:LimGluR2 fish with D-MAG-0 does not modify ASR threshold before receptor activation with 380 nm light. Individual head-mounted fish, D-MAG-0-labeled or controls, were exposed to stimuli of increasing amplitude stimulit with an ISI of 10 seconds. The threshold was defined as the lowest sound able to initiate an escape response in >50% of trials. Graph shows the initial threshold of individual fish in the two groups.

Construct	D-MAG-0	D-MAG-1
mGluR2wt	x	x
Q42C	x	Antagonist (9±4%; n=4)
D146C	x	x
D215C	x	x
L300C	Agonist (48±4%; n=10)	Antagonist (21±2%; n=7)
S302C	x	Antagonist (53±4%; n=5)
E373C	Antagonist (5±2%;n=3)	Antagonist (4±1%; n=4)
S376C	x	x

Table S3.1, Cysteine screen of mGluR2. Results of photoswitching of D-MAG-0 and D-MAG-1 attached at each of the 7 positions tested. "x" indicates no photoresponse. Agonistic and antagonistic effects are quantified relative to 1 mM glutamate. Data from $\geq$ 2 different coverslips for all conditions tested.

Chapter 4 Restoration of visual function by expression of a light-gated mammalian ion channel in retinal ganglion cells or ON-bipolar cells

This chapter was published in PNAS plus volume 111, no. 51, in December 2014 with me as first co-first author.

Introduction

Inherited retinal degenerative diseases affect 1 in 3000 humans worldwide [122]. Retinitis pigmentosa (RP) describes a family of over 50 different gene mutations that cause progressive loss of rod photoreceptors [122,123]. Rod loss is followed by degeneration of cone photoreceptors, ultimately leading to complete blindness in many patients [124]. Despite the complete loss of photoreceptors in the outer nuclear layer, many interneurons of the inner retina survive in a functional state for long periods, providing an opportunity for treatment [125,126].

Direct electrical stimulation of the surviving inner retina has proven to be successful in restoring useful vision [11,127,128]. One approach employs surgically implanted photovoltaic or electrode arrays to directly stimulate retinal ganglion cells (RGCs) [11] or bipolar cells [127,128] in the inner nuclear layer (INL) of the degenerated retina and promising results in clinical trials have lead to FDA approval for the ArgusII device [11]. The electrical implants demonstrate that inner retinal neurons in blind patients can respond to appropriate stimulation and lead to a useful visual percept allowing simple navigation and object recognition. These electronic designs are under continual development to increase the resolution, improve the surgical implantation procedures, and increase the sophistication of their signal encoding algorithms [129].

Microbial opsins, like channelrhodopsin and halorhodopsin, have been successfully tested as visual prosthetics in animal models of blindness [32,33,35,36,130,131]. Genetically encoded light-gated proteins can be exogenously expressed in retinal cells using viral or non-viral gene delivery vehicles, imparting a light-sensitive function to cone photoreceptors that have become insensitive to light from loss of their outer segments [33] but also to ON-BCs [35,36], as well as RGCs [32,130,132] leading to rescue of basic aspects of visual function in mice. Microbial opsins are appealing for this application due to the bioavailability of the light-sensitive ligand, retinal. However, there are potential drawbacks to this approach. Xenotransplantation is generally concerning as this might lead to immune responses and inflammation potentially spreading to brain via the optic

nerve. Additionally, once expressed, it is impossible to silence the system in case of adverse reactions in patients.

One promising alternative to microbial opsins is an optopharmacological strategy that uses synthetic azobenzene based photoswitches to endow light-sensitivity either to native ion channels of neurons [133,134] or to engineered mammalian receptors and channels that, like the microbial opsins, allow for genetic targeting to specific cells [63-65,135]. We previously showed that LiGluR, an engineered light-gated ionotropic glutamate receptor, restores light responses to blind *rd1* mice [34]. The gene encoding for LiGluR was delivered to RGCs by intravitreal injection of adeno-associated virus (AAV) and the photoswitchable tethered ligand, maleimide-azobenzene-glutamate (MAG), was delivered in a subsequent intravitreal injection [34]. LiGluR contains a single cysteine substitution, GluK2(439C), that serves as an anchoring site for MAG close to the ligand binding site. Upon illumination at 380 nm in the near ultraviolet (UV), the azobenzene linker in MAG photo-isomerizes from *trans* to *cis,* shortening the molecule and allowing the glutamate to bind into the ligand binding pocket to activate and open the channel.

The first generation MAG photoswitch suffered from two major limitations for vision restoration: 1) the UV light needed for activation is absorbed by the human lens and can damage the retina, and 2) MAG is bi-stable, requiring a second pulse of light at a longer wavelength for deactivation. We recently developed a second generation photoswitch, $MAG0_{460}$, to overcome these problems [60]. $MAG0_{460}$ is activated by white light, with peak efficiency at 460 nm, and spontaneously turns off in the dark. In the present study, we compare retinal light responses and both innate and learned visually-guided behaviors in the *rd1* mouse model of retinal degeneration when LiGluR-$MAG0_{460}$ is targeted to either RGCs or ON-BCs. We find both cell types to support robust light-induced retinal activity and visually-guided behavior. To demonstrate efficacy in a larger animal model, we targeted LiGluR-$MAG0_{460}$ to RGCs in a canine model of human blindness and restored light activated retinal responses *in vitro*. As LiGluR-$MAG0_{460}$ is functional in both mouse and dog, it is an attractive candidate for a genetically encoded retinal prosthetic for the blind.

Results

Restoration of light response to the retina of *rd1* mouse by LiGluR in RGCs or ON-BCs

Our first generation MAG photoswitch for LiGluR had limited utility for vision restoration since it required 380 nm UV light stimulation for activation and a second pulse of light at a longer wavelength for deactivation [63,136]. We therefore turned to a recently developed second-generation compound, $MAG0_{460}$, which is activated by blue or white light and spontaneously turns off in the dark (Fig. 4.1). Expression and labeling in HEK cells yielded robust LiGluR-$MAG0_{460}$ photocurrents that were stable and reversible over hundreds of switching cycles [60]. Importantly, LiGluR-$MAG0_{460}$ photocurrents scaled with light intensity, yielding a sigmoid intensity-response curve spanning three orders of magnitude (Fig. 4.1D, Fig. S4.1 and Supplementary Note). In addition, LiGluR responded dynamically to moderate frequencies of intensity modulation (Fig. S4.1C and D).

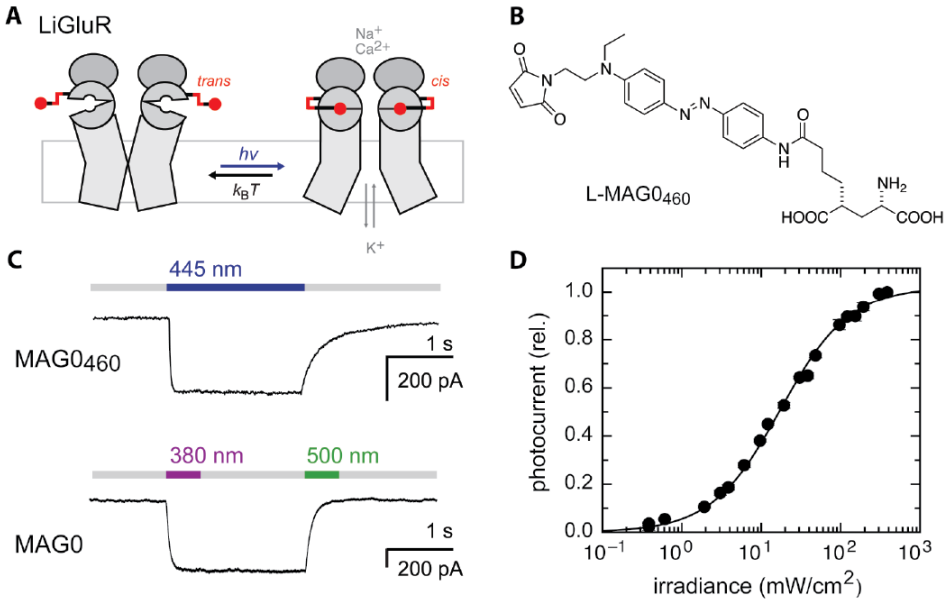

Figure 4.1 LiGluR-$MAG0_{460}$ expressed in HEK cells is activated by visible light, relaxes in the dark and detects changes in light intensity. (**A**) Schematic of the light-gated ionotropic glutamate receptor (LiGluR): after tethering a photoswitchable ligand, L-$MAG0_{460}$, the channel is activated by light and closes in darkness. (**B**) Structural formula of the 2nd generation L-$MAG0_{460}$ photoswitch [60]. (**C**) HEK cell recordings in voltage-clamp configuration at -75 mV. Top panel: LiGluR conjugated with $MAG0_{460}$ is activated by blue light and relaxes spontaneously in the dark. Bottom panel: For comparison, LiGluR gating with the 1st generation MAG0 photoswitch, which is bi-stable (380 nm light opens the channel, 500 nm light closes it). (**D**) Dynamic range of LiGluR-$MAG0_{460}$ with respect to light intensity. LiGluR-$MAG0_{460}$ responds over a wide range of intensities (0.5 mW/cm^2 to 500 mW/cm^2 or 1.1×10^{15} photons cm^{-2} s^{-1} to 1.1×10^{18} photons cm^{-2} s^{-1}) with a sigmoid intensity-response profile (normalized steady-state currents, mean ± S.D. n = 3 experiments). For details see Fig. S4.1 and the Supporting Information Note.

We tested expression and function of LiGluR-MAG0$_{460}$ in the retina of the *rd1* mouse, a small animal model of human blinding disease. The *rd1* mouse has a null mutation in the PDE6-beta subunit causing complete loss of rod and cone photoreceptors by p90 [137]. This is comparable to patients in the early stages of retinal degeneration that may still have a functioning network of all retinal cell types except for the photoreceptors. At later stages, however, only the RGCs may survive [125,138]. In order to address both early and late stages of the disease, we examined the effect of targeting LiGluR to either the RGCs or ON-BCs (Fig. 4.2C and E).

Good restriction of LiGluR expression in RGCs was achieved using an AAV vector combining the human synapsin promoter (hsyn-1) and the AAV 2/2 capsid as previously described [34]. The gene expression cassette (Fig. 4.2A) in a volume of 2 µl containing 10^9 - 10^{10} viral genomes was injected into the vitreous of *rd1* mice. Expression was visualized >4 weeks after injection using an antibody against the GluK2 subunit from which LiGluR is composed [63]. Intravitreal injection of the vector resulted in expression in the RGC layer (Fig. 4.2D and G, Fig. S4.2A). Due to the limited retinal penetration of the AAV2/2 serotype [32] and the lack of syn-1 expression in ChAT positive amacrine cells [139], these transduced cells are likely to be predominantly RGCs. LiGluR expression was pan-retinal and localized to soma and dendrites of both ON and OFF RGCs as seen by stratification of the dendritic terminals in both on and off-sublayers of the inner plexiform layer (IPL) (Fig. 4.2G, Fig. S4.2A).

Targeting ON-bipolar cells required the use of an AAV capsid with deeper tissue penetration and a bipolar cell specific promoter. For this we turned to the tyrosine mutant AAV2/2 capsids [45], which are protected from proteasome degradation, leading to better transduction in the inner retina. We restricted LiGluR expression to ON-BCs with a 4-copy concatemer of a minimal version of the cell-specific mGluR6 promoter (4xgrm6) [36,140]. This gene expression cassette (Fig. 4.2B) was packaged into AAV2/2(4YF) [45] and injected subretinally in *rd1* mice (1-2 month old), creating a 'bleb' covering approximately 25% of the retinal surface (Fig. S4.2B). Sub-retinal injections were used instead of intravitreal injections as this route enabled to deposit the AAV closer to the ON-bipolar target cells. Expression was confirmed >6 weeks after virus injection by staining with the anti-GluK2 antibody and was predominantly found in ON-BCs as seen by stratification of the axon terminals in the on-sublayer of the IPL in the area under the 'bleb' (Fig. 4.2F and H, Fig. S4.2B).

Retinal explants from *rd1* mice (>3 months old) were mounted on a 60-channel multi electrode array (MEA) to test light evoked activity. Aside from a small fraction of sluggish intrinsically photosensitive RGCs, retinas from untreated *rd1* mice showed no blue light induced firing (Fig. S4.2E), consistent with the absence of rods and cones. Incubation of untreated *rd1* retina with 100 µM MAG0$_{460}$ followed by washout left them unresponsive to blue light (Fig. S4.2F). In contrast, *rd1* retinas expressing LiGluR in RGCs, which were insensitive to blue light (Fig. 4.2I), showed strong light-induced firing following exposure to MAG0$_{460}$ (Fig. 4.2K and M). Similarly, *rd1* retinas expressing

LiGluR in ON-BCs were insensitive to blue light (Fig. 4.2J) until they were exposed to $MAG0_{460}$ (Fig. 4.2L and N). Stimulation with broad-spectrum (white) light triggered similar responses (Fig. S4.2G), as demonstrated previously in HEK cells [60]. Both in RGCs and ON-BCs, LiGluR-$MAG0_{460}$ was able to drive light responses at moderate intensities (0.3mW/cm^2 or 7.1x10^{14} photons cm^{-2} s^{-1} for RGC and 0.2mW/cm^2 or 4.7x10^{14} photons cm^{-2} s^{-1} for ON-BC respectively, Fig. 4.3A and B), representing an approximately 10-fold improvement in sensitivity compared to the published values for the first generation MAG photoswitch [34] (Fig. S4.8). LiGluR-$MAG0_{460}$ elicited graded changes in RGC firing rate in response to graded changes in light intensity (Fig. S4.5G), similar to what we saw in HEK cells (Fig. S4.1C).

Figure 4.2. LiGluR expression downstream in RGCs and upstream in ON-bipolar cells restores light responses in the *rd1* mouse retina *in vitro*. (light intensity for all recordings 27.7mW/cm^2 or 6.3x10^{16} photons cm^{-2} s^{-1}) (**A,B**) Viral DNA expression cassette. LiGluR is flanked by inverted terminal repeat domains (ITR) and stabilized by a polyadenylation signal sequence (polyA) and a woodchuck hepatitis post-transcriptional regulatory element (WPRE). LiGluR expression is driven by (**A**) the human synapsin promoter (hsyn-1) or (**B**) the metabotropic glutamate receptor 6 (4xgrm6) promoter. (**C,E**) Schematic of a degenerated *rd1* mouse retina with targeted cells highlighted in green. (**D,F,G,H**) Confocal images of LiGluR expression (**D,G**) in RGCs of *rd1* mouse retina >4 weeks after intravitreal injection of AAV2/2-hSyn-LiGLuR (2ul volume equal to 5x10^{11} viral genomes) or (**F,H**) ON-BCs of *rd1* mouse retina >6 weeks after subretinal injection of AAV2/2-(4YF)-4xgrm6-LiGLuR (2ul volume equal to 5x10^{11} viral genomes). Retinas were stained with an anti-GluK2 antibody (green) and nuclei were stained with DAPI (blue). Scale bar =10 µm. INL, inner nuclear layer. IPL, inner plexiform layer with indication of on and off sublayers. (**I-L**) MEA recordings from *rd1* mouse retinas expressing LiGluR in RGCs (**I,K**) or ON-BCs (**J,L**) in absence (**I,J**) or presence (**K,L**) of MAG0$_{460}$. Top: light stimulation protocol 5x 3 s blue light and 8 s dark. Middle: raster plot with spikes for all light sensitive RGCs (I,K: n=130 cells, J,L: n=46 cells), Bottom: peri-stimulus time histogram (PSTH) with 250 ms bins. (**M,N**) Comparison of the average firing rates (500 ms bins) in the light *vs.* dark for *rd1* retinas expressing LiGLuR in RGCs (**M**) and ON-BCs (**N**) in the absence (grey) (M: n=6 retinas, 478 cells, N: n=4 retinas, 416 cells) and presence (green) (M: n=5 retinas, 303 cells, N: n=4 retinas, 332 cells) of MAG0$_{460}$ and population mean (black and blue, respectively).

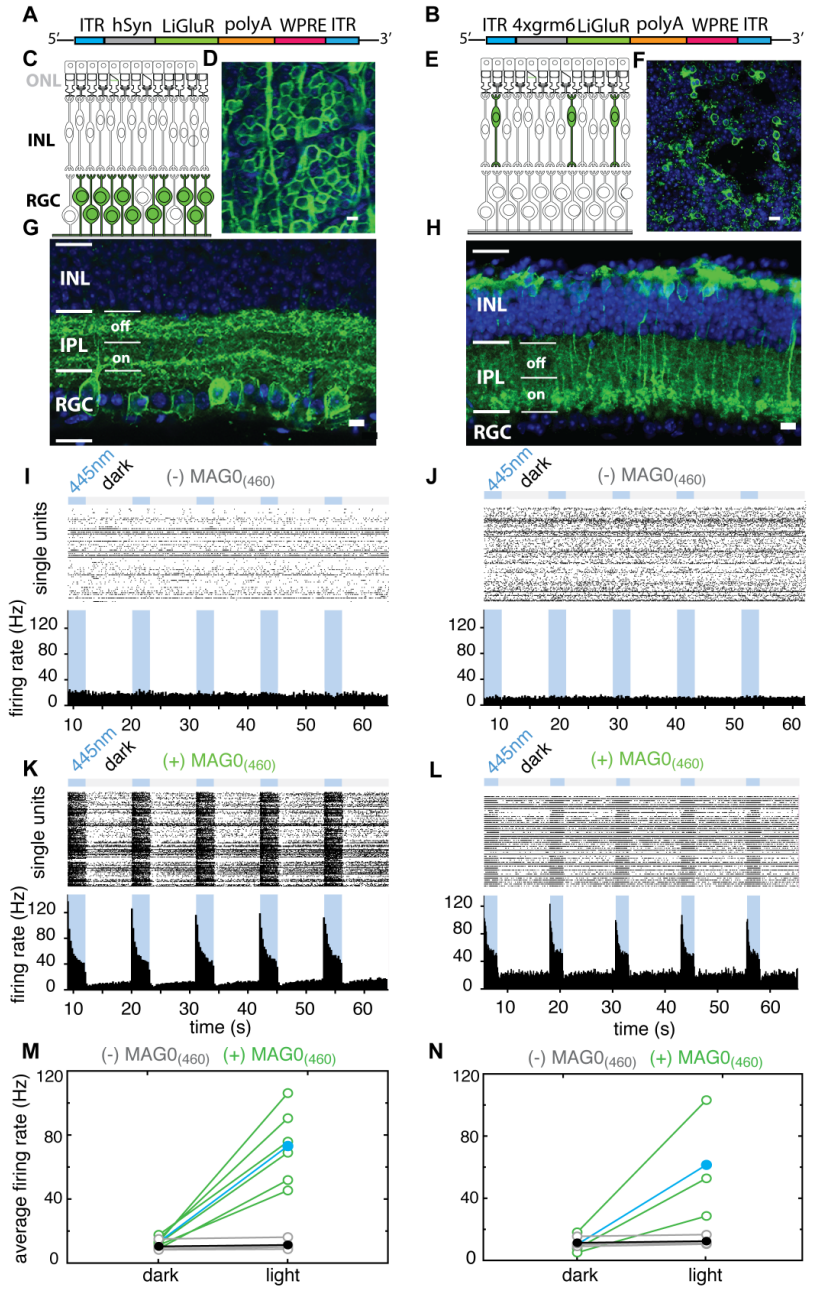

Figure 4.3 LiGluR-MAG0$_{460}$ in RGCs and ON-BCs of *rd1* mouse retina drives light responses with similar characteristics (other than for panels A and B, light intensity for all recordings is 24.7mW/cm^2 or 5.6x10^{16} photons cm^{-2} s^{-1}). (**A-H**) MEA recordings of *rd1* mouse retinas treated with LiGluR-MAG0$_{460}$ in RGCs (left row) or ON-BCs (right row). (**A,B**) Dynamic range with 3 s stimulation (A, n=4 retinas, 287 cells; B, n=4 retinas, 150 cells). Data are means ± S.D. (**C,D**) Responses to brief (35 ms) flashes of light. Inlays show responses of single cells in gray (C, n=47 cells; D n=33 cells) and population average in black with mean tau$_{off}$. All traces were fit exponentially and the time constants for the peak decay reflecting the MAG0$_{460}$ dark relaxation are shown as scatterplot and summarized in a boxplot. (**E-H**) LiGluR responses to frequency modulated stimulation (50 ms flashes). (E: n=77 cells, F: n=67 cells, G: n= 70 cells, H: n=65 cells) top: raster plots showing indication of light flashes in blue and single unit spikes in black (500ms bins); bottom: peri-stimulus time histograms showing population averages of all single cell responses to 4 Hz and 10 Hz stimulation in black with a gray shadow indicating standard error (SEM).

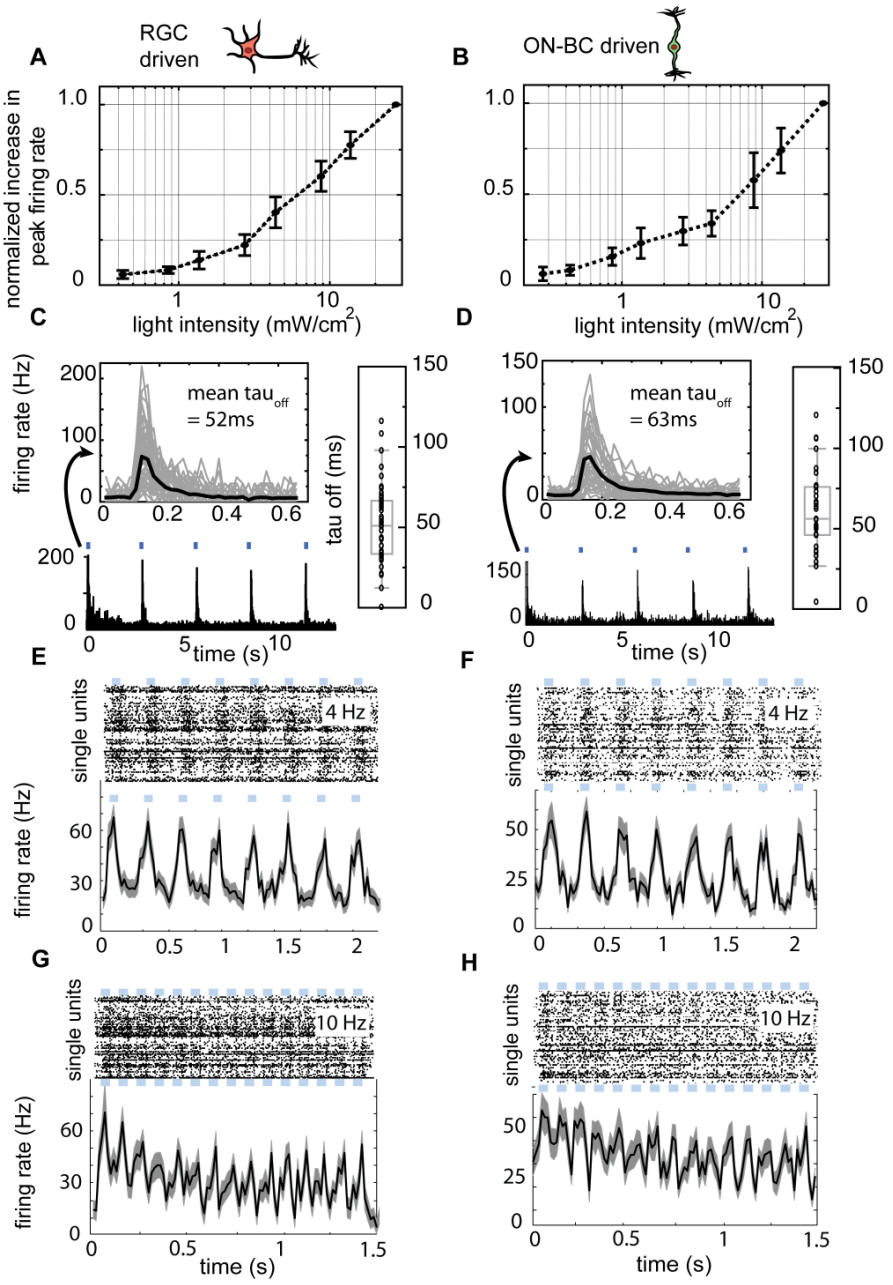

Kinetics and frequency detection supported by light-sensitive RGCs and ON-BCs

Ideally, a visual prosthetic should have fast dynamics to restore natural vision after loss of photoreceptor cells [53,141,142]. We found that light pulses as short as 35 ms in duration were sufficient to trigger robust RGC firing when LiGluR-MAG0$_{460}$ was expressed in either RGCs or ON-BCs (Fig. 4.3C and D). In both cases the responses reached a peak firing rate similar to that observed with much longer pulses of light (compare Fig. 4.2K and L with Fig. 4.3C and D).

The responses had a short delay following light onset and terminated rapidly from peak response to baseline (τ_{off} = 51.96 ms, SEM=3.48 with LiGluR-MAG0$_{460}$ in RGCs and τ_{off} = 62.87 ms, SEM=5.26 with LiGluR-MAG0$_{460}$ in ON-BCs) with values from steady state to baseline (LiGluR-MAG0$_{460}$ in RGCs: ΔT_{off} = 40 ms (Fig. S4.5C), LiGluR-MAG0$_{460}$ in ON-BCs: ΔT_{off} = 80 ms (Fig. S4.5D). The similarity between RGC driven (Fig. 4.3C and Fig. S4.5C) and ON-BC driven (Fig. 4.3D and Fig. S4.5D) termination suggests that the off kinetics are mostly governed by ligand inactivation from the *cis* to *trans* state and the speed (Fig. 4.3C and D) suggests that these systems should enable retinal output to follow high frequency modulation of light intensity. We tested this by measuring RGC firing in response to trains of short light pulses given at either 4 Hz (50 ms flashes at 200 ms inter-stimulus interval) or 10 Hz (50 ms flash with 50 ms inter-stimulus interval) with LiGluR-MAG0$_{460}$ in RGCs (Fig. 4.3E and G) or in ON-BCs (Fig. 4.3F and H). In both cases, at 4 Hz, the individual RGCs responded to every flash of light. With increasing frequency, the light-induced firing rate decreased (Fig. S4.5B) and individual cells stochastically missed some responses (S4.5A). At the population level, however, *rd1* retinas with LiGluR-MAG0$_{460}$ in RGCs and ON-BCs reliably followed 4Hz (Fig. 4.3E and F) and 10 Hz stimulation frequencies (Fig. 4.3G and H).

Differences between light-induced RGC firing with LiGluR in RGCs *versus* ON-BCs

More than 20 different subtypes of RGCs have been classified in the mouse retina to date based on physiology and morphology, including dendritic stratification and input pathways [143,144]. Some of the synaptic connections in the INL are maintained in early stages of degeneration [126,145]. Engaging those synaptic connections through LiGluR expression in ON-BCs may lead to diverse light responses in the downstream RGCs, indicating that aspects of RGC identity might be retained or restored. In contrast, bypassing these synaptic connections by LiGluR expression in RGCs themselves should lead to uniform responses across all LiGluR-RGCs regardless of their original identity (ON vs. OFF, transient vs. sustained etc.).

To explore this *in vitro* using the MEA, we examined single unit RGC responses to 1 s flashes of light for four different conditions: wt (Fig. 4.4A, left column), *rd1* LiGluR-MAG0$_{460}$ in either RGCs (Fig. 4.4B, second to left column) or ON-BCs (Fig. 4.4C, second to right column) and *rd10* LiGluR-MAG0$_{460}$ in ON-BCs (Fig. 4.4D, right column). A non-patterned light was used as stimulus to allow comparisons to be made without concern for variability of LiGluR expression levels and density (compare Fig

4.2D and F, S4.2A and B). Peri-stimulus time histograms were plotted for each recording (Fig. 4.4 E-H). In *rd1* mice, RGCs with LiGluR-MAG0$_{460}$ showed uniform responses, with similar onset delays and offset rates (Fig. 4.4B and F). The photoswitching index (normalized difference in firing rates in the light vs. dark) was positive for every cell (Fig. 4.4F) as expected for their direct excitation by LiGluR-MAG0$_{460}$. In contrast, *rd1* RGCs that received synaptic input upstream from ON-BCs with LiGluR-MAG0$_{460}$, showed more diverse responses (Fig. 4.4C). Some cells were excited by light and others were inhibited (Fig. 4.4C and G). The onset, offset and duration of the light response also varied between cells (Fig. 4.4C) similar to wild type retina (Fig. 4.4A and E).

The diversity of responses seen in single units prompted us to ask if this effect could be seen more globally at the level of the retina, taking into account all the cells from one recording. Rather than averaging across cells and thus masking cell to cell variation, we wanted to systematically analyze all responses from each cell individually in order to understand the relationship between the RGC firing patterns generated by LiGluR-MAG0$_{460}$ installed in the RGCs themselves or in the ON-BCs. To this end, we correlated the peri-stimulus time histograms (the firing rate of a given cell over time) of all cells with one another and constructed a correlation matrix in which each data point represents the correlation value (r). Responses during the 1 s light flash and responses 100 ms before and after the flash were used to construct the correlation matrices. Heat maps represent the correlation score with warm colors representing high correlation values. Using this unbiased and inclusive analysis, we confirmed that LiGluR-MAG0$_{460}$ in RGCs lead to uniform responses across all cells (Fig. 4.4J, Fig. S4.6B and C), whereas LiGluR-MAG0$_{460}$ in ON-BCs yielded overall lower correlation in RGC output (Fig. 4.4K, Fig. S4.6B and C). Wild type retinas with photoreceptor driven activity showed low levels of correlation (Fig. 4.4I, Fig. S4.6B), as expected due to the functional diversity of RGCs. The ON-BC LiGluR-MAG0$_{460}$ correlation matrix showed higher diversity of responses and shared more similarity with wt retinas than with retinas that have LiGluR-MAG0$_{460}$ in RGCs. LiGluR-MAG0$_{460}$ in ON-BCs of the *rd10* mouse retina, which undergoes slower retinal degeneration, also showed higher levels of diversity or low levels of correlation (Fig. 4.4D,H,L, Fig. S4.6B) similar to LiGluR-MAG0$_{460}$ installed in ON-BCs of the rd1 mouse retina, indicating that the effect we observed was specific to the different target cells and not a function of retinal degeneration.

LiGluR restores innate and learned associative light-guided behavior

We next asked whether LiGluR-MAG0$_{460}$ could restore basic visually guided behavior. Mice naturally avoid brightly lit open spaces (37). This preference is absent in adult rd1 mice that have lost all rod and cone photoreceptors (14, 16). To test for restoration of light avoidance, we placed wt mice and rd1 mice with LiGluR in RGCs or ON-BCs in an open field test (Fig. 4.5A) and tested their behavior before and after treatment with MAG0$_{460}$. Mice were first habituated to the testing environment, which consisted of an open-topped plastic box with dark and light compartments connected by a small opening (Fig. 4.5A), and then allowed to explore the box for 5 min. The percentage of time spent in the light compartment was recorded (16). Following intravitreal injection of MAG0$_{460}$,

mice with LiGluR in RGCs (n = 18) or ON-BCs (n = 13) showed a strong light avoidance, which was similar to the light avoidance of wt mice (n = 4) (Fig. 4.5B).

After establishing that we can restore light avoidance behavior, we asked how long the restoration of the light response would last following a single intravitreal injection of $MAG0_{460}$, as the receptor protein on the cell surface turns over. Following a single intravitreal injection of $MAG0_{460}$ in *rd1* mice expressing LiGluR in RGCs, the light-induced firing of RGCs in isolated retinas was found to decline with a time-constant of ~9 days (τ = 8.8 days) (Fig. 4.5C). The behavioral preference for the dark compartment declined over a similar time course following a single intravitreal injection of $MAG0_{460}$ (Fig. 4.5D).

Since LiGluR-$MAG0_{460}$ targeted to either RGCs or ON-BCs can restore the ability of blind mice to distinguish light from dark, we wanted to test whether it would also enable animals to distinguish temporal patterns of light and use this information in the context of a learned behavior. Based on our finding that LiGluR-$MAG0_{460}$ can follow moderate frequencies of intensity modulation (Fig. 4.3E and F), we created two visual stimuli of identical intensity, with the cue stimulus flashing at a rate of 2 Hz and the decoy stimulus emitting light of constant intensity. These visual stimuli were presented in a radial arm water-maze that was modified into a forced two-choice task (Fig. 4.5E). Mice were first habituated to the maze and then trained to associate a specific light cue with a hidden escape platform [146] for 8 days at 20 trials per day. These conditions were chosen to maximize exposure of mice to this task within the efficacy period of a single treatment with $MAG0_{460}$, as determined by the open field test (Fig. 4.5C and D). A correct trial was defined as a mouse finding the platform in under a minute without exploring the wrong arm of the maze first.

We used four groups of mice for this study: wt mice (positive control), *rd1* mice expressing LiGluR in RGCs or ON-BCs and injected intravitreally 24 hours prior to day 1 with $MAG0_{460}$ (experimental) and *rd1* mice that were sham injected (negative control). Wt mice (n=6) performed well, improved gradually and were able to learn the task ($p<0.016$) within 8 days (Fig. 4.5F, Fig. S4.7A), in agreement with earlier studies [146]. The performance of sham injected *rd1* mice (n=8) did not improve ($p=0.815$) over the 8 days (Fig. 4.5F, Fig. S4.7B). In contrast, *rd1* mice with LiGluR-$MAG0_{460}$ in either RGCs (n=9) or ON-BCs (n=6) learned to distinguish the temporally patterned stimulus from the decoy stimulus ($p<0.0025$ and $p<0.017$, respectively) (Fig. 4.5F, Fig. S4.7C and D). The light intensities used for the light avoidance and watermaze tasks were 7 mW/cm^2 or $1.6x10^{16}$ photons cm^{-2} s^{-1} and 5mW/cm^2 or $1.1x10^{16}$ photons cm^{-2} s^{-1}, respectively, which corresponds to outdoor light levels on a sunny day (see approximation in Fig. S4.8).

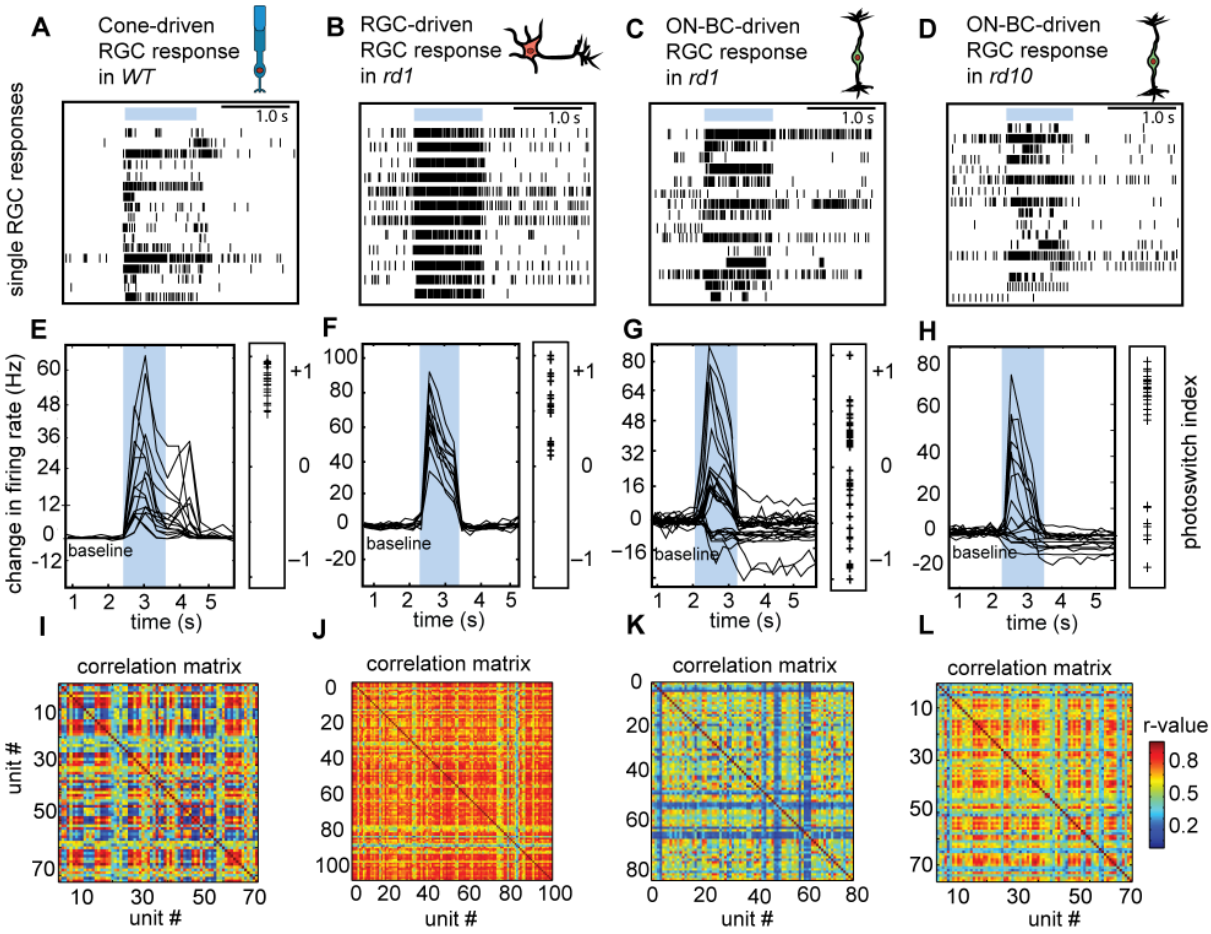

Figure 4.4. LiGluR expression downstream in RGCs synchronizes responses, LiGluR expression upstream in ON-BCs diversifies responses from the *rd1* mouse *in vitro* (light intensity for all recordings 24.7mW/cm^2 or 5.6x10^{16} photons cm^{-2} s^{-1}). **(A-L)** MEA data from wt retina (left column) (A,E,I), *rd1* retina treated with LiGluR-MAG0$_{460}$ in RGCs (second to left column) (B,F,J), ON-BCs (second to right column) (C,G,K) and *rd10* retina treated with LiGluR-MAG0$_{460}$ in ON-BCs (right column) (D,H,L). (**A,B,C,D**) Representative raster-plots of RGC responses to 1 s flash of light (A, n=17; B, n=12; C, n=15; D, n=17 cells) (**E,F,G,H**) Representative traces from single units in response to 1 s light flashes (D, n=16; E, n=14; F, n=28; G, n=17 cells; 250 ms bins). The blue bar indicates the light flash. The light responses are quantified by calculating the photoswitching index (normalized firing rate light-dark; E, n=20; F, n=17; G, n=57; H, n=29 cells). Positive values indicate an increase in firing rate, negative values a decrease in firing rate in response to light. (**I,J,K,L**) Correlation matrices showing correlations between all light sensitive single units. RGC responses during the 1s flash and 100 ms immediately before and after the flash were used for the correlation. The color of the heatmap indicates the magnitude of correlation value r, with warmer colors indicating higher values. (I, n=72 cells; J, n=111 cells; K, n=82; L, n=76 cells).

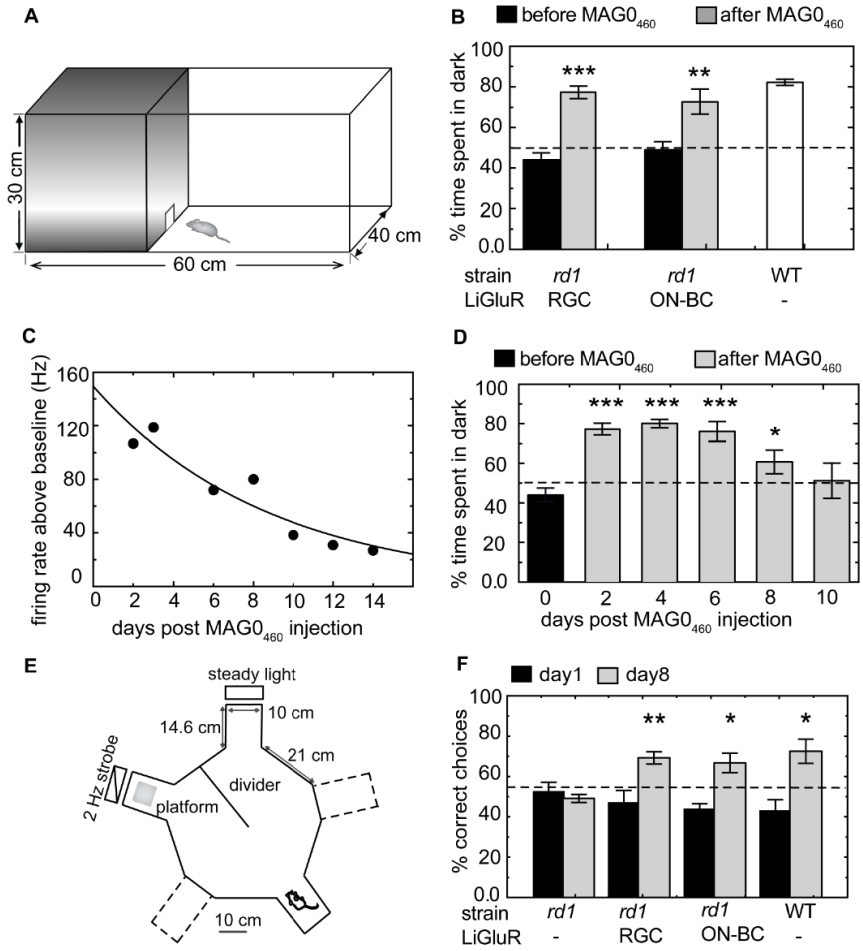

Figure 4.5 LiGluR expression restores innate and learned light guided behavior in *rd1* mice *in vivo*. (**A**) Schematic showing the light/dark box for the open field test. (**B**) Percent time spent in the dark compartment plotted before (black) and after (grey) administration of $MAG0_{460}$ for *rd1*-RGC-LiGluR (n=18), *rd1*-ON-BC-LiGluR (n=13) and wild type mice (n=4). Data are means ± SEM. **P<0.005, ***P<0.0005, paired student's t-test (light intensity 7 mW/cm^2 or 1.6x10^{16} photons cm^{-2} s^{-1}). (**C**) Biological half-life of intravitreally-injected MAG0460. RGC-LiGluR expressing *rd1* mice were injected with a single dose of $MAG0_{460}$ *in vivo* 24 hours before day 1. Subsequently, on days 2-14, retinal explants were prepared and responses to 3 s flashes were plotted. The decay of LiGluR-$MAG0_{460}$-induced light responses was fit with an exponential curve (A= 149.5±8.72, t_0= 8.75±0.79). (**D**) Efficacy of MAG over time *in vivo*. RGC-LiGluR expressing *rd1* mice (n=7) from (B) were tested over the course of 10 days. Percent time spent in the dark compartment is plotted for *rd1*-RGC-LiGluR before $MAG0_{460}$ (n=18) and *rd1*-RGC-LiGluR after receiving a single intravitreal dose of $MAG0_{460}$ at day 2 (n=18), day 4 (n=7), day 6 (n=7), day 8 (n=7), day 10 (n=7). Data are means ± SEM. *P<0.01, **P<0.001, ***P<0.0001, multiple t-tests with Bonferroni correction. (**E,F**) Forced 2-choice associative learning task with modified radial arm maze. (**E**) Schematic of the maze with dimensions in cm. (**F**) Performance of the 4 groups of mice on day 1 (black) vs. day 8 (grey). Percent correct choices are plotted for sham (PBS) treated *rd1* mice (-LigluR, -$MAG0_{460}$) (n=8), *rd1*-RGC-LiGluR +$MAG0_{460}$ (n=9), *rd1*-ON-BC-LiGluR +$MAG0_{460}$ (n=6) and wild type mice (n=6). Data are means ± SEM. *P<0.05, **P<0.005, ***P<0.0005, paired student's t-test (light intensity at the divider 5mW/cm^2 or 1.1x10^{16} photons cm^{-2} s^{-1})

LiGluR in RGCs restores the retinal light responses in a canine model of retinal blindness

Next, we wanted to confirm that LiGluR-MAG_{460} system could be virally delivered and drive functional light responses in a larger animal model. To assess whether LiGluR-$MAG0_{460}$ is safe and effective in a human sized eye, we expanded our study to the canine model, which provides both anatomical and pathological similarities that are clinically-relevant for testing retinal therapies [147]. The *rcd1* model has a nonsense mutation in the *PDE6B,* the same gene that is defective in the *rd1* and *rd10* mice. We used an AAV2/2(4YF) vector in combination with the ubiquitous promoter CAG to deliver the LiGluR transgene to RGCs (Fig. 4.6A and B). Intravitreal injection of AAV2/2(4YF)-CAG-LiGluR in the *area centralis*, a region of high RGC density in the canine retina [148], resulted in potent expression in RGCs by 8 weeks post-injection (Fig. 4.6C and D).

MEA recordings were performed in three degenerated retinas from two mutant *rcd1* dogs that had been intravitreally-injected 8-11 weeks earlier with AAV2/2(4YF)-CAG-LiGluR. Stimulation with high intensity (75 mW/cm^2 or 1.7x10^{17} photons cm^{-2} s^{-1}) blue light in the absence of $MAG0_{460}$ did not alter the baseline RGC firing activity (Fig. 4.6E). However, following 20 min of incubation in 100 μM $MAG0_{460}$ and thorough wash out, strong and repeated periods of light-induced firing were seen that peaked shortly after the onset of light (Fig. 4.6F and G). To explore the sensitivity of LiGluR-$MAG0_{460}$ to photopic light levels typically encountered within brightly illuminated working/living environment of humans, we performed MEA recordings in a *rcd1* canine retina at different levels of blue light ranging from 6.8 down to 0.43 mW/cm^2 or 1.5x10^{16} photons cm^{-2} s^{-1} to 9.7x10^{14} photons cm^{-2} s^{-1} respectively. Light stimulations (1 s duration) induced RGC firing that was still detectable at the lowest (0.43 mW/cm^2 or 9.7x10^{14} photons cm^{-2} s^{-1}) irradiance and increased with higher intensities (Fig. 4.6H). Responses to all 5 intensities had a transient and a sustained component, and showed similar kinetics with rapid inactivation time from steady-state to baseline levels (40 ms) upon offset of light (Fig. 4.6I).

In order to develop future psychophysical tests to be used in dogs and human patients for the assessment of visual function recovery after intervention with LiGluR-$MAG0_{460}$, we examined the response of the retina to a combination of higher frequency (4 Hz), shorter duration (50 ms) and low light intensity (0.85 mW/cm^2 or 1.9x10^{15} photons cm^{-2} s^{-1}) stimulations. While peak firing rate was reduced and a slight delay was introduced in comparison to responses achieved with longer stimulations at higher intensities, a distinct light-induced ON response of RGCs that peaked at the end of the 50 ms stimulation period could be detected (Fig. 4.6J). Rapid relaxation of the photoswitch ($\tau_{off} \approx$ 28 ms) occurred upon returning to darkness (Fig. 4.6J, inset).

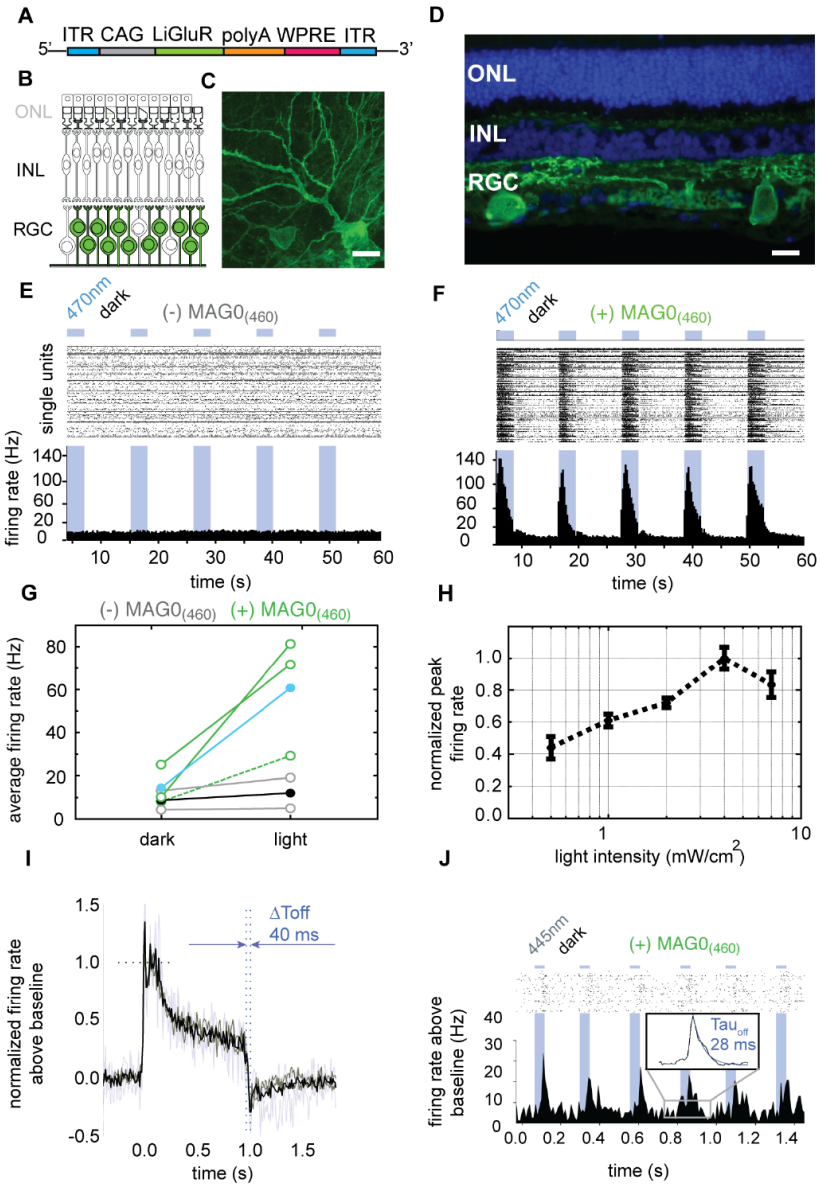

Figure 4.6 LiGluR expression in RGCs restores light responses in the *rcd1* canine retina *in vitro*. (**A**) Viral DNA expression cassette. LiGluR expression is driven by CAG promoter. (**B**) Schematic of degenerated canine retina with targeted RGCs in green. (**C,D**) Confocal images of LiGluR expression in canine retina 8 weeks after intravitreal injection of AAV2/2 (4YF)-CAG-LiGluR. Scale bar = 20µm. (C) Wholemount view of LiGluR expression in RGCs of *rcd1* canine retina. (D) Cross section of LiGluR expression in RGCs of wt canine retina. (**E-J**) MEA recordings (light intensity 75 mW/cm^2 or 1.7x10^{17} photons cm^{-2} s^{-1} if not specified otherwise) of *rcd1* mutant canine retinas. (E,F) MEA recording from a *rcd1* mutant dog expressing LiGluR (n=160 cells) before (**E**) and after (**F**) *in vitro* application of MAG0$_{460}$. (**G**) Comparison of the firing rate averaged over a 3 s flash of light (500 ms bins) on 3 LiGluR expressing *rcd1* retinas in the dark *vs.* light (dashed= 6.8 mW/cm^2 or 1.5x10^{16} photons cm^{-2} s^{-1}, solid= 75 mW/cm^2 1.7x10^{17} photons cm^{-2} s^{-1}) before (n=2 retinas, 193 cells, grey) and after (n=3 retinas, 291 cells, green) *in vitro* application of MAG0$_{460}$, with population means (black and blue, respectively). (**H**) Dynamic range of *rcd1* retina treated with LiGluR-MAG0$_{460}$ at lower light conditions (n=80 ± 5 cells). Data are means ± 2 SEM binned at 100 ms. (**I**) Averaged normalized response to stimulation with 5 light intensities (0.43, 0.85, 1.7, 3.4 and 6.8 mW/cm^2 or 9.7x10^{14}, 1.9x10^{15}, 3.8x10^{15}, 7.7x10^{15} and 1.5x10^{16} photons cm^{-2} s^{-1} respectively) shown in panel (**H**) with individual responses shown in grey, average response over all intensities shown in black and the response inactivation time shown in blue (deltaT$_{off}$). (**J**) MEA recording from an *rcd1* retina treated with LiGluR and MAG0$_{460}$ (n=77 cells) stimulated with low intensity (0.85 mW/cm^2 or 1.9x10^{15} photons cm^{-2} s^{-1}) at 4Hz (50 ms duration, 200 ms ISI) binned at 10 ms. Inlay shows average of 400 individual responses (5 ms bins) with a single exponential fit (blue trace) and time constant (τ_{off}≈28 ms) for MAG0$_{460}$ relaxation from peak response to baseline.

Discussion

In this study we show the translational potential of the LiGluR-MAG0$_{460}$ system for retinal gene therapy to cure human blindness. In a mouse model of the human retinal degenerative disease RP, we observed restoration of a useful retinal output in response to light when LiGluR was expressed either in the most upstream or the most downstream cell types that survive after photoreceptor degeneration. *In vivo*, these retinal responses restored an innate light-guided behavior and enabled light-associated learning based on cues with distinct temporal patterns.

Earlier work validated the use of LiGluR in conjunction with a first generation MAG0 photoswitch in RGCs for vision restoration [34]. However, the therapeutic utility of the first generation MAG0 was limited by two properties. First, the spectral sensitivity of the original MAG0 chromophore was outside of the visible range, peaking in the UV at 380 nm [61], which penetrates the lens poorly and is damaging to corneal, lens epithelial, and retinal cells. Second, LiGluR-MAG0 was bi-stable, requiring a second longer wavelength pulse of light to reset the system after each activating event [61,63], which would necessitate additional hardware for potential clinical applications. We solved these problems with our new photoswitch, MAG0$_{460}$, which is activated by blue light similar to blue cone photoreceptors, responds well to broad-spectrum visible light, and rapidly and spontaneously turns off in the dark [60]. LiGluR-MAG0$_{460}$ responds dynamically to incremental changes in light intensity and supports reliable retinal output with intensity modulations at moderate frequencies of 4-10 Hz.

We compared two gene therapy target cell types, RGCs and ON-BCs, for LiGluR-MAG0$_{460}$ expression in the degenerating mouse retina. RGCs are well-suited therapy targets for late stage disease, as they have been shown to stay morphologically intact [125] with minimal remodeling following photoreceptor degeneration compared to the other retinal cells [138]. Furthermore, RGCs are easily targeted due to their proximity to the vitreous, enabling strong, uniform and widespread expression after intravitreal injection of AAV vectors. ON-BCs, however, are promising therapeutic targets for early stage disease, since they are upstream in the retinal circuit, and provide an opportunity to preserve aspects of retinal processing [53,142].

Robust light responses were restored to the RGCs of retinas isolated from blind mice when LiGluR-MAG0$_{460}$ was installed in either the RGCs themselves or in ON-BCs. The sensitivity, the ability to follow frequency modulated light, and the on/off kinetics in response to full field illumination were similar for the two cell types. The similarity is striking considering the expression was much sparser after viral delivery to the ON-BCs (compare Fig. S4.2A and B). This suggests that the signal amplification due to convergence from BCs to RGCs [149] makes the ON-BC population particularly effective for vision restoration and highlights the value of further improvement for gene delivery to these cells.

There was an important distinction between the properties of the restored retinal output activity when LiGluR-MAG0$_{460}$ was installed in the two cell types. In *rd1* mouse ON-BCs, LiGluR-MAG0$_{460}$ drove RGC activity that was temporally diverse and which excited a subset of RGCs, whereas others were inhibited by light. In contrast, LiGluR-MAG0$_{460}$ in *rd1* mouse RGCs led to uniform light responses, as one would expect from direct excitation of the RGCs. The signal diversity that emerges from the retinal circuit, when LiGluR-MAG0$_{460}$ is installed in ON-BCs, could be beneficial for restoring critical aspects of visual processing, such as contrast and edge detection [150]. Single unit RGC responses from ON-BCs LiGluR-MAG0$_{460}$ in both *rd1* and *rd10* resembled the RGC responses seen in wt retina more closely than RGC LiGluR-MAG0$_{460}$. ON-BCs might therefore the target of choice in early stages of retinal degeneration, before substantial synaptic remodeling has occurred [138]. In late stages of retinal degeneration with severe circuit degeneration, it may be preferable to target the least affected cells, the RGCs, to generate a strong and synchronized output signal.

We tested function of LiGluR-MAG0$_{460}$ *in vivo* and found that the restored retinal activity supported normal light-avoidance behavior in blind treated mice using the open field test. Having established that our treatment supported light guided behavior we next asked whether the LiGluR-MAG0$_{460}$ system would enable blind mice to learn to distinguish different visual cues in the context of a forced two-choice variant of the Morris water-maze task. In this experiment, mice were challenged to associate a temporally patterned cue stimulus from a non-patterned intensity matched decoy stimulus. Wild type mice were able to learn to associate the patterned stimulus with the reward, whereas untreated *rd1* mice were not, and did not improve their performance over the 8 days of the experiment. *Rd1* mice treated with LiGluR-MAG0$_{460}$ in either the RGCs or ON-BCs learned to perform as well as wt animals, indicating that the LiGluR-MAG0$_{460}$ system operates as more than just a mere light meter and can inform mice about qualitative aspects of the visual world. In this study, we did not attempt to record visually evoked potentials (VEP), record electroretinograms (ERG), nor test for a pupillary light reflex (PLR) as we did for our previous study [34]. Instead, we focused our efforts on learned associations and demonstrated the ability of mice to recognize temporal patterns in the watermaze task. We have not yet tested these mice for spatial pattern recognition or temporal and spatial pattern resolution.

Our results in mouse encouraged us to test if our treatment could be translated to a larger animal model. Specifically, we set out to test virus-mediated expression of the LiGluR receptor and the ability of LiGluR-MAG0$_{460}$ to drive light responses in retinal explants. To this end, we selected the *rcd1* dog, that, like the *rd1* mouse, has a severe and early onset rod and cone degeneration [151,152]. We developed a virus for canine RGC transduction and tested patches of retina collected from the *area centralis* region for LiGluR-MAG0$_{460}$-induced light responses *in vitro*. LiGluR-MAG0$_{460}$ in the RGCs rendered the blind dog retina light sensitive with characteristics closely matching those observed in the *rd1* mouse. Our results show that the LiGluR-MAG0$_{460}$ system in excised *rcd1* dog retina responds well to stimulation at a light intensity found under natural

environmental conditions (0.43 mW/cm^2, approximately outdoor conditions (see Fig S4.8) and moderate frequencies (up to 4 Hz). This paves the way for future efforts in dog to determine toxicity and a therapeutic index for the MAG0$_{460}$ photoswitch and to perform behavioral testing in an advanced retinal degeneration.

A recent study restored the ability to distinguish light from dark using just a chemical photoswitch that acts on native ion channels, including those that are up-regulated in the RGCs of the degenerating mouse retina [133]. Compared to this optochemical therapy, which has advantages of not requiring gene transfer and being more sensitive to light (see comparison of threshold light intensities in Fig. S4.8), our two-component optochemical-genetic therapy has the advantage of designed cell-type targeting. In addition, covalent attachment of the chromophore allows us to work at lower concentrations of the photoswitch chemical, a factor that, along with targetability, could provide a better safety profile. In both the optochemical and optochemical-genetic therapy approaches a bolus supply of the photochemical restores light-guided behavior temporarily, for a period of days. In the optochemical case this is presumably due to washout of the molecule, whereas in our optochemical-genetic case it is most likely due to the turnover of the photoswitch-conjugated receptor. As a result, both of these approaches would benefit from sustained-release drug delivery technology.

An alternative purely optogenetic approach has proven successful for restoration of light responses in retinal cells, light responses in visual cortex, light aversion and learned association tasks using unpatterned light. For this approach, microbial opsins are expressed in specific cell types of the degenerated retina, from cone cell bodies that have lost their the outer segment to ON-BCs to RGCs [33,35,130,132]. The simplicity of this genetic therapy is appealing, as is the ability of the microbial opsins to use the retina's supply of retinal as the natural photoswitch. One concern about this approach is the possibility of an immune response to the foreign protein, which, in the worst case, could spread into the brain via the optic nerve. In addition, once expressed, these opsins cannot be turned off in case of an adverse reaction. Our success with a mammalian light-gated protein that is identical in amino acid sequence to the native protein, except for a single amino acid substitution that creates the photoswitch anchoring site, reduces the risk of immune reaction. In addition, the dependence on chronic delivery of the synthetic photoswitch should make it possible to discontinue treatment in case of an adverse reaction as well as to replace with improved photoswitches as they become available.

In summary, we have shown that the LiGluR-MAG0$_{460}$ system operates successfully in either ON-BCs, at the upstream end of the degenerating retina, or at the output end of the retina, in RGCs, to restore retinal light responses and enable innate and learned light-guided behavior to blind mice. Installation in the ON-BCs, which is probably most appropriate for early stage degeneration, provides more diverse retinal output characteristics, and may support higher quality vision, a notion that will require future testing. Importantly, the system is equally effective in the *rcd1* dog *in vitro*, paving the way for extensive testing of high-resolution vision in a pre-clinical setting and for

clinical development. Our approach should allow for the use of a receptor protein based on the patient's own receptor, reducing the chance of an immune response. Because the functional properties of the restored light response depend on the externally provided photoswitch it can be tailored to the patient, improved as new photoswitches become available and, equally importantly, the function of the system can be aborted in case of adverse effects by curtailing photoswitch delivery.

Methods

Animals. All mouse experiments were performed with approval of the University of California Animal Care and Use Committee. Wt mice (C57Bl/6J) and *rd1* mice (C3H) were purchased from Jackson Laboratory (Bar Harbor, ME) and housed on a 12-hour light dark cycle with food and water *ad libitum*. The age of mice ranged from p30-p60 for rAAV injections and p90-p160 for *in vivo* and *in vitro* experiments.

All experiments on dogs were approved by the Institutional Animal Care and Use Committee of the University of Pennsylvania, and were carried out in strict accordance with the recommendations in the Guide for the Care and Use of Laboratory Animals of the National Institutes of Health, the USDA's Animal Welfare Act and Animal Welfare Regulations, and complied with the ARVO Statement for the Use of Animals in Ophthalmic and Vision Research. Experimental. Three *rcd1* dogs (*PDE6B* mutation) [153] with late stage retinal degeneration (ages: 0.4, 1.8 and 3.7 years), and 1 normal dog (age: 2.4 years) were used to assess viral vector tropism and for MEA experiments (see details below).

Injection of rAAV and MAG photoswitch. Adeno-associated viruses were produced via standard methods [154]. We selected rAAV2/2 carrying the LiGluR transgene under the control of the human synapsin-1 (hsyn-1) promoter for RGC targeting. For ON-BC targeting, we selected rAAV2/2(4YF) carrying the LiGluR transgene under the control of the 4x repeat of the metabotropic glutamate receptor 6 promoter (4xgrm6), a kind gift from Botond Roska and Connie Cepko. The titer of AAV was determined via qPCR relative to inverted repeat domains (ITR) standard. Titers for these viruses ranged between 1 x 10^{13} vg/ml and 1 x 10^{14} vg/ml. Mice were anesthetized with IP ketamine (72 mg/kg) and xylazine (64 mg/kg). Eyes were additionally anesthetized with proparacaine (0.5%) and pupils were dilated with phenylephrine (2.5%) and tropicamide (1%). Injections consisted of 2-step process: First an incision was made posterior of the ora serrata using a sharp 30-gauge needle. Then, a 2 μl volume of $MAG0_{460}$ photoswitch diluted in PBS/DMSO or an estimated amount of $5x10^{11}$ viral genomes of AAV diluted in PBS (with 1% phenol red as contrast agent) was injected intravitreally for rAAV2/2-hsyn-LiGluR or subretinall for rAAV2/2(4YF)- 4xgrm6-LiGlUR using a blunt 32 gauge Hamilton syringe (Reno, NV). Efflux was minimized by keeping the Hamilton needle tip in the eye for >60 seconds.

Intravitreal injections in dogs were performed under general gas (isofluorane) anesthesia. A 150 μl volume of rAAV2/2 (4YF) carrying the GFP reporter gene under the control of the ubiquitous CAG promoter was delivered intravitreally (preretinally) to the superior/tapetal fundus region of a 20 week-old mutant *rcd1* dog using a 39-gauge polyimide cannula (RetinaJet; SurModics, Inc., Eden Prairie, MN). The right eye was injected with a viral titer of 1.46 x 10^{11} vg/ml, while the contralateral (left) eye received a

10 fold higher viral titer (1.46 x 10^{12} vg/ml). At 12 weeks post injection, expression of GFP was assessed by non-invasive retinal imaging, using a scanning confocal laser ophthalmoscope (Heidelberg, HRA/OCT) set on the autofluorescence mode. Following euthanasia, the eyes were processed for immunohistochemistry as stated below and localization of GFP expression to retinal cell populations was examined. Subsequently, an AAV2/2(4YF)-CAG-LiGluR viral construct was produced and injected pre-retinally to the *area centralis* region of one normal and the two *rcd1* mutant dogs. The rAAV was diluted in balanced salt colution (BSS, Alcon Laboratories, Fort Worth, TX), and 200 µl of two viral titers (1.46 x 10^{11} and 5 x 10^{11} vg/ml) were injected.

MAG preparation. A stock solution of 100 mM $MAG0_{460}$ (L-diastereomer) [60] in 100% pharmaceutical grade dimethyl sulfoxide (DMSO, Cryoserv, Bioniche Pharma) was diluted 1:100 in sterile PBS for a final working solution of 1 mM in 1% DMSO. Working solutions were prepared immediately before administration and were used within 20 min to avoid hydrolysis of the maleimide group. *In vitro* conjugation of $MAG0_{460}$ on retinal explants for electrophysiological recordings was performed in a volume of 200 µl at a concentration of 100 µM $MAG0_{460}$ (in PBS with >1% DMSO). For *in vivo* experiments and the MAG efficacy experiment (Fig. 2.5), a 2 µl volume of 1 mM $MAG0_{460}$ solution (in PBS with 1% DMSO) was injected into eyes that had been treated with AAV >6 weeks earlier. In dogs, 1 ml of 100 µM $MAG0_{460}$ (in Ringer's solution) was applied to the retinal explants for MEA recordings.

Tissue preparation and immunohistochemistry. Mice were sacrificed >4 weeks (for RGC-LiGluR) or >6 weeks (for ON-BC LiGluR) post AAV injection and the eyes were enucleated and fixed in 4% paraformaldehyde (PFA, Ted Pella) for 1 h. Wholemount retinas were prepared by making a complete circular incision around the ora serrata using scissors, removing the cornea while leaving the lens attached, gently tearing the eyecup apart using two forceps and finally removing the lens. Radial cuts were made to flatten the retina resulting in the typical clover-leaf shape. For retinal sections, wholemounts were embedded in agarose (Sigma, St Louis, MO) and sectioned transverse using a vibratome (Leica, Mannheim, Germany) at medium speed, maximum vibration and 150 µm thickness. Wholemounts and vibratome sections were incubated in blocking buffer (10% normal goat serum (NGS), 1% BSA, and 0.5% Triton X-100 in PBS (pH 7.4)) for 2 h at RT. Monoclonal antibody against GluK2/K3 (Millipore, Billerica, MA) was applied at 1:500 dilution in blocking buffer over night at 4°C. Secondary anti-rabbit Alexa-488 or Alexa 594 antibody (Invitrogen, Carlsbad, CA) was applied at 1:1000 in blocking buffer for 2 h at RT. Tissue was washed 3x for 10 min with PBS and mounted on slides using Vectashield (Vector labs, Burlingame, USA) mounting medium with DAPI (4',6-diamidino-2-phenylindole) to stain cell nuclei. Wholemounts and sections were imaged via confocal microscopy (LSM7, Carl Zeiss, Goettingen, Germany). In order to identify off target cell expression outside of the expected layer, we prepared a total of 44 vibratome sections from 4 treated retinas from 3 mice (previously injected with AAV2/2 hsyn-LiGluR or AAV2/2(4YF)-4xgrm6-LiGluR) and counted the number of labeled cell bodies outside of the RGC layer or the IPL on layer, respectively. In dogs, ocular tissues were collected following intravenous injection of a euthanasia solution (Euthasol;Virbac, Ft. Worth, TX). Retinal tissues used for immunohistochemistry on

retinal cryosections or wholemounts were processed as previously reported [148] and examined by confocal microscopy (Leica TCS SP5, Leica microsystems, Wetzlar, Germany).

HEK cell recordings. HEK 293T cells were transfected with a LiGluR expression vector (pcDNA-GluK2(Q) L439C) using Lipofectamine 2000 (Invitrogen) and yellow fluorescent protein (YFP) as transfection marker [60,155] Cells were labeled after expression for 24 - 48 h at 37 °C. Cells were washed with external solution, incubated for 2 min with 0.3 mg/ml concanavalin A (ConA) to block ligand-induced desensitization, and labeled with ~25 μM $MAG0_{460}$ or regular MAG0 [63] for 40 min in extracellular solution at RT in the dark. After labeling, any unreacted MAG was removed by thorough washing with external solution. Whole-cell HEK cell recordings were performed in voltage-clamp configuration, typically at -75 mV, on an inverted microscope (Olympus IX) using an Axopatch 200B headstage/amplifier (Molecular Devices) at 22 - 24 °C. Patch pipettes were pulled from borosilicate glass to give 3 - 7 MΩ resistance when filled with internal solution (135 mM K-gluconate, 10 mM NaCl, 10 mM HEPES, 2 mM MgCl2, 2 mM MgATP, 1 mM EGTA, pH 7.4). The extracellular solution was 138 mM NaCl, 1.5 mM KCl, 1.2 mM MgCl2, 2.5 mM CaCl2, 10 mM glucose, 10 mM HEPES, pH 7.3. Photoswitching (Fig. 1 C and D, Fig. S1A and B) was achieved with a xenon-lamp light source (DG4, Sutter Instruments) in combination with excitation filters (445/20 nm, 379/34 nm, and 500/24 nm ('center'/'full width >90%') and a set of neural density filters (XND, Omega Optical). The DG4 light source was coupled via liquid light guide to the back-port of the microscope to give homogeneous illumination through a 40x LUCPlanFLN NA 0.60 FN 22 objective (Olympus), yielding an irradiance up to 500 mW/cm^2 (445 nm) at the sample stage. Dynamic intensity modulation (Fig. S2.1C and D) was performed using a collimated LED light source (470 nm, Thorlabs) coupled to the back-port of the microscope. The intensity was modulated with an analog signal from the Digidata A/D-converter (Molecular Devices).

MEA recordings. MEA recordings were performed on wt (C57Bl/6J) mice, untreated control and treated *rd1* mice (fast retinal degeneration model) as well as *rd10* mice (slow degeneration model). Control mice and wt mice were used at age >p90. Experimental mice were used 6-10 weeks following AAV injection. *Rd10* mice were used at age >6 months. For recordings, the retina was placed ganglion cell side down **[156]** in the recording chamber (pMEA 100/30iR-Tpr, Multi Channel Systems, Reutlingen, Germany) of a 60-channel multi electrode array system with constant vacuum pump (perforated MEA1060 system with CVP; Multi Channel Systems, Reutlingen, Germany). A custom-made dialysis membrane weight was placed on the retina adding positive pressure from above. Additionally, vacuum was applied to the retina using the constant vacuum pump adding negative pressure improving electrode to tissue contact and signal-to-noise. During recording, a constant perfusion of oxygenated Ames media (34 °C) was provided to the recording chamber. For *rd10* mice retina we supplied LAP-4 (Sigma, St Louis, MO), a

group III metabotropic glutamate receptors agonist, in order to block any residual photoreceptor mediated response. Comparative analysis of responses before and after drug administration was used to ensure complete block of photoreceptor activity at 20 μM working concentration. Recordings lasted between one to three hours. Illumination was provided by two different light sources that were all coupled to a 4x objective. Light intensities were measured with a handheld power meter (Thorlabs Inc. Newton, NJ). A 300 Watt mercury arc lamp (DG-4, Sutter Instruments, Novato, CA) with a blue band pass filter (445/50 nm, Thorlabs Inc. Newton, NJ) was used for initial recordings in Fig. 2.2 and Fig. S4.2. For later recordings, an LED light source (470 nm, 24.7 mW/cm^2 or $6.3x10^{16}$ photons cm^{-2} s^{-1}, Thorlabs) with a collimator lens (Thorlabs Inc. Newton, NJ) was used for high frequency stimulation (Fig. 4.3 and Fig. S4.5) and for all MEA recordings in Fig. 4. Data was sampled at 25 kHz filtered between 300-2000 Hz and recorded using MCS rack software (Multi Channel Systems, Reutlingen, Germany) for off-line analysis. Voltage traces were converted to spike trains off-line by collecting responses using methods described below. Spikes recorded at one electrode were sorted into single units, which we defined as 'cells', via principal components analysis using Offline Sorter (Plexon, Dallas, TX). Single unit spike clusters were exported to MatLab and analyzed and graphed with custom software. For extracting firing rates in the dark, we averaged all bins over 3 s preceding the flash to minimize fluctuations. To extract firing rates in the light the maximum response was taken, typically the first two bins following the flash depending on bin size (bins ranged from 20ms-500ms). A cell was defined as 'responder' if the photoswitching index PI (firing rate light - firing rate dark)/(firing rate light + firing rate dark) satisfied the condition $PI > 0.1$ or $PI < -0.1$. All cells from one retina or all retinas per condition were plotted for analysis unless otherwise noted (Fig. 4.4A-D showing representative traces, Fig. S4.5 showing 'strong responders'). Two different approaches were implemented to set the threshold for spikes: i) For plots showing cell-to-cell or retina-to-retina variability (Fig. 4.3C-H, S4.3, S4.4 and Table S4.1), the baseline for each cell was set at a threshold just above electrical noise to include all possible spikes and show the full picture. ii) For plots that show different retinas from different experiments combined, the baseline for each retina was centered at a firing rate of 10-12 Hz in the dark to allow all retinas to be plotted on a similar axis (Fig. 4.2K-N and Fig. 4.3A,B). Correlation matrices (Fig. 4.4) were constructed in MatLab with custom software. Peri-stimulus time histograms of every cell were correlated with one another. The firing rates during the 1 s flash and 100 ms preceding the flash and 100 ms post flash were used to compute the correlation matrices. Correlation values ranged between 1 and 0. A heat map was used to represent the correlation value of each data point in the matrix with warmer colors indicating higher correlation values.

For MEA studies in dogs, a 5mm circular patch of neuroretina centered on the *area centralis* was collected with a biopsy punch. A similar MEA protocol as described above was followed in one *rcd1* mutant dog (both retinas). The preparation and recording of the second rcd1 dog retina differed slightly from the method described in the main text. Following transfer into an MEA chamber (60-channel 200/30iR ITO array, ALA

Scientific Instruments Inc., Farmingdale, NY) the retina was centered on the array ganglion cell side down and covered with a piece of dialysis membrane (Biotech RC Dialysis Tubing Trial Kit 20Kd Mwco, VWR, Radnor, PA) that was pre-soaked in Ringer's solution (119 mM NaCl, 2.5 mM KCl, 1 mM KH_2PO_4, 1.3 mM $MgCl_2$, 2.5 mM $CaCl_2$, 26.2 mM $NaHCO_3$, 20 mM D-glucose in ddH_20). A flat platinum ring (1 cm ring diameter, 1.0 mm wire diameter, 99.997%, VWR) was placed on top of the membrane to increase contact between the retina and the MEA. Oxygenated Ringer's solution equilibrated with 95% O_2 / 5% CO_2 was added to the chamber. The chamber was then transferred to the stage of an inverted microscope (Olympus IX51) and locked in place following installation of an MEA amplifier (MEA1060-Inv, Multi Channel Systems MCS GmbH, Germany). The retina was first perfused with oxygenated Ringer's solution (rate~ 3 ml/min) at room temperature for about 5 min, then a heating system was turned on to maintain the solution in the chamber in the 35-37 °C range. Recordings of RGC firing activity were done before and after a 20 min incubation of the retina in the photoswitch solution. Data was digitized at 10 kHz and stored on the computer hard drive using NI PCI-6071E DAQ board and custom software developed in LabView (National Instruments, Austin, TX). For light stimulation, a 450 or 470 nm blue LED driven by a custom-designed circuit under the control of a custom software developed in Matlab (MathWorks, Natick, MA) was used. Light intensity was controlled by modifying the LED duty cycle or using neutral density filters. The retina was stimulated from below the stage using an optical port and the 4x objective of the inverted microscope. Light intensities and stimulation timing accuracy were measured with a calibrated photodiode (OSI Optoelectronics, Boca Raton, FL). Light irradiances on the sample plane ranged from 0.43 to 75 mW/cm^2. A short pulse at the beginning of each stimulation series was used to trigger data acquisition, the duration and timing of light stimulation events were recorded alongside regular data on one of the unused channels. A custom Matlab code was used to retrieve, inspect and convert the data into 16-bit binary format compatible with Plexon Offline Sorter (Plexon Inc., Dallas, TX). In the Plexon Offline Sorter, data was high pass filtered at 200 Hz, spikes were detected using a 4 SD threshold, and separated into signals from individual cells using principal component analysis. The spikes with interspike interval of less than 1 ms were deleted. Spike sorting results were exported from Plexon back into Matlab for further analysis (generation of raster plots, calculation of firing rates and kinetics analysis).

Open field test. The open field test was performed as described previously [132] with minor modifications (Fig. 4.5A). Briefly, a plastic tub (dimensions l = 60 cm, w = 40 cm, h = 30 cm) was separated into a light compartment (l = 25 cm, w = 40cm, h = 30cm) with white walls and a dark compartment (l = 35 cm, w = 40 cm, h = 30 cm) with black walls. The light compartment was illuminated by a custom LED array (5x6 LEDs, 447.5 nm Rebel LED, Luxeon star, Brantford, Canada) centered over the compartment. The light intensity (7 mW/cm^2 or $1.6x10^{16}$ photons cm^{-2} s^{-1} at floor level) was homogenously distributed throughout the floor. The mice were able to move around the box through a

small opening (h = 5cm, w = 10cm) connecting the two compartments. Mice were brought into the testing room in their home cages, transferred into the testing box and allowed to habituate to the new environment with their littermates for 45 min. Mice were placed back in their home cage then tested individually. Mice were placed in the light compartment and were given a maximum of 3 min to discover that there is a second compartment. A 5 min trial began when they crossed into the dark compartment, and time spent in the light was recorded.

Mice that crossed the opening only once and stayed in the dark compartment for entire time were disqualified. Unlike wild type mice, we noticed that untreated *rd1* mice showed signs of fear (hiding in corners, freezing even in open spaces) in the new environment and did not move readily. We reasoned that this fear would mask any light aversion effect so we habituated the untreated *rd1* mice in the dark until they moved readily between compartments before testing. Mice injected >6 weeks earlier with AAV2/2 hsyn-LiGluR or AAV2/2(4YF) 4xgrm6-LiGluR were injected intravitreally with $MAG0_{460}$ and tested 2, 4, 6, 8 and 10 days later at a light intensity of 7 mW/cm^2. Permanent records were made using a video camera (GoproHero3).

Forced 2-choice water maze task. The water maze task was performed using the protocol described by Wong et al. [146] with minor modifications. A radial arm maze was modified into a forced two choice task by blocking two of the five arms of the maze (Fig. 4.5E) and adding a divider (dimensions: 25 cm x 25 cm) to separate the two potential 'escape arms'. Two custom built LED arrays (5x6 LEDs, 447.5 nm Rebel LED, Luxeon star, Brantford, Canada) were placed at the end of each "escape arm". The light intensities at the release site (2 mW/cm^2 or $4.4x10^{15}$ photons cm^{-2} s^{-1}) and at the divider (5 mW/cm^2 or $1.1x10^{16}$ photons cm^{-2} s^{-1}) were measured at the water level using a handheld power meter (Thorlabs Inc. Newton, NJ). The LED array that cued the escape platform was triggered with square pulses to flash at 2 Hz using a stimulus generator (Stanford Research Systems, Sunnyvale, CA).

The room was kept dark for the entire time of the experiment. Permanent records were made using a video camera (GoproHero3) positioned in the center above the maze. On the day before the start of an 8-day trial, mice were habituated to the maze. Mice were placed onto the platform for 1 min. Then they were released at increasing distances from the platform and finally they were released from the chute for 10 trials. The same was repeated with the platform on the opposite side. Additionally each day before the experiment, mice received a short habituation. They were placed onto the platform for 1 min on both sides and returned to the cages. For each trial, mice were removed from their cage, placed in a glass beaker (6 cm diameter) and then slowly (10-60 s) lowered into the water at the arm opposite of the divider. The mouse was given a maximum of 60 s to find the platform. Trials in which mice found the hidden platform without entering the alternative arm first were counted as correct trials. Trials in which mice explored the alternative arm first or took longer than 60 s to find the platform were counted as failed

trials. After the trial, mice were dried and placed into a warm chamber with a space heater and allowed to rest for at least 3 min before the next trial. All mice performed 10 trials per session with 2 sessions a day, with a total of 20 trials per mouse per day for 8 consecutive days. The platform and the flashing LED were moved between trials according to the following pattern: LRRLRLLRLR and RLLRLRRLRL on alternating days. Mice that received a $MAG0_{460}$ or sham (PBS) injection were allowed to rest for >24 h after to avoid masking effects from anesthesia.

Statistical analysis. The Students' t-test was used for statistical analysis of in-vivo mouse physiology. Paired t-tests were used for comparisons within the same group of mice before and after $MAG0_{460}$ treatment (Fig. 4.5C and F, Fig. S4.7). Multiple t-tests were corrected for type I errors using the Bonferroni correction.

Supplementary Note

The fast spontaneous *cis-to-trans* relaxation of LiGluR-MAG0$_{460}$ and the detection of changes in light intensity

The 1st generation MAG photoswitches [61,63,136,157] show bi-stable switching behavior on the experimental timescale (Fig. 4.1C, lower panel): UV light leads to a predominantly *cis* photo-stationary state that activates the receptors, but the thermal *cis*-to-*trans* relaxation of these photoswitches occurs on the tens of minutes timescale and consequently LiGluR-MAG0 stays activated in the dark for minutes [61], until it is turned off by green light, which shifts the photo-stationary state back to the *trans* configuration. As a consequence, the light intensity does not affect the steady-state photocurrent, which only depends on the wavelength. The light intensity only affects the speed of photo-activation and photo-deactivation [136].

The 2nd generation MAG photoswitch used in this study, MAG0$_{460}$, however, shows a fast thermal *cis*-to-*trans* relaxation, as LiGluR-MAG0$_{460}$ turns off in less than a second when the light is turned off (Fig. 4.1C, top panel) [60].This thermal relaxation occurs not only in the dark, but also competes with photoactivation by light and therefore significantly affects the photocurrent obtained at low and medium light intensities. We reasoned that this leads to two favorable properties, which we subsequently utilized in this study: i) The photocurrent reports on the light intensity over a wide dynamic range and ii) the system constantly resets itself, which allows to detect changes in the light intensity dynamically.

We characterized the photo-activation kinetics, deactivation kinetics and intensity- response properties of LiGluR-MAG0$_{460}$ in HEK cell voltage-clamp recordings at 22 - 24 ° C using different intensities of 445 nm light (Fig. 4.1D; Fig. S4.1A and B). Lowering the light intensity per area (irradiance) below 500 mW/cm^2 leads to a significant reduction of the steady-state photocurrent (Fig. 4.1D and Fig. S4.1A). As expected, a decrease in irradiance also decreases the apparent rate constant of photoactivation (Fig. S4.1A and B, closed symbols), however, the deactivation kinetics after turning the light off remains constant (Fig. S4.1A and B, open symbols). This deactivation due to thermal *cis*-to-*trans* relaxation shows biphasic behavior with a mean time constant t_{mean}= 0.7 s [60]. For the purpose of this study, the thermal relaxation was approximated by single exponential decays.

To quantitatively describe the LiGluR-MAG0$_{460}$ gating as a function of the irradiance (E_{light}), we developed a simple model that considers the transition between the inactive resting state (*trans*) and the activated state (*cis*):

$$\text{resting (}trans\text{)} \underset{k_{ct} \cdot E_{light} + k_{relax}}{\overset{k_{tc} \cdot E_{light}}{\rightleftharpoons}} \text{activated (}cis\text{)} \qquad \text{(Eq. 1)}$$

Light of a given wavelength affects both the forward (*trans*-to-*cis*) and backward (*cis*-to-*trans*) transition, yet to different extent (k_{tc} and k_{ct}). The speed of photo-isomerization further depends on the absorption of a photon, i.e. the irradiance. Consequently the units of k_{tc} and k_{ct} are chosen to be s^{-1} $(mW/cm^2)^{-1}$, whereas the thermal *cis*-to-*trans* relaxation is described by the first order rate constant k_{relax} (s^{-1}).

The kinetics of any changes in the two-state system (Eq. 1) are then given by the apparent rate constant k_{app}:

$$k_{app} = \left(k_{tc} + k_{ct}\right) \cdot E_{light} + k_{relax} \qquad \text{(Eq. 2a)}$$

In the dark Eq. 2a simplifies to:

$$k_{app} = k_{relax} \qquad \text{(Eq. 2b)}$$

The amplitude of the steady-state photocurrent is a function of the equilibrium constant K between the resting state and activated state, which according to Eq. 1 is given by:

$$K = \frac{k_{tc} \cdot E_{light}}{k_{ct} \cdot E_{light} + k_{relax}} \qquad \text{(Eq. 3a)}$$

The rel. photocurrent $A_{current}$ originating from the activated state is then:

$$A_{current} = \frac{K}{K+1} = \frac{k_{tc} \cdot E_{light}}{k_{tc} \cdot E_{light} + k_{ct} \cdot E_{light} + k_{relax}} \qquad \text{(Eq. 3b)}$$

Since the maximal current remains unknown the observed current is:

$$I = \frac{I_{max} \cdot k_{tc} \cdot E_{light}}{(k_{tc} + k_{ct}) \cdot E_{light} + k_{relax}} \qquad \text{(Eq. 3c)}$$

To test, whether this simplified model of the gating process describes our experiments, we performed a global fit using the apparent rate constants (Fig. S4.1B) and steady-state current (Fig. S4.1D) as a function of the irradiance, E_{light}. The results given by Eq. 2a and Eq. 3c are shown as solid lines in Fig. S1B and Fig. S1D, respectively, and demonstrate a good overall agreement with the experimental data. The combined data from three independent experiments yielded $(k_{ct}+k_{tc}) = 0.13$ s^{-1} $(mW/cm^2)^{-1}$ and $k_{relax} = 1.7$ s^{-1} at 445 nm and 22 - 24 °C. The dynamic range extends over more than two orders of magnitude from 2 to 200 mW/cm^2.

Another prediction of the fast thermal relaxation of LiGluR-MAG0$_{460}$ occurring on the hundreds of milliseconds timescale is that the photocurrent should directly follow intensity changes within the dynamic range. Indeed, stepwise changes of the light

intensity led to corresponding changes in the steady-state photocurrent (Fig. S4.1C). To further characterize the temporal resolution of the system, we compared sinusoidal intensity stimulation with different frequencies (Fig. S4.1D) to a fully activating, rectangular activation pulse. As expected from the *cis*-to-*trans* relaxation kinetics, low stimulation frequencies (0.5 Hz stimulation) allow for almost complete relaxation to the *trans* state, whereas deactivation remains partial at higher frequencies. Nevertheless, in this protocol dynamic changes can be faithfully detected up to 4 - 8 Hz. Similar properties are also expected for other fast relaxing photoswitches such as DENAQ and PhENAQ [102]. These soluble photoswitches, however, are likely to exhibit more complex intensity-response properties that also depend on the concentration of photoswitch molecules.

Supporting Figures

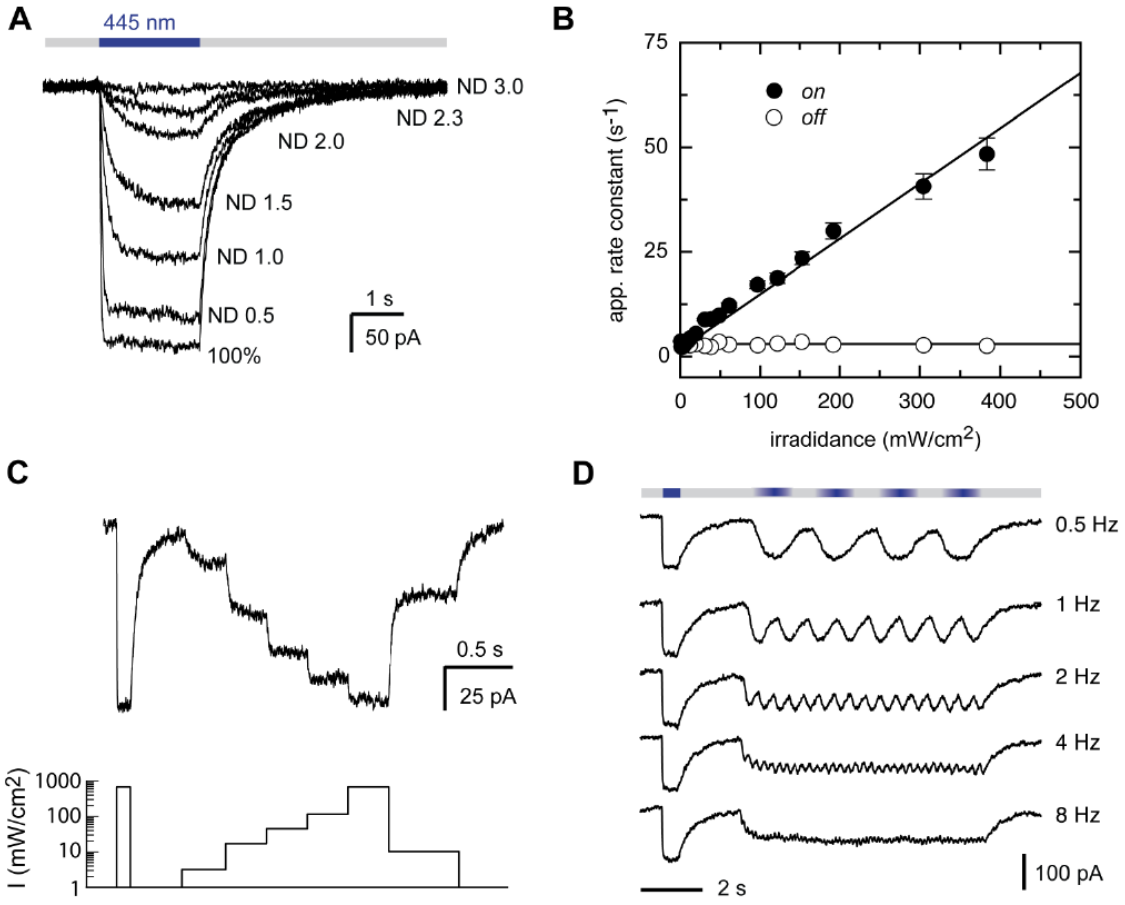

Figure S4.1. LiGluR-MAG0$_{460}$ currents in HEK cells scale with light intensity, can be dynamically regulated and follow moderate stimulation frequencies. (**A**-**D**) Intracellular recordings from HEK293-T cells transiently expressing LiGluR stimulated with a DG-4 light source (**A**) LiGLuR currents recorded from the same cell stimulated with light intensities ranging from 5 mW/cm^2 to 500 mW/cm^2. (**B**) On and off kinetics for LiGluR-MAG0$_{460}$ plotted against stimulating light intensity. (**C**) LiGluR-MAG0$_{460}$ currents assume discrete quantities and can precisely follow the stepwise modulation of light intensity of the stimulating light source. (**D**) LiGluR-MAG0$_{460}$ stimulation with sinusoidal modulated gratings. Responses between 0.5 and 8Hz are shown.

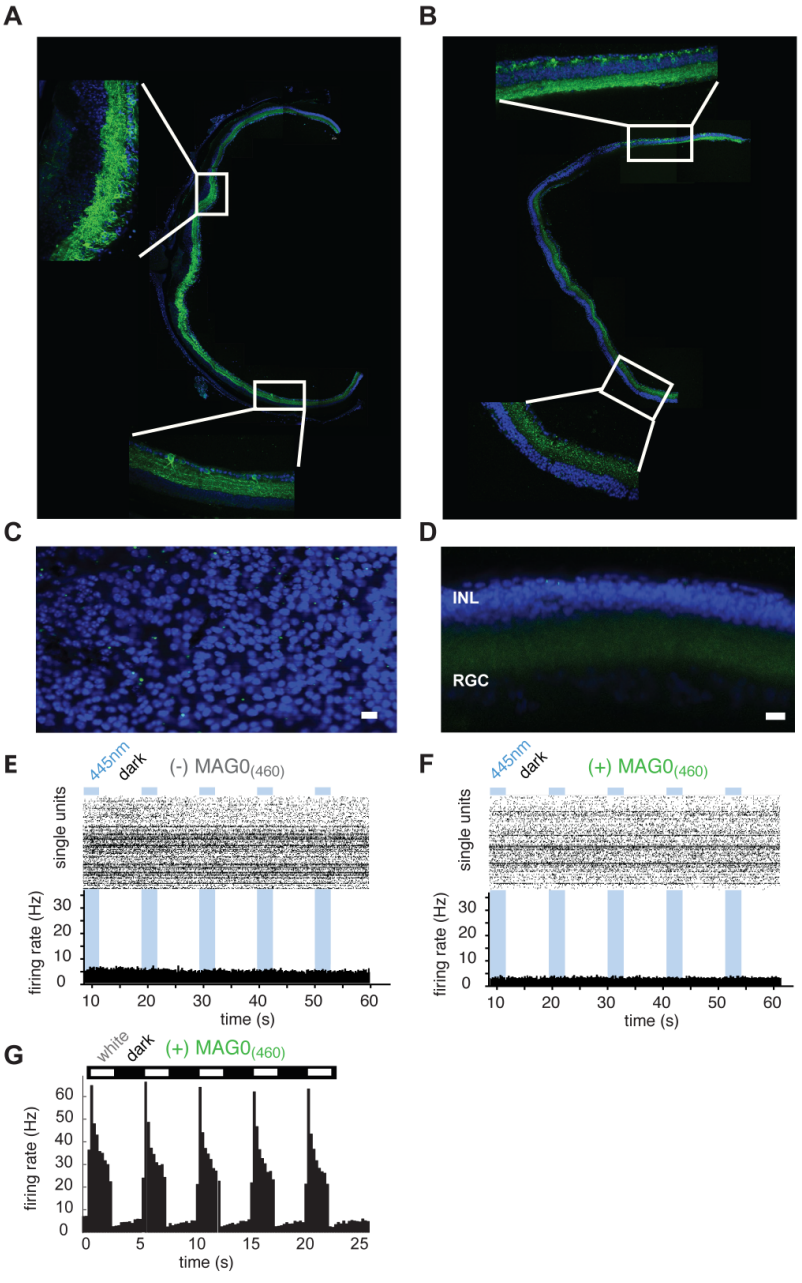

Figure S4.2. Control stains and control MEA recordings in *rd1* mice show specificity of LiGluR expression and function. (**A-D**) Retinas stained with a primary antibody against GluK2 and secondary antibodies conjugated with Alexa-594 (A) and Alexa-488 (B,C,D). (**A**) Confocal image of a cross-section of an *rd1*-RGC-LiGluR retina >4 weeks after intravitreal injection of AAV2-hsyn-LiGluR. A total of 8 images was taken at the same illumination settings with a 20x objective and combined post acquisition. The images were pseudo-colored in green to match panels (B,C,D); (**B**) Confocal image of a cross-section of an *rd1*-ON-BC-LiGluR retina >6 weeks after subretinal injection of AAV2(4YF)-4xgrm6-LiGluR. A total of 9 images was taken at the same illumination settings with a 20x objective and combined post acquisition. (**C,D**) Confocal images of a wholemount (C) and cross section (D) of a non-treated *rd1* mouse retina stained with the same reagents and under the same conditions as (A, B). Scale bar = 10 µm. (**E,F**) MEA recordings of an untreated *rd1* retina (> 3 months) in the absence (E) and presence (F) of $MAG0_{460}$. Top: light stimulation protocol with 5 repeats of 3 s blue light (445/50 nm) and 8 s dark. Middle: raster-plot with spikes for all RGCs (left: E, n=126 cells, right: F, n=103 cells), Bottom: peri-stimulus time histogram (PSTH) analyzed in 250 ms time bins. (**G**) MEA recording of *rd1* retina treated with LiGluR-$MAG0_{460}$ in RGCs stimulated with white light (polychromic unfiltered light from a mercury lamp, DG-4, Sutter instruments); PSTH showing response to 5 repeats of 5 s white light and 10 s dark with firing rates analyzed in 500 ms time bins (n=78 cells).

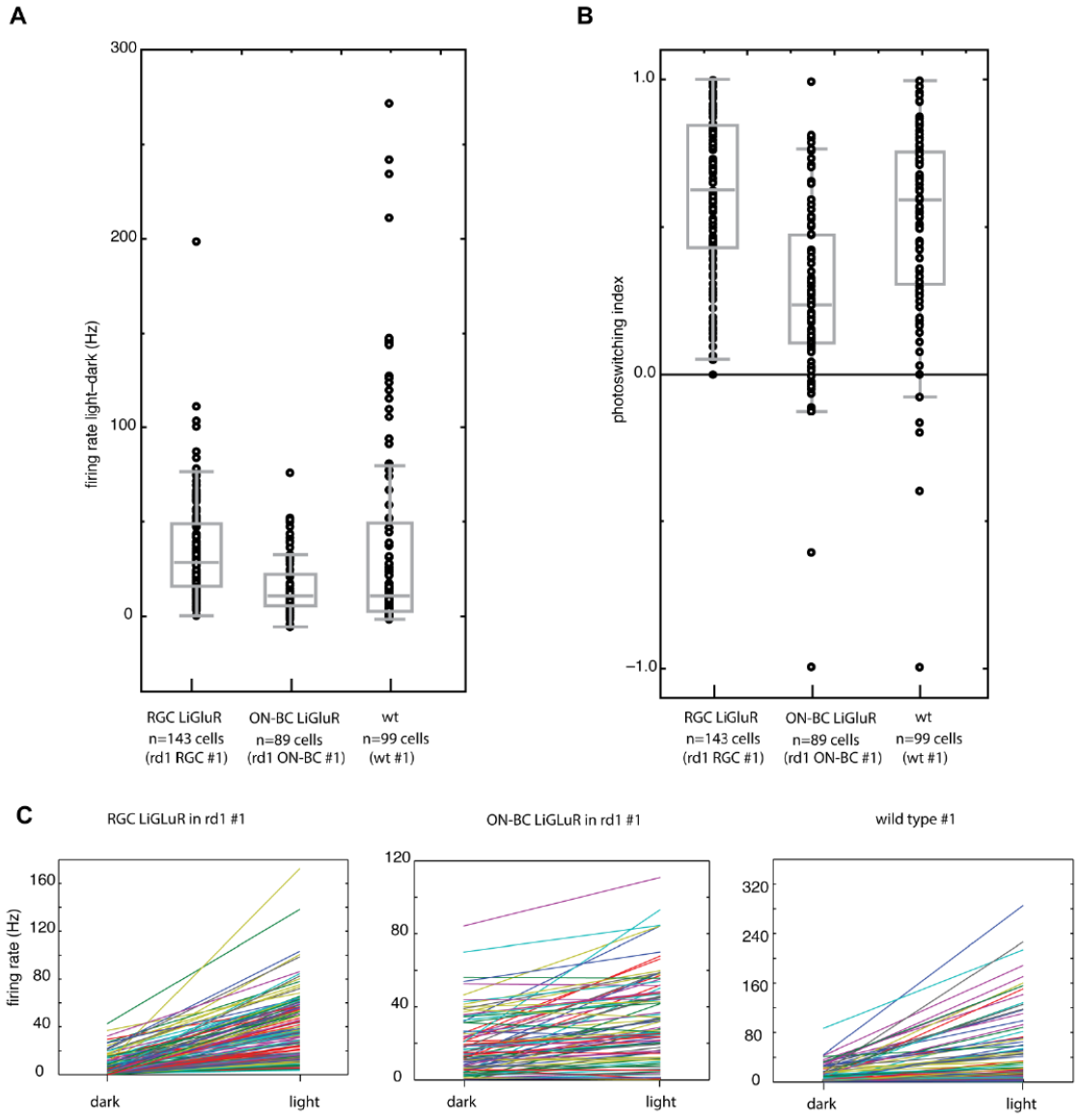

Figure S4.3. Cell to cell variability of the-LiGluR-MAG$_{460}$ system in *rd-1* mouse retinas. (**A-C**) MEA recordings of in *rd-1* mouse retinas treated with LiGluR-MAG0$_{460}$ or untreated wt mouse retinas. Light stimulation protocol was 5 repeats of 3 s blue light (445/50 nm) and 8 s dark. The light intensity was 24.7mW/cm^2 or 5.6x10^{16} photons cm^{-2} s^{-1}. (**A**) Variability of firing rate above baseline for the three conditions (RGC-LiGluR n=143 cells, ON BC LiGluR n=89 cells, wt n=99 cells). All cells from one recording are plotted in scatterplots with black circles and boxplots in grey in the background (mean, 1st and 3rd quartile are shown in the box). (**B**) Variability of photoswitching index ((firing rate light – firing rate dark) /(firing rate light + firing rate dark)) for the three conditions (RGC-LiGluR n=143 cells, ON BC LiGluR n=89 cells, wt n=99 cells). All cells from one recording are plotted in scatterplots with black circles and boxplots in grey in the background (mean, 1st and 3rd quartile are shown in the box). (**C**) Visual illustration of change in firing rate from dark to light for the three conditions (RGC-LiGluR n=143 cells, ON BC LiGluR n=89 cells, wt n=99 cells). Each cell is plotted in a different color.

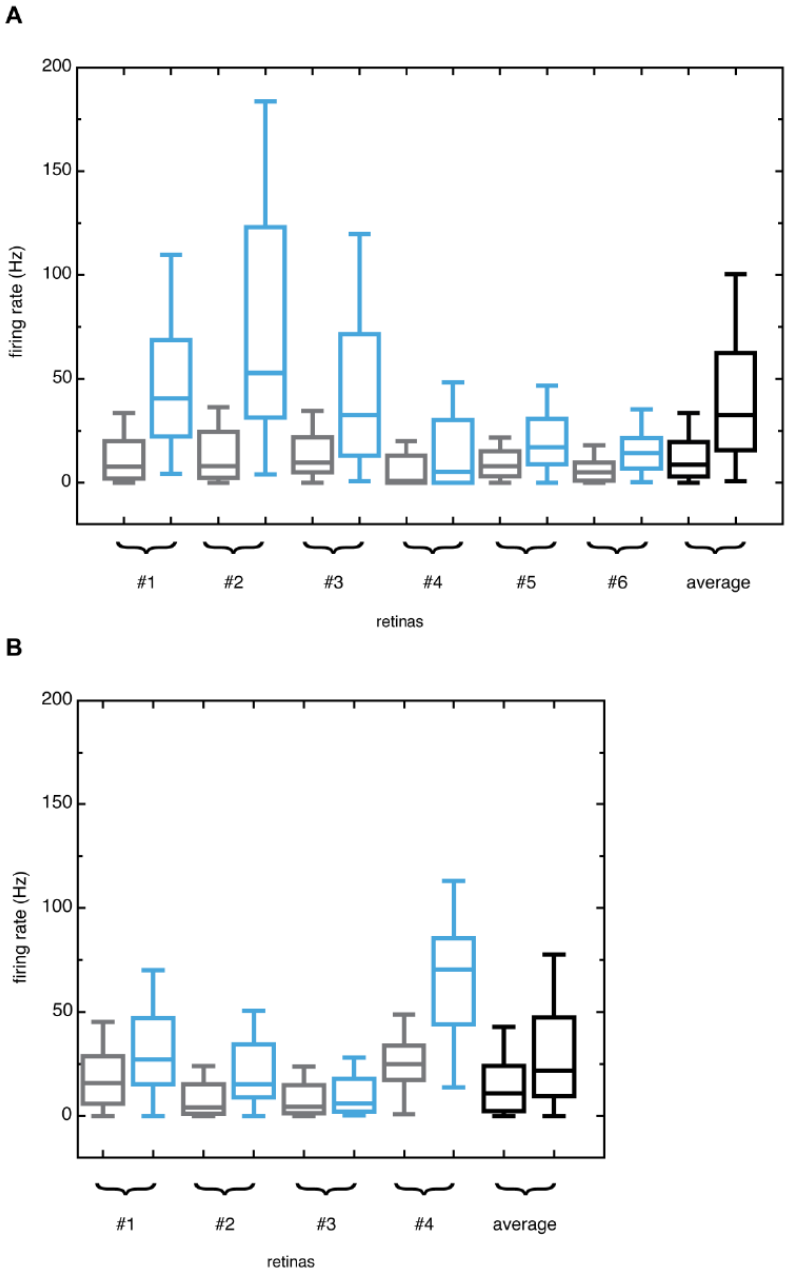

Figure S4.4. Retina to retina variability of the-LiGluR-MAG$_{460}$ system in *rd-1* mouse retinas. (**A-B**) MEA recordings of in *rd-1* mouse retinas treated with LiGluR-MAG0$_{460}$. Light stimulation protocol was 5 repeats of 3 s blue light (445/50 nm) and 8 s dark. The light intensity was 24.7mW/cm^2 or 5.6x10^{16} photons cm^{-2} s^{-1}. All plots show mean, 1st and 3rd quartile within the box (**A**) Variability of response for 6 RGC-LiGluR treated retinas. Boxplots show the firing rate before (grey) and during (blue) the light flash. A summary boxplot showing all cells (n=485) combined is shown in black. (**B**) Variability of response for 4 ON-BC-LiGluR treated retinas. Boxplots show firing rate before the flash (in grey) and during the light flash (blue). A summary boxplot showing all cells (n=322) combined is shown in black. Note: The statistics (number of cells, % responding cells, mean and median firing rates in light and dark, standard deviation, 1st and 3rd quartile, maximum and minimum and % excited and inhibited cells) for all retinas that were used for these plots are given in Table S1.

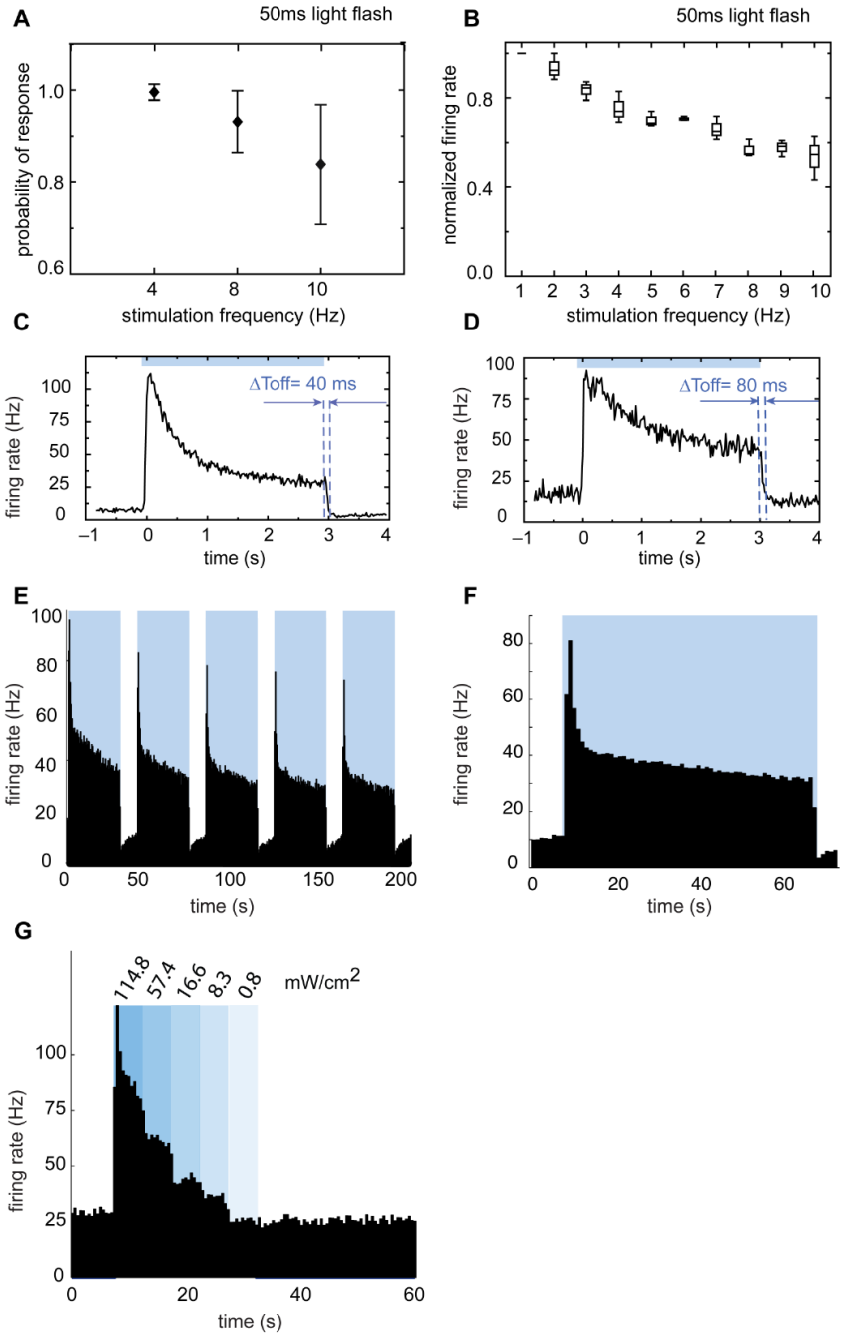

Figure S4.5. RGC-LiGluR driven response properties to short and extended stimulation pulses in *rd1* mouse retina (**A-G**) MEA recordings of retinas treated with LiGluR-MAG0$_{460}$ (**A**) Quantification of RGC output at moderate to high stimulation frequencies for 'strong responders' with PI>0.3. The probability of response given a 50 ms flash of light (470 nm) is plotted for 4 Hz, 8 Hz and 10 Hz stimulation (n=15 cells). The threshold for a response was set at 33% firing rate of initial flash response. Values are given as mean ± SD. (**B**) Quantification of firing rates in response to increased frequency of stimulating light for 'strong responders' with PI>0.3. The stimulating flash (470 nm) was 50 ms for all frequencies tested. The normalized peak firing rate (light – dark) is plotted for stimulating frequencies ranging from 1 - 10 Hz (n=3 retinas, 147 cells); (**C, D**) Responses to longer (3 s) stimulation showing the decay of peak response to steady state and the response inactivation time, ΔT_{off}, (C: RGC LiGluR n=240 cells; D: ON-BC LiGluR n=60 cells). (**E,F**) Steady state response for 5 single flashes (C) and for the 5-flash average (D). PSTH with 5 repeats of prolonged activation (30 s light, 10 s dark) with firing rates analyzed in 1 s time bins (n=64 cells); (**G**) RGC responses of 'strong responders' with PI>0.3 to stepwise modulation of light intensity in 5 s intervals. Light intensity was modulated ranging from 114.8 - 0.83 mW/cm^2. The average firing rate is plotted over time. Firing rates were analyzed in 500 ms time bins (n= 25 cells).

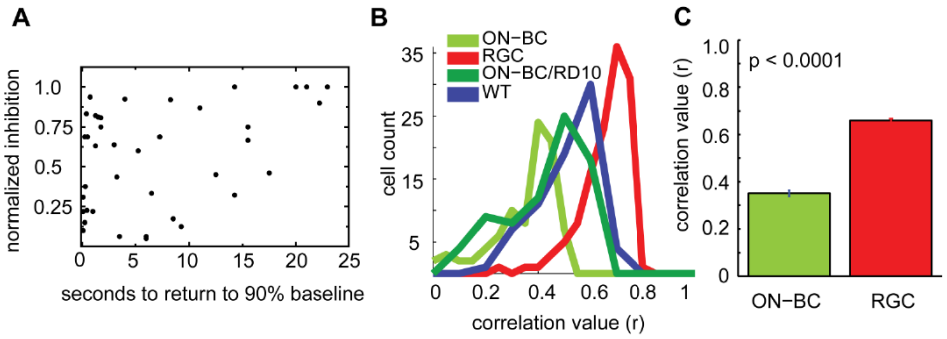

Figure S4.6. RGC response correlations differ when LiGluR is expressed in different target cells (RGCs vs. ON-BCs), but are similar within retinal degeneration mouse models having different *PDE6B* mutations (*rd1* vs. *rd10*). (**A**) Data obtained with MEA from *rd1*-ON-BC-LiGluR-MAG0$_{460}$. The normalized amount of inhibition of spontaneous firing rate in response to 1 s flash of light is plotted against time to 90% recovery for all inhibited cells that were analyzed (n=39 cells); (**B**) Quantification of correlation values (r) for correlation matrices in Fig. 4I-L (wt, blue n=72 cells; RGC-LiGluR in *rd1*, red, n=111 cells; ON-BC-LiGluR in *rd1*, green n=82 cells; ON-BC-LiGluR in *rd10*, n=76 cells). A pairwise t-test was used to test for significance. (**C**) Statistically significant (P< 0.0001) difference in RGC response between ON-BC and RGC expressing LiGluR-MAG0$_{460}$ *rd1* mice.

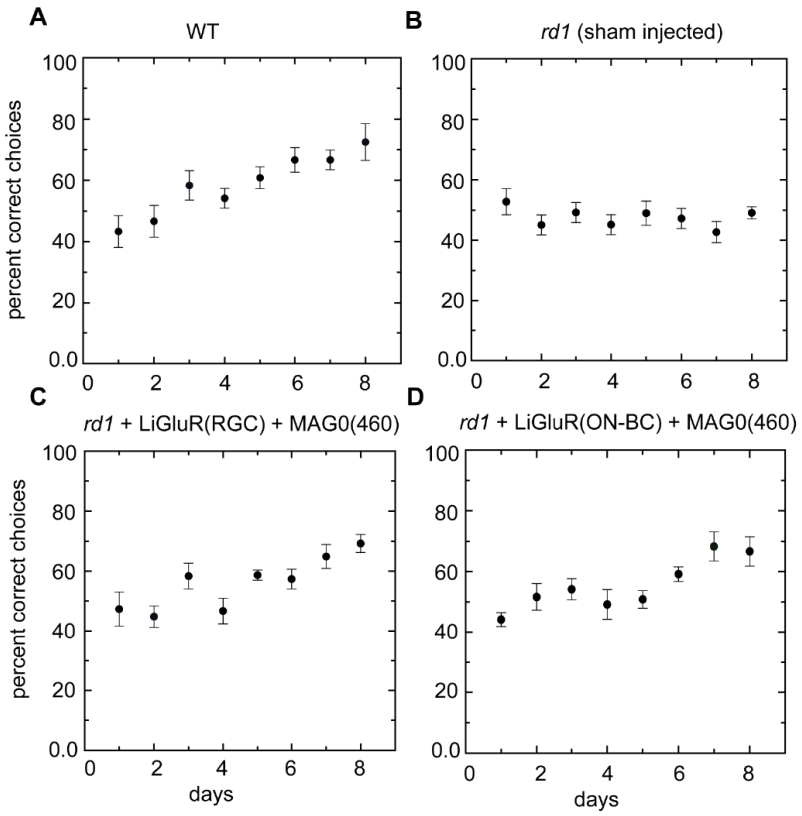

Figure S4.7. Water maze trials show a steady trend for wt and LiGluR-treated but not for sham (PBS) treated *rd1* mice. (**A**) wt mice (positive control) (n=6), (**B**) *rd1* mice sham injected intravitreally 24 h prior to day 1 (negative control) (n=8) and (**C,D**) *rd1* mice expressing LiGluR in (**C**) RGCs (n=9) or (**D**) ON-BCs (n=6) and injected intravitreally 24 h to day 1 with MAG0$_{460}$ (experimental). Values are given as mean ± SEM.

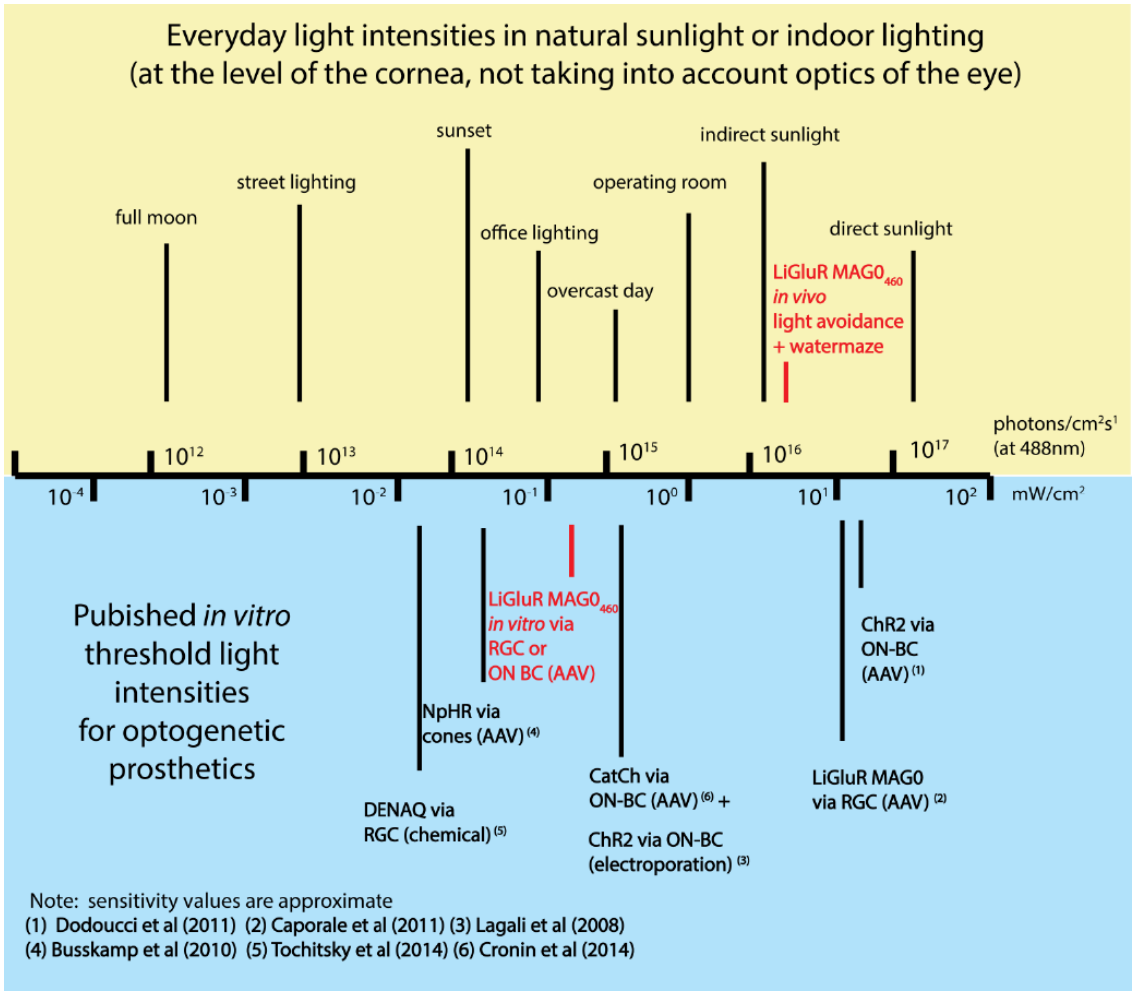

Figure S4.8. Overview of different visual prosthetics with published values for *in vitro* thresholds and approximated relationship to everyday light-intensities at the level of the cornea. Light intensities are given as mW/cm^2 and as photon flux in photons $cm^{-2}s^{-1}$ at 488nm. Top (yellow): radiometric measurements of everyday light intensities. Values were recorded with a handheld powermeter (Thorlabs) with the same settings that were used to measure light intensity for the *in vitro* experimental setup. These values do not take in to account the optics of the human eye, and thus represent light intensities at the level of the cornea and not the retina. Bottom (blue): published values for *in vitro* threshold sensitivities of recent optogenetic or optopharmacological vision restoration studies. The *in vitro* threshold for our LiGLuR-MAG_{460} system (Fig. 3A,B) in mouse is shown in red and was measured with the same settings of the power meter used for the upper part of the graph. The light intensity used for our in-vivo studies in mouse (Fig. 5) is also shown in red in the top part of the graph for reference. Note: values are approximate.

Table S1. Detailed description of *in vitro* MEA recordings from different retinas.													
Condition	**n cells** [a]	**Firing rate dark (Hz)** [b]		**Firing rate light (Hz)** [b]							**Responders** [c]	**PI> 0.1** [d]	**PI < 0.1** [d]
Retina		mean	median	mean	median	SD	1st quartile	3rd quartile	max	min			
RGC LiGluR													
rd1 #1	143	14.66	7.67	48.92	40.66	35.40	22.32	68.66	221.66	4.32	95%	95%	0%
rd1 #2	81	18.66	8.00	86.07	52.80	83.62	32.00	122.00	437.60	4.00	100%	100%	0%
rd1 #3	104	14.46	9.67	49.49	32.67	46.39	13.00	71.50	187.00	0.67	94%	94%	0%
rd1 #4	62	12.17	10.33	28.92	24.17	21.59	13.33	39.67	98.33	1.00	90%	90%	0%
rd1 #5	97	13.13	8.55	27.49	18.33	25.53	10.33	34.17	120.00	3.67	97%	97%	0%
rd1 #6	91	7.15	5.00	17.49	14.33	15.92	6.75	21.58	80.33	0.33	99%	99%	0%
RGC-LiGluR average[e] (n=485 cells)	**96.33**	**14.67**	**8.67**	**48.49**	**32.67**	**50.39**	**15.67**	**62.4**	**437.60**	**0.33**	**96%**	**96%**	**0%**
ON BC LiGLUR													
rd1 #1	89	15.80	5.90	32.69	27.20	23.44	15.30	47.00	110.90	0.00	85%	80%	6%
rd1 #2	116	11.66	4.17	26.69	15.32	29.42	9.00	34.50	170.00	0.00	97%	93%	3%
rd1 #3	59	8.64	4.40	10.18	6.10	10.00	2.15	17.85	47.40	0.30	61%	47%	14%
rd1 #4	58	27.56	24.90	67.64	70.35	33.06	44.00	85.40	218.10	3.20	98%	98%	0%
ON-BC-LiGluR average[e] (n=322 cells)	80.50	16.03	10.90	32.70	21.73	31.61	9.50	47.40	218.10	0.00	85%	80%	6%
ON BC LiGLUR													
rd10 #1	126	22.87	2.24	43.74	13.60	55.33	3.80	83.40	255.20	0.00	97%	92%	5%
No LiGluR													
wt #1	99	11.25	4.40	50.28	16.40	71.32	3.80	67.00	325.60	0.00	95%	90%	5%
wt #2	102	13.88	3.50	67.07	32.50	65.58	15.00	141.67	213.33	1.67	99%	99%	0%
wt all cell average[e] (n=201 cells)	**100.5**	**12.57**	**3.95**	**58.67**	**24.45**	**68.45**	**9.40**	**104.33**	**325.60**	**0**	**97%**	**94%**	**3%**

[a] Cells are defined by principal component analysis using spike sorting software (Plexon), see methods
[b] Firing rate dark = firing rate averaged over 3 s preceding light flash, Firing rate light = peak response during flash, see methods
[c] Responders are classified as having a photoswitching index (PI) of either >0.1 or <-0.1
[d] PI = Photoswitching index, defined as (Firing rate light – Firing rate dark) / (Firing rate light + Firing rate dark)
[e] Average over all cells per condition

Table S4.1 detailed description of the MEA recordings from different retinas.

Chapter 5 Optogenetic vision restoration using rhodopsin for enhanced sensitivity

This chapter was submitted to the journal Molecular Therapy for review with me as first author. This is current version at the time of writing (3/20/15)

Introduction

Most forms of inherited blindness result from photoreceptor cell death caused by mutations in photoreceptor cell specific genes. In many of these conditions, the second and third order retinal interneurons remain intact and electrically active [17,123,125,126], even after the retina has lost sensitivity to light due to loss of the photoreceptors, providing an opportunity for treatment. Tremendous progress has been made towards gene replacement therapy for certain retinal diseases [29,158,122]. Current gene therapy technology requires a specific vector for each gene defect, making clinical treatment very costly and creating a need for mutation independent approaches. One approach for late-stage retinal degeneration has recently been approved for human use and functions irrespective of the genetic cause of vision loss. It is based on electrical stimulation of the surviving neurons in the retina via implanted electrode arrays that receive input from a camera [11,127]. Spatial information about the surrounding environment is converted to electrical impulses, which in turn excite retinal neurons in proximity of the electrode. This has been shown to restore light sensitivity and low acuity vision to blind patients, but is costly, and current designs offer low resolution. Other proposed therapies impart light sensitivity to the surviving retinal interneurons using genetically-encoded light-gated proteins [32,33,35-37,46,132], photosensitive chemicals [133,134] or a combination of the two [34,52,64]. The microbial light-sensitive proteins channelrhodopsin (ChR2) and halorhodopsin (NpHr) have been targeted to cone photoreceptors that have lost their outer segments [33], ON-bipolar cells (ON-BCs) [35-37,46] and retinal ganglion cells (RGCs) [32], leading to successful restoration of basic visual functions in mouse models of blindness. Microbial opsins are relatively simple to work with and have important benefits – following the gene transfer to the target cell, the apo-protein is stably expressed [35] and the cell remains light sensitive without further additions due to bio-availability of the required chromophore 11-cis-retinal. In contrast, optochemical treatment utilizes synthetic azobenzene-based photoswitches designed to activate endogenous receptors [133,134] or engineered mammalian receptors and channels [34,52,64]. These synthetic photoswitches have a limited half-life and need to be re-supplied on a regular basis. All of these optogenetic and optochemical tools provide inadequate light sensitivity to function in normal daylight and avoid damage to residual photoreceptors by hardware-dependent intensification.

The operation of the optogenetic ion channels and pumps differs substantially from the rod and cone opsin GPCRs of wildtype photoreceptors. Only the GPCRs have integral signal amplification cascades in which a single photon can activate multiple G-proteins, leading to hydrolysis of hundreds to thousands of cGMP molecules that gate downstream cyclic nucleotide gated channels [58]. Attempting to increase light sensitivity by increasing the expression of the optogenetic sensor protein is problematic because of increased risk for cell toxicity [9] and immune response [9 159]. An elegant approach to circumvent these issues has been to use the native light-gated GPCR melanopsin from intrinsically photosensitive RGCs [132]. When targeted to all RGCs of *rd1* mice, melanopsin rescued retinal light responses and enabled innate and learned behavior at very dim light conditions [132]. Unfortunately, the slow (seconds) kinetics of melanopsin exclude it from practical use for vision of moving objects and visually-guided motility.

Here, we used another native opsin GPCR: rhodopsin. We expressed rhodopsin in ON-BCs, second order neurons, which receive synaptic input from photoreceptor cells. We chose to target ON-BCs [53,142] because they are located upstream in the retinal circuitry, do not exhibit significant remodeling until late stages of degeneration and because their normal mode of activation is by glutamate released from photoreceptors that acts on a GPCR, the metabotropic glutamate receptor mGluR6 [160]. Vertebrate rhodopsin delivered to ON-BCs by an AAV viral vector restored light responses to blind *rd1* mouse retinas, at light levels 2-3 orders of magnitude lower than required for ChR2 in ON-BCs. Enhanced light sensitivity was also seen *in vivo* in visually-evoked potentials (VEPs) recorded in primary visual cortex and in two visually-guided behaviors: an innate photo-phobic behavior, and a simple associative learning to discriminate moving from static stimuli. Taken together, we show that gene therapy with light-gated GPCRs presents a promising approach to developing a retinal prosthetic with increased sensitivity while avoiding complications associated with immunoreactivity.

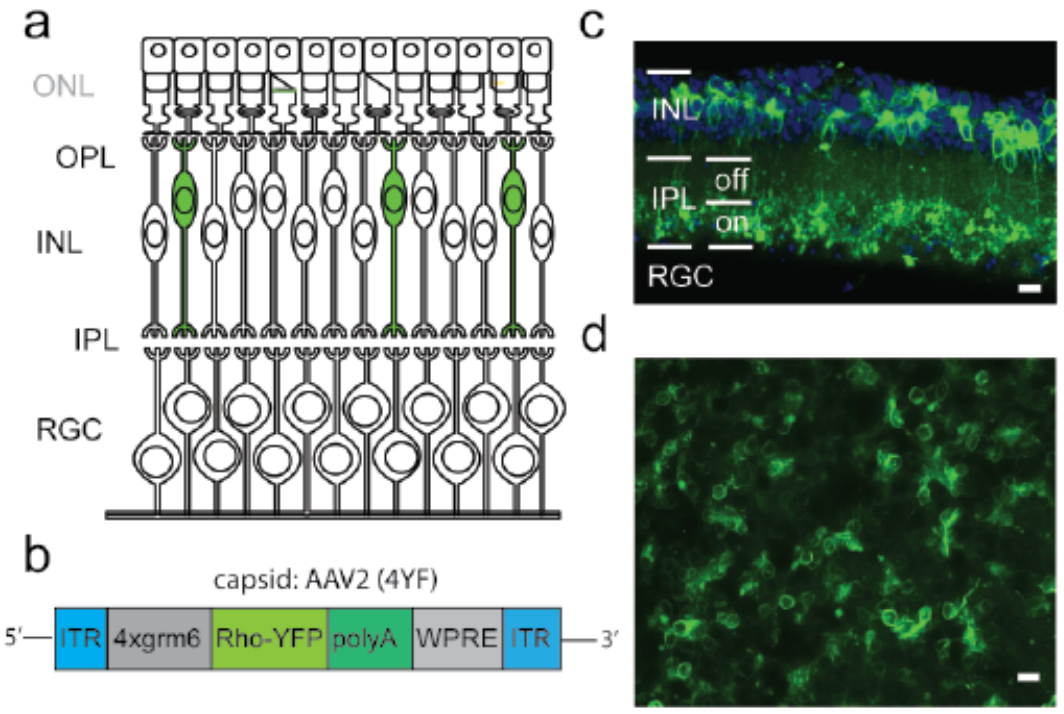

Figure 5.1. Rhodopsin can be expressed ectopically in ON-bipolar cells of the *rd1* mouse retina. **(a)** DNA expression cassette for the gene therapy vector. Rhodopsin is tagged (C-terminally) with yellow flourescent protein (YFP) and expression is driven by the metabotropic glutamate receptor 6 (4xgrm6) promoter. Promoter and rhodopsin-YFP sequences are flanked by inverted terminal repeat domains (ITR) and stabilized by a polyadenylation signal sequence (polyA) and a woodchuck hepatitis post-transcriptional regulatory element (WPRE). The cassette was packaged into the AAV2/2 (4YF) serotype. **(b)** Schematic of a degenerated *rd1* mouse retina with target cells (ON-BC) highlighted in green. ONL, outer nuclear layer. OPL, outer plexiform layer. INL, inner nuclear layer. IPL, inner plexiform layer with indication of on and off sublayers. RGC, retinal gangion cell layer. **(c, d)** Confocal images of section **(c)** or wholemount **(d)** of rhodopsin-YFP expression in ON-BCs of *rd1* mouse retina >6 weeks after intravitreal injection of AAV2/2(4YF)-4xgrm6-Rho-YFP (2 µl volume equal to $5x10^{11}$ viral genomes). Nuclei were stained with DAPI (blue). Scale bar =10 µm.

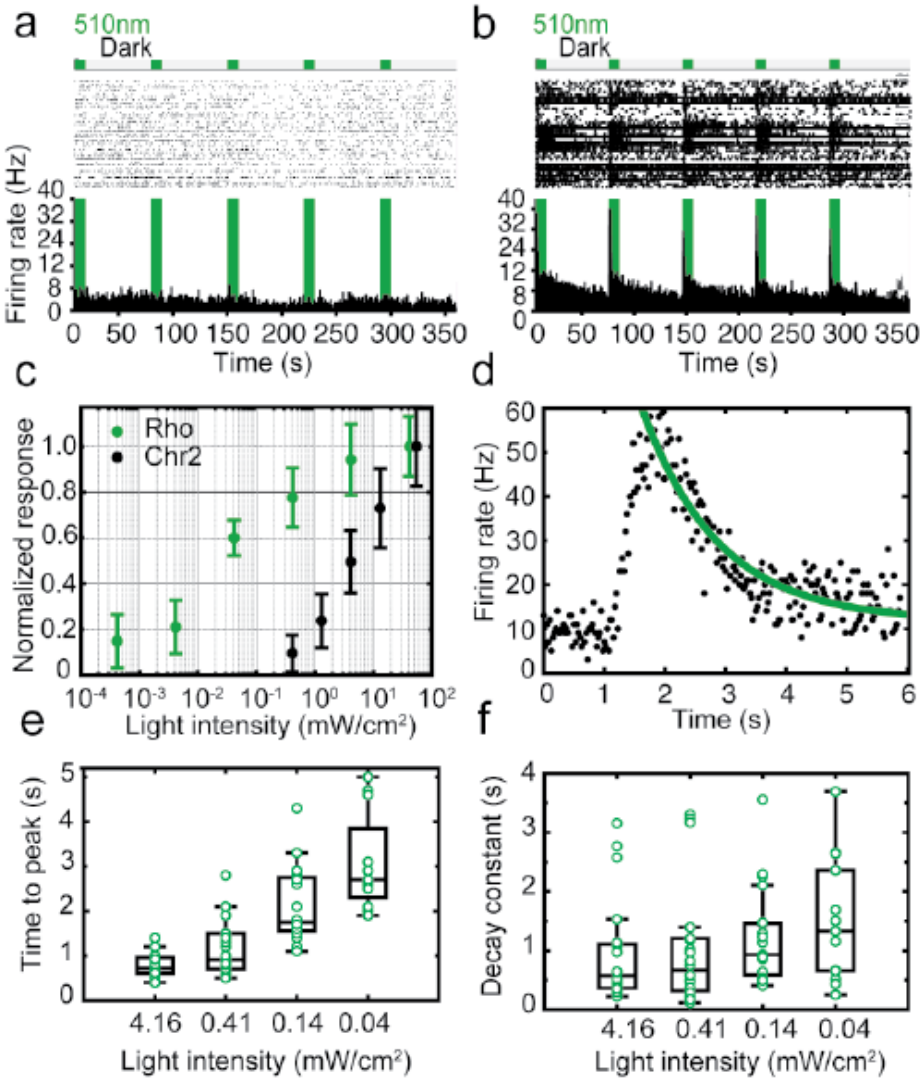

Figure 5.2. Rhodopsin expression in ON-BC restores light responses to retinal explants *in vitro*. **(a-f)** Data obtained by multi electrode array (MEA) recordings of retinal explants from *rd1* mice. **(a,b)** Representative rasterplots of *rd1* mice without **(a)** or with **(b)** expression of rhodopsin in ON-BCs. Top: light stimulation protocol 5x 10 s green light at 510/50nm and 60 s dark. Middle: raster plot with spikes for all light sensitive RGCs (A: n=36 cells, B: n=53 cells), Bottom: peri-stimulus time histogram (PSTH) with 250 ms bins. **(c)** Light sensitivity for ON-BC rhodopsin *rd1* (green circles) and ON-BC Chr2 *rd1* (black circles) at 3 s stimulation (rhodopsin n=20 cells, Chr2 n= 27 cells). Only the cells that responded to all 6 light steps were included in the plot. Firing rates are normalized and values are shown as means ± SEM. Light intensities on x-axis are given in mW/cm^2. **(d)** Kinetics for ON-BC rhodopsin *rd1*. The population averaged response (n=53 cells) from 3 s stimulation was plotted as a histogram (black circles) and the signal decay was exponentially fit (green). The time constant for the population peak response decay was 1.21 s. Time from light flash to peak was 850 ms. **(e,f)** Response kinetics for ON-BC rhodopsin *rd1* (n=20 cells) at 3 s stimulation with varying stimulating light intensities given as mW/cm^2. Only the cells that responded to all 4 light steps were included in the plot. **(e)** Time from flash to peak response and **(f)** peak response decay constants are shown as combined boxplot (in black showing mean, 1st and 3rd quartile) and scatterplot (green open circles).

Results

Rhodopsin can be expressed ectopically in ON-bipolar cells of the *rd1* mouse retina

We tested the functionality of rhodopsin for vision restoration in the *rd1* mouse in which retinal degeneration is caused by a mutation in the PDE-6-beta gene, resulting in rapid loss of rod photoreceptors, followed by progressive loss of cones, leading to blindness by postnatal day 90 [137]. We used an AAV viral vector and cell-specific promoter to drive expression of the rhodopsin protein in ON-BCs of the *rd1* mouse retina *in vivo*. Several groups have demonstrated successful targeting of ON-BCs in the mouse retina using a combination of different viral vectors and promoters [35,37,46,52]. ON-BCs are located in the middle layer of the retina between the RGC layer and the photoreceptor cell layer (Fig. 5.1a), making these cells difficult to access with viral vectors from either side of the retina. Modified virus variants have been developed with increased retinal penetration to access inner retinal neurons. Two recent studies used directed evolution to select for adeno-associated virus (AAV) variants with enhanced expression in photoreceptor cells [47] or ON-BCs [37,46] when injected in the vitreous. We chose a different strategy utilizing the quadruple tyrosine mutant AAV2/2(4YF) variant [45], which is protected from proteasome degradation, and thus leads to enhanced transduction of cells in the inner retina when injected intravitreally. We restricted expression to ON-BCs, using a cell-specific promoter construct 4xgrm6 [46], based on the mouse (mGluR6) promoter. To track rhodopsin expression, we added a yellow fluorescent protein tag to the C-terminal end of the rhodopsin protein [161]. The gene expression cassette 4xgrm6-Rho-YFP (Fig. 5.1b) was packaged into AAV2/2(4YF) and a volume of 2µl (10^{10} - 10^{11} viral particles) was injected intravitreally into retinas of 3-6 week old *rd1* mice. Expression was confirmed >6 weeks after injection by imaging retinal sections (Fig. 5.1c) and flat-mounted retinas (Fig. 5.1d). Flat-mounts showed strong pan-retinal rhodopsin expression and agarose sections confirmed ON-BC-specific expression, with fluorescently labeled processes terminating in the ON-sublayer of the inner plexiform layer (INL). For subsequent control experiments, we used the same promoter and vector combination (Fig. S5.1a) to target expression of the humanized enhanced (H134R) version of ChR2 to ON-BCs (Figs. S5.1b,c).

Rhodopsin expression in ON-BCs restores light responses to retinal explants *in vitro*

Strong rhodopsin expression in retinal ON-BCs prompted us to examine whether functional light responses were restored in retinal explants. We used a multi electrode array (MEA) to record the electrical activity of RGCs. Retinal explants from *rd1* mice (>3 months of age, n=4 mice total), which had been injected with AAV2(4YF) 4xgrm6-Rho-YFP *in vivo* 6-8 weeks earlier, were repeatedly stimulated with full field flashes of green light (13.0 mW/cm^2, 510/50 nm, 10 s light on, 60 s light off). We observed robust light-evoked spiking activity in rhodopsin treated retinas (Fig. 5.2b), whereas untreated,

age-matched control *rd1* retinas did not respond to the light stimulation (Fig. 5.2a). The recordings were performed without supply of exogenous 11-cis-retinal. To confirm that the light responses observed in treated mice were driven by expressed rhodopsin and not by intrinsic melanopsin, we added the glutamate receptor antagonist DNQX to the bath with the rationale that cell autonomous signaling in melanopsin-expressing intrinsically photosensitive RGCs would remain unperturbed, whereas signal transmission from ON-BCs to RGCs would be blocked. We found that DNQX caused loss of all fast light responses (Figs. S5.2a,b), indicating that the light responses originated upstream of the RGC layer and were independent of melanopsin. Rhodopsin elicited light responses in >50% of the electrodes of the MEA, with peak firing rates of approximately 40 Hz (Fig. 5.2b). The average firing rate in the light was similar for rhodopsin treated *rd1* retinas and wild type retinas (Fig. S5.2c). While the majority of RGCs (85%) showed an increase in firing rate upon exposure to a full field flash of light, consistent with an ON-response, a small fraction of RGCs (7%) showed a decrease in firing rate and had a negative photoswitching index (firing rate light – firing rate dark/ firing rate light + firing rate dark), consistent with OFF-responses found in other recent studies in which light sensitivity was restored with Chr2 expressed in ON-BCs [37,46] (Fig. S5.2d).

Since rhodopsin is a GPCR, we hypothesized that signal amplification may enhance light sensitivity of treated retinas compared to a light-gated ion channel. We stimulated rhodopsin treated retinas with a range of light intensities and found that rhodopsin was responsive over a wide range of intensities, spanning 5 log units from $4.2x10^{-4}$ mW/cm^2 to 41.6 mW/cm^2 (Fig. 5.2c). Robust light responses were obtained at the lowest light intensity tested ($4.2x10^{-4}$ mW/cm^2). By contrast, ChR2 expressed in the ON-BCs of *rd1* mice under the same conditions (same promoter, capsid, titer of virus, mode of injection and time of expression) showed a narrow intensity-response relationship, spanning only 2 log units, with a minimal light intensity requirement to elicit a response of 0.4 mW/cm^2 (Fig. 5.2c). The half-activation of rhodopsin-mediated signals occurred at ~200-fold lower light levels than for ChR2, a large improvement in sensitivity. We quantified the kinetics of rhodopsin-mediated signals. Fits of a single exponential function to the averaged response to a single flash of light (13.0 mW/cm^2, 510/50 nm, 3 s) of all of the responding cells (n=53 cells) in a single retinal region showed that the response decayed with a time-constant of ~1 second (Figs. 5.2d,f). Both the time to peak and the decay of the response were slower at lower intensities of the light flash (Figs. 5.2e,f; n=20 cells).

Rhodopsin activation in ON-BCs drives cortical responses *in vivo*

We tested if rhodopsin-mediated signals in ON-BCs would propagate from the retina to higher visual areas in the brain by *in vivo* recording of local field potentials in the visual cortex of wild type, control *rd1* and rhodopsin-treated *rd1* mice. Mice were stimulated with pulses (100-1000 ms) of light (455 nm, 15.0 mW/cm^2) delivered to the right eye using a fiber optic guide and VEPs were recorded in the contralateral primary visual

cortex using an extracellular electrode. Starting at the dura, we slowly lowered the electrode until the light response reached the maximal amplitude, typically at a depth of 300-400 μm. Responses were recorded and averaged over 10-30 stimuli. Sham injected *rd1* control mice (n=6) had no measurable VEPs (Fig. 5.3a, red trace), consistent with the lack of functional photoreceptors, as shown in other studies [34,36,37]. In contrast, *rd1* mice expressing rhodopsin in ON-BCs (n=8) (Fig. 5.3a, green trace, and 5.3b) had large VEPs, with amplitudes ~70% of that seen in wild type mice (n= 5) (Fig. 5.3b, black trace). We analyzed the kinetics of VEPs evoked by single 100 ms light pulses, given at long (60 seconds) intervals, and plotted the time to peak response and decay constant as a combined scatterplot and boxplot (n=9 rhodopsin-treated mice, n=7 wt mice) (Figs. 5.3c,d). VEPs from rhodopsin treated *rd1* mice had slower response kinetics (time to peak: 0.84 +/- 0.28 s, decay constant: 1.44 +/- 0.29 s) when compared to wt mice (time to peak: 0.07 +/- 0.02 s, decay constant: 0.02 +/- $3x10^{-3}$ s) and these responses were more variable. Importantly, we found that light flashes in rhodopsin treated *rd1* mice reliably triggered stable responses over dozens of stimuli presented to the same animal over a period of 1 hour of recording (Fig. 5.3e). In order to determine if the low light intensities that we intended to use for subsequent mouse behavior would elicit robust responses *in vivo*, we recorded cortical responses from ON-BC rhodopsin treated *rd1* mice (n=3) at low (0.1 mW/cm^2) and high (1.5 mW/cm^2) light intensities. Fig. S5.2e shows that stimulation with low light levels elicited robust responses, with peak amplitudes approaching 50% of the response of high light stimulation, confirming that the low light levels can sufficiently activate rhodopsin *in vivo*.

Rhodopsin expression restores innate light avoidance and enables learned visually-guided behavior in *rd1* mice

Having established that rhodopsin expression in ON-BCs of *rd1* mice restored light responses to retinal explants *in vitro* and elicited cortical responses *in vivo*, we asked whether our treatment would also enable visually-guided behavior. To answer this question, we initially tested rhodopsin treated *rd1* mice for light avoidance, a simple and robust behavior that is lost in *rd1* mice following the death of rod and cone photoreceptors [52,132]. Mice were habituated to a light / dark box (Fig. 5.4a) for 45 min together with their littermates and then tested for place preference individually in 5 min trials. The chamber was illuminated by a custom built LED array centered above the light side of the compartment (5 x 6 LED array, 445 nm, 0.1-0.2 mW/cm^2 at floor level). The time spent in the light and dark compartments was recorded on video and the percent time spent in the dark was calculated. Control mice (sham treated *rd1* mice, n=10) showed no preference for either compartment, as expected, whereas *rd1* mice expressing rhodopsin in ON-BCs (n=16) displayed a strong, significantly enhanced light avoidance, which was indistinguishable from that of sham-injected wild type animals (sham treated, n=7) (Fig. 5.4b).

Next, we tested if rhodopsin treated mice would overcome their innate light aversion by learning to associate light with a reward. We used a Y-maze variation of the Morris water maze (Fig. 5.4c) and trained mice to find a submerged, hidden escape platform that was cued by uniform (non-patterned) light, while the arm lacking the platform was dark [132,146]. Illumination in the arm containing the platform was produced by our 5 x 6 LED array (445 nm), which delivered 0.1 mW/cm^2 at the start of the divider, and 1 mW/cm^2 at the platform (Fig. 5.4c). Mice were habituated to the maze for 2 days prior to training (see Methods) and then subjected to 20 trials per day for 8 consecutive days. Their behavior was recorded on video and the performance was subsequently analyzed. Trials in which the mouse swam to the platform at the end of the illuminated arm of the maze without entering the dark arm were categorized as successes. Trials in which the mouse explored the dark arm first or took longer than 60 s to reach the platform were scored as failures. As in previous work [132,146], mice were considered to have learned the task when the performance was equal or above 70% correct choices. Control mice (sham treated *rd1* mice, n=6) did not improve their performance over the course of the experiment, in agreement with earlier studies[132,146] (but see: [162]). R*d1* mice that expressed rhodopsin in ON-BCs (n=6) showed improvement after 4 days and reached the 70% learning threshold after 6 days of training (Fig. 5.4d, green pound sign). Treated mice performed significantly better than controls on day 8 (Fig. 5.4d). Wild type mice (sham treated, n=7) improved after day 1 and had learned the task by day 4 (Fig. 5.4d, black pound sign).

Finding that rhodopsin expression in ON-BCs enabled *rd1* mice to distinguish light from dark, we next tested their ability to recognize and distinguish between distinct light patterns (moving vs. static spatial patterns) in the context of the visually cued fear-conditioning paradigm. In this paradigm, mice learn to associate electric foot shocks with light cues. We followed the protocol described by Tochitsky et al. [133] with slight modifications. Mice were habituated to the chamber on day 1, conditioned on day 2 and tested for memory recall on day 3 (Fig. 5.4e). Constant illumination of the chamber was provided by a static light pattern, consisting of a vertical bar that was generated by illumination of a single vertical row in a 5 x 6 LED array (0.1 mW/cm^2). We cued the foot shocks by switching from this static pattern to a dynamic pattern in which the single vertical row progressed horizontally at a speed that completed a cycle in 0.6 seconds (1.66 Hz refresh rate). The static and moving bars had equal luminescence. During the conditioning phase, a 10 s presentation of the dynamic pattern (blue stripes in Fig. 5.4e) was paired with short 2 s foot shocks (indicated by flash icons in Fig. 5.4e). For memory recall, the same pattern of lights was presented without the shocks. The mice were filmed during the recall period and freezing behavior was scored using FreezeFrame software (Coulbourne Instruments, PA). For the unpaired condition, mice were presented with the same number of moving patterns and shocks presented in a random sequence. We tested sham injected *rd1* control mice, rhodopsin treated mice and wt mice and subdivided each into two groups, one which received the paired stimulation and the other which received the unpaired stimulation. The videos taken during recall were analyzed and percent freezing above baseline (percent freezing after - before light cue) was plotted. Sham treated *rd1* mice (n=6 per group) showed freezing behavior to the cue but it was not

significantly different between paired and unpaired conditions (Fig. 5.4f). Rhodopsin treated *rd1* mice (n=8 per group), however, displayed robust freezing behavior in response to the moving pattern (Fig. 5.4g), similar to the level seen in wt mice (n=6 per group) (Fig. 5.4h).

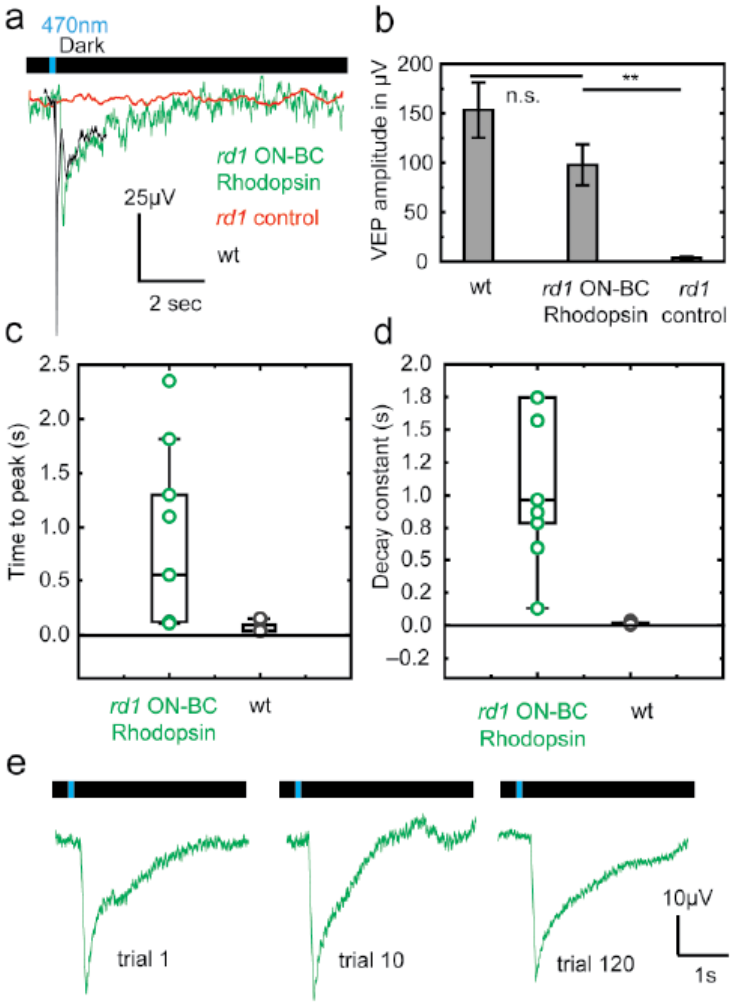

Figure 5.3. Rhodopsin activation in ON-BCs of *rd1* mice drives cortical responses *in vivo*. **(a)** Representative VEP traces from wild type (black), *rd1* control (red) and ON-BC rhodopsin *rd1* mice in (green). Traces are averages of 15 sweeps in response to 100 ms flash of blue light (LED, 455 nm, 15 mW/cm^2). **(b)** Quantification of VEP peak amplitudes in response to 100 ms light pulse for wild type mice (n=5), ON-BC rhodopsin *rd1* (n=9) and *rd1* control mice (n=6). Data are means ± SEM. **P<0.005, paired student's t-test. **(c,d)** Response kinetics for ON-BC rhodopsin *rd1* mice (n=9) and wt mice (n=7) with 100 ms stimulation at 455 nm. **(c)** Time from flash to peak response and **(d)** peak response decay constants are shown as combined boxplot (in black with mean, 1st and 3rd quartile) and scatterplot (rhodopsin with green open circles, wt with black open circles). **(e)** Repeatability of VEP response over time in ON-BC rhodopsin *rd1* mice. Shown are three traces of the same animal in response to 100 ms stimulation with 20 s ISI taken at different time points (trials 1, 10, 120).

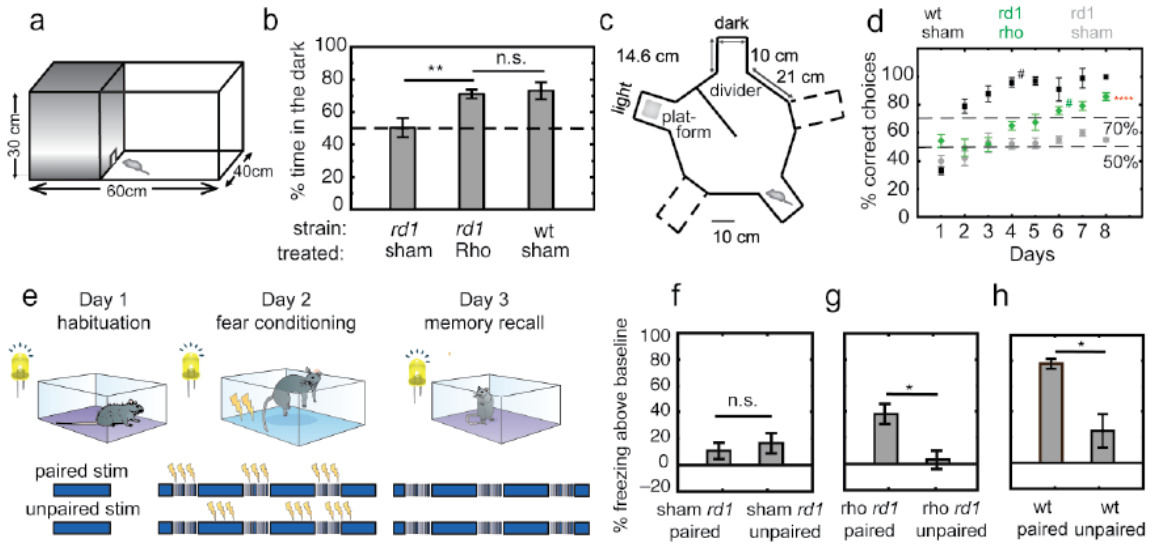

Figure 5.4. Rhodopsin expression restores innate light avoidance and enables learned visually guided behavior in *rd1* mice. **(a)** Schematic of the light/dark box. **(b)** Quantification of light/dark box test. Percent time spent in the dark compartment is plotted for *rd1* control (n=10), ON-BC rhodopsin *rd1* (n=16) and wild type mice (n=7). Data are means ± SEM. **P<0.005 (445 nm, 0.1-0.2 mW/cm^2). **(c,d)** Forced 2-choice associative learning task using a modified radial arm maze. **(c)** Schematic of the maze. **(d)** Performance of mice in y-maze over the course of 8 days. Percent correct choices are plotted for control *rd1* mice (grey, n=6), ON-BC rhodopsin *rd1* (green, n=6), and wild type mice (black, n=7). The dashed line at 50% indicates chance level while the 70% line indicates the threshold for pass (above) vs. fail (below). # indicates the day at which all animals of one group have performed > 70% correct choices and thus learned the task. Data are means ± SEM. Statistics done on the performance of rhodopsin treated *rd1* mice and sham treated *rd1* control mice on day 8 show ****P<0.00005 (445 nm, 100 µW/cm^2 at the divider, 1 mW/cm^2 at the platform). **(e)** Schematic for fear conditioning experiment. The blue bar represents the light stimulation (solid blue = non-patterned light, striped blue = spatial patterns) and flash icons represent 2 s footshocks. The paired paradigm is shown above, the unpaired shown below. **(f,g,h)** Quantification of fear response using spatially patterned stimulation. Percent freezing above baseline is shown for paired and unpaired paradigms for control *rd1* mice (n=6 paired, n=6 unpaired) **(f)**, ON-BC rhodopsin *rd1* (n=8 paired, n=8 unpaired) **(g)** and wild type mice (n=6 paired, n=6 unpaired) **(h)**. Data are means ± SEM. *P<0. 05 (light intensity at the floor level 0.1-0.2 mW/cm^2).

Discussion

Gene therapy approaches to treat retinal diseases have experienced a tremendous expansion in recent years, with ongoing clinical trials for several retinal dystrophies, including Leber congenital amaurosis type 2, Usher syndrome type 1B, Stargardt's disease neovascular AMD and choroideremia [163], all of which fall under the category of gene replacement or augmentation therapies. Optogenetic gene therapies are still in the process of testing and optimization in animal models of human blindness. Before moving to the clinic, major challenges have to be addressed and overcome.

In this study, we solved a major challenge of optogenetic gene therapy for blindness by introducing a native opsin of the mammalian retina, the light-gated GPCR rhodopsin, as an optogenetic actuator, which we found to provide orders of magnitude of enhancement in light sensitivity over the microbial opsin channelrhodopsin. We delivered rhodopsin to blind mice via intravitreal injection of a viral vector containing a cell-specific promoter and showed efficient, cell-specific expression in ON-BCs. We demonstrated that retinal explants expressing rhodopsin in ON-BCs respond to extremely low light intensities with moderately fast kinetics. *In vivo* cortical recordings also showed high sensitivity to light and were reproducible over extended periods of time, suggesting sufficient retinal recycling. Finally, we found that delivery of the rhodopsin gene to ON-BCs both restored innate light avoidance and enabled learned behavior that depended on mice distinguishing between light and dark or between static and moving spatial light patterns.

Several recent studies [35-37,46] have focused on ON-BCs as retinal gene therapy targets. ON-BCs are appealing target neurons, since they are upstream in the retinal circuitry, providing an opportunity to preserve some aspects of retinal processing [33,142]. Depolarization of ON-BCs with optogenetic actuators can generate both ON and OFF responses in downstream RGCs, reminiscent of the wild type retinal circuitry. Importantly for our study, ON-BCs have a GPCR-mediated signal transduction pathway that is triggered by glutamate, released by photoreceptor cells, acting on the ON-BC metabotropic glutamate receptor, mGluR6, and its apparent downstream effector, the TrpM1 channel [160]. Our hope was that rhodopsin would operate as a more sensitive optogenetic actuator than prior optogenetic treatments [32,34-36,64,134], which require very high light intensities, intensities that are potentially toxic to any remaining photoreceptors and other retinal cells [164]. Our intensity-response curves from *rd1* mice expressing rhodopsin in ON-BCs recorded *in vitro* showed strikingly high light sensitivity. Recent studies by other groups have reported a wide range of threshold light intensities needed to drive a response in retinas of *rd1* mice expressing ChR2 in ON-BCs [35 46 37]. These values could not be readily compared to our results with rhodopsin due to differences in light delivery, ChR2 variant, viral vector, cell-specific promoter and functional measurement. We therefore compared rhodopsin to one of the most widely used enhanced ChR2 variants, H134R, and did so under identical conditions of promoter, viral construct,

intravitreal viral delivery, light exposure and outcome measure. Under these identical conditions, using the most easily quantified MEA measurements, the lowest tested light intensities that evoked reliable responses in rhodopsin expressing retinas was 1000-fold lower than the threshold intensity required to elicit a response in ChR2 expressing retinas. It is important to note that the minimal intensity that was tested with rhodopsin elicited robust responses (18% normalized firing rate), suggesting an even lower threshold and larger advantage over ChR2.

It is important to consider that rhodopsin responded to a very broad range of intensities, spanning ~5 log units, whereas ChR2 had a narrow response range of ~2 log units. Wild type retinas also respond within a range of ~2 log units, but their sensitivity is adjusted by adaptation. Late stage retinal degeneration patients, who have few or no surviving photoreceptors may have lost much of their light adaptation, making a wide response range of the optogenetic actuator to luminance desirable, although it could mean a compromised detection of contrast.

In vivo measurements of light sensitivity in *rd1* mice expressing rhodopsin in ON-BCs also showed very high sensitivity Visually-evoked activity in primary visual cortex was evoked by dim light flashes and visually-guided behavior experiments were successfully performed at very dim light levels (0.1-0.2 mW/cm^2). The behavioral light intensity was measured using VEP in the primary visual cortex to ensure that the *in vivo* response was sufficient for driving complex behavior (Fig. S5.2e). A quantitative comparison of *in vitro* and *in vivo* sensitivity is not possible due to lens optics, differences in light sources, cell populations and experimental setup, but all the experiments described here support the notion that GPCRs generate substantially greater light sensitivity when compared to single ion channels.

Typically there is a tradeoff between speed and sensitivity of optogenetic actuators, whereby the more sensitive systems function at slower rates. In the case of ion channels (e.g. channelrhodopsin or halorhodopsin), the light sensor (opsin) and the effector (channel) are the same molecule, whereas GPCR cascades separate the sensor (opsin) and the effector (channel) functions. This separation allows for adaptation and regulation of the circuit, but the additional components and their individual kinetics are additive, resulting in a slower overall signal transduction mechanism. In addition, the proteins and processes evolved to rapidly terminate the light response in rod photoreceptors (rhodopsin kinase and arrestin, [59]) are not found in ON-BCs, significantly slowing down the return from the light activated to the dark adapted state. We characterized the kinetics of the rhodopsin-mediated signal *in vitro* and *in vivo* and found average decay constants ranging between 1.2 s (Fig. 5.2d) and 0.97 s (Fig. 5.3d). With varying stimulating light intensities, however, the kinetics shifted, and both time to reach peak as well as the time to reach baseline increased with decreasing light intensities (Figs. 5.2e,f). The notion that on kinetics should be a function of light intensity is intuitive, whereas the mechanism for light dependent decay is more surprising. Cortical measurements *in vivo* (Figs. 5.3c,d) matched closely with those *in vitro* and confirmed

that both on and off kinetics were in the 1-3 second range for moderate light intensities and in the sub-second range for high light intensities. This is a great improvement over previous studies using melanopsin [132]. Recent work using cone opsins has indicated that they may be inherently faster [165], providing a potential strategy to further improve kinetics.

To test if rhodopsin treatment could provide useful visual information for mice, we tested their ability to perform visually guided behavior tasks. We found that rhodopsin expression restored innate light avoidance in the open field test. However, in a subsequent experiment, we found that treated mice could also learn to overcome this aversion and associate light with reward using a Y-maze task. Importantly a visual prosthetic should allow basic forms of spatial and temporal pattern recognition. To test spatial pattern recognition, we conditioned mice to associate a marching bar of LEDs with electric foot shocks and distinguish this stimulus from an intensity matched static decoy stimulus (still LED bar). We tested the ability of mice to recall this association and were able to demonstrate that rhodopsin expression in ON-BC enabled mice to detect and distinguish dynamic light stimuli from static decoy stimuli. While we have not yet tested temporal pattern recognition, our kinetics analysis (Figs. 5.2d-f and Fig. 5.3g) predicts that treated mice can resolve frequencies of ~1Hz.

Rhodopsin-mediated signals showed a high amount of variability between cells and retinas *in vitro and in vivo* (Figs. 5.2e,f and Figs. 5.3c,d), but are consistent in their response characteristics over time. Cortical VEP responses over >120 trials (Fig. 5.3e) indicated stable functioning of the GPCR and the visual retinoid cycle. Despite trial-to-trial stability, the response properties covered a wide range (time to peak and decay constant Figs. 5.3c,d), indicating that other factors might play a role in variability. The non-linearity introduced by the GPCR, saturation of G-protein levels within the cell, differential expression of G-protein gated channels for different subsets of ON-BCs as well as the degeneration state of the retina are all likely to contribute to the observed variability. In wild type photoreceptors, light triggers rhodopsin to activate the G-protein transducin (G_T), which in turn leads to closure of cyclic GMP-gated channels and subsequently hyperpolorizes the cell [58]. Exogenously-expressed rhodopsin is known to be promiscuous and can activate $G_{i/o}$ in the absence of G_T [166] and is therefore functional in many different contexts such as HEK cells and C-elegans [166,167]. Surprisingly, in our experiments, rhodopsin activation lead to light-induced depolarization of ON-BCs. Rhodopsin's ability to "hijack" preexisting messaging systems and function at low light levels via amplification may be more widely applicable. Future work will be needed to determine the identity of the signaling mechanism that leads to this light dependent depolarization.

In summary, we have presented an optogenetic approach for a retinal prosthesis that is: a) native to the retina, b) far more sensitive than other optogenetic treatments, and c) potentially safer for human applications since it circumvents the need for microbially derived proteins.

Materials and Methods

Animals. University of California Animal Care and Use Committee approved all mouse experiments. Wt mice (C57Bl/6J) and *rd1* mice (C3H) were purchased from Jackson Laboratory (Bar Harbor, ME) and injected with rAAV between p30-p60 and used for *in vivo* and *in vitro* experiments between p90-p160. All mice were housed on a 12-hour light dark cycle with food and water *ad libitum*.

Packaging and Injection of rAAV. Adeno-associated viruses were made using via standard procedures [154]. The Rho construct with the rAAV2/2(4YF) capsid carried the vertebrate rhodopsin transgene tagged C-terminally [161] with yellow fluorescent protein and controlled control by the 4x repeat of the metabotropic glutamate receptor 6 promoter (4xgrm6). The Chr2 construct was also packed with the rAAV2/2(4YF) capsid carrying the humanized version of the Chr2 (H134R) transgene tagged C-terminally with yellow fluorescent protein under the control of the 4xgrm6 promoter. The titer of AAVs was determined via qPCR relative to inverted repeat domains (ITR) standard. Titers for these viruses ranged between 1 x 10^{13} vg/ml and 1 x 10^{14} vg/ml. Mice were anesthetized with IP ketamine (72 mg/kg) and xylazine (64 mg/kg). Eyes were anesthetized with proparacaine (0.5%) and pupils were dilated with phenylephrine (2.5%) and tropicamide (1%). During the injection procedure an incision was made posterior of the ora serrata using a sharp 30-gauge needle. A 2 µl volume containing an estimated amount of $5x10^{11}$ viral genomes of AAV diluted in PBS (with 1% phenol red as contrast agent) was then fed through the incision site and injected intravitreally using a blunt 32 gauge Hamilton syringe (Reno, NV). Hamilton needle tip was left in the eye for >60 seconds to allow homogenization and reduce the efflux.

Tissue preparation and immunohistochemistry. Mice were sacrificed >6 weeks after AAV injection and the eyes were enucleated and fixed in 4% paraformaldehyde (PFA, Ted Pella) for 1 h. Using scissors, the cornea was removed by making a circular incision around the ora serrata. Placing two forceps around the edges of the eyecup and genteelly tearing separates the retina from the sclera. Radial cuts were made to flatten the retina in forming the typical clover-leaf shape. For retinal sections, wholemounts were embedded in agarose (Sigma, St Louis, MO) and transverse sections were taken using a vibratome (Leica, Mannheim, Germany) at medium speed, maximum vibration and 150 µm thickness. Both wholemounts and sections were incubated in blocking buffer (10% normal goat serum (NGS), 1% BSA, and 0.5% Triton X-100 in PBS (pH 7.4)) for 2 h at RT. A 1:500 dilution of polyclonal antibody against PKC alpha (Abcam) was applied over night at 4°C and secondary anti-rabbit Alexa 594 antibody (Invitrogen, Carlsbad, CA) was applied at 1:1000 for 2 h at RT. After three 10 min PBS washes, tissue was mounted on slides using Vectashield (Vector labs, Burlingame, USA) mounting medium with DAPI (4',6-diamidino-2-phenylindole) to stain cell nuclei. Wholemounts and sections were imaged using a confocal microscopy (LSM7, Carl Zeiss, Gottingen, Germany).

MEA recordings. MEA recordings were performed on treated and untreated *rd1* mice as well as untreated wt (C57Bl/6J) mice. Control mice and wt mice were used at age >p90. Experimental mice were used 6-10 weeks following AAV injection. The excised retina was placed ganglion cell side down [156] in the recording chamber (pMEA 100/30iR-Tpr, Multi Channel Systems, Reutlingen, Germany) of a 60-channel multi electrode array system and constant with constant vacuum pump (perforated MEA1060 system with CVP; Multi Channel Systems, Reutlingen, Germany). A mesh weight (Scientific Instruments- Slice grids) was placed on the retina to improve electrode contact and signal-to-noise. In some instances, vacuum was also applied to the base of the retina (Multi Channel Systems vacuum system). During recording, a constant perfusion of oxygenated Ames media (32 °C) was provided to the recording chamber. Recordings lasted between one to two hours. Illumination coupled to a 4x objective and produced using a 300 W mercury arc lamp (DG-4, Sutter Instruments, Novato, CA) with a green band pass filter (510/50 nm, Thorlabs Inc. Newton, NJ). All light intensities reported were measured with a handheld power meter (Thorlabs Inc. Newton, NJ). Data was sampled at 25 kHz filtered between 300-2000 Hz and recorded using MCS rack software (Multi Channel Systems, Reutlingen, Germany) for off-line analysis. Voltage traces were converted to spike trains off-line by collecting responses using methods described below. Spikes recorded at one electrode were sorted into single units, which we defined as 'cells', via principal components analysis using Offline Sorter (Plexon, Dallas, TX). Single unit spike clusters were exported to MatLab and analyzed and graphed with custom software. For extracting firing rates in the dark, the 3 s preceding the flash were averaged to minimize fluctuations. The firing rates in the light were taken as peak response during the light stimulation. Photoswitching index PI was calculated using the formula (firing rate light - firing rate dark)/(firing rate light + firing rate dark). Cells were considered responsive if PI > 0.1 or PI < -0.1. All cells per figure are from the same retina unless otherwise specified. Two methods were used for setting the threshold for spikes: i) For raster plots (Figs. 2a, b), the baseline for each cell was set at a threshold just above electrical noise to include all possible spikes and provide a more global perspective. ii) For plots that show changes in firing rate due to light intensity (Figs. 5.2c,e,f) the thresholds were set to include all responding cells (PI > 0.1 or PI < -0.1). Peri-stimulus time histograms of every cell were correlated with one another.

Recording of VEPs. Adult *rd1* and wt mice were anesthetized using chlorprothixene (2 mg/kg, intraperitoneally) and urethane (1.5 g/kg, intraperitoneally) and supplemented with 0.5%-1% isoflurane for the first 30 min. Body temperature was maintained throughout the experiment using a DC temperature controller and a heating pad (FHC, Bowdoin, ME). Pupils were dilated with tropicamide (1%) and a small headplate was attached. A small craniotomy and durotomy was made over the primary visual cortex (1.7 mm lateral to midline and 0.7 mm anterior to lambda). Electrodes with a resistance of 3 MΩ were pulled from borosilicate glass (1.5 mm OD, 1.16 mm ID, Warner Instruments) using a horizontal puller (Sutter Instruments, Novato, CA). Electrodes were filled with ACSF (124 mM NaCl, 2.5 mM KCl, 2.0 mM $MgSO_4$, 1.25 mM KH_2PO_4, 26 mM $NaHCO_3$, 10 mM glucose, 4 mM sucrose, 2.5 mM $CaCl_2$ all purchased from Sigma,

St Louis), placed over the craniotomy and slowly lowered to a final depth of 400 μm, to layer 4 of the visual cortex. The contralateral eye was stimulated using 100-1000 ms pulses of blue light (455 nm, 15 mW/cm^2) and responses were recorded using the Axoclamp 200B amplifier (Axon Instruments, Foster City, CA). For each condition, 20-100 sweeps were recorded at 10 kHz, filtered at 2 kHz and analyzed with custom software in MatLab.

Open field test. The open field test was performed as described previously [52,132], with minor modifications, see Fig. 5.4a. Briefly, a plastic box (dimensions l = 60 cm, w = 40 cm, h = 30 cm) was divided into a light compartment (l = 25 cm, w = 40 cm, h = 30 cm) with white walls and a dark compartment (l = 35 cm, w = 40 cm, h = 30 cm) with black walls. The light compartment was illuminated by a custom LED array (5x6 LEDs, 447.5 nm Rebel LED, Luxeon star, Brantford, Canada) centered over the compartment. The light intensity was 100-200 μW/cm^2 at floor level. A small opening allowed the mice to move between the two compartments (h = 5 cm, w = 10 cm). Mice were brought into the testing room in their home cages, transferred to the open field box with their littermates and allowed to habituate to the new environment for 45 min. Mice were placed back in their home cage then tested individually. Mice were placed in the light compartment and were given a maximum of 3 min to discover that there is a second compartment. A 5 min trial began when they crossed into the dark compartment, and time spent in the light was recorded. Mice that crossed the opening only once and stayed in the dark compartment for entire time were disqualified. Permanent records were made using a video camera (GoproHero3).

Forced 2-choice water maze task. The water maze task was performed using the protocol described by Wong et al. [146] and Gaub et al. [52] with minor modifications. A radial arm maze was modified into a forced two choice task by blocking two of the five arms of the maze (Fig. 5.4c) and adding a divider (dimensions: 25 cm x 25 cm) to separate the two potential 'escape arms'. A custom built LED array (5x6 LEDs, 447.5 nm Rebel LED, Luxeon star, Brantford, Canada) was placed at the end of one of the "escape arms" cuing the escape platform. The light intensities at the divider (0.1 mW/cm^2) and (1 mW/cm^2) were measured at the water level using a handheld power meter (Thorlabs Inc. Newton, NJ).

Light cued fear conditioning. Fear conditioning experiments were performed using Colbourn shock chambers-Colbourn Habitest chamber with test cage (Coulbourn Instruments, PA). Control *rd1* and wt mice were sham (PBS) injected prior the experiment to control for the virus treatment. On the first day, animals were brought into the testing room in their home cages and then individually acclimated to clean Colbourn shock chambers (Coulbourn Instruments, PA) for 30 min. On the second day animals

received training. Mice were subjected to paired or unpaired light cued fear conditioning, consisting of 5 min habituation to the chamber with "non-patterned lights-on" followed by 3 cued shock trials at 0.7 mA. For paired trials the 20 sec "patterned lights-on" cue conincided with 3x 2s footshocks at 4 s inter-shock-interval. Intertrial interval was 40 sec. For unpaired trials, animals received the same amount of footshocks and the same time of patterned light cue but the footshocks occured independent from the light cue. These brief, low current shocks provided the minimal aversive stimuli to create a fearful memory associated with patterned light (custom built LED array with 5x6 LEDs, 447.5 nm Rebel LED, Luxeon star, Brantford, Canada) with moving bar (1 row at a time) with a 600 ms cycle, 100-150 $\mu W/cm^2$). On the third day, animals were tested in a fear probe trial. Thefloor to deliver footshocks was replaced with a solid floor. Mice were habituated to the chamber for 5 min, and subjected to the same light stimulation protocol as on day 2, but without shock, while being recorded by Colbourn's FreezeFrame software. The recordings were used to analyze conditioned fear behavior (time spent freezing, a typical rodent fear response) associated with the learned light cue.

Statistical analysis. The Students't-test was used for statistical analysis of *in-vivo* mouse physiology (Figs. 5.3,5.4).

Supplementary Material

Supplementary Note: Light unit conversion from mW/cm^2 to photons cm^{-2} s^{-1}

The conversions are adapted from Newport Corporation, see [168]. In order to calculate the number of photons $N_{p\lambda}$ in a joule of monochromatic light at wavelength λ we start with the energy of each photon given by:

$$E = h\frac{c}{\lambda}\ Joules$$

where:

h= Planck's constant (6.626 x 10^{-34} J s)

c= speed of light (2.998 x 10^8 m/s)

λ= wavelength in m

So the number of photons per Joule is:

$$\mathrm{Np}\lambda = \lambda \text{ x } 5.03 \text{ x } 10^{15}$$

$$\frac{d\mathrm{Np}\lambda}{dt} = \mathrm{P}_\lambda \text{ x } \lambda \text{ x } 5.03 \text{ x } 10^{15}$$

with: P_λ as energy in Watts and λ as wavelength in nm

Supplementary Figures

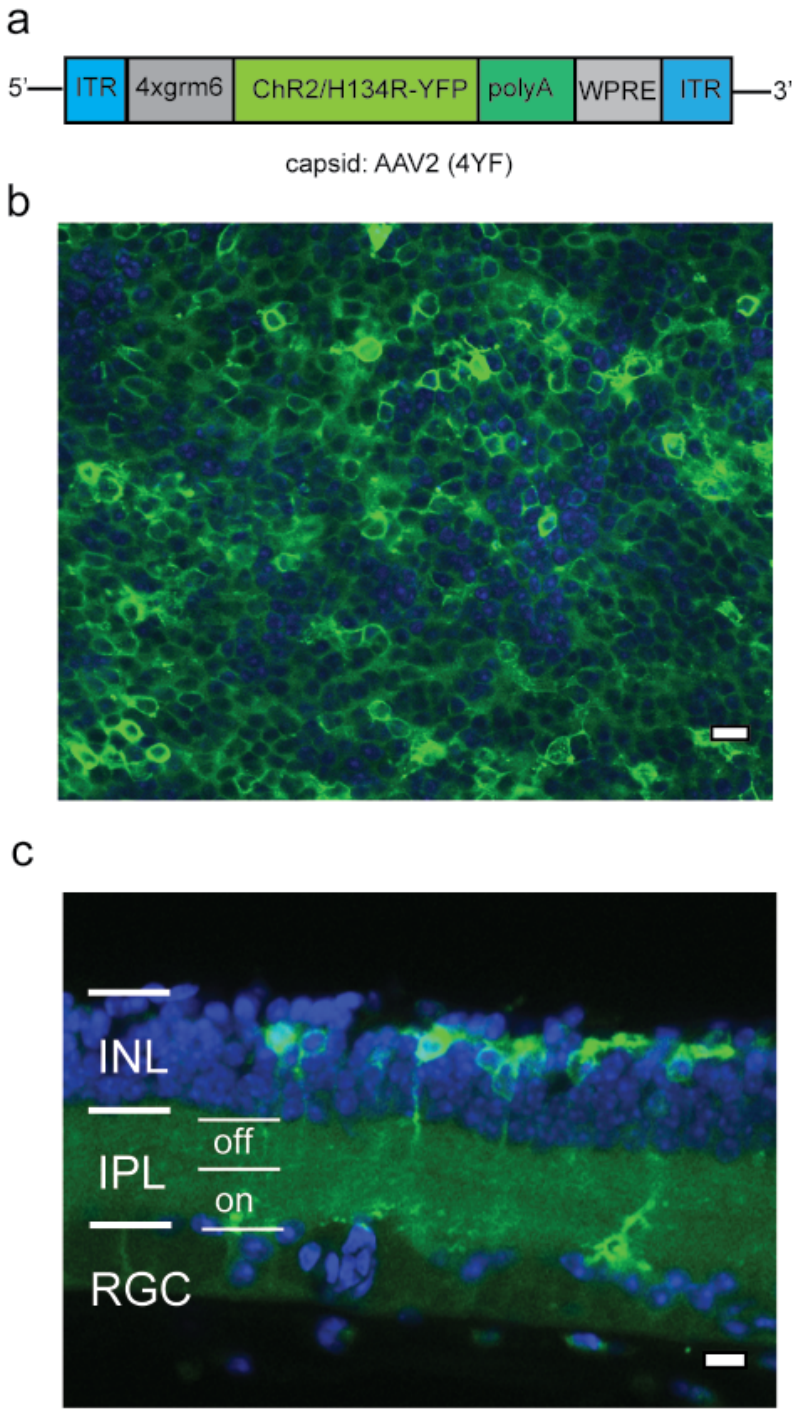

Figure S5.1. Targeted expression of Channelrhodopsin in ON-bipolar cells of *rd1* mouse retina. **(a)** DNA expression cassette for the gene therapy vector. Channelhodopsin2 variant H134R is tagged (C-terminally) with yellow fluorescent protein (YFP) and expression is driven by the metabotropic glutamate receptor 6 (4xgrm6) promoter. Promoter and ChR2-YFP sequences are flanked by inverted terminal repeat domains (ITR) and stabilized by a polyadenylation signal sequence (polyA) and a woodchuck hepatitis post-transcriptional regulatory element (WPRE). The cassette was packaged into the AAV2/2 (4YF) serotype. **(b,c)** Confocal images of wholemount **(c)** or vibratome section **(d)** of ChR2-YFP expression in ON-BCs of *rd1* mouse retina >6 weeks after intravitreal injection of AAV2/2(4YF)-4xgrm6-ChR2-YFP (2 µl volume equal to $5x10^{11}$ viral genomes). Nuclei were stained with DAPI (blue). Scale bar =10 µm.

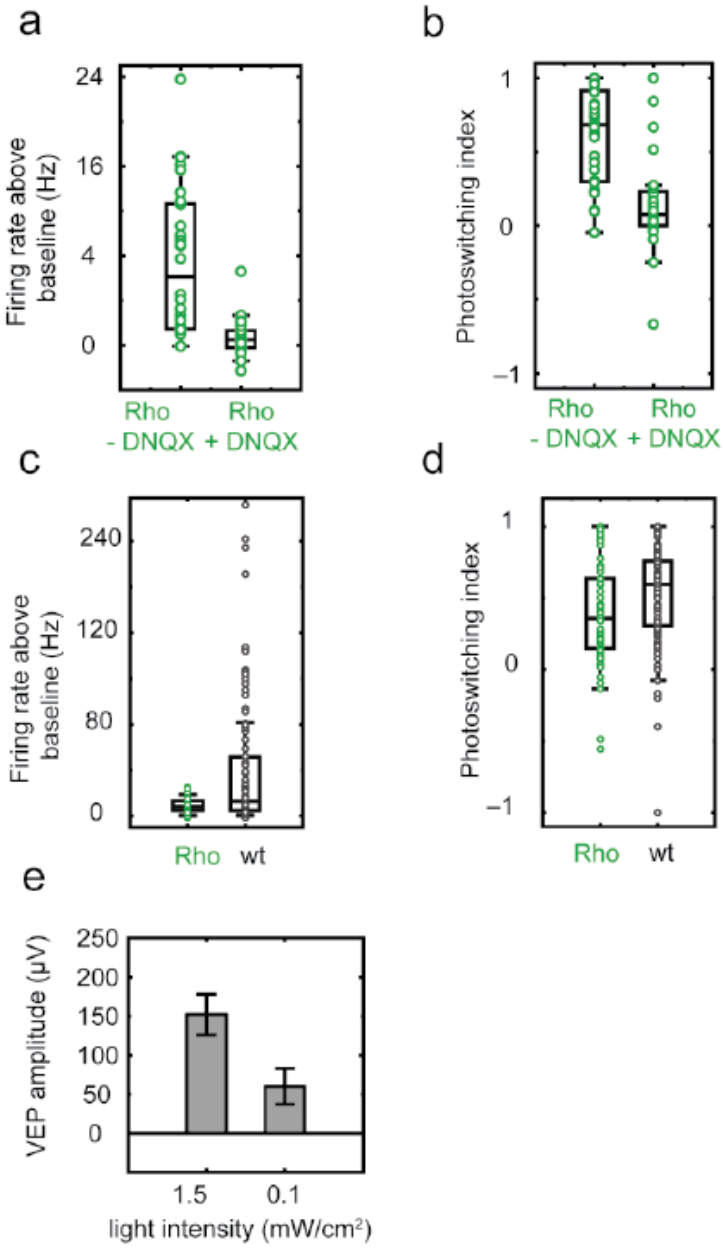

Figure S5.2. Characterization of rhodopsin-mediated signals. **(a-d)** *In vitro* characterization via multi electrode array recordings. **(a,b)** DNQX application blocks light responses in ON-BC rhodopsin expressing *rd1* mouse retinas. All cells represent average responses plotted on a scatterplots with green open circles and boxplots in black in the background (mean, 1st and 3rd quartile are shown in the box). **(a)** Variability of peak firing rate above base line are shown (n=32 cells) before (left) and after (right) application of AMPA/Kainate receptor antagonist DNQX (20 µM) and **(b)** recapitulated using photoswitching index ((firing rate light – firing rate dark) /(firing rate light + firing rate dark)) **(c,d)** Comparison of light responses in wild type and *rd1* ON-BC rhodopsin expressing mouse retinas. All cells from one recording are plotted in scatterplots in green (rhodopsin) and black (wt) circles overlayed with boxplots (in black with mean, 1st and 3rd quartile shown in the box). **(c)** Variability of firing rate above baseline for the two conditions (ON-BC rhodopsin *rd1*: n=62 cells, wt: n=99 cells). **(d)** Variability of photoswitching index ((firing rate light – firing rate dark) /(firing rate light + firing rate dark)) for the two conditions (ON-BC rhodopsin *rd1*: n=62 cells, wt: n=99 cells). **(e)** *In vivo* VEP responses to low light conditions used for subsequent behavior (Fig. 5.4). ON-BC rhodopsin treated *rd1* mice (n=3) were stimulated with 1 s pulses of blue light (LED, 445 nm). VEP responses to bright (1.5 mW/cm^2) and low (0.1 mW/cm^2) light conditions are shown confirming that the low light intensities used for mouse behavior (Fig.5.4) can still elicit strong responses *in vivo*. Data are means ± SEM.

Chapter 6 A device for human ultrasonic echolocation

This chapter was published in issue 99 or IEEE biomechanical engineering, in January 2015 with me as a co-author.

Introduction

A. Echolocation in Animals

In environments where vision is ineffective, some animals have evolved echolocation – perception using reflections of self-made sounds. Remarkably, some blind humans are also able to echolocate to an extent, frequently with vocal clicks. However, animals specialized for echolocation typically use much higher sound frequencies for their echolocation, and have specialized capabilities to detect time delays in sounds.

The most sophisticated echolocation abilities are found in microchiropteran bats (microbats) and odontocetes (dolphins and toothed whales). For example, microbats catch insects on the wing in total darkness, and dolphins hunt fish in opaque water. Arguably simpler echolocation is also found in oilbirds, swiftlets, Rousettas megabats, some shrews and tenrecs, and even rats [2]. Evidence suggests microbats form a spatially structured representation of objects in their environment using their echolocation [3].

Microbats use sound frequencies ranging from 25-150 kHz in echolocation, and use several different kinds of echolocation calls [4]. One call – the broadband call or chirp, consisting of a brief tone (< 5 ms) sweeping downward over a wide frequency range – is used for localization at close range. A longer duration call – the narrowband call, named for its narrower frequency range – is used for detection and classification of objects, typically at longer range.

In contrast to microbats, odontocetes use clicks; shorter in duration than bat calls and with sound frequencies up to 200 kHz [5]. Odontocetes may use shorter calls as sound travels ~ 4 times faster in water, whereas bat calls may be longer to have sufficient energy for echolocation in air. Dolphins can even use echolocation to detect features that are unavailable via vision: for example, dolphins can tell visually identical hollow objects apart based on differences in thickness [6].

B. Echolocation in Humans

Humans are not typically considered among the echolocating species. However, some blind persons have demonstrated the use of active echolocation, interpreting reflections from self-generated tongue clicks for such tasks as obstacle detection [7], distance discrimination [8], and object localization [9], [10]. The underpinnings of human echolocation in blind (and sighted) people remain poorly characterized, though some informative cues [11], neural correlates [12], [13], [14], and models [15] have been proposed. While the practice of active echolocation via tongue clicks is not commonly taught, it is recognized as an orientation and mobility method [16], [17]. However, most evidence in the existing literature suggests that human echolocation ability, even in blind, trained experts, does not approach the precision and versatility found in organisms with highly specialized echolocation mechanisms. For instance, due to their shorter wavelengths the ultrasonic pulses employed by echolocating animals yield higher spatial resolution, stronger directionality, and higher bandwidth than pulses at human-audible frequencies [18].

An understanding of the cues underpinning human auditory spatial perception is crucial to the design of an artificial echolocation device. Left-right (laterality) localization of sound sources depends heavily on binaural cues in the form of timing and intensity differences between sounds arriving at the two ears. For elevation and front/back localization, the major cues are direction-dependent spectral transformations of the incoming sound induced by the convoluted shape of the pinna, the visible outer portion of the ear [19]. Audi- tory distance perception is less well characterized than the other dimensions, though evidence suggests that intensity and the ratio of direct-to-reverberant energy play major roles in distance judgments [20]. Notably, the ability of humans to gauge distance using pulse-echo delays has not been well characterized, though these serve as the primary distance cues for actively echolocating animals [21].

Studies of human hearing suggest that it is very adaptable to altered auditory cues, such as those provided by remapped laterality cues [22] or altered pinna shapes [23], [24]. Additionally, in blind subjects the visual cortex can be recruited to also represent auditory cues [12], [25], further illustrating the plasticity of human auditory processing.

C. The Sonic Eye Device

Here we present a device, referred to as the Sonic Eye, that uses a forehead-mounted speaker to emit ultrasonic “chirps” (FM sweeps) modeled after bat echolocation calls. The echoes are recorded by bilaterally mounted ultrasonic microphones, each mounted inside an artificial pinna, also modeled after bat pinnae to produce direction-dependent spectral cues. After each chirp, the recorded chirp and reflections are played back to the user 1/m of normal speed, where m is an adjustable magnification factor. This magnifies all temporally based cues linearly by a factor of m and lowers frequencies into the human

audible range. For empirical results reported here, m is 20 or 25 as indicated. That is, cues that are normally too high or too fast for the listener to use are brought into the usable range simply by replaying them more slowly.

Although a number of electronic travel aids that utilize sonar have been developed (e.g., [26], [27], [28], [29]), none appear to be in common use, and very few provide information other than range-finding or a processed localization cue. For example in [27], distance to a single object is calculated and then mapped to a sound frequency, providing only extremely limited information about the world. The device presented in [26] is the most similar to the Sonic Eye. In [26] ultrasonic downward frequency sweeps are emitted, and then time stretched before presentation to the user. However the signals are time stretched in 2 μs chunks sampled every 100 μs, the overall playback of the echoes is not time stretched, no pinnae are used, the binaural microphones are placed only 2 cm apart, and microphone and transducer fidelity is unknown.

In contrast, the Sonic Eye provides a minimally processed input which, while initially challenging to use, has the capacity to be much more informative and integrate better with the innate human spatial hearing system. The relatively raw echoes contain not just distance information but horizontal location information and also vertical location information (from the pinnae), as well as texture, geometric, and material cues.

Behavioral testing suggests that novice users can quickly judge the laterality and distance of objects, and with experience can also judge elevation, and that the Sonic Eye thus demonstrates potential as an assistive mobility device.

A sample of audio and video from the Sonic Eye from the user's perspective is provided in the supplemental video to this manuscript, and is also available at http://youtube/md-VkLDwYzc.

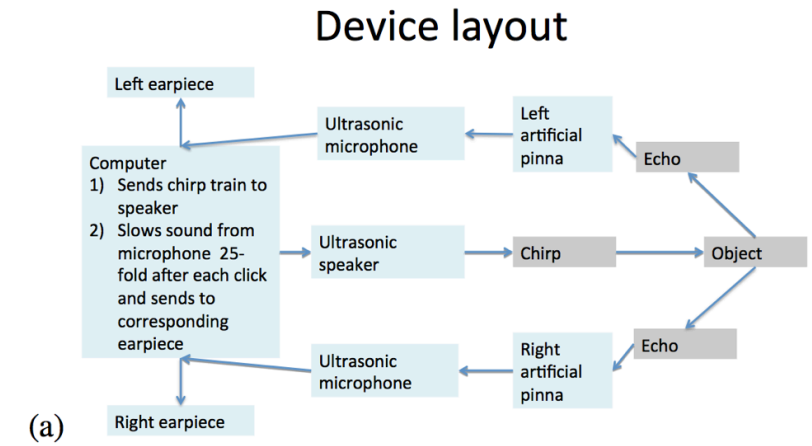

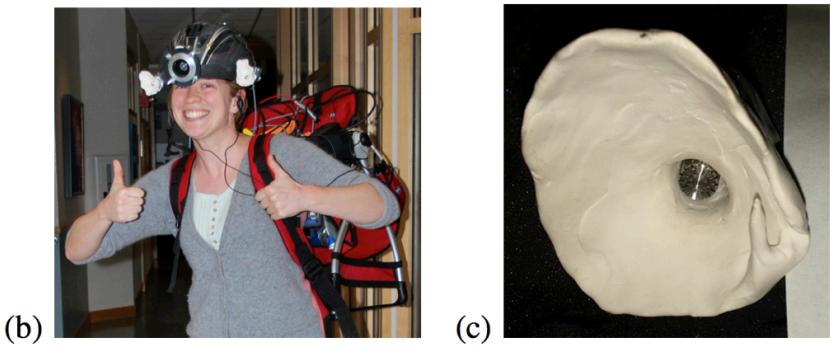

Fig. 6.1 *(a)* Diagram of components and information flow. *(b)* Photograph of the current hardware. *(c)* Photograph of one of the artificial pinnae used, modeled after a bat ear.

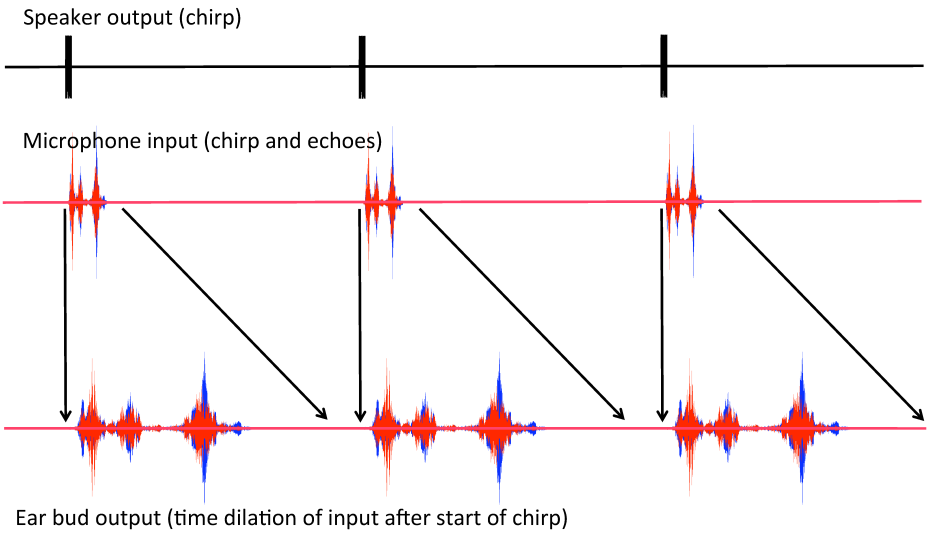

Fig. 6.2 Schematic of waveforms at several processing stages, from ultrasonic speaker output to stretched pulse-echo signal headphone output presented to user. Red traces correspond to the left ear signal, and blue traces to right ear signal. Note that the relative temporal scales are chosen for ease of visualization, and do not correspond to the temporal scaling used experimentally.

Specifications and Signal Processing

The flow of information through the Sonic Eye is illustrated in Figure 6.1a, and the device is pictured in Figure 6.1b. Recordings of a sound waveform moving through the system are presented in Figure 6.2. A video including helmet-cam video of the device experience is included in Supplemental Material.

The signal processing steps performed by the Sonic Eye, and the hardware used in each step, are as follows:

Step 1: The computer generates a chirp waveform, consisting of a 3 ms sweep from 25 kHz to 50 kHz with a constant sweep rate in log frequency. The initial and final 0.3 ms are tapered using a cosine ramp function. The computer, in a small enclosure mini-ITX case, runs Windows 7 and per- forms all signal processing using a custom Matlab program.

Step 2: The chirp is played through the head-mounted tweeter speaker. In order to play the chirp, it is output through an ESI Juli@ soundcard with stereo 192 kHz input and output, amplified using a Lepai TRIPATH TA2020 12 Volt stereo amplifier, and finally emitted by a Fostex FT17H Realistic SuperTweeter speaker.

Step 3: The computer records audio through the helmet mounted B&K Type 4939 microphones. For all experiments, the recording duration was 30 ms, capturing the initial chirp and the resulting echoes from objects up to 5 m away. The signal from the microphones passes through a B&K 2670 preamp followed by a B&K Nexus conditioning Amplifier before being digitized by the ESI Juli@ soundcard.

Step 4: The recorded signal is bandpass-filtered using Butter- worth filters from 50 to 25 kHz, and time-dilated by a factor of m. For m = 25, the recorded ultrasonic chirp and echoes now lie between 1 and 2 kHz.

Step 5: The processed signal is played to the user through AirDrives open-ear headphones, driven by a Gigaport HD USB sound card. Critically, the open-ear design leaves the ear canal unobstructed, ensuring safety in applied situations. (Note that in Experiments 6.1 and 6.2 described below, conven- tional headphones were used for stimulus delivery.)

The chirps are played at a steady rate with a period of approximately 1.5 s. This is a sufficient delay that in all experiments the echoes from the previous chirp have attenuated before the next chirp is played. In the current version of the device, the speaker and two ultrasonic microphones housed in artificial pinnae are mounted on a bicycle helmet. The pinnae are hand-molded from clay to resemble bat ears. The rest of the components are mounted within a baby carrier backpack, which provides portability, ventilation, and a

sturdy frame. A lithium-ion wheelchair battery is used to power the equipment. We note that in its current form, the Sonic Eye prototype is a proof-of-principle device whose weight and size make it unsuited to everyday use by blind subjects and extensive open-field navigation testing. To overcome these limitations we are developing a low-cost miniaturized version that retains all the functionality, with a user interface specifically for the blind. However, user testing with the current version has provided a proof of principle of the device's capabilities, as we describe below.

A. Measurement of Transfer Functions

We measured angular transfer functions for the ultrasonic speaker and microphone in an anechoic chamber (Figure 6.3). The full-width half-max (FWHM) angle for speaker power was ~ 50°, and for the microphone was ~ 160°. Power was measured using bandpass Gaussian noise between 25 kHz and 50 kHz. We expect the FWHM of the speaker and microphone to determine the effective field of view of The Sonic Eye.

(a)

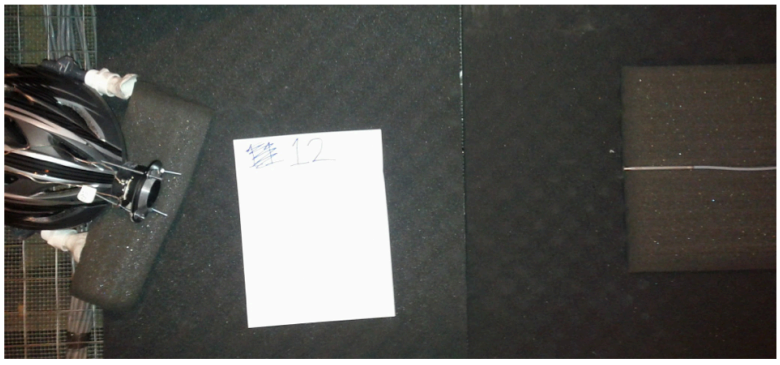

(b)

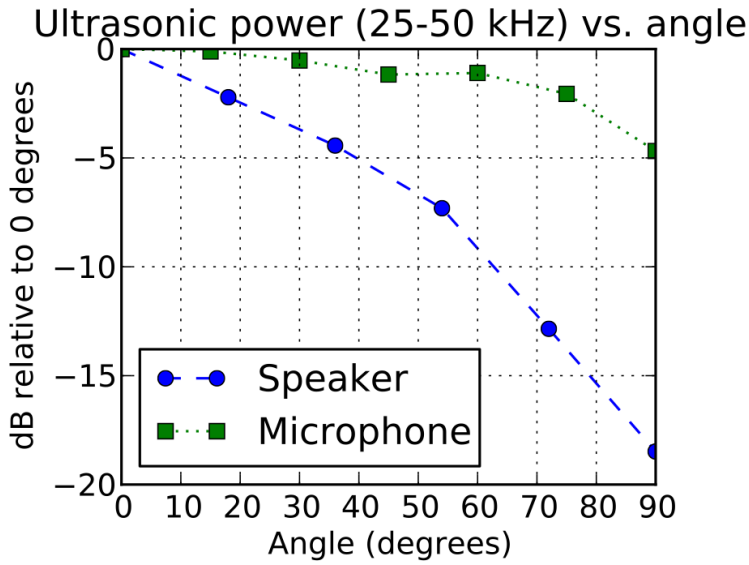

Fig. 6.3 Measurement of transfer functions for ultrasonic microphones and ultrasonic speaker as a function of angle. *(a)* Angular transfer function measurement setup. *(b)* Angular transfer function data. For the microphone, the sensitivity relative to the sensitivity at zero degrees is plotted; for the speaker, the emission power relative to the emission power at zero degrees is plotted.

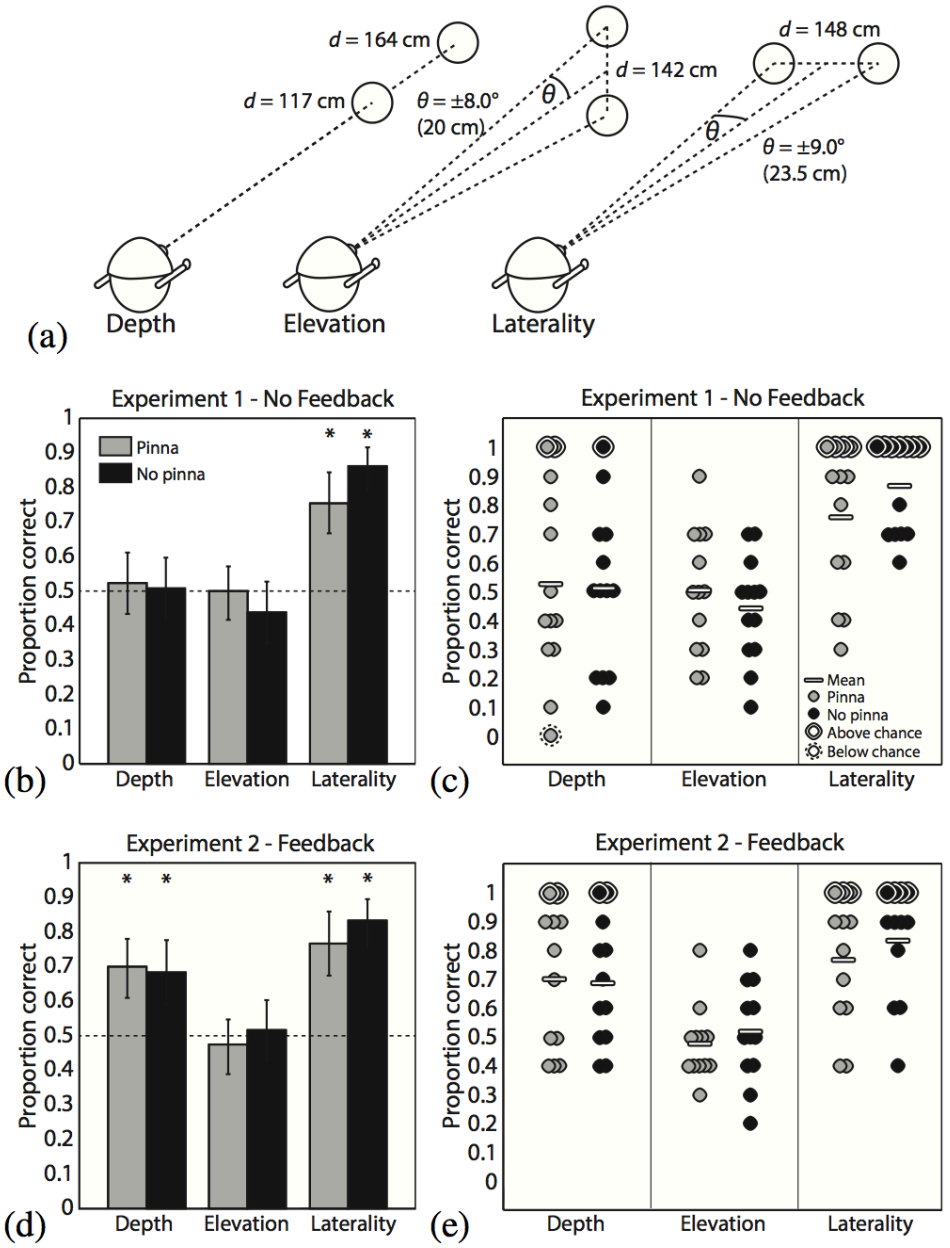

Fig. 6.4 Two alternative forced choice spatial localization testing. *(a)* A diagram of the configurations used to generate stimuli for each of the depth, elevation, and laterality tasks. *(b)* The fraction of stimuli correctly classified with no feedback provided to subjects (N = 13). Light gray bars indicate results for stimuli recorded with artificial pinnae, while dark gray indicates that pinnae were absent. The dotted line indicates chance performance level. Error bars represent 95% confidence intervals, computed using Matlab's binofit function. Asterisks indicate significant differences from 50% according to a two-tailed binomial test, with Bonferroni-Holm correction for multiple comparisons. *(c)* The same data as in (b), but with each circle representing the performance of a single subject, and significance on a two-tailed binomial test determined after Bonferroni-Holm correction over 13 subjects. *(d)* and *(e)* The same as in (b) and (c), except that after each trial feedback was provided on whether the correct answer was given (N = 12).

Methods

To explore the perceptual acuity afforded by the artificial echoes, we conducted three behavioral experiments: two in which we presented pulse-echo recordings (from the Sonic Eye) via headphones to naive sighted participants, and a practical localization test with three trained users wearing the device. In both Experiments 6.1 and 6.2, we tested spatial discrimination performance in separate two-alternative forced-choice (2AFC) tasks along three dimensions: i) laterality (left-right), ii) depth (near-far), and iii) elevation (high-low). The difference between Experiments 6.1 and 6.2 is that we provided trial-by-trial feedback in Experiment 6.2, but not Experiment 6.1. This allowed us to assess both the intuitive discriminability of the stimuli (Experiment 6.1) as well as the benefit provided by feedback (Experiment 6.2).

In Experiment 6.3 we tested laterality and elevation localization performance in a separate task on three users each of whom had between four and six hours of total experience wearing the Sonic Eye.

A. Methods, Experiment 6.1

1) Stimuli: For each of the three spatial discrimination tasks (laterality, depth and elevation), echoes were recorded from an 18-cm-diameter plastic disc placed in positions appropriate to the stimulus condition, and with the plate face normal to the emitter's line of sight, as illustrated in Figure 6.4a. For laterality judgments, the disc was suspended from the testing room ceiling via a thin (< 1 cm thick) wooden rod 148 cm in front of the emitter and 23.5 cm to the left or right of the midline. The "left" and "right" conditions were thus each ~ 9° from the midline relative to the emitter, with a center- to-center separation of ~ 18°. For depth judgments, the disc was suspended on the midline directly facing the emitter at a distance of 117 or 164 cm, separating the "near" and "far" conditions by 47 cm. Finally, for elevation judgments, the disc was suspended 142 cm in front and 20 cm above or below the midline, such that the "high" and "low" conditions were ~ 8° above and below the horizontal median plane, respectively, separated by ~ 16°. In all cases, the helmet with microphones and speakers was mounted on a Styrofoam dummy head.

To reduce the impact of any artifactual cues from a single echo recording, we recorded five "chirp" pulses (3-ms rising frequency sweeps, time dilation factor m = 25, truncated to 1 s length) and the corresponding echoes from the disc for each stimulus position (pulse-echo exemplars). Additionally, pulse-echo exemplars from each stimulus position were recorded with and without the artificial pinnae attached to the microphones. Thus, for each of the six stimulus positions, we had 10 recorded pulse-echo exemplars, for a total of 60 stimuli.

2) Procedure: Sighted participants (N = 13, 4 female, mean age 25.5 y) underwent 20 trials for each of the three spatial discrimination tasks, for a total of 60 trials per session. The trials were shuffled such that the tasks were randomly interleaved. Sound stimuli were presented on a desktop or laptop PC using closed-back circumaural headphones (Sennheiser HD202) at a comfortable volume, ~ 70 dB SPL. Assessment of these headphones using modified Sennheiser KE4-211- 2 microphones (from AuSIM) in the ear canal showed at least ~ 30dB attenuation (no distinguishable sound above the microphone noise floor) at one ear when a 70dB SPL 1-2kHz passband noise was played through the headphone speaker at the other ear. Thus there was negligible sound transfer between the ears. No visual stimuli were presented; the screen remained a neutral gray during auditory stimulus presentation. On each trial, the participant listened to a set of three randomly selected 1s exemplars (pulse-echo recordings) for each of two stimulus conditions. Depending on the spatial task, the participant then followed on-screen instructions to select from two options; whether the second exemplar represented an object to the left or right; nearer or farther; or above or below relative to the echoic object from the first exemplar. Upon the participant's response, a new trial began immediately, without feedback.

B. Methods, Experiment 6.2

1) Stimuli: Stimuli in Experiment 6.2 were nearly identical to those in Experiment 6.1, except that we now provided trial-by-trial feedback. To prevent participants from improving their performance based on artifactual noise that might be present in our specific stimulus set, we filtered background noise from the original recordings using the spectral noise gating function in the program Audacity (Audacity Team, http://audacity.sourceforge.net/). All other stimulus characteristics remained as in Experiment 6.1.

2) Procedure: Sighted volunteers (N = 12, 5 female, mean age 23.3 y) were tested on the same spatial discrimination tasks as in Experiment 6.1. After each response, participants were informed whether they had answered correctly or incorrectly. All other attributes of the testing remained the same as in Experiment 6.1.

C. Methods, Experiment 6.3

We conducted a psychophysical localization experiment with three sighted users (all male, mean age 33.7 y), who had between four and six hours of self-guided practice in using the device, largely to navigate the corridors near the laboratory. The participants were blindfolded throughout the experiment, and they wore the Sonic Eye device. The task was to localize a plate, ~ 30 cm (17°) in diameter, held at one of 9 positions relative to the user (see Figure 6.5), with the face of the plate oriented to be approximately normal to the emitter's line of sight. In each of 100 trials, the plate (on a long thin pole) was held

at a randomly selected position at a distance of 1 m, or removed for a 10th "absent" condition. Each of the 10 conditions was selected with equal probability. The grid of positions spanned 1 m on a side, such that the horizontal and vertical offsets from the center position subtended ~ 18°. The subjects stood still and initially fixated centrally, but were able to move their head during the task (although Subject 1 kept their head motionless). Responses consisted of a verbal report of grid position. After each response the participant was given feedback on the true position. The experiment took place in a furnished seminar room, a cluttered echoic space.

The hardware configuration for Subjects 2 and 3 was identical to that in Experiments 6.1 and 6.2. Subject 1 used an earlier hardware configuration, which differed as follows. The output of the B&K Nexus conditioning amplifier was fed into a NIDAQ USB-9201 acquisition device for digitization. Ultrasonic audio was output using an ESI GIGAPORT HD sound card. The temporal magnification factor m was set to 20. The backpack used was different, and power was provided by extension cord. Subject 1 did not participate in Experiments 6.1 or 6.2, although Subjects 2 and 3 did.

Results

A. Results, Experiment 6.1

Laterality judgments were robustly above chance for pinna (mean 75.4% correct, $p < 0.001$, $n = 130$, two-tailed binomial test, Bonferroni-Holm multiple comparison correction over 6 tests) and no-pinna conditions (mean 86.2% correct, $p < 0.001$, $n = 130$, two-tailed binomial test, Bonferroni-Holm multiple comparison correction over 6 tests), indicating that the binaural echo input produced reliable, intuitive cues for left-right judgments. Depth and elevation judgments, however, proved more difficult; performance on both tasks was not different from chance for the group. The presence or absence of the artificial pinnae did not significantly affect performance in any of the three tasks: logistic regression results were nonsignificant for the effect of pinnae ($p = 0.193$) and the pinna/task interaction ($p = 0.125$). Population and single subject results are shown in Figure 6.4b-c.

B. Results, Experiment 6.2

Results for laterality and elevation judgments replicated those from Experiment 6.1: strong above-chance performance for laterality in both pinna (76.7% correct, $p < 0.001$, $n = 120$, two-tailed binomial test, Bonferroni-Holm multiple comparison correction over 6 tests) and no-pinna (83.3% correct, $p < 0.001$, $n = 120$, two-tailed binomial test, Bonferroni-Holm multiple comparison correction over 6 tests) conditions. Because there appeared to be little benefit from feedback for these judgments, we conclude that it may be unnecessary for laterality judgments. Performance was still at chance for elevation, indicating that feedback over the course of a single experimental session was insufficient for this task.

However, performance on depth judgments improved markedly over Experiment 6.1, with group performance above chance for both pinna (70% correct, $p < 0.001$, $n = 120$, two-tailed binomial test, Bonferroni-Holm multiple comparison correction over 6 tests) and no-pinna (68.3% correct, $p < 0.001$, $n = 120$, two-tailed binomial test, Bonferroni- Holm multiple comparison correction over 6 tests) conditions. Performance ranges were also lower (smaller variance) for depth judgments compared to Experiment 6.1, suggesting that feedback aided a more consistent interpretation of depth cues. As in Experiment 6.1, the presence or absence of the artificial pinnae did not significantly affect performance in any of the three tasks: logistic regression results were nonsignificant for the effect of pinnae ($p = 0.538$) and the pinna/task interaction ($p = 0.303$). Population and single subject results are shown in Figure 6.4d-e.

C. Results, Experiment 6.3

The subjects typically performed well above chance in determining the exact position of the plate from 10 positions, the plate's absence/presence, its horizontal position (laterality), and its vertical position (elevation). This is illustrated in Figure 6.5b, the dotted line indicating chance performance, and a ringed gray dot indicating the subject performed significantly better than chance by the binomial test.

For Subject 1, the spatially arranged confusion matrix of Figure 6.5c indicates that the subject reported the exact correct position from the 10 positions with high probability. Overall performance was 48% correct, significantly greater than a chance performance of 10% ($p \ll 0.001$, $n = 100$, two- tailed binomial test, Bonferroni-Holm multiple comparison correction over all tests and subjects of Experiment 3). For all non-absent trials, 72% of localization judgments were within one horizontal or one vertical position of the true target position. Figure 6.5d shows the confusion matrix collapsed over spatial position to show only the absence or presence of the plate. The present/absent state was reported with 98% accuracy, significantly better than chance ($p < 0.001$, $n = 100$, two-tailed binomial test, Bonferroni-Holm corrected). Figure 6.5e shows the confusion matrix collapsed over the vertical dimension (for the 93 cases where the plate was present), thus showing how well the subject estimated horizontal position in the horizontal dimension. The horizontal position of the plate was correctly reported 56% of the time, significantly above chance performance ($p \ll 0.001$, $n = 93$, two-tailed binomial test, Bonferroni-Holm corrected). Figure 6.5f shows the confusion matrix collapsed over the horizontal dimension, thus showing how well the subject estimated position in the vertical dimension. The vertical position of the plate was correctly reported 68% of the time, significantly above chance performance ($p \ll 0.001$, $n = 93$, two-tailed binomial test, Bonferroni-Holm corrected).

The remaining two subjects showed similar results to Subject 1. Subject 2 was significantly above chance for exact position, for absent vs. present, for horizontal localization, and for vertical localization (respectively 44%, $p \ll 0.001$, $n=100$; 94%, $p=0.0084$, $n=100$; 69%, $p \ll 0.001$, $n = 90$; 49%, $p \ll 0.001$, $n = 90$, two-tailed binomial test, Bonferonni-Holm corrected). Subject 3 was significantly above chance for exact position, for absent vs. present, and for horizontal localization, but not for vertical localization (respectively 26%, $p \ll 0.001$, $n = 100$; 95%, $p = 0.0084$, $n=100$; 61%, $p \ll 0.001$, $n=93$; 34%, $p=0.25$, $n=93$, two-tailed binomial test, Bonferroni-Holm corrected). Figure 6.5g-n shows the confusion matrices for Subjects 2 and 3.

Discussion

In Experiments 6.1 and 6.2, we found that relatively precise spatial discrimination based on echolocation is possible with little or no practice in at least two of three spatial dimensions. Echoic laterality cues were clear and intuitive regardless of feedback, and likely made use of interaural level and/or time differences of the individual echoes. Echoic distance cues were also readily discriminable with feedback. Depth judgments without feedback were characterized by very large variability compared to the other tasks: performance ranged from 0 - 100% (pinna) and 10 - 100% (no-pinna) across subjects. This suggests the presence of a cue that was discriminable but nonintuitive without trial-by-trial feedback.

While we did not vary distances parametrically, as would be necessary to estimate psychophysical thresholds, our results permit some tentative observations about the three-dimensional spatial resolution achieved with artificial echolocation. Direct comparison with previous work on non- ultrasonic human echolocation is difficult; e.g., [30] tested absolute rather than relative laterality, did not alter the echo stimuli, and included a third "center" condition. However, the reflecting object in that experiment was a large rectangular board subtending $29^\circ \times 30^\circ$, such that lateral center-to-center separation was 29°, whereas disc positions in the present study were separated by a smaller amount, 19.9°, and presented less than 10% of the reflecting surface. [30] reported ~ 60- 65% correct laterality judgments for sighted subjects which is somewhat less than our measures (they reported ~ 75% for blind subjects). Another study [31] reported a threshold of 6.7° azimuth in a virtual echo discrimination task; the reflecting surfaces in that study were virtualized and presented at radially normal angles to the listener. Using flat circular stimuli similar to those reported in the current study, [10] reported horizontal discrimination thresholds averaging ~ 3.5° in a relative localization task among blind trained echolocation experts, but sighted subjects varied widely in performance and were, as a group, unable to perform the task. Prior results such as these suggest an increase in effective sensitivity when using artificial ultrasonic echo cues, but also hint at considerable potential for threshold improvement with larger surfaces, optimized reflection angles, or subject expertise.

Depth judgments were reliably made at a depth difference of 47 cm in Experiment 6.2, corresponding to an unadjusted echo- delay difference of ~ 2.8 ms, or ~ 69 ms with a dilation factor of 25. A 69-ms time delay is discriminable by humans but was only interpreted correctly with feedback, suggesting that the distance information in the echo recordings, although initially nonintuitive, became readily interpretable with practice.

Our signal recordings included complex reverberations inherent in an ecological, naturalistic environment. Thus the discrimination task was more complex than a simple delay between two isolated sounds. The cues indexing auditory depth include not only

variation in pulse-echo timing delays, but also differences in overall reflected energy and reverberance which are strongly distance-dependent. In fact, as cues produced by active echoes, discrete pulse-echo delays are not typically encountered by the human auditory system. Single-subject echoic distance discrimination thresholds as low as ~ 11 cm [8] (~ 30 cm in extensively trained sighted subjects [32]) have been reported for natural human echolocation. Thus, it is likely that training would improve depth discrimination considerably, especially with time-dilated echo information, in theory down to ~ 0.5 cm with 25-fold dilation.

Performance was low on the elevation task in both pinna and no-pinna conditions. It is possible that the echo recordings do not contain the elevation information necessary for judgments of 16° precision. However, our tasks were expressly designed to assess rapid, intuitive use of the echo cues provided, while the spectral cues from new pinnae take time to learn; elevation judgments in humans depend strongly on pinna shape [19], [33], and recovering performance after modifying the pinna can take weeks [23]. Vertical localization behavior in bats depends on direction dependent filtering due details of pinna and tragus shape and position [34], [35], and also on active outer ear position adjustments [36]. Thus, the design and construction of the artificial pinnae used in the present experiment may not provide the full benefits of their bat counterparts, and would likely benefit from refinement to optimize their filtering properties. For instance, pinnae could be optimized to maximize the learnability of the new pinna transform by humans. Considering left-right localization, the time dilation employed by the Sonic Eye, by expanding the interaural time differences, may improve interaural time discrimination in some cases, possibly allowing for supernor- mal laterality localization with practice, especially near the midline. For peripheral sound sources the time dilation will cause unecologically large interaural time differences which although discriminable, tend to be harder to discriminate by a degree that approximately counteracts the advantage of the time-dilation [37]. We do not expect time-dilation to strongly influence vertical localization capacities in our setup.

In line with these observations, Experiment 6.3 suggests that both laterality and elevation localization cues were available to a user with a moderate amount of training. This is qualitatively consistent with previous measures of spatial resolution in blind and sighted subjects performing unaided spatial echolo- cation tasks [9], [38]. While further research is needed to validate such comparisons and, more generally, characterize the behavioral envelope of Sonic Eye-aided echolocation, we consider the results presented here as encouraging. Specifically, they suggest that performance on behaviorally relevant tasks is amenable to training. Informal observations with two further participants suggest an ability to navigate through hallways, detecting walls and stairs, while using the Sonic Eye blindfolded. A degree of shape discrimination may also be present (for example an open vs. closed hand), consistent with [39], who demonstrated human object discrimination using downsampled ultrasonic recordings of dolphins' reflected click

trains, and with [12], in which blind humans discriminated echoically between 3-D shapes.

Any practical configuration such as that tested in Experiment 6.3 should minimize interference between echolocation signals and environmental sounds (e.g., speech or approaching vehicles). To this end, open-ear headphones ensure that the ear remains unobstructed, as described in Section 2. However, future testing should include evaluations of auditory perfor- mance with and without the device, and training designed to assess and improve artificial echolocation in a naturalistic, acoustically noisy environment.

We note that performance on the experiments reported here likely underestimates the sensitivity achievable by using the device for several reasons. First, in Experiments 6.1 and 6.2, the head was virtually fixed relative to the target object (due to the headphone presentation of recorded echoes). This would not apply to a user in a more naturalistic context. Second, we assessed the intuitive and immediately usable perceptual information in the echoes, while extensive training would only build on that baseline. Third, the participants tested were not just untrained, but normally sighted. Blind and visually impaired users may differ in performance from sighted users due to some combination of superior auditory capabilities [40], [41], [42] and reported deficits, e.g. [43]. Testing this device with blind subjects will be an important direction for future work. Finally, ongoing development of the prototype continues to improve the quality of the emitted, received, and processed signal and its interface.

Summary and Conclusion

Here we present a prototype assistive device to aid in navigation and object perception via ultrasonic echolocation. The ultrasonic signals exploit the advantages of high-frequency sonar signals and time-stretch them into human-audible frequencies. Depth information is encoded in pulse-echo time delays, made available through the time-stretching process. Azimuthal location information is encoded as inter-aural time and intensity differences between echoes recorded by the stereo microphones. Finally, elevation information is captured by artificial pinnae mounted to the microphones as direction-dependent spectral filters. Thus, the device presents a three-dimensional auditory scene to the user with high theoretical spatial resolution, in a form consistent with natural spatial hearing. Behavioral results from two experiments with naive sighted volunteers demonstrated that two of three spatial dimensions (depth and laterality) were readily available with no more than one session of feedback/training. Elevation information proved more difficult to judge, but a third experiment with moderately trained users indicated successful use of elevation information as well. Taken together, we interpret these results to suggest that while some echoic cues provided by the device are immediately and intuitively available to users, perceptual acuity is potentially highly amenable to training. Thus, the Sonic Eye may prove to be a useful assistive device for persons who are blind or visually impaired.

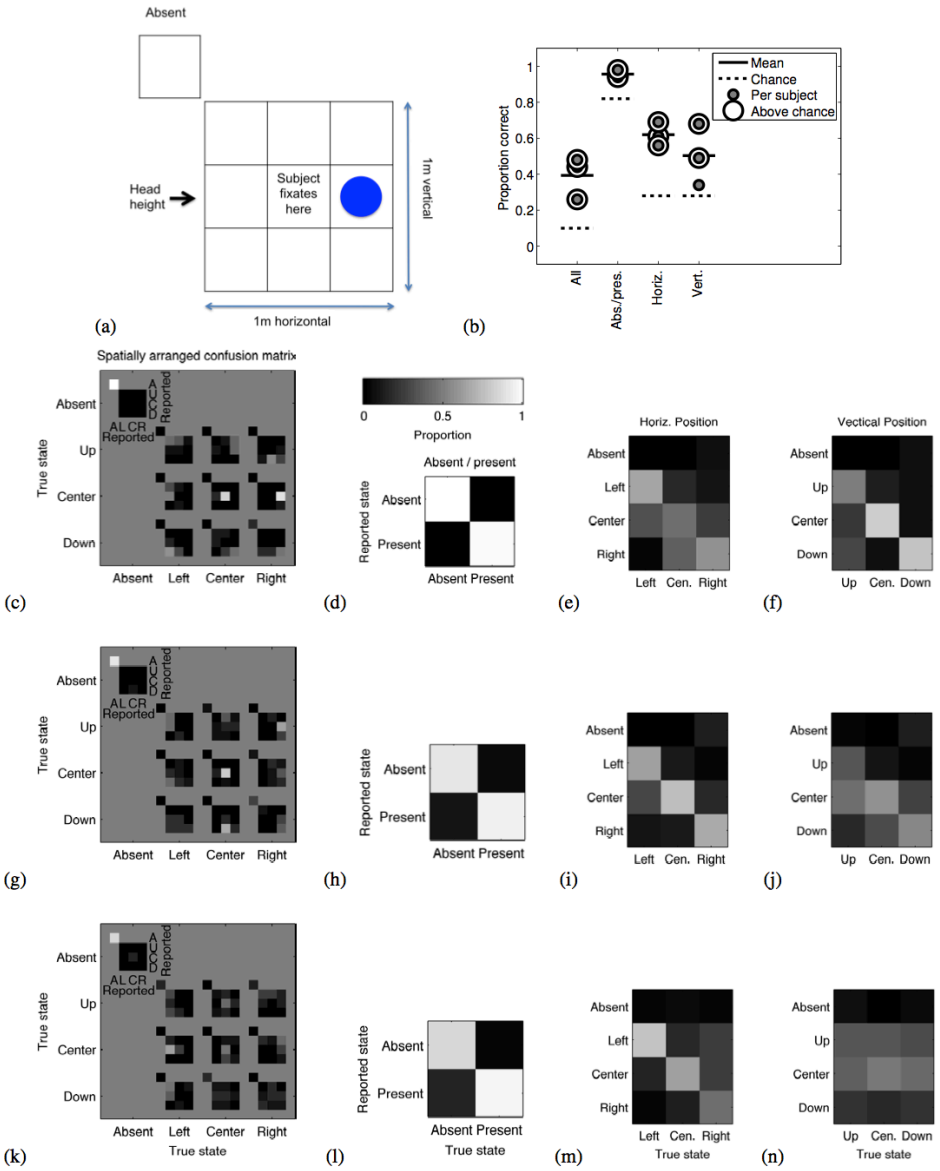

Fig. 6.5 Ten-position localization in three trained participants. A subject was asked to identify the position of an ~ 30 cm plastic plate held at 1 m distance. *(a)* Schematic illustration of the 10 possible configurations of the plate, including nine spatial locations and a tenth 'absent' condition. *(b)* Summary of fraction correct for the 3 subjects, for exact identification, and for identification of absent/present, horizontal position, and vertical position. *(c)* Spatially arranged confusion matrix of behavioral results for Subject 1. Each sub-figure corresponds to a location of the plate, and the intensity map within each sub-figure indicates the fraction of trials the subject reported each position for each plate location. Black corresponds to a subject never indicating a location, and white corresponds to a location always being indicated. Each sub-figure sums to 1. *(d)* Confusion matrix grouped into plate absent and present conditions for Subject 1. *(e)* Confusion matrix grouped by horizontal position of the plate for Subject 1. *(f)* Confusion matrix grouped by vertical position of the plate for Subject 1. *(g-j)* Same as in c-f, but for Subject 2. *(k-n)* Same as in c-f, but for Subject 3.

Chapter 7 Conclusion and future directions

In this dissertation, I have investigated strategies for optical control of biological function using azobenze-based photos-witches and I have applied light sensitive proteins towards restoration of visual function in animal models of human blindness. Moreover, I have expanded my research and helped develop a non-invasive sensory substitution device as navigational aid for the blind.

In chapters 2 and 3, I describe my efforts to develop new light-sensitive proteins. Chapter 2 is focused on developing a light gated ion channel, the light gated nicotinic acetylcholine receptor or 'LinAChR' and in chapter 3, I describe developing a family of light gated GPCRs, the light gated metabotropic glutamate receptors or 'LimGluRs'. In order to understand the contribution of receptor subtypes to physiological function, new tools are needed. Pharmacological agents have poor spatial and temporal resolution and often times cannot distinguish between subtypes of receptors. In order to gain precise spatiotemporal control we turned to optogenetics. Using azobenzene-derived photo-switches I screened mutant receptors for anchoring sites in proximity to the ligand-binding domain that would either activate or inhibit receptor function in a light-dependent fashion. Using these new tools we should be able to get a better understanding of the role that these receptors play both in healthy organisms as well as their contribution in neurological diseases and disorders.

My hope was that I could apply one of the LimGluR subtypes, specifically LimGluR6 towards vision restoration. In patients that develop retinitis pigmentosa, photoreceptor cells degenerate causing loss of light-dependent glutamate release. Consequently, this leads to a gradual loss of the postsynaptic signaling partner, mGluR6, in ON-BCs. My idea was to express LimGluR6 in ON-BCs of the degenerating mouse retina in order to replace the lost mGluR6 while at the same time providing these cells with a light-dependent glutamate signal. Unfortunately, I never succeeded in expressing LimGluR6 or any of the other LimGluRs in ON-BCs using AAV. I suspect receptor trafficking or regulatory mechanisms may have played an important role in preventing expression. During retinal degeneration, the cellular compartment in which mGluR6 is expressed in wild type retina, is lost which could also explain the lack of LimGluR expression.

Chapters 4 and 5 describe my efforts towards application of light-gated receptors for restoration of visual function in animal models of human blindness. In chapter 4, I applied the light-gated ionotropic glutamate receptor LiGluR as optical actuator and compared two target cells for their ability to act as artificial photoreceptors. I showed that both target cells have the capability to re-animate retinal light responses as well as visually guided behavior. On the level of the retina, I showed that ON-BCs create a more diverse signal whereas RGCs create a highly synchronized output. I concluded that cells upstream in the retinal circuitry, e.g. ON-BCs, would be good targets for early stage

diseases whereas the cells furthest downstream in the retina, the RGCs, would be better suited for late stage intervention. Furthermore, I was able to show that our treatment could be translated from mouse to dogs paving the way to the clinic. In chapter 5, I showed that the retina-native GPCR rhodopsin can be expressed in upstream targets, the ON-BCs and that this strategy greatly improves light-sensitivity over that of ion channels, presumably due to recruitment of signal amplification via G-protein cascades. Although a lot of mechanistic questions remain open at this stage, the notion that light gated GPCRs can be expressed ectopically in ON-BCs and drive visual function at the level of the retina, cortex and behaviorally, is quite remarkable.

To conclude chapters 4 and 5, upstream target cells are well suited for early stage intervention, downstream targets like RGCs are better for later stages of the disease. Light-gated ion channels like LiGluR are fast but not very sensitive, light-gated GPCRs like rhodopsin are very sensitive but not fast enough.

Cone opsins might be able to provide a solution to the sluggish kinetics seen in rhodopsin. The Herlize group has shown recently that cone opsins have three times faster off rates in HEK cells[165], which would argue that this effect might be even more dramatic in neurons. An open question is which factor is limiting the kinetics – the termination of rhodopsin in absence of arrestin and GRK or downstream signaling molecules of the G-protein cascade? To test this, cone opsins and rhodopsin could be expressed in the same cell type and response kinetics to a single flash of light could be compared at the level of the retina using the multi electrode array. Cone opsins could also allow multi-color vision restoration with their respective absorption spectra covering blue, red and green. However, preliminary attempts at expressing cone opsins in ON-BCs RGCs using the same promoters and vectors that showed efficacy in chapter 4 and 5, have not been successful. Chimeric proteins with cone opsin backbone fused to putative n-terminal or c-terminal signal sequences from rhodopsin may help promote receptor trafficking[169-172].

Alternatively, sensitivity of the azobenzene system could be improved using new variants of the LimGluRs. New photo-switches (PEGlyated azobenzene compounds) and new anchoring sites (e.g. SNAP domain) are now available that show great photo-switching efficacy in HEK cells and neuronal cultures. Preliminary data suggests that these new LimGluRs express well in RGCs, however it remains to be seen if they will express in ON-BCs.

We are currently in the process of designing new LED arrays to present complex patterns at high light intensities. I have shown that mice can distinguish between static and dynamic patterns using our *in vivo* visually guided behavioral tasks (chapter 4 and 5). It will be interesting to probe if treated mice can distinguish two static patterns with different shapes. Furthermore, it will be of major importance to determine the spatial and temporal resolution of treated mice.

Finally, in chapter 6, I describe the design of a prototype for technology-assisted human echolocation, which we named ‘the Sonic Eye’. I showed that trained subjects

could locate objects in space at a high success rate. To my surprise, I also found that naïve subjects were able to make laterality and distance judgments, but not elevation judgments using our device. I conclude from these experiments that humans have an innate capacity for echolocation. Further prototyping and miniaturization are needed in order to turn the sonic eye into a commercial navigational aid for the blind.

References

1. Darwin, C. *On the origin of species*, (Appleton and Co, New York, 1871).
2. Nilsson, D.E. & Pelger, S. A pessimistic estimate of the time required for an eye to evolve. *Proc Biol Sci* **256**, 53-8 (1994).
3. Land, M.F.a.N., D.-E. *Animal Eyes*, (Oxford University Press, Oxford, 2002).
4. Fernald, R.D. Evolving eyes. *Int J Dev Biol* **48**, 701-5 (2004).
5. Masland, R.H. The fundamental plan of the retina. *Nat Neurosci* **4**, 877-86 (2001).
6. Franze, K. *et al.* Muller cells are living optical fibers in the vertebrate retina. *Proc Natl Acad Sci U S A* **104**, 8287-92 (2007).
7. Garcia, D.M. & Koke, J.R. Astrocytes as gate-keepers in optic nerve regeneration--a mini-review. *Comp Biochem Physiol A Mol Integr Physiol* **152**, 135-8 (2009).
8. Sparrow, J.R., Hicks, D. & Hamel, C.P. The retinal pigment epithelium in health and disease. *Curr Mol Med* **10**, 802-23 (2010).
9. Restoring Vision to the Blind: The Lasker/IRRF Initiative for Innovation in Vision Science. *Trans. Vis. Sci. Tech* **3**(2014).
10. Yonehara, K. & Roska, B. Motion detection: neuronal circuit meets theory. *Cell* **154**, 1188-9 (2013).
11. Humayun, M.S. *et al.* Interim results from the international trial of Second Sight's visual prosthesis. *Ophthalmology* **119**, 779-88 (2012).
12. Zrenner, E. Fighting blindness with microelectronics. *Sci Transl Med* **5**, 210ps16 (2013).
13. Daiger, S.P., Bowne, S.J. & Sullivan, L.S. Genes and Mutations Causing Autosomal Dominant Retinitis Pigmentosa. *Cold Spring Harb Perspect Med* (2014).
14. Wang, D.Y. *et al.* Gene mutations in retinitis pigmentosa and their clinical implications. *Clin Chim Acta* **351**, 5-16 (2005).
15. Solinis, M.A., Del Pozo-Rodriguez, A., Apaolaza, P.S. & Rodriguez-Gascon, A. Treatment of ocular disorders by gene therapy. *Eur J Pharm Biopharm* (2014).
16. Hoon, M., Okawa, H., Della Santina, L. & Wong, R.O. Functional architecture of the retina: development and disease. *Prog Retin Eye Res* **42**, 44-84 (2014).
17. Santos, A. *et al.* Preservation of the inner retina in retinitis pigmentosa. A morphometric analysis. *Arch Ophthalmol* **115**, 511-5 (1997).

18. Stronks, H.C. & Dagnelie, G. The functional performance of the Argus II retinal prosthesis. *Expert Rev Med Devices* **11**, 23-30 (2014).

19. Carr, A.J. *et al.* Protective effects of human iPS-derived retinal pigment epithelium cell transplantation in the retinal dystrophic rat. *PLoS One* **4**, e8152 (2009).

20. Warre-Cornish, K., Barber, A.C., Sowden, J.C., Ali, R.R. & Pearson, R.A. Migration, integration and maturation of photoreceptor precursors following transplantation in the mouse retina. *Stem Cells Dev* **23**, 941-54 (2014).

21. Pearson, R.A. *et al.* Restoration of vision after transplantation of photoreceptors. *Nature* **485**, 99-103 (2012).

22. Zhong, X. *et al.* Generation of three-dimensional retinal tissue with functional photoreceptors from human iPSCs. *Nat Commun* **5**, 4047 (2014).

23. Nakano, T. *et al.* Self-formation of optic cups and storable stratified neural retina from human ESCs. *Cell Stem Cell* **10**, 771-85 (2012).

24. Chinskey, N.D., Besirli, C.G. & Zacks, D.N. Retinal cell death and current strategies in retinal neuroprotection. *Curr Opin Ophthalmol* **25**, 228-33 (2014).

25. LaVail, M.M. *et al.* Multiple growth factors, cytokines, and neurotrophins rescue photoreceptors from the damaging effects of constant light. *Proc Natl Acad Sci U S A* **89**, 11249-53 (1992).

26. Li, Y. *et al.* CNTF induces regeneration of cone outer segments in a rat model of retinal degeneration. *PLoS One* **5**, e9495 (2010).

27. Mey, J. & Thanos, S. Intravitreal injections of neurotrophic factors support the survival of axotomized retinal ganglion cells in adult rats in vivo. *Brain Res* **602**, 304-17 (1993).

28. Wen, R., Tao, W., Li, Y. & Sieving, P.A. CNTF and retina. *Prog Retin Eye Res* **31**, 136-51 (2012).

29. Maguire, A.M. *et al.* Age-dependent effects of RPE65 gene therapy for Leber's congenital amaurosis: a phase 1 dose-escalation trial. *Lancet* **374**, 1597-605 (2009).

30. MacLaren, R.E. *et al.* Retinal gene therapy in patients with choroideremia: initial findings from a phase 1/2 clinical trial. *Lancet* **383**, 1129-37 (2014).

31. Nguyen, A.T., Campbell, M., Kiang, A.S., Humphries, M.M. & Humphries, P. Current therapeutic strategies for P23H RHO-linked RP. *Adv Exp Med Biol* **801**, 471-6 (2014).

32. Bi, A. *et al.* Ectopic expression of a microbial-type rhodopsin restores visual responses in mice with photoreceptor degeneration. *Neuron* **50**, 23-33 (2006).

33. Busskamp, V. *et al.* Genetic reactivation of cone photoreceptors restores visual responses in retinitis pigmentosa. *Science* **329**, 413-7 (2010).

34. Caporale, N. *et al.* LiGluR restores visual responses in rodent models of inherited blindness. *Mol Ther* **19**, 1212-9 (2011).

35. Doroudchi, M.M. *et al.* Virally delivered channelrhodopsin-2 safely and effectively restores visual function in multiple mouse models of blindness. *Mol Ther* **19**, 1220-9 (2011).

36. Lagali, P.S. *et al.* Light-activated channels targeted to ON bipolar cells restore visual function in retinal degeneration. *Nat Neurosci* **11**, 667-75 (2008).

37. Mace, E. *et al.* Targeting Channelrhodopsin-2 to ON-bipolar Cells With Vitreally Administered AAV Restores ON and OFF Visual Responses in Blind Mice. *Mol Ther* (2014).

38. Kramer, R.H., Mourot, A. & Adesnik, H. Optogenetic pharmacology for control of native neuronal signaling proteins. *Nat Neurosci* **16**, 816-23 (2013).

39. Liu, X. *et al.* Herpes simplex virus mediated gene transfer to primate ocular tissues. *Exp Eye Res* **69**, 385-95 (1999).

40. Greenberg, K.P., Geller, S.F., Schaffer, D.V. & Flannery, J.G. Targeted transgene expression in muller glia of normal and diseased retinas using lentiviral vectors. *Invest Ophthalmol Vis Sci* **48**, 1844-52 (2007).

41. Bainbridge, J.W. *et al.* In vivo gene transfer to the mouse eye using an HIV-based lentiviral vector; efficient long-term transduction of corneal endothelium and retinal pigment epithelium. *Gene Ther* **8**, 1665-8 (2001).

42. Flannery, J.G. *et al.* Efficient photoreceptor-targeted gene expression in vivo by recombinant adeno-associated virus. *Proc Natl Acad Sci U S A* **94**, 6916-21 (1997).

43. Acland, G.M. *et al.* Gene therapy restores vision in a canine model of childhood blindness. *Nat Genet* **28**, 92-5 (2001).

44. Wu, Z., Asokan, A. & Samulski, R.J. Adeno-associated virus serotypes: vector toolkit for human gene therapy. *Mol Ther* **14**, 316-27 (2006).

45. Petrs-Silva, H. *et al.* Novel properties of tyrosine-mutant AAV2 vectors in the mouse retina. *Mol Ther* **19**, 293-301 (2011).

46. Cronin, T. *et al.* Efficient transduction and optogenetic stimulation of retinal bipolar cells by a synthetic adeno-associated virus capsid and promoter. *EMBO Mol Med* **6**, 1175-90 (2014).

47. Dalkara, D. *et al.* In vivo-directed evolution of a new adeno-associated virus for therapeutic outer retinal gene delivery from the vitreous. *Sci Transl Med* **5**, 189ra76 (2013).

48. Klimczak, R.R., Koerber, J.T., Dalkara, D., Flannery, J.G. & Schaffer, D.V. A novel adeno-associated viral variant for efficient and selective intravitreal transduction of rat Muller cells. *PLoS One* **4**, e7467 (2009).

49. Dalkara, D. *et al.* Inner limiting membrane barriers to AAV-mediated retinal transduction from the vitreous. *Mol Ther* **17**, 2096-102 (2009).

50. Liang, Y. *et al.* Rhodopsin signaling and organization in heterozygote rhodopsin knockout mice. *J Biol Chem* **279**, 48189-96 (2004).

51. Tan, E. *et al.* The relationship between opsin overexpression and photoreceptor degeneration. *Invest Ophthalmol Vis Sci* **42**, 589-600 (2001).

52. Gaub, B.M. *et al.* Restoration of visual function by expression of a light-gated mammalian ion channel in retinal ganglion cells or ON-bipolar cells. *Proc Natl Acad Sci U S A* (2014).

53. Busskamp, V. & Roska, B. Optogenetic approaches to restoring visual function in retinitis pigmentosa. *Curr Opin Neurobiol* **21**, 942-6 (2011).

54. Cideciyan, A.V. *et al.* Human retinal gene therapy for Leber congenital amaurosis shows advancing retinal degeneration despite enduring visual improvement. *Proc Natl Acad Sci U S A* **110**, E517-25 (2013).

55. Chuong, A.S. *et al.* Noninvasive optical inhibition with a red-shifted microbial rhodopsin. *Nat Neurosci* **17**, 1123-9 (2014).

56. Klapoetke, N.C. *et al.* Independent optical excitation of distinct neural populations. *Nat Methods* **11**, 338-46 (2014).

57. Miyashita, T., Shao, Y.R., Chung, J., Pourzia, O. & Feldman, D.E. Long-term channelrhodopsin-2 (ChR2) expression can induce abnormal axonal morphology and targeting in cerebral cortex. *Front Neural Circuits* **7**, 8 (2013).

58. Arshavsky, V.Y. & Burns, M.E. Current understanding of signal amplification in phototransduction. *Cell Logist* **4**, e29390 (2014).

59. Burns, M.E. & Arshavsky, V.Y. Beyond counting photons: trials and trends in vertebrate visual transduction. *Neuron* **48**, 387-401 (2005).

60. Kienzler, M.A. *et al.* A red-shifted, fast-relaxing azobenzene photoswitch for visible light control of an ionotropic glutamate receptor. *J Am Chem Soc* **135**, 17683-6 (2013).

61. Gorostiza, P. *et al.* Mechanisms of photoswitch conjugation and light activation of an ionotropic glutamate receptor. *Proc Natl Acad Sci U S A* **104**, 10865-70 (2007).

62. Szobota, S. *et al.* Remote control of neuronal activity with a light-gated glutamate receptor. *Neuron* **54**, 535-45 (2007).

63. Volgraf, M. *et al.* Allosteric control of an ionotropic glutamate receptor with an optical switch. *Nat Chem Biol* **2**, 47-52 (2006).

64. Tochitsky, I. *et al.* Optochemical control of genetically engineered neuronal nicotinic acetylcholine receptors. *Nat Chem* **4**, 105-11 (2012).

65. Levitz, J. *et al.* Optical control of metabotropic glutamate receptors. *Nat Neurosci* **16**, 507-16 (2013).

66. Striem-Amit, E., Guendelman, M. & Amedi, A. 'Visual' acuity of the congenitally blind using visual-to-auditory sensory substitution. *PLoS One* **7**, e33136 (2012).

67. Ward, J. & Meijer, P. Visual experiences in the blind induced by an auditory sensory substitution device. *Conscious Cogn* **19**, 492-500 (2010).

68. Kish, D. (2015).

69. Thaler, L., Arnott, S.R. & Goodale, M.A. Neural correlates of natural human echolocation in early and late blind echolocation experts. *PLoS One* **6**, e20162 (2011).

70. Thaler, L., Milne, J.L., Arnott, S.R., Kish, D. & Goodale, M.A. Neural correlates of motion processing through echolocation, source hearing, and vision in blind echolocation experts and sighted echolocation novices. *J Neurophysiol* **111**, 112-27 (2014).

71. Albuquerque, E.X., Pereira, E.F.R., Alkondon, M. & Rogers, S.W. Mammalian nicotinic acetylcholine receptors: from structure to function. *Physiological Reviews* **89**, 73-120 (2009).

72. Kew, J.N.C. & Davies, C.H. *Ion Channels: From Structure To Function*, xiii, 562 p. (Oxford University Press, Oxford, 2010).

73. Neher, E. & Sakmann, B. Single-channel currents recorded from membrane of denervated frog muscle fibres. *Nature* **260**, 799-802 (1976).

74. Unwin, N. Refined structure of the nicotinic acetylcholine receptor at 4A resolution. *J Membr Biol* **346**, 967-989 (2005).

75. Nowak, M.W. *et al.* Nicotinic receptor binding site probed with unnatural amino acid incorporation in intact cells. *Science* **268**, 439-442 (1995).

76. Noda, M. *et al.* Primary structure of alpha-subunit precursor of *Torpedo californica* acetylcholine receptor deduced from cdna sequence. *Nature* **299**, 793-797 (1982).

77. Noda, M. *et al.* Structural homology of *Torpedo californica* acetylcholine-receptor subunits. *Nature* **302**, 528-532 (1983).

78. Taly, A., Corringer, P.-J., Guedin, D., Lestage, P. & Changeux, J.-P. Nicotinic receptors: allosteric transitions and therapeutic targets in the nervous system. *Nat Rev Drug Discov* **8**, 733-750 (2009).

79. Kramer, R.H., Fortin, D.L. & Trauner, D. New photochemical tools for controlling neuronal activity. *Current Opinion in Neurobiology* **19**, 544-552 (2009).

80. Fehrentz, T., Schonberger, M. & Trauner, D. Optochemical genetics. *Angew Chem Int Ed Engl* **50**, 12156-82 (2011).

81. Fortin, D.L. *et al.* Optogenetic photochemical control of designer K+ channels in mammalian neurons. *Journal of Neurophysiology* **106**, 488-496 (2011).

82. Mourot, A. *et al.* Probing the reorganization of the nicotinic acetylcholine receptor during desensitization by time-resolved covalent labeling using [3H]AC5, a photoactivatable agonist. *Molecular Pharmacology* **69**, 452-461 (2006).

83. Hunt, R. & Renshaw, R.R. Some effects of derivatives of betaine amide and of choline ethers on the autonomic nervous system. *Journal of Pharmacology and Experimental Therapeutics* **35**, 99-128 (1929).

84. Wong, K.C. & Long, J.P. Nicotinic and muscarinic activity of phenacyl and phenylalkyl trimethylamines. *J Pharmacol Exp Ther* **137**, 70-5 (1962).

85. Gotti, C. *et al.* 4-Oxystilbene compounds are selective ligands for neuronal nicotinic αBungarotoxin receptors. *British Journal of Pharmacology* **124**, 1197-1206 (1998).

86. Celie, P.H.N. *et al.* Nicotine and carbamylcholine binding to nicotinic acetylcholine receptors as studied in AChBP crystal structures. *Neuron* **41**, 907-914 (2004).

87. Le Novère, N., Grutter, T. & Changeux, J.-P. Models of the extracellular domain of the nicotinic receptors and of agonist- and Ca2+-binding sites. *Proc. Natl. Acad. Sci. USA* **99**, 3210-3215 (2002).

88. Brejc, K. *et al.* Crystal structure of an ACh-binding protein reveals the ligand-binding domain of nicotinic receptors. *Nature* **411**, 269-276 (2001).

89. Hansen, S.B. *et al.* Structures of *Aplysia* AChBP complexes with nicotinic agonists and antagonists reveal distinctive binding interfaces and conformations. *EMBO J* **24**, 3635-3646 (2005).

90. Chavez-Noriega, L.E. *et al.* Pharmacological characterization of recombinant human neuronal nicotinic acetylcholine receptors hα2β2, hα2β4, hα3β2, hα3β4, hα4β2, hα4β4 and hα7 expressed in *Xenopus* oocytes. *Journal of Pharmacology and Experimental Therapeutics* **280**, 346-356 (1997).

91. Gotti, C., Zoli, M. & Clementi, F. Brain nicotinic acetylcholine receptors: native subtypes and their relevance. *Trends in Pharmacological Sciences* **27**, 482-491 (2006).

92. Nishimura N. *et al.* Thermal cis-to-trans isomerization of substituted azobenzenes II. Substituent and solvent effects. *Bulletin of the Chemical Society of Japan* **49**(1976).

93. Pozhidaeva, N., Cormier, M.E., Chaudhari, A. & Woolley, G.A. Reversible photocontrol of peptide helix content: adjusting thermal stability of the cis state. *Bioconjug Chem* **15**, 1297-303 (2004).

94. Bartels, E., Wassermann, N.H. & Erlanger, B.F. Photochromic activators of the acetylcholine receptor. *Proc. Natl. Acad. Sci. USA* **68**, 1820-1823 (1971).

95. Lester, H.A., Krouse, M.E., Nass, M.M., Wassermann, N.H. & Erlanger, B.F. A covalently bound photoisomerizable agonist: comparison with reversibly bound agonists at *Electrophorus* electroplaques. *J Gen Physiol* **75**, 207-232 (1980).

96. Barrantes, F.J. Modulation of acetylcholine receptor states by thiol modification. *Biochemistry* **19**, 2957-2965 (1980).

97. Cox, R.N., Kawai, M., Karlin, A. & Brandt, P.W. Voltage fluctuations at the frog sartorius motor endplate produced by a covalently attached activator. *J Membr Biol* **51**, 145-159 (1979).

98. Chabala, L.D. & Lester, H.A. Activation of acetylcholine receptor channels by covalently bound agonists in cultured rat myoballs. *J Physiol* **379**, 83-108 (1986).

99. Gorostiza, P. *et al.* Mechanisms of photoswitch conjugation and light activation of an ionotropic glutamate receptor. *Proc. Natl. Acad. Sci. USA* **104**, 10865-10870 (2007).

100. Banghart, M., Borges, K., Isacoff, E., Trauner, D. & Kramer, R.H. Light-activated ion channels for remote control of neuronal firing. *Nat Neurosci* **7**, 1381-6 (2004).

101. Sadovski, O., Beharry, A.A., Zhang, F.Z. & Woolley, G.A. Spectral tuning of azobenzene photoswitches for biological applications. *Angew. Chem. Int. Ed.* **48**, 1484-1486 (2009).

102. Mourot, A. *et al.* Tuning photochromic ion channel blockers. *ACS Chem Neurosci* **2**, 536-43 (2011).

103. Corringer, P.-J. *et al.* Atomic structure and dynamics of pentameric ligand-gated ion channels: new insight from bacterial homologues. *J Physiol* **588**, 565-572 (2010).

104. Bocquet, N. *et al.* A prokaryotic proton-gated ion channel from the nicotinic acetylcholine receptor family. *Nature* **445**, 116-119 (2007).

105. Hilf, R.J.C. & Dutzler, R. X-ray structure of a prokaryotic pentameric ligand-gated ion channel. *Nature* **452**, 375-379 (2008).

106. Law, R.J., Henchman, R.H. & McCammon, J.A. A gating mechanism proposed from a simulation of a human alpha7 nicotinic acetylcholine receptor. *Proc. Natl. Acad. Sci. USA* **102**, 6813-8 (2005).

107. Sullivan, D.A. & Cohen, J.B. Mapping the agonist binding site of the nicotinic acetylcholine receptor. Orientation requirements for activation by covalent agonist. *J Biol Chem* **275**, 12651-60 (2000).

108. Hibbs, R.E. & Gouaux, E. Principles of activation and permeation in an anion-selective cys-loop receptor. *Nature* **474**, 54-60 (2011).

109. Langmead, C.J., Watson, J. & Reavill, C. Muscarinic acetylcholine receptors as CNS drug targets. *Pharmacology & Therapeutics* **117**, 232-243 (2008).

110. Dani, J.A. & Bertrand, D. Nicotinic acetylcholine receptors and nicotinic cholinergic mechanisms of the central nervous system. *Annual Review of Pharmacology and Toxicology* **47**, 699-729 (2007).

111. Aravanis, A.M. *et al.* An optical neural interface: in vivo control of rodent motor cortex with integrated fiberoptic and optogenetic technology. *J Neural Eng* **4**, S143-56 (2007).

112. Thomas, K.R. & Capecchi, M.R. Site-directed mutagenesis by gene targeting in mouse embryo-derived stem cells. *Cell* **51**, 503-12 (1987).

113. Mourot, A., Bamberg, E. & Rettinger, J. Agonist- and competitive antagonist-induced movement of loop 5 on the alpha subunit of the neuronal alpha4beta4 nicotinic acetylcholine receptor. *J Neurochem* **105**, 413-24 (2008).

114. Friesner, R.A. *et al.* Glide: a new approach for rapid, accurate docking and scoring. 1. Method and assessment of docking accuracy. *J Med Chem* **47**, 1739-49 (2004).

115. Eldridge, M.D., Murray, C.W., Auton, T.R., Paolini, G.V. & Mee, R.P. Empirical scoring functions: I. The development of a fast empirical scoring function to estimate the binding affinity of ligands in receptor complexes. *J Comput Aided Mol Des* **11**, 425-45 (1997).

116. Baxter, C.A., Murray, C.W., Clark, D.E., Westhead, D.R. & Eldridge, M.D. Flexible docking using Tabu search and an empirical estimate of binding affinity. *Proteins: Structure, Function, and Bioinformatics* **33**, 367-382 (1998).

117. Larkin, M.A. *et al.* Clustal W and Clustal X version 2.0. *Bioinformatics* **23**, 2947-8 (2007).

118. Goujon, M. *et al.* A new bioinformatics analysis tools framework at EMBL-EBI. *Nucleic Acids Research* **38**, W695-W699 (2010).

119. Chatrenet, B. *et al.* Photoactivatable Agonist of the Nicotinic Acetylcholine-Receptor - Potential Probe to Characterize the Structural Transitions of the Acetylcholine Binding-Site in Different States of the Receptor. *Molecular Pharmacology* **41**, 1100-1106 (1992).

120. Hilf, R.J.C. & Dutzler, R. X-ray structure of a prokaryotic pentameric ligand-gated ion channel. *Nature* **452**, 375-U12 (2008).

121. Haghbeen, K. & Tan, E.W. Facile synthesis of catechol azo dyes. *Journal of Organic Chemistry* **63**, 4503-4505 (1998).

122. Shintani, K., Shechtman, D.L. & Gurwood, A.S. Review and update: current treatment trends for patients with retinitis pigmentosa. *Optometry* **80**, 384-401 (2009).

123. Marc, R.E., Jones, B.W., Watt, C.B. & Strettoi, E. Neural remodeling in retinal degeneration. *Prog Retin Eye Res* **22**, 607-55 (2003).

124. Leveillard, T. & Sahel, J.A. Rod-derived cone viability factor for treating blinding diseases: from clinic to redox signaling. *Sci Transl Med* **2**, 26ps16 (2010).

125. Mazzoni, F., Novelli, E. & Strettoi, E. Retinal ganglion cells survive and maintain normal dendritic morphology in a mouse model of inherited photoreceptor degeneration. *J Neurosci* **28**, 14282-92 (2008).

126. Haverkamp, S. *et al.* Synaptic plasticity in CNGA3(-/-) mice: cone bipolar cells react on the missing cone input and form ectopic synapses with rods. *J Neurosci* **26**, 5248-55 (2006).

127. Zrenner, E. *et al.* Subretinal electronic chips allow blind patients to read letters and combine them to words. *Proc Biol Sci* **278**, 1489-97 (2011).

128. Mandel, Y. *et al.* Cortical responses elicited by photovoltaic subretinal prostheses exhibit similarities to visually evoked potentials. *Nat Commun* **4**, 1980 (2013).

129. Twyford, P., Cai, C. & Fried, S. Differential responses to high-frequency electrical stimulation in ON and OFF retinal ganglion cells. *J Neural Eng* **11**, 025001 (2014).

130. Thyagarajan, S. *et al.* Visual function in mice with photoreceptor degeneration and transgenic expression of channelrhodopsin 2 in ganglion cells. *J Neurosci* **30**, 8745-58 (2010).

131. Nirenberg, S. & Pandarinath, C. Retinal prosthetic strategy with the capacity to restore normal vision. *Proc Natl Acad Sci U S A* **109**, 15012-7 (2012).

132. Lin, B., Koizumi, A., Tanaka, N., Panda, S. & Masland, R.H. Restoration of visual function in retinal degeneration mice by ectopic expression of melanopsin. *Proc Natl Acad Sci U S A* **105**, 16009-14 (2008).

133. Tochitsky, I. *et al.* Restoring Visual Function to Blind Mice with a Photoswitch that Exploits Electrophysiological Remodeling of Retinal Ganglion Cells. *Neuron* **81**, 800-13 (2014).

134. Polosukhina, A. *et al.* Photochemical restoration of visual responses in blind mice. *Neuron* **75**, 271-82 (2012).

135. Sandoz, G., Levitz, J., Kramer, R.H. & Isacoff, E.Y. Optical control of endogenous proteins with a photoswitchable conditional subunit reveals a role for TREK1 in GABA(B) signaling. *Neuron* **74**, 1005-14 (2012).

136. Reiner, A. & Isacoff, E.Y. Tethered ligands reveal glutamate receptor desensitization depends on subunit occupancy. *Nat Chem Biol* **10**, 273-80 (2014).

137. Sancho-Pelluz, J. *et al.* Photoreceptor cell death mechanisms in inherited retinal degeneration. *Mol Neurobiol* **38**, 253-69 (2008).

138. Marc, R.E. *et al.* Neural reprogramming in retinal degeneration. *Invest Ophthalmol Vis Sci* **48**, 3364-71 (2007).

139. Mandell, J.W., Czernik, A.J., De Camilli, P., Greengard, P. & Townes-Anderson, E. Differential expression of synapsins I and II among rat retinal synapses. *J Neurosci* **12**, 1736-49 (1992).

140. Masu, M. *et al.* Specific deficit of the ON response in visual transmission by targeted disruption of the mGluR6 gene. *Cell* **80**, 757-65 (1995).

141. Roska, B., Busskamp, V., Sahel, J.A. & Picaud, S. [Retinitis pigmentosa: eye sight restoration by optogenetic therapy]. *Biol Aujourdhui* **207**, 109-21 (2013).

142. Busskamp, V., Picaud, S., Sahel, J.A. & Roska, B. Optogenetic therapy for retinitis pigmentosa. *Gene Ther* **19**, 169-75 (2012).

143. Rockhill, R.L., Daly, F.J., MacNeil, M.A., Brown, S.P. & Masland, R.H. The diversity of ganglion cells in a mammalian retina. *J Neurosci* **22**, 3831-43 (2002).

144. Kong, J.H., Fish, D.R., Rockhill, R.L. & Masland, R.H. Diversity of ganglion cells in the mouse retina: unsupervised morphological classification and its limits. *J Comp Neurol* **489**, 293-310 (2005).

145. Gargini, C., Terzibasi, E., Mazzoni, F. & Strettoi, E. Retinal organization in the retinal degeneration 10 (rd10) mutant mouse: a morphological and ERG study. *J Comp Neurol* **500**, 222-38 (2007).

146. Wong, A.A. & Brown, R.E. Visual detection, pattern discrimination and visual acuity in 14 strains of mice. *Genes Brain Behav* **5**, 389-403 (2006).

147. Beltran, W.A. The use of canine models of inherited retinal degeneration to test novel therapeutic approaches. *Vet Ophthalmol* **12**, 192-204 (2009).

148. Beltran, W.A. *et al.* Canine retina has a primate fovea-like bouquet of cone photoreceptors which is affected by inherited macular degenerations. *PLoS One* **9**, e90390 (2014).

149. Wassle, H., Puller, C., Muller, F. & Haverkamp, S. Cone contacts, mosaics, and territories of bipolar cells in the mouse retina. *J Neurosci* **29**, 106-17 (2009).

150. Jacobs, A.L. & Werblin, F.S. Spatiotemporal patterns at the retinal output. *J Neurophysiol* **80**, 447-51 (1998).

151. Ray, K., Baldwin, V.J., Acland, G.M., Blanton, S.H. & Aguirre, G.D. Cosegregation of codon 807 mutation of the canine rod cGMP phosphodiesterase beta gene and rcd1. *Invest Ophthalmol Vis Sci* **35**, 4291-9 (1994).

152. Buyukmihci, N., Aguirre, G. & Marshall, J.A.G. Retinal degenerations in the dog. II. Development of the retina in rod-cone dysplasia. *Exp Eye Res* **30**, 575-91 (1980).

153. Suber, M.L. *et al.* Irish setter dogs affected with rod/cone dysplasia contain a nonsense mutation in the rod cGMP phosphodiesterase beta-subunit gene. *Proc Natl Acad Sci U S A* **90**, 3968-72 (1993).

154. Grieger, J.C., Choi, V.W. & Samulski, R.J. Production and characterization of adeno-associated viral vectors. *Nat Protoc* **1**, 1412-28 (2006).

155. Reiner, A. & Isacoff, E.Y. Photoswitching of cell surface receptors using tethered ligands. in *Photoswitching Proteins*, Vol. 1148 (ed. Sidney, C.) (Springer, 2014).

156. Roska, B., Molnar, A. & Werblin, F.S. Parallel processing in retinal ganglion cells: how integration of space-time patterns of excitation and inhibition form the spiking output. *J Neurophysiol* **95**, 3810-22 (2006).

157. Numano, R. *et al.* Nanosculpting reversed wavelength sensitivity into a photoswitchable iGluR. *Proc Natl Acad Sci U S A* **106**, 6814-9 (2009).

158. Bainbridge, J.W. *et al.* Effect of gene therapy on visual function in Leber's congenital amaurosis. *N Engl J Med* **358**, 2231-9 (2008).

159. Vinores, S.A. *et al.* Blood-retinal barrier breakdown in retinitis pigmentosa: light and electron microscopic immunolocalization. *Histol Histopathol* **10**, 913-23 (1995).

160. Shen, Y. *et al.* A transient receptor potential-like channel mediates synaptic transmission in rod bipolar cells. *J Neurosci* **29**, 6088-93 (2009).

161. Moritz, O.L., Tam, B.M., Papermaster, D.S. & Nakayama, T. A functional rhodopsin-green fluorescent protein fusion protein localizes correctly in transgenic Xenopus laevis retinal rods and is expressed in a time-dependent pattern. *J Biol Chem* **276**, 28242-51 (2001).

162. Brown, T.M. *et al.* Melanopsin-based brightness discrimination in mice and humans. *Curr Biol* **22**, 1134-41 (2012).

163. Dalkara, D. & Sahel, J.A. Gene therapy for inherited retinal degenerations. *C R Biol* **337**, 185-92 (2014).

164. Morgan, J.I. *et al.* Light-induced retinal changes observed with high-resolution autofluorescence imaging of the retinal pigment epithelium. *Invest Ophthalmol Vis Sci* **49**, 3715-29 (2008).

165. Masseck, O.A. *et al.* Vertebrate cone opsins enable sustained and highly sensitive rapid control of Gi/o signaling in anxiety circuitry. *Neuron* **81**, 1263-73 (2014).

166. Cao, P. *et al.* Light-sensitive coupling of rhodopsin and melanopsin to G(i/o) and G(q) signal transduction in Caenorhabditis elegans. *FASEB J* **26**, 480-91 (2012).

167. Li, X. *et al.* Fast noninvasive activation and inhibition of neural and network activity by vertebrate rhodopsin and green algae channelrhodopsin. *Proc Natl Acad Sci U S A* **102**, 17816-21 (2005).

168. Newport. Optical-Radiation-Terminology-and-Units. Newport.

169. Concepcion, F., Mendez, A. & Chen, J. The carboxyl-terminal domain is essential for rhodopsin transport in rod photoreceptors. *Vision Res* **42**, 417-26 (2002).

170. Kodama, T. *et al.* Expression and localization of an exogenous G protein-coupled receptor fused with the rhodopsin C-terminal sequence in the retinal rod cells of knockin mice. *Exp Eye Res* **80**, 859-69 (2005).

171. Krautwurst, D., Yau, K.W. & Reed, R.R. Identification of ligands for olfactory receptors by functional expression of a receptor library. *Cell* **95**, 917-26 (1998).

172. Lodowski, K.H. *et al.* Signals governing the trafficking and mistrafficking of a ciliary GPCR, rhodopsin. *J Neurosci* **33**, 13621-38 (2013).